8-2017

Surface modification of icy satellites: Space weathering of the large moons of Uranus and alluvial fan formation on Saturn's moon Titan

Richard John Cartwright
University of Tennessee, Knoxville, rcartwri@vols.utk.edu

To the Graduate Council:

I am submitting herewith a dissertation written by Richard John Cartwright entitled "Surface modification of icy satellites: Space weathering of the large moons of Uranus and alluvial fan formation on Saturn's moon Titan." I have examined the final electronic copy of this dissertation for form and content and recommend that it be accepted in partial fulfillment of the requirements for the degree of Doctor of Philosophy, with a major in Geology.

Joshua P. Emery, Devon M. Burr, Major Professor

We have read this dissertation and recommend its acceptance:

Jeffrey Moersch, Nicholas Nagle

Accepted for the Council:
Dixie L. Thompson

Vice Provost and Dean of the Graduate School

(Original signatures are on file with official student records.)

Surface modification of icy satellites: Space weathering of the large moons of Uranus and alluvial fan formation on Saturn's moon Titan

A Dissertation Presented for the
Doctor of Philosophy
Degree
The University of Tennessee, Knoxville

Richard John Cartwright
August 2017

DEDICATION

To my wife and parents for their unending support.

ACKNOWLEDGEMENTS

First and foremost, I want to express my unending gratitude for the support I have received from my wife and family as I pursued my Ph.D. I want to express my deepest appreciation for the guidance provided by my advisors, Joshua Emery and Devon Burr, as well as the other members of my committee, Jeffrey Moersch and Nicholas Nagle. I thank Noemi Pinilla-Alonso, Sean Lindsay, Driss Takir, and all members of the EMERGE and BRIGHT research groups for providing guidance and lending their wisdom along the way. I also thank the Infrared Telescope Facility (IRTF) staff, support astronomers, and the people of Hawaii for allowing me to use the IRTF on Mauna Kea. Funding for the work presented in this dissertation was provided by the, the Planetary Astronomy Program (grant NNX10AB23G), the NASA Earth and Space Science Fellowship program (grant PLANET14F-0020), and the Solar System Observing program (grant 16-SSO016_2-0070). I thank Tom Cronin and Helen Sestak for providing additional financial support during my tenure at the University of Tennessee.

ABSTRACT

The surfaces of icy satellites are continually modified by space weathering and geologic processes. This dissertation explores the processes changing the surface compositions of the large moons of Uranus and mechanisms for development of possible alluvial fans on the Saturnian moon, Titan. On the Uranian satellites, I hypothesize that the origin and distribution of carbon dioxide ice results from charged particle bombardment, and that spectrally red material originated on retrograde irregular satellites. On Titan, I hypothesize that landforms identified as alluvial fans at low and mid latitudes were formed by sheetfloods, whereas possible alluvial fans at high latitudes were formed by debris flows.

To test whether charged particle radiolysis drives carbon dioxide ice synthesis on the classical Uranian moons, I gathered new near-infrared (NIR) reflectance spectra over a range of satellite longitudes, and measured the areas of carbon dioxide ice bands in these data to constrain its distribution on their surfaces. I found that the abundance of carbon dioxide ice peaks on the trailing hemispheres of the moons closer to Uranus (Ariel and Umbriel), consistent with radiolytic production of carbon dioxide ice via magnetospherically-embedded charged particle bombardment. Using these same NIR spectra, I measured the spectral slopes and areas of water ice bands to constrain the distribution of red material on these moons. My water ice band area and spectral slope measurements indicate that red material is most abundant on the leading hemispheres of the outer moons, Titania and Oberon, consistent with delivery of red dust from the irregular moons.

To test alluvial fan formation mechanisms on Titan, I measured the radar backscatter of possible alluvial fans located at different latitudes on Titan, and compared these backscatter measurements to alluvial fans formed by sheetfloods and debris flows on Earth. My results indicate that backscatter from possible fans at high latitudes on Titan is more consistent with sheetflood fans on Earth, and backscatter from low- and mid-latitude possible fans on Titan is more consistent with terrestrial debris flow fans. I explore the geomorphic and sedimentological implications of these results.

TABLE OF CONTENTS

LIST OF TABLES

LIST OF FIGURES

INTRODUCTION

The 'classical' (i.e., large and tidally-locked) icy satellites orbiting the giant planets display a wide diversity of surface compositions and landforms that are continually evolving. Most of these icy moons have surfaces dominated by H_2O ice (e.g., Johnson and McCord, 1971, Fink et al., 1976, Johnson and Pilcher, 1977; Cruikshank et al., 1977; Cruikshank, 1980; Cruikshank et al., 2000). Many icy satellite surfaces have deposits of volatile, carbon-rich constituents, such as CO_2 ice, exposed on their surfaces (e.g., Cruikshank et al., 1993; Carlson et al., 1996; Johnson et al., 1998; Grundy et al., 2006; Cruikshank et al., 2010). Icy moons display a wide range of surface features, including impact craters and basins, tectonic provinces dominated by faults and ridges, extrusive jets streaming material into space, and other remarkable geologic landforms (e.g., Johnson, 2005, and references therein, Porco et al., 2006, Collins et al., 2013, and references therein).

The inhospitable environments surrounding classical icy satellites contain charged and neutral particles and dust grains that bombard the surfaces of these moons. These agents of space weathering promote chemical changes in exposed constituents in the regoliths and tenuous atmospheres of these moons (e.g., Bennett et al., 2013, and references therein). Because classical satellites are tidally-locked, their orbital and rotational periods are the same. Therefore, these moons have 'leading' and 'trailing' hemispheres that face in the forwards and backwards directions, respectively, as they orbit their giant planet primaries. Over time, space weather and geologic processes can enhance compositional asymmetries between the leading and trailing hemispheres of classical moons.

Unlike other icy satellites, the surface of the Saturnian moon, Titan, is shielded from space weathering due to its thick and vertically extended atmosphere, dominated by N_2, CH_4, and other species (Kuiper, 1944; Trafton, 1972; Hunten, 1974; Atreya et al., 1978). Titan's atmosphere is continually irradiated by charged particles caught in Saturn's magnetic field and UV photons, generating a wide range of complex organic aerosols (e.g., Atreya et al., 1978; Niemann et al., 2005; Lunine and Atreya, 2008). Titan's thick atmosphere has played a key role in reshaping the surface of Titan through aeolian and fluvial processes, as evidenced by the large sand seas (Lorenz et al., 2006) and liquid hydrocarbon lakes (Stofan et al., 2007), which are likely filled by precipitated methane and other species from Titan's atmosphere, possibly similar to H_2O rain on Earth (e.g., Lunine and Atreya, 2008). Therefore, the processes modifying the surface of Titan are similar to those we experience on Earth, albeit, they operate at vastly lower temperatures (mean equatorial surface temperature ~94 K). This dissertation investigates surface modification by space weathering processes of the large moons of Uranus (Chapters 1 and 3) and fluvial modification of the surface of Titan (Chapter 2).

The surfaces of the classical Uranian moons are primarily composed of H_2O ice, mixed with a dark, spectrally neutral, and likely carbonaceous, constituent (e.g., Cruikshank, 1980; Cruikshank and Brown, 1981; Soifer et al., 1981; Brown and Cruikshank, 1983; Brown and Clark, 1984). Near-infrared (NIR) observations (~0.7 – 2.5

μm) of these moons, over southern latitudes (subsolar point between ~6 – 24ºS) have detected pure and segregated CO_2 ice, primarily on the trailing hemispheres of the inner moons, Ariel and Umbriel (Grundy et al., 2003; 2006), but not on Miranda (*e.g.*, Bauer et al., 2002). Because Uranus rotates faster (~17 hours) than the orbital periods of the classical moons (~1.5 to 13.5 days), charged particles caught in Uranus' magnetic field should preferentially interact with the trailing hemispheres of the classical satellites as Uranus' magnetic field lines sweep past them.

In Chapter 1, I hypothesize that magnetospherically-embedded charged particles drive a radiolytic production cycle of CO_2 ice from native H_2O ice and C-rich materials exposed on their surfaces. To test this hypothesis, I gathered new NIR reflectance spectra (~0.7 – 2.5 μm) of the Uranian moons' leading and trailing hemispheres over northern latitudes (subsolar point ~17 – 35ºN), using the SpeX spectrograph on NASA's Infrared Telescope Facility (IRTF) on Mauna Kea (Rayner et al., 1998; 2003). I measured the areas and central positions of the three strongest CO_2 ice bands, located between 1.9 and 2.1 μm. I found that the strength of these CO_2 bands peaks on the trailing hemispheres of the moons closest to Uranus, consistent with previous observations of these moons at southern latitudes (Grundy et al., 2006). Additionally, my measurements indicate that the relative areas of these bands and their central positions (near 1.966, 2.012, and 2.070 μm) are consistent with pure CO_2 ice (e.g., Gerakines et al., 2005), in particular on Ariel. Thus, CO_2 ice has been detected on the trailing hemispheres of these moons, over both southern (Grundy et al., 2003; 2006) and northern (Cartwright et al., 2015) latitudes. The longitudinal and latitudinal distribution of CO_2 ice supports the charged particle bombardment hypothesis for the origin of this volatile constituent on these moons.

Observations made by the Imaging Science System during the Voyager 2 flyby of the Uranian system indicated that the leading hemispheres of the classical Uranian moons are spectral redder (i.e., increasing reflectance with increasing wavelength) than their trailing hemispheres (Bell and McCord, 1991; Buratti and Mosher, 1991; Helfenstein et al.1991). Furthermore, the degree of reddening increases with distance from Uranus, peaking on the farthest classical satellite, Oberon (Buratti and Mosher, 1991). These observations were made near southern summer solstice (subsolar point ~81ºS), when the northern hemispheres of these moons were shrouded in winter darkness. Dynamical modeling suggests that the most plausible process for reddening the leading hemispheres of the outer moons is accumulation of planetocentric dust from the retrograde irregular satellites (Tamayo et al., 2013), which are redder than the classical moons (e.g., Maris et al., 2007).

In chapter 3, I hypothesize that the red material observed on these moons originated on the retrograde irregular satellites of Uranus. To test this hypothesis, I analyzed the spectral slopes (between 0.7 and 1.3 μm) in the NIR spectra we gathered using IRTF/SpeX over the now observable northern hemispheres of these moons. Analysis of these data demonstrates that the leading hemispheres of these moons are redder than their trailing hemispheres, and that the outer moons are redder than the inner moons. Thus, the observed planetocentric and hemispherical trends in reddening support the hypothesis that red material originated on the surfaces of the irregular satellites.

Fluvial landforms are found at all latitudes on Titan (e.g., Burr et al., 2013). Some of these landforms have been identified as alluvial fans (Moore and Howard, 2010; Radebaugh et al., 2016; Birch et al., 2016). The possible presence of alluvial fans on Titan could shed light on the hydrological ('methanological') cycle on Titan, as well as the dominant grain sizes of fluvially-transported sediments. On Earth, alluvial fans form via two types of processes: fluid-gravity (sheetfloods) and sediment-gravity (debris flows) flows (e.g., Costa, 1988). Along the Panamint mountains in Death Valley, California, seven sheetflood fans are located adjacent to seven debris flow fans. The climate and tectonic history of these fourteen fans are essentially the same; however, their catchment lithologies are quite different, with the debris flow fan catchments rich in clays and poor in sand, and the sheetflood fan catchments rich in sand whereas clay sediments are scarce (e.g., Blair and McPherson, 1994; Blair, 1999). On Titan, the low and mid latitudes are dominated by sand seas, indicating that sand-sized particles are available for transport, whereas at high latitudes, sand seas are entirely absent (e.g., Lopes et al., 2010; Moore et al., 2014), suggesting that transportable sand is scarce. Given this inferred latitudinal dichotomy in the dominant grain size of available sediment on Titan, different alluvial fan formation mechanisms could operate at different latitudes.

In Chapter 2, I hypothesize that low- and mid-latitude possible fans on Titan are formed primarily by sheetfloods, and high-latitude possible fans are formed primarily by debris flows. To test this hypothesis, I measured the mean radar backscatter (σ^0), and normalized downfan σ^0, for the sheetflood and debris flow fans along the Panamint Range on Earth. My results and analyses demonstrate clear differences in σ^0 between these two fan types, with greater radar signal returned from debris flow fan surfaces. I compared these results to possible fans on Titan and found that the backscatter from low- and mid-latitude possible fans is more consistent with terrestrial debris flow fans, and the backscatter from high-latitude possible fans is more consistent with sheetflood fans. Consequently, my results and analyses do not support my hypotheses for this project. Possible explanations include: (1) the lack of rugged terrains at high latitudes limits the availability of coarse grained sediment (*i.e.*, cobbles and boulders), spurring alluvial fan formation primarily via sheetfloods at high latitudes, whereas coarse grained sediment is more abundant at low latitudes, spurring alluvial fan formation via debris flows and sheetfloods, (2) radar backscatter from debris flow and sheetflood deposits are different on the organic-rich surface of Titan compared to the silicate-rich surface of Earth, (3) alluvial fan formation is different in the low gravity environment of Titan, and (4) the observed possible fans formed from non-alluvial processes.

In summary, this dissertation explores surface modification of airless moons in the Uranian system (by space weathering processes) and modification of the atmosphere-enveloped surface of Titan (by fluvial processes). The work presented here adds new key knowledge regarding the compositions and origin of constituents on the classical Uranian satellites, and on the processes that could be forming fan-shaped fluvial features on Titan.

References

Atreya, S.K., Donahue, T.M. and Kuhn, W.R., 1978. Evolution of a nitrogen atmosphere on Titan. *Science*, *201*(4356), p.611-613.

Bell III, J.F. and McCord, T.B., 1991. A search for spectral units on the Uranian satellites using color ratio images. In *Lunar and Planetary Science Conference Proceedings* (Vol. 21, p. 473-489).

Bennett, C.J., Pirim, C. and Orlando, T.M., 2013. Space-weathering of solar system bodies: a laboratory perspective. *Chemical reviews*, *113* (12), p.9086-9150.

Birch, S.P.D., Hayes, A.G., Howard, A.D., Moore, J.M. and Radebaugh, J., 2016. Alluvial Fan Morphology, distribution and formation on Titan. *Icarus*, *270*, p.238-247.

Blair, T.C. and McPherson, J.G., 1994. Alluvial fans and their natural distinction from rivers based on morphology, hydraulic processes, sedimentary processes, and facies assemblages. *Journal of sedimentary research*, *64* (3).

Blair, T.C., 1999. Cause of dominance by sheetflood vs. debris-flow processes on two adjoining alluvial fans, Death Valley, California.*Sedimentology*, *46* (6), p.1015-1028.

Brown, R.H. and Clark, R.N., 1984. Surface of Miranda: Identification of water ice. *Icarus*, *58* (2), p.288-292.

Brown, R.H. and Cruikshank, D.P., 1983. The Uranian satellites: Surface compositions and opposition brightness surges. *Icarus*, *55* (1), p.83-92.

Buratti, B.J. and Mosher, J.A., 1991. Comparative global albedo and color maps of the uranian satellites. *Icarus*, *90* (1), p.1-13.

Burr, D.M., Drummond, S.A., Cartwright, R., Black, B.A. and Perron, J.T., 2013. Morphology of fluvial networks on Titan: Evidence for structural control. *Icarus*, *226* (1), p.742-759.

Carlson, R. et al., 1996. Near-infrared spectroscopy and spectral mapping of Jupiter and the Galilean satellites: Results from Galileo's initial orbit. *Science, 274* (5286), p.385-388.

Cartwright, R.J., Emery, J.P., Rivkin, A.S., Trilling, D.E. and Pinilla-Alonso, N., 2015. Distribution of CO_2 ice on the large moons of Uranus and evidence for compositional stratification of their near surfaces. *Icarus*, *257*, p.428-456.

Collins, G.C., McKinnon, W.B., Moore, J.M., Nimmo, F., Pappalardo, R.T., Prockter, L.M. and Schenk, P.M., 2009. Tectonics of the outer planet satellites. *Planetary Tectonics*, *11*, p.264.
Costa, J.E., 1988. Rheologic, geomorphic, and sedimentologic differentiation of water floods, hyperconcentrated flows, and debris flows. *Flood Geomorphology. John Wiley & Sons New York.* p.113-122.

Cruikshank, D.P., 1980. Near-infrared studies of the satellites of Saturn and Uranus. *Icarus*, *41* (2), p.246-258.

Cruikshank, D.P. and Brown, R.H., 1981. The uranian satellites: Water ice on Ariel and Umbriel. *Icarus*, *45* (3), p.607-611.

Cruikshank, D.P. et al., 2010. Carbon dioxide on the satellites of Saturn: Results from the Cassini VIMS investigation and revisions to the VIMS wavelength scale. *Icarus, 206*, 561-572, doi:10.1016/j.icarus.2009.07.012.

Cruikshank, D.P. et al., 2000. Water ice on Triton. *Icarus*, *147* (1), pp.309-316.
Cruikshank, D.P., Morrison, D. and Pilcher, C.B., 1977. Identification of a new class of satellites in the outer solar system. *The Astrophysical Journal*, *217*, p.1006-1010.

Cruikshank, D.P., Roush, T.L., Owen, T.C., Geballe, T.R., De Bergh, C., Schmitt, B., Brown, R.H. and Bartholomew, M.J., 1993. Ices on the surface of Triton. *Science*, *261* (5122), p.742-746.

Fink, U., Dekkers, N.H. and Larson, H.P., 1973. Infrared spectra of the Galilean satellites of Jupiter. *The Astrophysical Journal*, *179*, p.L155.

Gerakines, P.A., Bray, J.J., Davis, A. and Richey, C.R., 2005. The strengths of near-infrared absorption features relevant to interstellar and planetary ices. *The Astrophysical Journal*, *620* (2), p.1140.

Grundy, W.M., Young, L.A. and Young, E.F., 2003. Discovery of CO_2 ice and leading–trailing spectral asymmetry on the uranian satellite ariel. *Icarus*, *162* (1), p.222-229.

Grundy, W.M., Young, L.A., Spencer, J.R., Johnson, R.E., Young, E.F. and Buie, M.W., 2006. Distributions of H 2 O and CO 2 ices on Ariel, Umbriel, Titania, and Oberon from IRTF/SpeX observations. *Icarus*, *184* (2), p.543-555.

Helfenstein, P. et al., 1991. Oberon color photometry from Voyager and its geological implications. Icarus 90, p.14–29.

Hunten, D.M., 1974. The atmosphere of Titan. *Icarus*, *22* (1), p.111-116.

Johnson, T.V., 2005. Geology of the Icy Satellites. *Space Science Reviews, 116*, p.401-420.

Johnson, T.V. and McCord, T.B., 1971. Spectral geometric albedo of the Galilean satellites, 0.3 to 2.5 microns. *The Astrophysical Journal, 169*, p.589.

Johnson, T.V. and Pilcher, C.B., 1977. Satellite spectrophotometry and surface compositions. In *IAU Colloq. 28: Planetary Satellites*, p. 232-268.

Kuiper, G.P., 1944. Titan: a Satellite with an Atmosphere. *The Astrophysical Journal*, *100*, p.378.

Lopes, R.M.C. et al., 2010. Distribution and interplay of geologic processes on Titan from Cassini radar data. *Icarus*, *205* (2), p.540-558.

Lorenz, R.D., Wall, S., Radebaugh, J., Boubin, G., Reffet, E., Janssen, M., Stofan, E., Lopes, R., Kirk, R., Elachi, C. and Lunine, J., 2006. The sand seas of Titan: Cassini RADAR observations of longitudinal dunes. *Science*, *312*(5774), p.724-727.

Lunine, J.I. and Atreya, S.K., 2008. The methane cycle on Titan. *Nature Geoscience*, *1* (3), p.159-164.

Maris, M., Carraro, G. and Parisi, M.G., 2007. Light curves and colours of the faint Uranian irregular satellites Sycorax, Prospero, Stephano, Setebos, and Trinculo. *Astronomy & Astrophysics*, *472* (1), p.311-319.

McCord, T.A. et al., 1998. Non-water-ice constituents in the surface material of the icy Galilean satellites from the Galileo near-infrared mapping spectrometer investigation. *Journal of Geophysical Research: Planets*, *103* (E4), p.8603-8626.
Moore, J.M. and Howard, A.D., 2010. Are the basins of Titan's Hotei Regio and Tui Regio sites of former low latitude seas?. *Geophysical Research Letters*, *37* (22).

Moore, J.M., Howard, A.D. and Morgan, A.M., 2014. The landscape of Titan as witness to its climate evolution. *Journal of Geophysical Research: Planets*, *119* (9), p.2060-2077.

Niemann, H.B. et. al., 2005. The abundances of constituents of Titan's atmosphere from the GCMS instrument on the Huygens probe. *Nature*, *438* (7069), p.779-784.

Porco, C.C. et al., 2006. Cassini observes the active south pole of Enceladus. *science*, *311* (5766), p.1393-1401.

Radebaugh, J. et al., 2016. Alluvial and fluvial fans on Saturn's moon Titan reveal processes, materials and regional geology. *Geological Society, London, Special Publications*, *440*, p.SP440-6.

Rayner, J.T. et al., 1998. SpeX: A medium-resolution IR spectrograph for IRTF. Proc. SPIE 3354, p.468–479.

Rayner, J.T. et al., 2003. SpeX: A medium-resolution 0.8–5.5 micron spectrograph and imager for the NASA Infrared Telescope Facility. Astron. Soc. Pacific, p.115, 362.

Soifer, B.T., Neugebauer, G. and Matthews, K., 1981. Near-infrared spec.trophotometry of the satellites and rings of Uranus. *Icarus*, *45*(3), p.612-617.

Stofan, E.R. et al., 2007. The lakes of Titan. *Nature*, *445* (7123), p.61-64.

Tamayo, D., Burns, J.A. and Hamilton, D.P., 2013. Chaotic dust dynamics and implications for the hemispherical color asymmetries of the Uranian satellites. *Icarus*, *226* (1), p.655-662.

Trafton, L., 1972. The bulk composition of Titan's atmosphere. *The Astrophysical Journal*, *175*, p.295.

CHAPTER 1:

DISTRIBUTION OF CO_2 ICE ON THE LARGE MOONS OF URANUS AND EVIDENCE FOR COMPOSITIONAL STRATIFICATION OF THEIR NEAR-SURFACES

This chapter is a reformatted version of a paper by the same name published in Icarus in 2015 by Richard Cartwright, Joshua Emery, Andy Rivkin, David Trilling, and Noemi Pinilla-Alonso. The work presented here includes additional changes not included in the published version of this manuscript. All data collection and analyses were performed by Richard Cartwright.

Cartwright, R.J., Emery, J.P., Rivkin, A.S., Trilling, D.E., and Pinilla-Alonso, N., 2015. Distribution of CO_2 ice on the large moons of Uranus and evidence for compositional stratification of their near-surfaces. *Icarus*, *257*, 428-456.
http://dx.doi.org/10.1016/j.icarus.2015.05.020

Abstract

The surfaces of the large Uranian satellites are characterized by a mixture of H_2O ice and a dark, potentially carbon-rich, constituent, along with CO_2 ice. At the mean heliocentric distance of the Uranian system, native CO_2 ice should be removed on timescales shorter than the age of the Solar System. Consequently, the detected CO_2 ice might be actively produced. Analogous to irradiation of icy moons in the Jupiter and Saturn systems, we hypothesize that charged particles caught in Uranus' magnetic field bombard the surfaces of the Uranian satellites, driving a radiolytic CO_2 production cycle. To test this hypothesis, we investigated the distribution of CO_2 ice by analyzing near-infrared (NIR) spectra of these moons, gathered using the SpeX spectrograph at NASA's Infrared Telescope Facility (IRTF) (2000 – 2013). Additionally, we made spectrophotometric measurements using images gathered by the Infrared Array Camera (IRAC) onboard the Spitzer Space Telescope (2003 – 2005). We find that the detected CO_2 ice is primarily on the trailing hemispheres of the satellites closest to Uranus, consistent with other observations of these moons. Our band parameter analysis indicates that the detected CO_2 ice is pure and segregated from other constituents. Our spectrophotometric analysis indicates that IRAC is not sensitive to the CO_2 ice detected by SpeX, most likely because CO_2 is retained beneath a thin surface layer dominated by H_2O ice that is opaque to photons over IRAC wavelengths. Thus, our combined SpeX and IRAC analyses suggest that the near-surfaces (i.e., top few 100 microns) of the Uranian satellites are compositionally stratified. We briefly compare the spectral characteristics of the CO_2 ice detected on the Uranian moons to icy satellites elsewhere, and consider the most likely drivers of the observed distribution of CO_2 ice.

Introduction

Spatially resolved images gathered by the Imaging Science System (ISS) onboard Voyager 2 revealed that the surfaces of the classical (*i.e.*, large and tidally-locked) Uranian satellites Miranda, Ariel, Umbriel, Titania, and Oberon (Table 1.1) are grayish in tone, with bright patches generally associated with impact features and tectonized terrain (*e.g.*, Smith et al., 1986). Analysis of ISS images demonstrated that the Uranian satellites' leading hemispheres are spectrally redder than their trailing hemispheres, and the amount of reddening appears to increase with increasing distance from Uranus (Bell and McCord, 1991; Buratti and Mosher, 1991; Helfenstein et al., 1991). These satellites display abundant evidence of tectonic resurfacing, ranging from tectonized coronae and chasmata on Miranda (*e.g.*, Pappalardo et al., 1997; Beddingfield et al., 2015) to subtle polygonal basins observed on Umbriel (Helfenstein et al., 1989). Numerous studies have presented evidence for potential cryovolcanic landforms on each of these moons, from flow bands with medial grooves on Ariel, smooth patches with convex edges on Titania, and smooth, low and high albedo deposits on crater floors on Umbriel and Oberon (*e.g.*, Jankowski and Squyres, 1989; Schenk, 1991; Croft and Soderblom, 1991; Kargel 1994). Surface age estimates range from a few 100 Ma for younger terrains on Ariel to > 4 Ga for most of the ancient surface of Umbriel (Zahnle et al., 2003). Geologic interpretation of these satellites' surfaces, however, is limited by the low spatial resolution of the ISS dataset, ranging from a few 100 m/pixel on Miranda to ~6 km/pixel on Oberon.

While Voyager 2's flyby of Uranus returned a wealth of information, (*e.g.*, Stone and Miller, 1986) it is the only spacecraft to visit the Uranian system. Consequently, compositional analysis of Oberon, Titania, Umbriel, Ariel, and Miranda is much less-well developed than that of their Jovian and Saturnian counterparts, which have been imaged extensively by the Galileo and Cassini spacecraft, respectively. Ground-based observations of the large Uranian satellites indicate that their surfaces are dominated by H_2O ice mixed with a low-albedo constituent, which is spectrally neutral over NIR wavelengths (*e.g.*, Soifer et al., 1981; Brown and Cruikshank, 1983; Brown and Clark, 1984). Although the low albedo constituent detected on the surfaces of the Uranian satellites has yet to be uniquely identified, spectral modeling suggests that it is likely carbon-rich (*e.g.*, Clark and Lucey, 1984).

More recent NIR observations of these moons led to the detection of CO_2 ice on Ariel, Umbriel, and Titania, principally on their trailing hemispheres (Grundy et al., 2003, 2006). Additionally, Grundy et al. (2006) found that the abundance of CO_2 ice decreases with increasing orbital radius, with no detection on the most distant classical satellite, Oberon. This trend of increasing CO_2 ice abundance on the inner moons is not observed on the innermost Miranda, where CO_2 ice has yet to be detected (Bauer et al., 2002; Grundy et al., 2006). A host of loss mechanisms (*e.g.*, sublimation, UV photolysis, micrometeorite bombardment, and charged particle sputtering) should effectively remove CO_2 from their surfaces over timescales shorter than the age of the Solar System (*e.g.* Grundy et al., 2006). Consequently, the detection of CO_2 on the Uranian moons suggests that it is actively produced by non-native processes. Grundy et al. (2006) suggest that bombardment of native H_2O ice and C-rich constituents on the Uranian satellite surfaces

by magnetospherically-bound charged particles could drive a radiolytic production cycle of CO_2 ice.

Magnetic field interactions with icy satellite surfaces are well documented in the Jupiter and Saturn systems. UV spectra of Europa's trailing hemisphere display an enhanced absorption feature near 280 nm (attributed to SO_2) that likely originated from magnetospherically-embedded sulfur ions irradiating H_2O ice on Europa's surface (Lane et al., 1981; Ockert et al., 1987; Noll et al., 1995). An albedo minimum near 260 nm in UV spectra of Rhea and Dione has been attributed to magnetospherically-generated O_3 trapped in the H_2O ice matrix on these moons' surfaces (Noll et al., 1997). The magnetic fields of Jupiter, Saturn, and Uranus all co-rotate with the planets, and at a faster rate than the orbital periods of their regular moons. Consequently, charged particles caught in these planet's magnetic fields preferentially interact with the trailing hemispheres of their classical satellite systems. Unlike the magnetic fields of Jupiter and Saturn, Uranus' magnetic field is substantially offset from its rotational axis (~58.6°) and from its center of mass (~0.3 Uranian radii). Thus, the Uranian moons orbit through a wide range of magnetic latitudes and L shells (*i.e.*, magnetic field lines that cross the magnetic equator at whole number intervals in units of R_{Uranus}) (*e.g.*, Ness et al., 1986; Cao and Paty, 2017). Full modeling of interactions between Uranus' moons and its magnetic field is therefore even more complex than modeling a co-aligned system like Saturn.

In order to test the hypothesis that CO_2 ice on the surfaces of Ariel, Umbriel, Titania, and Oberon is generated by magnetospherically-trapped charged particle irradiation, we have collected new SpeX spectra of these moons' previously unobserved northern hemispheres. Because CO_2 ice has not been detected on Miranda, spectra of this moon were not analyzed in this project. Using these new SpeX spectra of the four largest Uranian satellites, along with two other SpeX datasets collected over their southern hemispheres, and spectrophotometry measured by IRAC, we investigate the spatial distribution and mixing regime of CO_2 ice on these satellites. We also explore the distribution of H_2O ice on these moons. Additionally, the broad wavelength range of the SpeX (~0.81 – 2.42 μm) and IRAC (~3.1 – 9.5 μm) datasets enables us to characterize vertical layering in these moons' near-surfaces.

Observations and data reduction

IRTF/SpeX

Observations of the Uranian satellites reported in this work were gathered between 2000 and 2013 using the short wavelength cross-dispersed mode (SXD) of the NIR spectrograph/imager SpeX at the IRTF on Mauna Kea, Hawaii (Rayner et al., 1998, 2003). These observations were made by three different teams (summarized in Table 1.2, mid-observation 'sub-observer' latitudes and longitudes displayed in Figure 1.1). The observations by Cartwright and those by Rivkin are presented here for the first time, whereas the data from Grundy were published in Grundy et al. (2003, 2006), and we refer the reader to these publications for details regarding their data reduction procedures.

SpeX includes two detectors: a 1024 x 1024 InSb array for the spectrograph (0.15

arcsec/pixel), and a 512 x 512 InSb array that images the slit (0.12 arcsec/pixel). All Uranian satellite spectra gathered between 2000 and 2012 have a spectral range of ~0.81 – 2.42 μm. Data gathered by Cartwright in 2013 utilized the visible/near-infrared (VNIR) MORIS camera co-mounted with SpeX, resulting in a slightly reduced spectral range for those SpeX spectra (covering ~0.94 – 2.42 μm). Observations made by Rivkin and Cartwright used a 0.8 x 15 arcsecond slit, providing spectral resolution ($R = \lambda/\Delta\lambda$) of ~650 – 750. Grundy et al. (2003, 2006) used two different slit width settings (0.3 x 15 arcseconds and 0.5 x 15 arcseconds), resulting in spectral resolutions of ~1600 – 1700 and ~1300 – 1400, respectively.

For all three SpeX datasets, spectra were gathered as pairs, with the object imaged in two positions (referred to as A and B beams) separated by 7.5 arcsec along the 15-arcsec slit. Subtraction of these A-B image pairs provides first order removal of sky emission. Maximum exposure time per frame was limited to 120 s to minimize sky emission variability. In order to improve the signal to noise ratio (S/N), object frames from each night were co-added during data reduction. Nearby solar analog stars were observed by each team to ensure good correction of atmospheric absorption (summarized in Table 1.3). These solar analogs were observed repeatedly throughout the observations at multiple airmasses. Flat field images and wavelength calibration files were obtained using observations of SpeX's internal integrating sphere illuminated by a quartz lamp and an argon lamp, respectively.

Background subtraction and extraction of spectra gathered by Rivkin and those gathered by Cartwright were conducted using custom programs and the Spextool data reduction package (Cushing et al., 2004; Vacca et al., 2003). Extracted satellite spectra were divided by solar analog spectra from the same night, at similar air masses. Solar-analog-divided spectra were then combined using custom programs and the Spextool program suite (Cushing et al., 2004). We applied several additional corrections to the spectra gathered by Cartwright in 2012 and 2013 to remove residual telluric contributions, including: sub-pixel shifting of object and solar analog spectra, interpolation of solar analog airmasses to better match object airmasses, and dividing spectra by an appropriately scaled atmospheric transmission spectra (gathered at Mauna Kea). A scaled spectrum of Uranus (Rayner et al., 2009) was used to correct for scattered light in the Ariel and Umbriel spectra collected in 2013. Finally, we photometrically scaled all three SpeX datasets to I-band geometric albedos (~0.957 μm, albedos listed in Table 1.1), using values presented in Karkoschka (2001).

Spitzer/IRAC

The Spitzer Space Telescope was launched in 2003 into an Earth-trailing, heliocentric orbit to observe the universe at infrared wavelengths (~3.1 – 160 μm) (Werner et al., 2004). IRAC is a NIR imager onboard Spitzer that gathers data in four broadband channels, centered near 3.6, 4.5, 5.8, and 8.0 μm with pass band widths of 0.68, 0.87, 1.25, 2.52 μm, respectively (Fazio et al., 2004). Each channel has a field of view (FOV) of 5.8 x 5.8 arcmin, with ~1.2 arcsec/pixel spatial resolution. IRAC exposures are collected as simultaneous image pairs; channel 1 and 3 share the same

FOV, as do channel 2 and 4. While one pair of channels observes the target, the other pair records data from the adjacent sky (with no overlap in FOV).

Near-infrared photometry of the large Uranian satellites was obtained by IRAC on eight nights between 2003 and 2005 (Program 71). The IRAC dither pattern was set to cycling, gathering three images per channel pair (six total frames per observation) with an exposure time of 26.8 seconds per frame. IRAC observed each moon twice, with one targeted observation of their leading hemispheres and one of their trailing hemispheres (close to 'sub-observer' satellite longitudes of 90° and 270°, respectively). In each of these leading/trailing Uranian satellite image pairs, the other three moons were also imaged in the frames; thus, IRAC effectively imaged each moon a total of eight times. Some of the IRAC observations of the four largest Uranian moons are clearly contaminated by scattered light from Uranus and other background sources, making reliable aperture photometry much more difficult on these frames. Here, we only report our aperture photometry results for the IRAC frames devoid of significant flux contamination (summarized in Table 1.4, mid-observation 'sub-observer' latitudes and longitudes displayed in Figure 1.1).

IRAC frames have been processed by the standard Spitzer Science Center (SSC) data reduction pipeline, where dark subtraction, flat fielding, and flux calibration procedures are conducted (reduction procedures described in greater detail in the IRAC instrument handbook[1]. The SSC reduction pipeline generates corrected basic calibrated data (CBCD) products, which were further processed to remove common IRAC artifacts like mux stripe, column pulldown, banding, saturation, and stray light contributions (see the instrument handbook for details of each of these potential artifacts and methods used to mitigate them). All IRAC images analyzed in this study are CBCD products. Using corrections supplied by the SSC, we corrected for variations in the pixel solid angle and for photometric variations in different parts of the array before converting the images in to units of mJy/pixel.

We conducted aperture photometry using aperture sizes of 2 and 3 pixels, with corresponding background annulus radii of 2 – 6 and 3 – 7 pixels, respectively. We also performed aperture photometry using a background annulus with a radius of 10 – 20 pixels for each aperture, making a total of four flux estimates per moon. Our chosen aperture sizes allow us to measure the maximum possible source flux while minimizing sky background, cosmic ray hits, and other non-source contributions to flux within the aperture. In order to account for the finite size of our apertures compared to the SSC-calibrated aperture sizes (10 pixel radius), we multiplied our flux estimates by the channel-dependent aperture corrections listed in the IRAC instrument handbook. Because we are measuring reflected flux from Solar System objects, we assumed that the primary source of the measured fluxes matches a solar spectral slope through each IRAC channel's pass band. Consequently, we divided our flux estimates by color corrections calculated for the spectrum of the Sun (from Smith and Gottlieb, 1974). The absolute flux calibration of IRAC is accurate to 2% (Reach et al. 2005).

[1] *http://irsa.ipac.caltech.edu/data/SPITZER/docs/irac/iracinstrumenthandbook/*

After calibration of the data was completed, we calculated an average flux using the 2 and 3 pixel flux measurements with the small background annuli and another average flux using the two apertures and the larger annuli. We then combined these two averages into one final flux estimate and propagated errors (Table 1.5). The listed uncertainties in Table 1.5 account for photon counting statistics, variation among the individual CBCD frames, and uncertainty from our chosen aperture/annulus size combinations.

After completing photometry on the IRAC frames, we converted the object fluxes in each channel into geometric albedos using $p_\lambda = F_\lambda r^2_{AU} \Delta^2 / F_{\odot,\lambda} \Phi R^2$, where p_λ is the broadband geometric albedo for each IRAC channel, F_λ is the measured flux, r_{AU} is the target's heliocentric distance in AU, Δ is the distance between the observer and the target, $F_{\odot,\lambda}$ is the solar flux at 1 AU for each channel, Φ is a phase correction, and R is the target's radius. We used Uranian satellite photometric parameters provided in Karkoschka (2001) for the phase correction: $\Phi = 10exp(-(((\beta * \alpha) + (0.5 * \alpha)/(\alpha\_0 + \alpha)))/2.5)$, where α is the phase angle of the observation, β is the phase coefficient for each moon (Ariel 0.025, Umbriel 0.027, Titania 0.023, and Oberon 0.023) and α_0 is the width of the opposition surge (Ariel 0.2, Umbriel 0.7, Titania 0.5, and Oberon 0.5) (β and α_0 values provided in Table 7 of Karkoschka, 2001).

Results

SpeX spectra

Figure 1.2 displays examples of leading and trailing observations of each moon gathered by Cartwright and Rivkin. The rest of the spectra we collected are displayed in Appendix A, along with spectra previously presented in Grundy et al. (2003, 2006). Observations made by Rivkin and Grundy et al. (2003, 2006) were centered on the southern latitudes of the Uranian moons (sub-solar latitudes of ~10 – 30° S). Observations made by Cartwright were centered on these satellites' northern hemispheres (sub-solar latitudes of ~17 – 24° N). Throughout the following sections, we refer to all SpeX and IRAC data points gathered between satellite longitudes of 1 to 180° as *leading hemisphere* observations, and all data points gathered between 181 and 360° are referred to as *trailing hemisphere* observations.

All 43 of the spectra analyzed in this study show clear evidence for overlapping combination and overtone H_2O ice bands centered near 1.52 μm and 2.02 μm, along with another feature centered near 1.65 μm, which is indicative of crystalline H_2O ice (*e.g.,* Mastrapa et al., 2008). Visual comparison with icy satellites in the Saturnian system reveals that H_2O bands on the Uranian moons are weaker (*i.e.*, smaller band areas and depths) than those on Saturn's moons (see Emery et al. (2005) for examples of icy Saturnian moon spectra gathered using SpeX). All 43 Uranian satellite spectra are relatively neutral or display reddish slopes from ~0.8 to 1.3 μm. From ~1.4 to 2.5 μm, the spectra are slightly blueish, characteristic of H_2O ice-rich objects (*e.g.*, Clark et al., 2013 and references therein). Additionally, the 'arch-like' shape of the H_2O ice continuum between ~2.15 and 2.3 μm is noticeably flattened in our spectra as compared to pure H_2O

ice. The subtle slopes of these spectra's continua, along with the absence of the 1.05- and 1.25-μm H_2O ice bands, and relatively weak 1.52-μm and 2.02-μm H_2O bands, is consistent with surfaces dominated by small H_2O ice grains mixed with a spectrally featureless material.

The spectra gathered over the trailing hemispheres of Ariel and Umbriel display visibly apparent evidence for CO_2 ice combination and overtone bands between 1.9 and 2.2 μm. Weak CO_2 bands between 1.9 and 2.2 μm are also present in some of the spectra collected over the trailing hemisphere of Titania. We do not detect visibly apparent CO_2 bands in the Oberon spectra.

IRAC photometry

We report our IRAC flux and geometric albedo results for all four channels in Table 1.5 and present lightcurves in Figure 1.3. While the S/N ratios are > 100 for channels 1 and 2 (3.6 and 4.5 μm), they are as low as ~12 and ~6 for channels 3 and 4 (5.8 and 8.0 μm), respectively. In some cases the channel 3 and 4 fluxes are below the 3σ threshold of the background flux uncertainties (indicated with italicized 3σ upper limits in Table 1.5). We exclude all IRAC observations that are below the 3σ threshold from our subsequent analyses. We also report mean IRAC geometric albedos for the leading and trailing hemispheres of each moon (Table 1.6).

Ariel displays a clear leading/trailing hemispherical asymmetry in its mean albedos for both channels 1 and 2, with > 3σ higher albedos on its trailing hemisphere. Umbriel displays a subtle hemispherical asymmetry, with a slightly brighter mean albedo on its trailing hemisphere in channel 1 (> 1σ). We see no evidence for brighter trailing hemispheres on the other satellites. For all four moons, we see a clear drop in geometric albedo from channel 1 to 2, and then another reduction in albedo from channel 2 to 3. Channel 4 geometric albedos vary widely on each moon, and we see no discernable trends within the results from this channel, which may in part be due to their low S/N. Of note, the IRAC images utilized by this study represent a previously unexplored wavelength range for these satellites.

Analysis

In the following sections we analyze the distribution of CO_2 and H_2O on the four largest Uranian moons and provide compositional analysis of our IRAC results. We also use synthetic spectra, generated using numerical models, to further test the robustness of our CO_2 ice detections (described in Appendix B). As defined above, we refer to all SpeX and IRAC data points gathered between satellite longitudes of 1 to 180° as leading hemisphere observations, and all data points gathered between 181 and 360° are referred to as trailing hemisphere observations. In the following sections, when our analysis deals specifically with data gathered within 45° longitude of the apex (46° – 135°) and antapex (226 – 315°), we refer to these data as leading quadrant and trailing quadrant observations, respectively.

CO_2 ice band parameter analysis

In order to investigate the distribution of CO_2 on the four largest moons of Uranus, we measured the band areas of the three strongest CO_2 bands between 1.9 and 2.2 μm in each spectrum. We then used an F-test (e.g., Spiegel, 1992) to determine if there are statistically significant differences between the measured CO_2 band areas on the leading and trailing hemispheres of these satellites. For spectra with visibly apparent CO_2 bands, we fit their band centers using Gaussian curves in order to estimate deviations between the position of the detected CO_2 bands and pure CO_2 ice (e.g., Gerakines et al., 2005). Band parameter analyses were conducted using a modified version of the Spectral Analysis Routine for Asteroids program (SARA, Lindsay et al., 2015), which we repurposed for the analysis of CO_2 and H_2O ice bands.

Pure CO_2 ice displays many IR-active features, including the strong asymmetric stretch fundamental mode (υ_3) centered near 4.27 μm, two degenerate bending modes centered near 15.2 μm (υ_2), and numerous combination and overtone bands between ~1.0 and 3.5 μm (the symmetric stretch mode (υ_1) of CO_2 is not IR-active). The three strongest CO_2 ice combination and overtone bands that are readily observable from Earth's surface occur between 1.9 and 2.1 μm, which we refer to as CO_2 band 1, CO_2 band 2, and CO_2 band 3 (Table 1.7). Figure 1.4 displays a SpeX spectrum collected over the trailing hemisphere of Ariel with visibly apparent CO_2 bands.

CO_2 ice band area measurements

We measured the integrated areas of CO_2 bands 1, 2, and 3 in all 43 SpeX spectra (Table 1.8). To do this, we first defined the width of these bands and adjacent continua using the same wavelength ranges as Grundy et al. (2006, 2010) (summarized in Table 1.7). Using a line, we connected the two continua pieces on either side of each band, and divided each band by its continuum. Using the trapezoidal rule, we computed the integrated area of each continuum-divided band, and then added these three bands together to get the total CO_2 area in each spectrum. We estimated the 1σ errors for our band area measurements by running Monte Carlo simulations, resampling from within a Gaussian distribution, represented by the 1σ error bars for each spectral channel. This process was iterated 20,000 times. The summed CO_2 band areas for each spectrum, along with their 1σ errors, are shown in Figure 1.5 as a function of satellite longitude. CO_2 ice band areas are influenced by a variety of factors, including constituent abundances, grain size, mixing style (intimate vs. areal), and albedo. Although CO_2 band area measurements are influenced by these different factors, band areas generally increase with increasing abundance. Thus, band areas are a useful proxy for constituent abundances. Using spectral modeling codes, we explore the influence of these different factors on CO_2 band areas in Appendix 1-B.

Our band area results are consistent with two trends previously observed by Grundy et al. (2006): (1) peak abundances in CO_2 ice tend to be in spectra gathered near the antapex (270° longitude) of each moon, while the spectra with the lowest CO_2 abundances were collected near their apexes (90° longitude). (2) The overall abundance in CO_2 appears to decrease with increasing distance from Uranus, with the most CO_2 on Ariel and the least on Oberon. A computational error in the band measurement procedure

used by Grundy et al. (2006) led to systematic under-estimation of their CO_2 ice band areas (Grundy, personal communication). Consequently, our band parameter code is able to reproduce the relative relationships amongst CO_2 band areas presented in Grundy et al. (2006), but the CO_2 integrated band areas reported here are ~20 – 40% higher.

Testing the robustness of the CO_2 band area measurements

It is possible that our measured CO_2 band areas are enhanced by random noise spikes that coincide with the wavelength regions of the CO_2 bands. We see clear evidence of incorporated noise in those cases where our band parameter code returned negative band areas (21 out 129 measured CO_2 bands), leading to negative summed CO_2 band areas for two spectra gathered over Umbriel (mid-observation longitudes of 38.4º and 75.2º), one spectrum over Titania (160º longitude), and two spectra over Oberon (85.9º and 216.2º longitude) (Figure 1.5 and Table 1.8). Importantly, of the 21 cases where our band analysis program generated negative band area measurements, 17 are in spectra gathered over their leading hemispheres, with one trailing hemisphere Oberon spectrum accounting for 3 of the remaining 4 negative band area measurements (summarized in Table 1.8). Enhancement of both positive and negative band areas with random noise might be particularly important for spectra with limited visibly apparent evidence for CO_2 bands (i.e., Titania and Oberon).

In order to further test the robustness of our CO_2 ice detections, we investigated the relative band area contributions of CO_2 bands 1, 2, and 3 in the SpeX spectra, along with a wide range of noise-free and noise-added synthetic spectra generated using numerical models, including pure H_2O ice, pure CO_2 ice, and various mixtures of H_2O, CO_2, and amorphous C (described in Appendix B). For the mean Oberon spectrum, (i.e., the one with the lowest summed CO_2 band areas), none of the pure H_2O ice models we generated match its measured CO_2 levels, nor the relative contributions of Oberon's CO_2 bands.

In summary, all of the spectral models we tested (both noise-free and noise-added) require CO_2 to be present at least at the 1% level of the continuum, and in many cases at the 5% or higher level of the continuum, in order to match the measured CO_2 band areas and relative band ratios of the mean Uranian satellite spectra and their best fit models. It is therefore unlikely that the low levels of CO_2 ice detected in SpeX spectra of Oberon can be explained as the result of integrated noise. Additionally, the relative band area contributions of the models that include areally mixed CO_2 ice are more consistent with the relative band area contributions of the mean trailing hemisphere spectra than particulate mixtures of CO_2, providing further support for the presence of segregated CO_2 on the Uranian moons.

Along with our analysis of the relative band area ratios of synthetic spectra, we also considered how contributions from telluric CO_2 might alter the relative band ratios in the mean spectra. Telluric CO_2 has several prominent absorption features between 1.9 and 2.1 μm, coincident with solid state CO_2. However, the narrow 'peaked' profiles of the detected CO_2 bands clearly contrast with the broad 'double lobe' profiles of telluric CO_2 bands (Figure 1-B.2). Consequently, it appears that telluric contamination of the measured CO_2 bands is minimal.

Statistical analysis of the distribution of CO_2

In order to investigate whether the observed preferential accumulation of CO_2 ice on the trailing hemispheres of the Uranian moons is statistically significant, we compared the fits provided by two different models to the measured band areas (weighted by their uncertainties). We used a sinusoidal model with three coefficients (amplitude, phase shift, vertical offset) to represent hemispherical asymmetries in the distribution of CO_2 (dashed black lines in Figure 1.5), and a simple average of the measured band areas on each moon (mean model) to represent a globally homogenous distribution of CO_2 (dash-dot gold-colored lines in Figure 1.5). We then used an F-test to determine the level of correlation between these two models. Our null hypothesis is that the sinusoidal and mean models are statistically indistinguishable, and by extension, that there is no statistical significance to the observed asymmetry in the distribution of CO_2. We rejected this null hypothesis for the cases where the probability (p) of a significant difference between the models was $\leq$ 0.05.

The F-test results (Table 1.9) demonstrate that a sinusoidal fit is significantly better at describing the distribution of CO_2 ice on all four moons (Ariel, Umbriel, Titania, and Oberon with $p < 0.001$, < 0.03, <0.009, < 0.006, respectively), and we reject the null hypothesis for all four moons. Therefore, our F-test analysis indicates that there are statistically significant accumulations of CO_2 ice on the trailing hemispheres of these moons.

Previous work has demonstrated that hemispherical asymmetries in cratering rates (e.g., Zahnle et al., 2003) and ion sputtering rates (e.g., Cassidy et al., 2013) are greatest between the leading and trailing quadrants (46° – 135° and 226° – 315° longitude, respectively) of icy satellites in the Jovian system. If micrometeorite and/or magnetospheric charged particle bombardment dominate the production of CO_2 ice in the Uranian system, and, by extension, dominate the observed hemispherical asymmetries in the distribution of CO_2 ice, then perhaps these asymmetries are strongest between the leading and trailing quadrants of these moons. Therefore, we also used F-tests to compare sinusoidal and mean model fits to the data points within the leading and trailing quadrants of these moons (Table 1.10). We find that a sinusoidal fit is significantly better at describing the distribution of the CO_2 ice on Ariel and Titania ($P < 0.001$, < 0.01, respectively). However, the sinusoidal model is not significantly better than the mean model at describing the distribution of CO_2 on Umbriel ($P = 0.45$) and is slightly below the significance threshold for Oberon ($P = 0.06$).

Thus, the full-hemisphere and quadrant-limited F-tests demonstrate that the distribution of CO_2 ice on Ariel and Titania is statistically significant, but they generate dissimilar probabilities for the distribution of CO_2 on Umbriel and Oberon. Given the lower number of data points in the quadrant-limited F-tests for these two moons (five and seven for Umbriel and Oberon, respectively) compared to the full-hemisphere F-tests (nine and eleven for Umbriel and Oberon, respectively), we favor our full-hemisphere results for the distribution of CO_2 ice. Furthermore, the summed CO_2 bands in one of the spectra gathered over the leading quadrant of Umbriel (mid-observation longitude of 92.1°) are substantially larger than the other two leading quadrant spectra for this moon. This spectrum does not have visibly apparent CO_2 bands, unlike the spectra collected

over Umbriel's trailing quadrant. If this leading quadrant spectrum is removed from the analysis, then the sinusoidal model provides a significant fit (P = 0.05) to the data points gathered over the leading and trailing quadrants of Umbriel.

CO_2 band center modeling

For spectra with visibly apparent CO_2 bands (i.e., trailing hemisphere spectra on Ariel and Umbriel), we estimate the position of their band centers (Table 1.8) by fitting Gaussian curves to the bands. We used an iterative Monte Carlo procedure to estimate the uncertainties of these band center fits (described above). The Gaussian fits to each band have centers that are close (within ± 0.003 μm) to the band centers of pure CO_2 ice (1.966 μm, 2.012 μm, and 2.070 μm), as determined by laboratory experiments (e.g., Gerakines et al., 2005). Laboratory spectra of intimate mixtures of H_2O and CO_2 ice also lead to subtle CO_2 band position shifts to longer wavelengths (0.002 – 0.004 μm) (Bernstein et al., 2005), unlike the CO_2 band Gaussian fits presented here, which are shifted to both shorter and longer wavelengths – presumably because of the point-to-point variation within each CO_2 band. The relatively close matches in wavelength position, along with the strength and narrow profiles of the CO_2 ice bands, suggests that our detections are dominated by pure (*i.e.*, CO_2 molecules bonded to other CO_2 molecules) and segregated (*i.e.*, CO_2 grains predominantly surrounded by other CO_2 grains) deposits of CO_2 ice.

CO_2 band parameter analysis summary

We measured the areas of CO_2 bands 1, 2, and 3 in all 43 SpeX spectra. Our band parameter codes measured non-zero CO_2 ice band areas on the trailing hemispheres of all four moons, peaking near their antapexes (270º longitude). Our analysis indicates that the abundance of CO_2 ice is greatest on Ariel and decreases with distance from Uranus, which is consistent with band area results presented in Grundy et al. (2006). As a check on our band area results, we investigated the relative band area contributions for CO_2 bands 1, 2, and 3 in our spectra, and compared them to the relative CO_2 band areas in a wide range of synthetic spectra and best fit models (described in Appendix 1-B). The results of this relative band area analysis indicate that the detected CO_2 is most consistent with synthetic spectra that include pure CO_2 ice that is segregated from other species, and telluric contributions to the measured bands are likely negligible.

Previously, CO_2 ice had not been detected on the trailing hemisphere of Oberon (albeit, based on the analysis of only one SpeX spectrum in Grundy et al. (2006)). Our team has increased the number of SpeX observations of Oberon's trailing hemisphere to five (Table 1.2). While we find no compelling evidence for visibly apparent CO_2 bands, our F-test analysis indicates that there is a statistically significant accumulation of CO_2 on the trailing hemispheres of all four moons, including Oberon.

For the spectra with visibly apparent CO_2 bands, we modeled the band centers of the three CO_2 bands using Gaussian curves. We detected small shifts to both shorter and longer wavelengths in the center position of some of the CO_2 features, which we attribute to noise within the bands. Therefore, our CO_2 band center modeling does not support the presence of intimately mixed or complexed CO_2 ice on these moons. Furthermore, the absence of evidence for the CO_2 'forbidden transition' ($2\upsilon_3$) near 2.134 μm in our spectra,

which is ~100 times stronger than CO_2 bands 1, 2, and 3 in intimate mixtures of CO_2 and H_2O (Bernstein et al., 2005), also suggests that the detected CO_2 is pure and isolated from other surface species.

Investigating the distribution of CO_2 using IRAC

NIR ground-based observations are mostly limited to windows defined by strong telluric bands, which make observations of the Uranian system at wavelengths longer than ~2.5 μm difficult and completely block incoming light near the CO_2 asymmetric stretch fundamental (υ_3). The wavelength range covered by IRAC channel 2 (~4.0 – 5.0 μm) includes the wide CO_2 υ_3 feature. This absorption feature is roughly a factor of 1000 stronger than the shorter wavelength combination and overtone bands (e.g., Hansen, 1997, 2005) detected in SpeX spectra of these satellites. Thus, the wavelength range covered by IRAC is ideal for investigating potentially low levels of CO_2 on the Uranian moons.

The CO_2 υ_3 feature (centered near 4.27 μm in pure CO_2) is coincident with numerous overlapping H_2O absorption bands that absorb strongly across the entire IRAC wavelength range (Figure 1.6). This CO_2 absorption feature is flanked by bright 'wings' that cause the geometric albedos of IRAC channels 1 and 3 to be higher than channel 2. This arrangement of channel 1 through 3 geometric albedos leads to a broad absorption feature centered in IRAC channel 2. Although the Uranian satellite channel 1 geometric albedos are higher than channel 2 in all cases, only in one trailing hemisphere observation of Umbriel is the channel 3 albedo slightly higher than channel 2 (Table 1.5). Given the presence of visibly apparent combination and overtone CO_2 bands on Ariel and Umbriel over SpeX wavelengths, we expected to find clear evidence for the much stronger CO_2 υ_3 fundamental in our IRAC results, at least on these two moons.

Compositional analysis of IRAC photometry

In order to characterize the composition of the Uranian satellites using our IRAC results, we converted the geometric albedos into spectral colors and plotted them in magnitude space. We also extrapolated the best fit models for the mean trailing hemisphere SpeX spectra (described in Appendix B) over IRAC wavelengths, and plotted them in magnitude space as well. $Mag_1 - Mag_2 = 2.5 * \log p_2/p_1$, where Mag_1 and Mag_2 represent the magnitudes of two IRAC channels, and p_1 and p_2 represent the geometric albedos of the same two IRAC channels. After converting each moon's mean leading and trailing geometric albedos into magnitudes, we generated a color-color plot with IRAC channel 1 – channel 2 on the y-axis and IRAC channel 2 – channel 3 on the x-axis (Figure 1.7).

We computed IRAC colors from spectral models of pure H_2O, CO_2, and amorphous carbon (grain sizes 0.5 – 100 μm) (Figure 1.7a), and then plotted these synthetic spectra in the same color-color space in order to compare them to the Uranian satellite IRAC colors. The Uranian satellite IRAC data plot adjacent to the pure H_2O ice zone, which we expected for these H_2O-rich icy moons. Surprisingly, the best fit models for the mean SpeX spectra (extended to cover IRAC wavelengths) do not plot near the Uranian moon IRAC data (Figure 1.7b, box 2). We also generated a set of best fit models

for the mean SpeX spectra, without CO_2 (*i.e.*, models that only fit the H_2O ice bands and continua), and plotted them in the same magnitude space (Figure 1.7c, box 3). This set of models also plot in a zone distinctly different from the Uranian satellite IRAC data.

We generated new sets of synthetic spectra using much smaller grain sizes (0.2 – 5 μm) than the dominant grain sizes of our SpeX best fit models (10 – 50 μm). By including substantial abundances (~20 – 90 %) of 0.5 – 2 μm H_2O ice in our models, we were able to replicate the spectral colors of the Uranian satellites. Additionally, these best fit IRAC models can also include up to ~5 % of larger H_2O ice grains (5 and 10 μm grain sizes), 1 – 5 % CO_2 ice (1 – 2 μm grain sizes), and 1 – 20% amorphous C (1 – 5 μm grain sizes) and still plot within the Uranian satellite zone (Figure 1.7c, asterisk 4).

IRAC photometry summary

We analyzed the geometric albedos for IRAC channels 1, 2, and 3, finding that they are inconsistent with the detection of CO_2. We converted the geometric albedos of these three channels into spectral colors, and plotted them in magnitude space along with a range of synthetic spectra (including pure end-member compositional models and intimate mixtures). Our color-color analysis suggests that the surfaces of these moons are composed primarily of segregated H_2O ice grains that tend to be small (~20 – 90% with ≤ 2 μm diameters). At the same time, the best fit spectral models for the SpeX spectra suggest that these moons are dominated by intimate mixtures of H_2O ice (mostly 10 – 50 μm grain sizes) with substantial amounts of amorphous carbon (2 – 40%) and pure and segregated CO_2 ice (3 – 27%).

CO_2 production by charged particle irradiation

The abundances of CO_2 ice observed on the Uranian moons is consistent with production of CO_2 by charged particle irradiation in laboratory experiments. Numerous studies have demonstrated that irradiation of H_2O ice mixed with a range of different carbonaceous substrates can readily generate CO_2 ice in the laboratory (*e.g.*, Mennella et al., 2004; Gomis and Strazzulla, 2005; Raut et al., 2012). All of these laboratory studies showed that CO_2 abundance increases up to a steady state value (*i.e.*, saturation), where CO_2 production and destruction rates are balanced. The concentration of CO_2 at saturation can vary by a factor of ~15 – 20, depending on the starting composition of the C-rich substrate and temperature of the experimental run. We utilize these experimental results to investigate the amount of CO_2 ice that can be generated by radiolysis on the Uranian moons, and the timescales to reach CO_2 saturation on each moon.

In one typical experiment, Raut et al. (2012) irradiated 0.1 μm thin films of H_2O ice, mantling a layer of amorphous C, with 100 KeV H^+ protons (experiments run at 20 K and 120 K). After accumulating a fluence of ~$30x10^{15}$ protons cm^{-2}, the column density of CO_2 molecules reached saturation at column densities of ~$1.0x10^{15}$ and ~$2.8x10^{15}$ CO_2 molecules per cm^{-2} for the 20 K and 120 K experiments, respectively. We used three related approaches to convert from experimental CO_2 column densities to mixing ratios: (1) compared the fraction of the experimental substrate occupied by synthesized CO_2 ice to the initial amount of H_2O ice (volume mixing ratio), (2) compared the number of synthesized CO_2 ice molecules to the number of initial H_2O ice molecules ($276x10^{15}$

molecules cm^{-2}) (number mixing ratio), and (3) the mass fraction of synthesized CO_2 to initial H_2O (mass mixing ratio). To convert to volume mixing ratio, we divided the saturation column density of CO_2 (number of CO_2 molecules cm^{-2}) by the experimental substrate thickness (0.0001 cm) to get the saturation volume density. We then divided by Avogadro's number ($6.022x10^{23}$ molecules mol^{-1}), multiplied by the molar mass of CO_2 (18.02 g mol^{-1}), and divided by the density of CO_2 ice (1.5 g cm^{-3}). The resulting volume mixing ratios are ~0.5% and ~1.4% for the 20 K and 120 K experimental runs, respectively. Similar conversions to number and mass mixing ratios give values of ~0.4 to 2.5%.

Experiments with different carbonaceous substrates produce saturation CO_2 column densities that vary by more than an order of magnitude from each other. For example, the saturation CO_2 column density reported in Mennella et al. (2004) is ~$15x10^{15}$ CO_2 molecules cm^{-2} in thin H_2O ice films irradiated with 30 KeV He+ ions. Converting this CO_2 saturation column density into mixing ratios, using the three approaches described above, leads to a CO_2 mixing ratio range of ~0.5% to 13%. Furthermore, saturation column densities for radiolytically-produced species increase with increasing temperature (*e.g.*, Hudson and Moore, 2001; Raut et al., 2012). Scaling the CO_2 saturation column density measured by Mennella et al. (2004) (at 16 K) to the Raut et al. (2012) experiments (run at 120 K), increases the resulting range in mixing ratios to ~0.5 to ~37%. This range of CO_2 mixing ratios encompasses the CO_2 mixing ratio of our best fit numerical model for Ariel's trailing hemisphere (27%), supporting our hypothesis that the detected CO_2 ice was generated by charged particle bombardment.

Using the charged particle fluxes measured at the orbital radii of the four largest classical moons, we estimated the timescales required to reach the proton fluence (~$30x10^{15}$ protons cm^{-2}) observed by Raut et al. (2012) at CO_2 saturation. The Low Energy Charged Particle (LECP) instrument onboard Voyager 2 measured a flux for 100 KeV protons of 100 – 300 s^{-1}, 50 – 100 s^{-1}, 0.1 – 1 s^{-1}, and 0.01 – 0.5 s^{-1} at the orbital radius of Ariel, Umbriel, Titania, and Oberon, respectively (*e.g.*, Lanzerotti et al., 1986). Using these proton fluxes, we calculated the timescales needed to reach a proton fluence of $30x10^{15}$ protons cm^{-2}: ~5 – 10 Myr for Ariel, ~10 – 20 Myr for Umbriel, ~1 – 10 Gyr for Titania, and ~2 – 100 Gyr for Oberon (Table 1.11). Therefore, over geologically short timescales, irradiation by 100 KeV protons should lead to radiolytically-produced CO_2 saturation on Ariel and Umbriel, but Titania and Oberon might not have accumulated sufficient fluence to reach saturation.

Thus, laboratory experiments demonstrate that charged particle irradiation of surfaces composed of H_2O ice and carbonaceous species readily produces CO_2. The 100 KeV proton fluxes measured at Ariel and Umbriel should spur synthesis of CO_2 up to saturation over geologically short timescales, and this process might have generated smaller amounts of CO_2 on the outer moons, Titania and Oberon. Although charged particle radiolysis should readily produce CO_2 on Miranda (100 KeV proton flux of ~500 – 1000 s^{-1}), this constituent has yet to be detected on the innermost classical moon. The lower mass of Miranda compared to the other classical moons allows CO_2 molecules to escape more readily, reducing CO_2 retention timescales on Miranda (Grundy et al., 2006). Consequently, radiolytic production of CO_2 is likely occurring on Miranda, but the

generated CO_2 might escape too rapidly to build up to detectable levels ($\gtrsim$ 5% mixing ratio).

H_2O band parameter analysis

Along with characterizing the distribution and near-surface mixing regime of CO_2 ice, we analyzed the H_2O ice bands present in the Uranian satellite spectra, measuring their areas and depths. We used an F-test to statistically compare the H_2O band areas and depths on their leading and trailing hemispheres. Additionally, we generated leading/trailing hemisphere ratios of H_2O band areas (as well as band depths) for each moon in order to investigate the distribution of H_2O ice.

Within the spectral region covered by the SXD mode of the SpeX spectrograph (~0.81 – 2.42 μm), H_2O ice has multiple band complexes composed of overlapping combination and overtone bands centered near 0.9, 1.04, 1.25, 1.52, and 2.02 μm. These bands increase in depth with increasing wavelength, and the 1.04, 1.25, 1.52, and 2.02 μm bands are readily detected by SpeX on icy Saturnian moons (*e.g.*, Emery et al., 2005). The presence of intimately mixed, low albedo material on the Uranian satellites weakens the H_2O ice bands and effectively masks the 1.04 and 1.25 μm bands in almost all of the SpeX spectra we analyzed. Hence, we focus our analysis on the visibly apparent 1.52-μm and 2.02-μm bands.

H_2O band area measurements

Similar to our CO_2 ice band area procedure, we defined two continua on either side of the H_2O ice bands: 1.318 – 1.440 μm and 1.720 – 1.750 μm for the 1.52-μm H_2O ice band complex (1.44 – 1.72 μm band width), and 1.769 – 1.924 μm and 2.215 – 2.230 μm for the 2.02-μm H_2O band (1.924 – 2.215 μm band width) (see Figure 1.4). We used large continua on the short wavelength end of each band in order to ensure robust area measurements for our spectra with significant atmospheric contributions from telluric bands centered near 1.4 and 1.9 μm. We used a third order polynomial to fit the arch-shaped, long wavelength end of the 2.02-μm band. After anchoring the continua for both H_2O ice bands, we connected them with a line, and divided each band by its continuum. We then measured the integrated areas and depths of both bands. To estimate the uncertainty of our band area measurements, we used the same iterative Monte Carlo procedure.

The H_2O ice integrated areas and 1σ uncertainties are presented in Figure 1.8 and summarized, along with H_2O ice band depths, in Table 1.12. A hemispherical asymmetry in Ariel's H_2O ice band areas, with an increased abundance of H_2O ice near the apex of it leading hemisphere, is visibly apparent. The relative difference between H_2O band areas on the leading and trailing hemispheres of Umbriel, Titania, and Oberon are much less pronounced, but the peak in H_2O ice band area is near the apexes of Umbriel and Titania for both the 1.52-μm and 2.02-μm bands (but only the 2.02-μm band for Oberon).

Previous studies (*e.g.*, Brown and Cruikshank et al., 1983) have noted a trend between Uranian satellite H_2O ice band depths and their visible wavelength (VIS) albedos, with the brightest moon (Ariel) displaying the deepest H_2O ice bands and the darkest moon (Umbriel) displaying the weakest. Our analysis supports this trend on the

leading hemispheres of these moons, with both geometric albedo and the mean 1.52-μm and 2.02-μm H_2O ice band depths and areas decreasing from Ariel, Titania, Oberon, to Umbriel. However, this trend does not hold for their trailing hemispheres, with the mean band depths and areas decreasing from Titania, Ariel, Oberon, to Umbriel (Figure 1.9, Table 1.13).

Statistical analysis of the distribution of H_2O

The same F-test procedure was applied to the measured H_2O ice band areas in order to quantify the distribution of H_2O ice on these moons. The F-test results (Table 1.9) demonstrate that a sinusoidal fit is significantly better at describing the distribution of H_2O ice on all four moons (for both the 1.52-μm and 2.02-μm bands). We calculated P values of < 0.001, < 0.04, <0.01, and < 0.04 for Ariel, Umbriel, Titania, and Oberon, respectively, for both H_2O ice bands. Therefore, our F-test analysis indicates that H_2O ice band areas are significantly stronger on the leading hemispheres of these moons compared to their trailing hemispheres.

We also conducted F-tests using data points limited to the leading and trailing *quadrants* (Table 1.10). F-test results for Ariel and Titania ($P < 0.001$ and < 0.01, respectively, for both the 1.52-μm and 2.02-μm bands) and Umbriel's 2.02-μm H_2O band ($P = 0.01$) indicate that a sinusoidal model is significantly better at describing the distribution of H_2O than a mean model. Asymmetries in the H_2O band areas on Oberon's leading and trailing quadrants are not statistically significant for either band. Similar to the CO_2 ice spatial analysis, we favor our full-hemisphere F-test results for the H_2O ice bands because of the lower number of data points in the quadrant-only analysis; there are only 5 and 7 H_2O band area measurements for Umbriel and Oberon, respectively, compared to 9 and 11 data points for the full-hemisphere analysis for Umbriel and Oberon, respectively.

H_2O band area and depth ratios

We also present leading/trailing ratios for the mean areas and depths of the 1.52-μm and 2.02 μm bands on each moon (for example, $\langle \text{band area}_{1.52\text{-}\mu m} \rangle_{\text{Ariel-leading}} / \langle \text{band area}_{1.52\text{-}\mu m} \rangle_{\text{Ariel-trailing}}$) (Table 1.13). When plotted as a function of orbital radius, it is clear that the 1.52-μm and 2.02 μm leading/trailing band area and depth ratios decrease with distance from Uranus (Figures 1.10a and 1.10b). We find no such trend when these same ratios are plotted as a function of satellite geometric albedo (Figures 1.10c and 1.10d). Additionally, the 1.52-μm band ratios are greater than the 2.02-μm band ratios, suggesting that the 1.52-μm band is more sensitive to changes in H_2O ice abundance and grain size. The clear trend of decreasing band area and depth ratios with distance from Uranus suggests that the controlling mechanism operates at a system-wide level, and its efficiency either falls off with distance from Uranus (for example, magnetospherically-driven radiolysis), or increases with distance from Uranus (for example, accumulation of in-falling dust from irregular satellites).

We also made mean 1.52-μm / mean 2.02-μm band area ratios for the leading and trailing hemispheres of each moon (Table 1.13), which increase with increasing geometric albedo (Figure 1.11a). Additionally, the difference between the leading and

trailing 1.52-μm/2.02-μm band area ratios for each moon becomes progressively smaller with increasing orbital radius (Figure 1.11b).

H_2O band parameter analysis summary

We measured the areas and depths of the 1.52-μm and 2.02-μm H_2O ice bands in all 43 SpeX spectra. Our H_2O band parameter and F-test results indicate that H_2O bands are stronger on the leading hemispheres of these satellites. Furthermore, there is a clear trend between albedo and H_2O band strength, with the strongest H_2O bands on the leading hemisphere of Ariel and the weakest on the trailing hemisphere of Umbriel. One notable exception to this trend is the H_2O bands on the trailing hemisphere of Ariel, which are weaker than the H_2O bands on the trailing hemisphere of Titania. To make sure that the addition of CO_2 ice on the trailing hemisphere is not skewing our interpretation, we generated spectral models of Ariel's trailing hemisphere, without CO_2 ice. These spectral models still display weaker H_2O bands compared to Ariel's leading hemisphere, indicating that CO_2 ice alone cannot account for the large hemispherical asymmetries in H_2O ice band strengths on Ariel.

Our analysis of the H_2O ice bands demonstrates that hemispherical asymmetries are more pronounced for the 1.52-μm band, compared to the 2.02-μm band for all four moons. Both grain size and contaminants can reduce H_2O ice band depths, and our analysis indicates that the 2.02-μm band is more resistant to these effects than the 1.52-μm band on the Uranian satellites. Determining the relative importance of grain size and contaminant abundance in the reduction of H_2O band depths is beyond the scope of this study, and we will explore the Uranian satellites' H_2O ice bands in greater detail in future work (Cartwright et al. [In prep]). Thus, both the abundance of CO_2 ice and hemispherical asymmetries in H_2O band areas decrease with distance from Uranus (Figure 1.12), suggesting that the effectiveness of the process (or processes) modifying the surfaces of these moons decreases with increasing orbital radius.

Discussion

In the following sections we consider the implications of our analyses, focusing on the differences between the SpeX and IRAC best fit models. We also briefly compare the CO_2 ice detected on the four largest Uranian moons to CO_2 detected on icy satellites elsewhere in the Solar System. Finally, we include a short discussion of the possible sources of CO_2 ice, and likely controls on its distribution, in the Uranian system.

Near-surface layering

Our best fit SpeX models, extrapolated over IRAC wavelengths, are poor matches to the IRAC geometric albedos for these moons (Figures 1.6 and 1.7). One possible explanation for this disparity between our SpeX and IRAC results is that these two instruments probe distinct layers in the near-surfaces of the Uranian satellites. To investigate this possibility, we converted the Mastrapa et al. (2008, 2009) crystalline H_2O ice extinction coefficients (κ) into absorption coefficients (α): $\alpha = 4\pi\kappa / \lambda$. The inverse of α gives the e-folding penetration depth of photons, which represents the depth

at which there is a ~63% probability of an incident photon (of a given wavelength) being absorbed. The e-folding penetration depth has been used in other studies as an indicator of sensible depths for reflectance spectroscopy (*e.g.*, Palmer and Brown, 2011).

Over SpeX wavelengths (~0.81 – 2.42 μm), NIR photons penetrate to greater depths (~0.1 mm to 100's of mm depths) than over IRAC wavelengths (~3.1 – 9.5 μm) into crystalline H_2O ice (~0.0003 to 0.05 mm depths) (Figure 1.13). Specifically, over the wavelength range of CO_2 bands 1, 2, and 3 (~1.9 to 2.1 μm), photons have a high probability of traveling ~100 μm into a pure H_2O ice surface, but over the wavelength range of the CO_2 υ_3 fundamental (~4.0 to 4.5 μm), photons only travel ~10 μm into H_2O ice (see Figure 1.6 for width and position of CO_2 bands over these wavelength ranges).

The penetration depth above assumes a solid slab with no scattering. Recognizing that scattering off grain boundaries is important in a regolith, Clark and Roush (1984) show that the mean optical path length (MOPL) represents the average distance light travels through a medium (without being absorbed) multiplied by the reflectance of a spectrum, accounting for scattering off internal boundaries. From Hapke (2012, p. 405-406): $MOPL = -1/\alpha * \ln(r)$, where r is reflectance. Utilizing our best fit synthetic spectra as the input for r, we calculate a MOPL of ~100 to 150 μm in the wavelength range of CO_2 bands 1, 2, and 3 and a MOPL of ~15 to 25 μm over the wavelength range covered by the CO_2 υ_3 fundamental.

Consequently, both our calculations of e-folding penetration depths and MOPL indicate that photons penetrate to greater depths in the wavelength range of CO_2 bands 1, 2, and 3 compared to the wavelength region of the CO_2 υ_3 fundamental. Thus, SpeX and IRAC are sensitive to NIR photons scattered from different depths, and these instruments may be probing two compositionally distinct layers in the Uranian satellite near-surfaces. Therefore, the CO_2 ice detected by SpeX could plausibly be retained beneath a thin veneer of mostly pure H_2O frost that strongly absorbs photons over IRAC wavelengths, and alters the expected relationships between the geometric albedos of IRAC channels 1, 2, and 3.

The Hapke-Mie hybrid modeling program utilized by this study generates synthetic spectra composed of areal and intimate mixtures of H_2O, CO_2, and amorphous C. This program does not include parameters for modeling stratified layers with heterogeneous compositions and/or grain sizes. Subsequent spectral analysis efforts will need to utilize codes that include components for modeling discrete compositional layers, along with multiple scattering of photons from more than one layer, in order to further investigate whether the Uranian satellites' near-surfaces are compositionally stratified. Additionally, the penetration depths discussed above do not take amorphous C into account, which strongly absorbs photons over the wavelength ranges of both SpeX and IRAC. Given the fairly flat absorption of amorphous C over the wavelength ranges covered by SpeX and IRAC, the depths probed by SpeX into H_2O-amorphous C particulate mixtures should still be greater than those probed by IRAC (assuming amorphous C is intimately mixed to depths of at least ~150 μm). Subsequent numerical modeling of the penetration potential of photons into intimate mixtures of H_2O ice and low albedo materials like amorphous C is also needed to further investigate near-surface layering on these satellites.

Jupiter to Neptune: CO_2 on icy satellites

To help provide context, we briefly compare the CO_2 ice detected on icy satellites elsewhere in the Solar System to the CO_2 detected on the four largest Uranian moons. CO_2 ice has been detected on icy moons in all four giant planet systems (*e.g.*, McCord et al., 1997; Clark et al., 2005; Grundy et al, 2003; Cruikshank et al., 1993). The nature of CO_2 in each of these systems is a strong function of mean surface temperature; complexed and/or trapped CO_2 molecules in refractory matrices dominate the spectral signature of CO_2 at Jupiter and Saturn, while pure CO_2 frost dominates at Uranus and Neptune (*e.g.*, Clark et al., 2013 and references therein). On airless icy satellites with minimal surface pressures, CO_2 is susceptible to sublimation, except on distant Triton where surface temperatures are too low to drive CO_2 removal via sublimation (Lebofsky, 1975). Therefore, pure CO_2 ice is unstable over the age of the Solar System in the Jovian, Saturnian, and Uranian systems, and deposits of pure CO_2 must be actively synthesized and/or represent native deposits recently exposed by impacts, tectonism, or emplaced by cryovolcanism.

CO_2 deposits in the Jovian and Saturnian systems are associated with low albedo, and likely organic rich regions (*e.g.*, McCord et al., 1998; Hansen and McCord, 2008; Clark et al., 2005, 2008; Cruikshank et al., 2010). Aside from the CO_2 ice associated with some fresh impact craters on Callisto (Hibbitts et al., 2000, 2002), and the CO_2 detected in Enceladus' plumes (Waite et al., 2006), there is no clear correlation of CO_2 with geologic features. The spatial correlation between dirty H_2O ice and CO_2 band strength on Jovian and Saturnian icy satellites supports active synthesis mechanisms, driven by UV photolysis (*e.g.*, Palmer and Brown, 2011) and charged particle radiolysis (*e.g.*, Cassidy et al., 2010).

Europa, Callisto, Dione, and Rhea are all embedded within their primary's magnetosphere, and they all have deeper CO_2 bands on their trailing hemispheres, which is consistent with CO_2 synthesis via charged particle radiolysis on these bodies. While Ganymede is also embedded within the magnetosphere of Jupiter, its intrinsic magnetic field deflects charged particles, which might explain why its surface does not display a clear leading/trailing asymmetry in CO_2 band strength (Hibbitts et al., 2003). Hyperion (chaotic rotation) and Phoebe (non-synchronous rotation) also do not display global asymmetries in CO_2 distribution. Iapetus does display hemispherical asymmetries in CO_2 abundance, but unlike the inner satellites Dione and Rhea, its deepest CO_2 bands are found in association with transitional longitudes between its low albedo leading hemisphere and H_2O ice-rich trailing hemisphere (Pinilla-Alonso et al., 2011). Palmer and Brown (2011) estimated that CO_2 synthesis via UV photolysis on Iapetus should be rapid enough to roughly balance out sublimation and other loss mechanisms. Photolysis of localized materials (*i.e.*, H_2O and organics) can neatly explain the deep CO_2 bands at leading and transitional longitudes on Iapetus, as well as the weak CO_2 bands on the trailing hemisphere, which is dominated by relatively pure H_2O, devoid of organic materials.

Similar to spectra of the large Uranian satellites, NIR observations have detected CO_2 combination and overtone bands between 1.9 and 2.2 μm on Triton (Cruikshank et al., 1993), suggestive of pure CO_2 ice. However, these CO_2 bands display no longitudinal

variation (Grundy et al., 2010), unlike the clear hemispherical asymmetries in CO_2 band areas observed on the Uranian moons. At Triton's estimated mean surface temperature (~38 K), CO_2 ice is very stable and is unlikely to participate in volatile migration cycles (Grundy et al., 2010). CO_2 ice on the relatively warmer Uranian satellite surfaces (~70 – 80 K, Grundy et al., 2006), is unstable and should be effectively removed by sublimation over the age of the Solar System.

Our band parameter and statistical analyses demonstrate that CO_2 bands are strongest on the trailing hemispheres of the satellites closest to Uranus. Similar hemispherical asymmetries in CO_2 band strength are seen in spectra of Europa, Callisto, Dione and Rhea, which is consistent with CO_2 generation via charged particle radiolysis on these magnetospherically-embedded satellites. Furthermore, the low geometric albedos of Ariel, Umbriel, Titania, and Oberon (~0.25 – 0.55), along with Voyager 2 images of their gray-toned surfaces, indicates that they are coated in a mixture of H_2O ice and low albedo, presumably C-rich, materials. Whereas UV photolysis likely generates some amount of CO_2 in all four planets' satellite systems, this mechanism should lead to a fairly uniform distribution, without leading/trailing asymmetries in CO_2 band strength. Iapetus is a notable exception, with a non-homogenous distribution in CO_2 likely driven by UV photolysis involving non-homogeneously distributed carbon-bearing low-albedo material (Palmer and Brown, 2011). Iapetus, however, is unique in its dramatic hemispheric dichotomy due to the moon sweeping up dust from Phoebe.

Thus, comparisons between the distribution of CO_2 on the Uranian satellites with the distribution on the Jovian and Saturnian satellites tends to support active production of CO_2 in the Uranian system, most likely driven by magnetospheric charged particle radiolysis. The detected spectral features suggest that CO_2 is pure and segregated from other surface species on the classical Uranian moons, similar to the CO_2 detected on Triton.

Possible sources of CO_2 and relevant removal mechanisms

The statistically significant accumulation of CO_2 on the trailing hemispheres of the Uranian satellites suggests that a system-wide mechanism is controlling the observed CO_2 distribution – most likely, magnetospherically-embedded charged particles. However, a wide range of processes can account for the presence of CO_2 on icy satellites. We explore each of these potential sources of CO_2 in Appendix C and only summarize our conclusions here. Potential sources of CO_2 fall into three broad categories: (1) native CO_2 that was accreted along with other primordial materials as they were forming (impact/tectonically exposed and cryovolcanically emplaced CO_2), (2) deposition of non-native CO_2 molecules sourced from a different body (interplanetary, interstellar, and intraplanetary dust), or re-deposition of sublimated native CO_2 in cold traps, and (3) non-native CO_2 synthesized by ion, electron, and UV irradiation of H_2O ice and carbon-rich species.

It seems unlikely that native CO_2 exposed by impacts and tectonism, or emplaced by cryovolcanism, could generate the observed preferential accumulation of CO_2 on the trailing hemispheres of all four moons, along with the observed planetocentric trend (reduction in CO_2 abundance with distance from Uranus). Although the impact energy

from heliocentric and planetocentric dust could drive CO_2 synthesis, this mechanism would likely lead to preferential accumulation of CO_2 on the leading hemispheres of these satellites, counter to the observed distribution. Sublimation of CO_2 driven by subsolar heating is unlikely to influence the observed distribution given that this mechanism should operate evenly on both hemispheres of all four satellites, which would tend to homogenize the distribution of CO_2 and mask hemispherical and planetocentric trends. Similarly, CO_2 synthesis and destruction via UV photolysis should also operate evenly throughout the Uranian system and is an unlikely driver of hemispherical and planetocentric asymmetries.

Laboratory experiments demonstrate that radiolysis of H_2O ice and C-rich substrates, driven by charged particle irradiation, can readily generate CO_2 (e.g., Spinks and Wood, 1990; Mennella et al., 2004; Gomis and Strazzulla, 2005; Sedlacko et al., 2005; Jamieson et al., 2006; Kim et al., 2012; Raut et al., 2012) (Appendix C). Charged particles embedded in Uranus' magnetosphere should preferentially bombard the trailing hemispheres of these satellites, which is consistent with the observed hemispherical trend. Additionally, magnetospheric particle densities fall off rapidly with distance from the primary, which is consistent with the observed planetocentric trend in CO_2. The Uranian magnetosphere is dominated by protons and electrons, with no evidence for C^+ or other heavy ions (see Appendix D for a brief review of Uranus' magnetic field and plasma environment). However, the surfaces of these moons are dominated by intimately mixed H_2O ice and a low albedo, presumably C-rich, constituent, which represents an ideal substrate for CO_2 production via irradiation. Consequently, C^+ ion implantation is not required to explain the presence of radiolytically-generated CO_2 on the Uranian satellites. Additionally, experiments investigating the irradiation potential of the Uranian satellites demonstrated that the electron and proton fluxes measured by Voyager 2 are sufficient to chemically modify their surfaces (Lanzerotti et al., 1987). Thus, we conclude that irradiation by magnetospherically-trapped charged particles is the most likely mechanism for explaining the observed distribution in CO_2. Detailed numerical modeling of Uranian satellite-magnetospheric interactions, which is beyond the scope of this study, would help constrain the regions on these satellites' surfaces that experience the largest charged particle fluxes.

Summary and Conclusions

We have used multiple methodologies to quantify the distribution of CO_2 ice on Ariel, Umbriel, Titania, and Oberon, including: (1) visual identification of bands, (2) band area measurements, (3) band center modeling, (4) statistical analysis of the distribution of CO_2, (5) spectral modeling of mean trailing hemisphere spectra, and (6) relative CO_2 band area ratios for the mean spectra and a wide range of synthetic spectra. Combining the results of these procedures, we find clear evidence for significant ($> 2\sigma$) amounts of CO_2 ice on the trailing hemispheres of Ariel, Umbriel, Titania, and Oberon. While Oberon lacks visibly apparent CO_2 bands, our statistical analysis of the distribution of CO_2, as well as our extensive spectral modeling and relative band area ratio analysis (Appendix B), supports the presence of CO_2 on this satellite. Additionally, the narrow

profiles of the CO_2 bands and the lack of the CO_2 $2\upsilon_3$ feature near 2.134 μm, along with the results of our CO_2 relative band area ratio analysis, suggests that the detected CO_2 is dominantly pure and segregated from other constituents.

The mismatch between our best fit SpeX and IRAC numerical models suggests that we are probing distinct layers in the near-surfaces of these moons. Our SpeX models include intimate mixtures of H_2O and amorphous C, mixed areally with CO_2 ice (5 – 50 μm grain sizes for all three components), whereas our IRAC models are dominated by small H_2O ice grains with only minor amounts of CO_2 ice and/or amorphous C (0.5 – 2 μm grain sizes for all three components). Thus, the results of our spectral color analysis, along with our photon penetration depth estimates, suggests that the CO_2 ice detected by SpeX is present at greater depths (~100 μm) than those probed by IRAC (~10 μm) into pure crystalline H_2O ice. Spectral models that can account for multiple heterogeneous layers are needed to further investigate whether the near-surfaces of these moons are compositionally stratified.

We also investigated the distribution of H_2O ice on these moons using band parameter and statistical analyses on the 1.52-μm and 2.02-μm H_2O bands. Our results indicate that H_2O ice bands are stronger on the leading hemispheres of all four moons. Ratios between the mean H_2O band areas on the leading and trailing hemispheres of these satellites demonstrate that hemispherical asymmetries in H_2O band strength decrease with distance from Uranus, with only a slight asymmetry on the farthest classical moon, Oberon.

Our analyses demonstrate that these moons display clear hemispherical asymmetries in composition. Both the abundance of CO_2 ice and hemispherical asymmetries in H_2O ice band strengths decrease with increasing orbital radius. We have identified magnetospheric charged particle bombardment as the most likely driver of the observed distribution of CO_2. Radiolytic production of CO_2, and other oxidized carbonaceous species, could lead to the removal and/or masking of native H_2O ice on the trailing hemispheres of these moons, which in turn, would enhance leading/trailing asymmetries in H_2O band strengths on the moons closest to Uranus. Thus, charged particle bombardment might account for the hemispherical and planetocentric trends in the distribution of both CO_2 and H_2O ices on the classical Uranian satellites. Numerical models that investigate interactions between Uranus' magnetosphere and the Uranian satellites are needed to further test whether magnetospheric charged particle bombardment represents the primary control on the distribution of CO_2 and H_2O. Additionally, future NIR observations of the Uranian satellites will continue to improve our understanding of their surface composition and further constrain the distribution of CO_2 and H_2O on these moons.

References

Beddingfield, C.B., Burr, D.M., Emery, J.P., 2015. Fault geometries on Uranus' satellite Miranda: Implications for internal structure and heat flow. *Icarus*, *247*, p.35-52, http://dx.doi.org/10.1016/j.icarus.2014.09.048.

Bell III, J.F., McCord, T.B., 1991. A search for spectral units on the Uranian satellites using color ratio images. *Lunar Planetary Science Conference XXI*: p.473 – 489 (abstract).

Bernstein, M.P., Cruikshank, D.P., Sandford, S.A., 2005. Near-infrared laboratory spectra of solid H_2O/CO_2 and CH_3OH/CO_2 ice mixtures. *Icarus*, *179*, p.527–534.

Bohren, C.F., Huffman, D.R., 1983. Absorption and scattering of light by small particles. *John Wiley & Sons, Inc*., Weinheim.

Borucki, J.G., Khare, B., Cruikshank, D.P., 2002. A new energy source for organic synthesis in Europa's surface ice. *Journal of Geophysical Research, 107*, p.24-1-24-5, DOI: 10.1029/2002JE001841.

Brown, R.H., Clark, R.N., 1984. Surface of Miranda: Identification of water ice. *Icarus 58*, p.288-292.

Brown R.H., Cruikshank, D.P., 1983. The Uranian satellites: Surface compositions and opposition brightness surges. *Icarus*, *55*, p.83-92.

Buratti, B.J., Mosher, J.A., 1991. Comparative global albedo and color maps of the Uranian satellites. *Icarus*, *90*, p.1-13.

Cassidy, T.A., Coll, P., Raulin, F., Carlson, R.W., Johnson, R.E., Loeffler, M.J., Hand, K.P., Baragiola, R.A., 2010. Radiolysis and photolysis of icy satellite surfaces: Experiments and theory. *Space Science Reviews*, *153*, p.299-315, DOI 10.1007/s11214-009-9625-3.

Cassidy, T.A., Paranicas, C.P., Shirley, J.H., Dalton, J.B., Teolis, B.D., Johnson, R.E., Kamp, L., Hnedrix, A.R., 2013. Magnetospheric ion sputtering and water ice grain size at Europa. *Planetary Space Science*, 77, p.64-73.

Cao, X. and Paty, C., Diurnal and Seasonal Variability of Uranus' Magnetosphere. *Journal of Geophysical Research: Space Physics, 122*, p.6318-6331.

Chakarov, D.V., Gleeson, M.A., Kasemo, B., 2001. Photoreactions of water and carbon at 90 K. *Journal of Chemical Physics*, *115*, p.9477-9483, http://dx.doi.org/10.1063/1.1414375.

Cheng, A.F., Krimigis, S.M., Mauk, B.H., Keath, E.P., Maclennan, C.G., Lanzerotti, L.J., Paonessa, M.T., Armstrong, T.P., 1987. Energetic ion and electron phase space densities in the magnetosphere of Uranus. *Journal of Geophysical Research*, *92*, p.15315-15328.

Clark, R.N., Lucey, P.G., 1984. Spectral properties of ice-particulate mixtures and implications for remote sensing 1. Intimate mixtures. *Journal of Geophysical Research, 89*, p.6341-6348.

Clark, R.N. and Roush, T.L., 1984. Reflectance spectroscopy: Quantitative analysis techniques for remote sensing applications. *Journal of Geophysical Research: Solid Earth, 89* (B7), p.6329-6340.

Clark, R.N. et al. 2005. Compositional maps of Saturn's moon Phoebe from imaging spectroscopy. *Nature, 435*, p.66–69.

Clark R.N., Curchin J.M., Jaumann R., Cruikshank D.P., Brown R.H., Hoefen T.M., Stephan K., Moore, J.M., Buratti B.J., Baines K.H., Nicholson P.D., Nelson R.M., 2008. Compositional mapping of Saturn's satellite Dione with Cassini VIMS and implications of dark material in the Saturn system. *Icarus, 193*, p.372–386.

Clark, R.N., Carlson, R., Grundy, W.M., Noll, K., 2013. Observed ices in the Solar System. In: Gudipati, M.S., Castillo-Rogez, J. (Eds), The Science of Solar System Ices. *Springer*, New York, p.3-46, DOI: 10.1007/978-1-4614-3076-6.

Connerney, J.E.P., Acuna, M.H., Ness, N.F., 1987. The Magnetic Field of Uranus. *Journal of Geophysical Research, 92*, p.15329-15336.

Croft, S.K., Soderblom, L.A., 1991. Geology of the uranian satellites. In: Bergstralh, J.T., Miner, E.D., Matthews, M.S. (Eds.), Uranus. *University of Arizona Press*, Tucson, p.561–628.

Cruikshank, D.P., Roush, T.L., Owen, T.C., Geballe, T.R., de Bergh, C., Schmitt, B., Brown, R.H., Bartholomew, M.J., 1993. Ices on the surface of Triton. *Science, 261*, p.742–745.

Cruikshank, D.P. et al., 2010. Carbon dioxide on the satellites of Saturn: Results from the Cassini VIMS investigation and revisions to the VIMS wavelength scale. *Icarus, 206*, p.561-572, doi:10.1016/j.icarus.2009.07.012.

Cushing, M.C., Vacca, W.D., Rayner, J.T., 2004. Spextool: A Spectral Extraction Package for SpeX, a 0.8 – 5.5 Micron Cross-Dispersed Spectrograph. *Astronomical Society of the Pacific, 116*, p.362-376.

Delitsky, M.L., Lane, A.L., 1998. Ice chemistry on the Galilean satellites. *Journal of Geophysical Research, 103*, p.31391–31403.

Emery, J.P., Burr, D.M., Cruikshank, D.P., Brown R.H., Dalton, J.B., 2005. Near-infrared (0.8–4.0 μm) spectroscopy of Mimas, Enceladus, Tethys, and Rhea. *Astronomy & Astrophysics, 435*. p.353-362, DOI: 10.1051/0004-6361:20042482.

Emery, J.P., Cruikshank, D.P., Van Cleve, J., 2006. Thermal emission spectroscopy (5.2 – 38 μm) of three Trojan asteroids with the Spitzer Space Telescope: Detection of fine-grained silicates. *Icarus, 182*, p.496-512, doi:10.1016/j.icarus.2006.01.011.

Fazio G.G. et al., 2004. The Infrared Array Camera (IRAC) for the Spitzer Space Telescope. *Astrophysical Journal Supplemental Series, 154*, p.10-17.

Gerakines, P.A., Moore, M.H., 2001. Carbon suboxide in astrophysical ice analogs. *Icarus, 154*, p.372–380

Gerakines, P.A., Bray, J.J., Davis, A., Richey, C.R., 2005. The strengths of near-infrared absorption features relevant to interstellar and planetary ices. *Astrophysical Journal, 620*, p.1140–1150.

Gomis, O., Strazzulla, G., 2005. CO_2 production by ion irradiation of H_2O ice on top of carbonaceous materials and its relevance to the Galilean satellites. *Icarus, 177*, p.570–576.

Grundy, W.M., Young, L.A., Young, E.F., 2003. Discovery of CO_2 ice and leading-trailing spectral asymmetry on the Uranian satellite Ariel. *Icarus, 162*, p.222-229.

Grundy, W.M., Young, L.A., Spencer, J.R., Johnson, R.E., Young, E.F., Buie, M.W., 2006. Distributions of H_2O and CO_2 ices on Ariel, Umbriel, Titania, and Oberon from IRTF/SpeX observations. *Icarus, 184*, p.543-555.

Grundy, W.M., Young, L.A., Stansberry, J.A., Buie, M.W., Olkin, C.B., Young E.F., 2010. Near-infrared spectral monitoring of Triton with IRTF/SpeX II: Spatial distribution and evolution of ices. *Icarus, 205*, p.594-604.

Hansen, G.B., 1997. The infrared absorption spectrum of carbon dioxide ice from 1.8 to 333 microns. *Journal of Geophysical Research, 102*, p.21569–21587.

Hansen, G.B., 2005. Ultraviolet to near-infrared absorption spectrum of carbon dioxide ice from 0.174 to 1.8 μm. *Journal of Geophysical Research*, 110, p.1-18.

Hansen, G.B., McCord, T.B., 2008. Widespread CO_2 and other non-ice compounds on the anti-Jovian and trailing sides of Europa from Galileo/NIMS observations. *Geophysical Research Letters, 35*, p.LO1202, doi:10.1029/2007GL031748.

Hapke, B., 2002. Theory of reflectance and emittance spectroscopy. *Cambridge University Press*, New York.

Hapke, B., 2012. Theory of reflectance and emittance spectroscopy (2^{nd} Ed.). *Cambridge University Press*, New York, p.405-406.

Helfenstein, P., Veverka, J., 1988. Early resurfacing of Umbriel: Evidence from Voyager 2 photometry. *Lunar Planetary Science Conference XIX*: p.477-478 (abstract).

Helfenstein, P., Thomas, P.C., Veverka, J., 1989. Evidence from Voyager II photometry for early resurfacing of Umbriel. *Nature*, 338, p.324-326.

Helfenstein, P., Hillier, J., Weitz, C., Veverka, J., 1991. Oberon Color Photometry from Voyager and Its Geological Implications. *Icarus*, 90, p.14-29.

Hibbitts, C.A., McCord, T.B., Hansen, G.B., 2000. Distributions of CO_2 and SO_2 on the surface of Callisto. *Journal of Geophysical Research, 105*, p.22541–22557.

Hibbitts, C.A., Klemaszewski, J., McCord, T.B., Hansen, G.B., Greeley, R., 2002. CO_2-rich impact craters on Callisto, *Journal of Geophysical Research, 107*, doi:10.1029/2000JE001412.

Hibbitts, C.A., Pappalardo, R.T., Hansen, G.B., McCord, T.B., 2003. Carbon dioxide on Ganymede. *Journal of Geophysical Research, 108*. p.1956.1-22

Hudson, R.L., Moore, M.H., 2001. Radiation chemical alterations in Solar System ices: An overview. J. Geophys. Res. 106, p.33275–33284.

Jamieson, C.S., Mebel, A.M., Kaiser, R.I., 2005. Understanding the kinetics and dynamics of radiation-induced reaction pathways in carbon monoxide ice at 10 K. Astrophys. J. Sup. Series 163, p.184-206.

Jankowski, D.G., Squyres, S.W., 1988. Solid-State Ice Volcanism on the Satellites of Uranus. Science 241, p.1322-1325.

Jarmillo-Botero, A., Cheng, Q.A.M., Goddard, W.A., 2012. Hypervelocity Impact Effect of Molecules from Enceladus' Plume and Titan's Upper Atmosphere on NASA's Cassini Spectrometer from Reactive Dynamics Simulation. Phys. Rev. Let. 109, p.213201-1-213201-5.

Johnson, R.E., Lanzerotti, L.J., Brown, W.L., 1984. Sputtering processes: Erosion and chemical change. Adv. Space Rev. 4, p.41-51.

Kargel, J.S., 1994. Cryovolcanism on the icy satellites. Earth Moon Planets 67, p.101-113.

Karkoschka, E., 2001. Comprehensive photometry of the rings and 16 satellites of Uranus with the Hubble Space Telescope. Icarus 151, p.51-68, doi:10.1006/icar.2001.6596.

Kim, Y.S., Kaiser, R.I., 2012. Electron irradiation of Kuiper Belt surface ices: Ternary N_2-CH_4-CO mixtures as a case study. Astrophys. J. 758, p.37-42. doi:10.1088/0004-637X/758/1/37.

Krimigis, S.M., Armstrong, T.P., Axford, W.I., Cheng, A.F., Gloeckler, G., Hamilton, D.C., Keath, E.P., Lanzerotti L.J., Mauk, B.H., 1986. The magnetosphere of Uranus: Hot plasma and radiation environment. Science 233, p.97-102.

Lane, A.L., Nelson, R.M., Matson, D.L., 1981. Evidence for sulphur implantation in Europa's UV absorption band. Nature 292, p.38–39.

Lanzerotti, L.J., Brown, W.L., Maclennan, C.G., Cheng, A.F., Krimigis, S.M., Johnson, R.E., 1987. Effects of charged particles on the surfaces of the satellites of Uranus. J. Geophys. Res. 92, p.14949-14957.

Lebofsky, L.A., 1975, Stability of frosts in the Solar System. Icarus 25, p.205-217.

Lindsay, S.S., Marchis, F., Emery, J.P., Enriquez, J.E., Assafin, M., 2015. Composition, mineralogy, and porosity of multiple asteroid systems from visible and near-infrared spectral data. Icarus 247, p.53-70. http://dx.doi.org/10.1016/j.icarus.2014.08.040

Loeffler, M.J., Baratta, G.A., Palumbo, M.E., Strazzulla, G., Baragiola, R.A., 2005. CO_2 synthesis in solid CO by Lyman-α photons and 200 keV protons. Astro. & Astrophys. 435, p.587-594, DOI: 10.1051/0004-6361:20042256.

Mastrapa, R.M., Bernstein, M.P., Sandford, S.A., Roush, T.L., Cruikshank, D.P., Dalle Ore, C.M., 2008. Optical constants of amorphous and crystalline H2O-ice in the near infrared from 1.1 to 2.6 μm. Icarus 197, p.307-320.

Mastrapa, R.M., Sandford, S.A., Roush, T.L., Cruikshank, D.P., Dalle Ore, C.M., 2009. Optical constants of amorphous and crystalline H2O-ice: 2.5 – 22 μm (4000 – 455 cm^{-1}) optical constant of H_2O-ice. Astro. J. 701, p.1347-1356.

McCord, T.B. et al., 1997. Organics and other molecules in the surfaces of Callisto and Ganymede. Science 278, p.271–275.

McCord, T.B. et al., 1998. Nonwater-ice constituents in the surface material of the icy Galilean satellites from the Galileo near-infrared mapping spectrometer investigation. J. Geophys. Res. 103, p.8603–8626

Mennella, V., Palumbo, M.E., Baratta, G.A., 2004. Formation of CO and CO_2 molecules by ion irradiation of water ice-covered hydrogenated carbon grains. Astrophys. J. 615, p.1073–1080.

Mennella, V., Baratta, G.A., Palumbo, M.E., Bergin, E.A., 2006. Synthesis of CO and CO_2 molecules by UV irradiation of water ice-covered hydrogenated carbon grains. Astro. J. 643, p.923-931.

Moersch, J.E. and Christensen, P.R., 1995. Thermal emission from particulate surfaces: A comparison of scattering models with measured spectra. Journal of Geophysical Research: Planets, 100 E4, p.7465-7477

Ness, N.F., Acuna, M.H., Behannon, K.W., Burlaga, L.F., Connerney, J.E.P., Lepping, R.P., Neubauer, F.M., 1986. Magnetic Fields at Uranus. Science 233, p.85-89.

Noll, K.S., Weaver, H.A., Gonnella, A.M., 1995. The albedo spectrum of Europa from 2200 to 3300 A˚. J. Geophys. Res. 100, p.19057–19059.

Noll, K.S., Roush, T.L., Cruikshank, D.P., Johnson, R.E., Pendleton, Y.J., 1997. Detection of ozone on Saturn's satellites Rhea and Dione. Nature 388, p.45–47.

Ockert, M.E., Nelson, R.M., Lane, A.L., Matson, D.L., 1987. Europa's ultraviolet absorption band (260 to 320 nm) – temporal and spatial evidence from IUE. Icarus 70, p.499–505.

Palmer, E.E., Brown, R.H., 2011. Production and detection of carbon dioxide on Iapetus. Icarus 212, p.807-818.

Pappalardo, R.T., Reynolds, S.J., Greeley, R., 1997. Extensional tilt blocks on Miranda: Evidence for an upwelling origin of Arden Corona. J. Geophys. Res.: Planets 102 (E6), p.13369–13379.

Pinilla-Alonso, N., Roush, T.L., Marzo, G.A., Cruikshank, D.P., Dalle Ore, C.M., 2011. Iapetus surface variability revealed from statistical clustering of a VIMS mosaic: The distribution of CO_2. Icarus 215, p.75-82.

Raut, U., Fulvio, D., Loeffler, M.J., Baragiola, R.A., 2012. Radiation synthesis of carbon dioxide in ice-coated carbon: Implications for interstellar grains and icy moons. Astrophys. J. 752, p.159, doi:10.1088/0004-637X/752/2/159.

Rayner, J.T., Toomey, D.W., Onaka, P.M., Denault, A.J., Stahlberger, W.E., Watanabe, D.Y., Wang, S.I., 1998. SpeX: A medium-resolution IR spectrograph for IRTF. Proc. SPIE 3354, p.468–479.

Rayner, J.T., Toomey, D.W., Onaka, P.M., Denault, A.J., Stahlberger, W.E., Vacca, W.D., Cushing, M.C., Wang, S., 2003. SpeX: A medium-resolution 0.8-5.5 micron spectrograph and imager for the NASA Infrared Telescope Facility. Astron. Soc. of the Pacific 115, p.362.

Rayner, J.T., Cushing, M.C., Vacca, W.D., 2009. The Infrared Telescope Facility (IRTF) Spectral Library: Cool stars. Astrophys. J. Sup. Series 185, p.289-432. doi:10.1088/0067-0049/185/2/289

Reach, W.T. et al., 2005. Absolute Calibration of the Infrared Array Camera on the Spitzer Space Telescope. Astron. Soc. of the Pacific 117, p.978-990.

Schenk, P.M., 1991. Fluid volcanism on Miranda and Ariel: Flow morphology and composition. J. Geophys. Res. 96, p.1887-1906.

Schmidt, J.A., Johnson, M.S., Schinke, R., 2013. Carbon dioxide photolysis from 150 to 210 nm: Singlet and triplet channel dynamics, UV spectrum, and isotope effects. Proceed. Nation. Acad. Sci. 110, p.17691-17696. www.pnas.org/cgi/doi/10.1073/pnas.1213083110

Sedlacko, T., Balog, R., Lafosse, A., Stano, M., Matejcik, S., Azria, R., Illenberger, E., 2005. Reactions in condensed formic acid (HCOOH) induced by low energy (< 20 eV) electrons. Phys. Chem. 7, p.1277-1282, DOI:10.1039/b419104h.

Shoemaker, E.M., Wolfe, R.A., 1982. Cratering timescales for the Galilean satellites, in: Morrison, D. (Ed.), Satellites of Jupiter, Univ. of Arizona Press, Tucson, p. 277–339.

Smith, B.A. et al., 1986. Voyager 2 in the Uranian System: Imaging Science Results. Science 233, p.43-64.

Smith, E.V.P., Gottlieb, D.M., 1974. Solar Flux and its Variations. Space Sci. Rev., 16, p.771-802.

Soifer, B.T., Neugebauer, G., Matthews, K., 1981. Near-infrared spectrophotometry of the satellites and rings of Uranus. Icarus 45,p. 612-617.

Spiegel, M.R., 1992. Theory and Problems of Probability and Statistics. McGraw-Hill, New York, p. 117-118.

Spinks, J.W.T., Woods, R.J., 1990. An Introduction to Radiation Chemistry. John Wiley, New York, p. 574.

Stone, E.C., Miller, E.D., 1986. The Voyager-2 encounter with the Uranian system. Science 233, p.39-43.

Stone, E.C., Cooper, J.T., Cummings, A.C., McDonald, F.B., Trainor, J.H., Lal, N., McGuire, R., Chenette, D.L., 1986. Energetic Charged Particles in the Uranian Magnetosphere. Science 233, p.93-97.

Stryk, T., Stooke, P.J., 2008. Voyager 2 images of Uranian satellites: Reprocessing and new interpretations. Lunar Planet. Sci. XXXIX, 1362 (abstract).

Tamayo, D., Burns, J.A., Hamilton, D.P., 2013. Chaotic dust dynamics and implications for the hemispherical color asymmetries of the Uranian satellites. Icarus 226, p.655-662, http://dx.doi.org/10.1016/j.icarus.2013.06.018.

Tittemore, W.C., Wisdom, J., 1990. Tidal Evolution of the Uranian Satellites. Icarus 85, p. 394-443.

Vacca, W.D., Cushing, M.C., Rayner, J.T., 2003. A method of correcting near-infrared spectra for telluric absorption. Astron. Soc. of the Pacific 115, p.389-409.

Waite, J.H. et al., 2006. Cassini Ion and Neutral Mass Spectrometer: Enceladus plume composition and structure. Science 311, p.1419-1422, DOI: 10.1126/science.1121290.

Werner, M.W. et al., 2004. The Spitzer Space Telescope Mission. Astrophys. J. Supple. Series, 154, p.1-9.

Zahnle, K., Schenk, P., Sobieszczyk, S., Dones, L., Levison, H.F., 2001. Differential cratering of synchronously rotating satellites by ecliptic comets. Icarus 153, p.111–129.

Zahnle, K., Schenk, P., Levison, H., Dones, L., 2003. Cratering rates in the outer Solar System. Icarus 163, p.263–289.

Appendix 1

Table 1.1. Classical Uranian satellites.

Satellite	Orbital Radius (km)	Orbital Radius (R_{Uranus})	Orbital Period (days)	Radius (km)	Density (g cm^{-3})	*Geometric Albedo (~0.957 μm)
Miranda	129,900	5.12	1.41	236	1.21	0.45 ± 0.02
Ariel	190,900	7.53	2.52	579	1.59	0.56 ± 0.02
Umbriel	266,000	10.5	4.14	585	1.46	0.26 ± 0.01
Titania	436,300	17.2	8.71	789	1.66	0.39 ± 0.02
Oberon	583,500	23.0	13.46	762	1.56	0.33 ± 0.01

*Geometric albedos digitally extracted from Figure 7 in Karkoschka (2001).

Table 1.2. IRTF/SpeX Observations.

Satellite	Satellite Long. (°)	Satellite Lat. (°)	Hemisphere Observed†	UT Date	UT Time (mid-expos)	t_{int} (min)	Spectral Resolution ($\lambda/\Delta\lambda$)	Observing PI
Ariel	53.6	-16.0	Leading	8/9/2003	12:15	156	~1600 – 1700	Grundy
	79.8	-19.4	Leading	7/17/2002	13:25	108	~1300 – 1400	Grundy
	87.8	24.0	Leading	9/5/2013	11:10	92	~650 – 750	Cartwright
	93.5	-18.1	Leading	10/4/2003	5:45	108	~1600 – 1700	Grundy
	159.9	-11.1	Interm. (L)	7/15/2004	12:00	112	~1600 – 1700	Grundy
	200.0	-15.9	Interm. (T)	8/5/2003	12:00	84	~1600 – 1700	Grundy
	219.8	-17.2	Interm. (T)	9/7/2003	9:35	90	~1600 – 1700	Grundy
	233.8	-23.1	Trailing	7/5/2001	14:10	50	~1300 – 1400	Grundy
	257.6	-29.5	Trailing	9/6/2000	7:35	76	~650 – 750	Rivkin
	278.3	24.8	Trailing	8/7/2013	13:20	44	~650 – 750	Cartwright
	294.8	-19.3	Trailing	7/16/2002	13:10	140	~1300 – 1400	Grundy
	304.8	-23.2	Trailing	7/8/2001	14:40	48	~1300 – 1400	Grundy
	316.6	-18.2	Interm. (T)	10/8/2003	7:55	132	~1600 – 1700	Grundy
Umbriel	38.4	20.3	Interm. (L)	8/13/2012	13:55	60	~650 – 750	Cartwright
	75.2	-29.3	Leading	9/6/2000	10:00	80	~650 – 750	Rivkin
	92.1	-11.1	Leading	7/16/2004	14:25	74	1600 – 1700	Grundy
	131.3	17.5	Leading	11/1/2012	9:30	78	~650 – 750	Cartwright
	216.2	-10.9	Interm. (T)	7/5/2004	14:10	80	~1600 – 1700	Grundy
	219.8	-23.0	Interm. (T)	7/7/2001	14:10	52	~1300 – 1400	Grundy
	261.3	-9.4	Trailing	9/18/2005	9:21	196	~1600 – 1700	Grundy
	264.0	23.7	Trailing	9/5/2013	13:55	52	~650 – 750	Cartwright
	317.6	-11.4	Interm. (T)	7/27/2004	11:30	184	~1600 – 1700	Grundy
Titania	13.6	19.0	Interm. (L)	9/21/2012	11:25	32	~650 – 750	Cartwright
	86.5	23.6	Leading	9/6/2013	10:50	60	~650 – 750	Cartwright

Table 1.2. Continued. IRTF/SpeX observations.

Satellite	Satellite Long. (°)	Satellite Lat. (°)	Hemisphere Observed†	UT Date	UT Time (mid-expos)	t_{int} (min)	Spectral Resolution ($\lambda/\Delta\lambda$)	Observing PI
	98.0	-18.1	Leading	10/8/2003	5:45	64	~1600 – 1700	Grundy
	160.0	18.2	Interm. (L)	10/12/2012	10:15	60	~650 – 750	Cartwright
	213.9	-11.1	Interm. (T)	7/15/2004	14:25	64	~1600 – 1700	Grundy
	237.0	-23.0	Trailing	7/6/2001	13:25	56	~1300 – 1400	Grundy
	258.9	-29.3	Trailing	9/5/2000	9:55	60	~650 – 750	Rivkin
	277.8	-23.0	Trailing	7/7/2001	13:10	36	~1300 – 1400	Grundy
	299.6	-10.2	Trailing	10/13/2005	9:05	106	~1600 – 1700	Grundy
	342.7	-29.4	Interm. (T)	9/7/2000	10:35	44	~650 – 750	Rivkin
Oberon	1.0	-29.4	Interm. (L)	9/7/2000	8:30	32	~650 – 750	Rivkin
	64.8	18.1	Leading	10/12/2012	11:05	98	~650 – 750	Cartwright
	85.9	-3.7	Leading	8/4/2006	?	?	~1600 – 1700	Grundy
	91.0	23.7	Leading	9/1/2013	11:40	56	~650 – 750	Cartwright
	110.6	-10.2	Leading	10/13/2005	6:30	124	~1600 – 1700	Grundy
	164.0	-23.0	Interm. (L)	7/6/2001	14:25	32	~1300 – 1400	Grundy
	216.2	-23.1	Interm. (T)	7/8/2001	13:10	48	~1300 – 1400	Grundy
	223.7	18.9	Trailing	9/21/2012	10:20	64	~650 – 750	Cartwright
	236.1	17.4	Trailing	11/1/2012	6:55	40	~650 – 750	Cartwright
	266.5	20.2	Trailing	8/13/2012	15:15	28	~650 – 750	Cartwright
	307.2	-29.3	Trailing	9/5/2000	8:10	60	~650 – 750	Rivkin

†'Leading' and 'trailing' table entries represent spectra collected over these moons' leading (046 – 135°) and trailing 226 – 315°) quadrants, respectively. 'Interm. (L)' and 'Interm. (T)' represent spectra collected over Uranus-facing (316 – 045°) and anti-Uranus (136 – 225°) quadrants, respectively.

Table 1.3. Local standard and analog stars.

Observing Team	UT date	Solar analogs
Rivkin et al.	9/5/2000	SAO 164, 16 Cygni A
	9/6/2000	SAO 164, 16 Cygni Q
	9/7/2000	Sao 164
Cartwright et al.	8/13/2012	SAO 109348, SA 115-271
	9/21/2012	SAO 109182, SAO 110201, SA 115-271
	10/12/2012	SAO 109182, SA 115-271, Hyades 64
	11/1/2012	SAO 109182, SAO 126133, Hyades 64
	8/7/2013	SAO 109426, SAO 109450
	9/1/2013	SAO 109426, SAO 109450, SAO 109348
	9/5/2013	SAO 109426, SAO 109450, SAO 109348
	9/6/2013	SAO 109426, SAO 109450, SAO 109348

Table 1.4. Spitzer/IRAC observations.

Satellite	Satellite Long. (°)	Satellite Lat. (°)	Program 71 Observation	UT Date	UT Time (mid-expos)	t_{int} per channel (sec)	Phase Angle	Heliocentric Distance	Observer Distance
Ariel	28.2	-6.6	Umbriel-L	6/29/2004	21:55	80	2.57	20.0485	19.5529
	54.0	-18.4	Titania-T	12/3/2003	11:08	80	2.84	20.0372	20.1741
	87.8	-6.7	Ariel-L	6/10/2005	4:04	80	2.90	20.0660	20.0770
	93.9	-6.7	Umbriel-T	6/15/2005	6:03	80	2.90	20.0661	19.9914
	127.4	-14.6	Oberon-L	11/23/2004	8:16	80	2.86	20.0556	19.8728
	255.5	-18.4	Oberon-T	12/2/2003	8:28	80	2.84	20.0361	20.1543
	276.5	-14.6	Ariel-T	11/26/2004	21:48	80	2.88	20.0566	19.9335
Umbriel	34.7	-10.5	Titania-L	11/29/2005	9:13	80	2.81	20.0748	19.7977
	110.4	-6.6	Umbriel-L	6/29/2004	21:55	80	2.57	20.0488	19.5532
	149.9	-18.3	Oberon-T	12/2/2003	8:28	80	2.84	20.0349	20.1532
	151.8	-14.5	Ariel-T	11/26/2004	21:48	80	2.88	20.0550	19.9319
	246.5	-18.2	Titania-T	12/3/2003	11:08	80	2.84	20.0358	20.1727
	276.7	-6.7	Umbriel-T	6/15/2005	6:03	80	2.90	20.0663	19.9916
Titania	83.1	-10.5	Titania-L	11/29/2005	9:13	80	2.81	20.0737	19.7966
	216.7	-18.3	Oberon-T	12/2/2003	8:28	80	2.84	20.0341	20.1524
	219.5	-14.5	Oberon-L	11/23/2004	8:16	80	2.86	20.0541	19.8713
	258.9	-6.6	Umbriel-L	6/29/2004	21:55	80	2.57	20.0492	19.5537
	262.6	-18.3	Titania-T	12/3/2003	11:08	80	2.84	20.0361	20.1729
Oberon	88.3	-14.6	Oberon-L	11/23/2004	8:16	80	2.86	20.0564	19.8736
	141.9	-6.7	Umbriel-T	6/15/2005	6:03	80	2.90	20.0632	19.9884
	174.0	-6.7	Umbriel-L	6/29/2004	21:55	80	2.57	20.0460	19.5504
	261.9	-18.3	Oberon-T	12/2/2003	8:28	80	2.84	20.0358	20.1541
	290.3	-10.6	Titania-L	11/29/2005	9:13	80	2.81	20.0747	19.7975
	291.6	-18.3	Titania-T	12/3/2003	11:08	80	2.84	20.0378	20.1747

Table 1.5. Summary of IRAC fluxes and geometric albedos.

Target	IRAC Ch.l	Obser.	Sate. Long. (°)	Sate. Lat. (°)	Flux (mJy)	Δ Flux mJy	Geo. Alb.	ΔGeo. Alb.
Ariel	Ch.1	Titania_T	54.0	-18.4	0.595	0.015	0.191	0.005
		Ariel_L	87.8	-6.7	0.594	0.033	0.189	0.010
		Umbriel_L	92.8	-10.7	0.621	0.019	0.185	0.006
		Umbriel_T	93.9	-6.7	0.568	0.008	0.188	0.006
		Oberon_L	127.4	-14.6	0.597	0.028	0.186	0.009
		Oberon_T	255.5	-18.4	0.721	0.014	0.230	0.004
		Ariel_T	276.5	-14.6	0.744	0.016	0.233	0.005
	Ch.2	Titania_T	54.0	-18.4	0.212	0.022	0.104	0.011
		Ariel_L	87.8	-6.7	0.195	0.026	0.095	0.012
		Umbriel_L	92.8	-10.7	0.187	0.017	0.085	0.008
		Umbriel_T	93.9	-6.7	0.185	0.018	0.089	0.008
		Oberon_L	127.4	-14.6	0.187	0.025	0.089	0.012
		Oberon_T	255.5	-18.4	0.261	0.014	0.127	0.007
		Ariel_T	276.5	-14.6	0.254	0.018	0.121	0.008
	Ch.3	Titania_T	54.0	-18.4	*0.027*	-	-	-
		Ariel_L	87.8	-6.7	0.042	0.015	0.033	0.012
		Umbriel_L	92.8	-10.7	0.094	0.018	0.070	0.011
		Umbriel_T	93.9	-6.7	0.103	0.020	0.081	0.016
		Oberon_L	127.4	-14.6	0.108	0.036	0.084	0.028
		Oberon_T	255.5	-18.4	0.097	0.029	0.078	0.023
		Ariel_T	276.5	-14.6	0.127	0.025	0.099	0.020
	Ch.4	Titania_T	54.0	-18.4	0.333	0.111	0.485	0.161
		Ariel_L	87.8	-6.7	0.153	0.046	0.221	0.066
		Umbriel_L	92.8	-10.7	0.118	0.034	0.160	0.046
		Umbriel_T	93.9	-6.7	0.114	0.019	0.164	0.028
		Oberon_L	127.4	-14.6	0.157	0.054	0.222	0.076
		Oberon_T	255.5	-18.4	0.332	0.091	0.482	0.131
		Ariel_T	276.5	-14.6	0.168	0.033	0.239	0.047
Umbriel	Ch.1	Titania_L	34.7	-10.5	0.542	0.010	0.155	0.003
		Umbriel_L	82.8	-10.7	0.590	0.027	0.163	0.008
		Oberon_T	149.9	-18.3	0.502	0.011	0.149	0.003
		Ariel_T	151.8	-14.5	0.501	0.014	0.146	0.004
		Titania_T	246.5	-18.2	0.536	0.005	0.159	0.002
		Umbriel_T	276.7	-6.7	0.535	0.006	0.157	0.002
	Ch.2	Titania_L	34.7	-10.5	0.198	0.020	0.087	0.009
		Umbriel_L	82.8	-10.7	0.174	0.011	0.073	0.005
		Oberon_T	149.9	-18.3	0.171	0.014	0.077	0.006

Table 1.5. Continued. Summary of IRAC fluxes and geometric albedos.

Target	IRAC Ch.l	Obser.	Sate. Long. (°)	Sate. Lat. (°)	Flux (mJy)	Δ Flux mJy	Geo. Alb.	ΔGeo. Alb.
		Ariel_T	151.8	-14.5	0.167	0.023	0.074	0.010
		Titania_T	246.5	-18.2	0.177	0.009	0.080	0.004
		Umbriel_T	276.7	-6.7	0.166	0.008	0.074	0.004
	Ch.3	Titania_L	34.7	-10.5	0.101	0.043	0.072	0.030
		Umbriel_L	82.8	-10.7	0.084	0.016	0.058	0.011
		Oberon_T	149.9	-18.3	0.074	0.027	0.055	0.020
		Ariel_T	151.8	-14.5	*0.054*	-	-	-
		Titania_T	246.5	-18.2	0.069	0.060	0.051	0.044
		Umbriel_T	276.7	-6.7	0.113	0.019	0.083	0.014
	Ch.4	Titania_L	34.7	-10.5	0.115	0.022	0.150	0.028
		Umbriel_L	82.8	-10.7	0.102	0.033	0.128	0.041
		Oberon_T	149.9	-18.3	0.295	0.117	0.397	0.157
		Ariel_T	151.8	-14.5	0.192	0.051	0.254	0.068
		Titania_T	246.5	-18.2	0.291	0.049	0.393	0.067
		Umbriel_T	276.7	-6.7	0.136	0.032	0.181	0.043
Titania	Ch.1	Titania_L	83.1	-10.5	1.001	0.008	0.160	0.001
		Oberon_T	216.7	-18.3	0.956	0.010	0.157	0.002
		Oberon_L	219.5	-14.5	0.982	0.004	0.158	0.001
		Titania_T	262.6	-18.3	0.982	0.011	0.162	0.002
		Umbriel_L	285.1	-10.7	1.063	0.005	0.163	0.001
	Ch.2	Titania_L	83.1	-10.5	0.261	0.009	0.063	0.002
		Oberon_T	216.7	-18.3	0.263	0.008	0.066	0.002
		Oberon_L	219.5	-14.5	0.263	0.004	0.064	0.001
		Titania_T	262.6	-18.3	0.265	0.004	0.067	0.001
		Umbriel_L	285.1	-10.7	0.279	0.006	0.065	0.001
	Ch.3	Titania_L	83.1	-10.5	0.112	0.016	0.044	0.006
		Oberon_T	216.7	-18.3	0.091	0.046	0.037	0.019
		Oberon_L	219.5	-14.5	0.106	0.036	0.042	0.015
		Titania_T	262.6	-18.3	0.077	0.026	0.032	0.011
		Umbriel_L	285.1	-10.7	0.098	0.022	0.038	0.008
	Ch.4	Titania_L	83.1	-10.5	0.130	0.033	0.094	0.024
		Oberon_T	216.7	-18.3	0.305	0.053	0.228	0.039
		Oberon_L	219.5	-14.5	0.100	0.019	0.073	0.014
		Titania_T	262.6	-18.3	0.225	0.047	0.168	0.035
		Umbriel_L	285.1	-10.7	0.143	0.023	0.100	0.016
Oberon	Ch.1	Oberon_L	88.3	-14.6	0.967	0.006	0.167	0.001

Table 1.5. Continued. Summary of IRAC fluxes and geometric albedos.

Target	IRAC Ch.l	Obser.	Sate. Long. (°)	Sate. Lat. (°)	Flux (mJy)	Δ Flux (mJy)	Geo. Alb.	ΔGeo. Alb.
		Umbriel_T	141.9	-6.7	0.939	0.005	0.164	0.001
		Oberon_T	261.9	-18.3	0.968	0.006	0.167	0.002
		Titania_L	290.3	-10.6	0.983	0.005	0.168	0.001
		Titania_T	291.6	-18.3	0.955	0.007	0.169	0.002
	Ch.2	Oberon_L	88.3	-14.6	0.255	0.006	0.067	0.002
		Umbriel_L	133.5	-10.7	0.269	0.004	0.067	0.001
		Umbriel_T	141.9	-6.7	0.255	0.003	0.068	0.001
		Oberon_T	261.9	-18.3	0.276	0.005	0.074	0.001
		Titania_L	290.3	-10.6	0.285	0.003	0.074	0.001
		Titania_T	291.6	-18.3	0.293	0.019	0.079	0.005
	Ch.3	Oberon_L	88.3	-14.6	0.117	0.020	0.050	0.009
		Umbriel_L	133.5	-10.7	0.111	0.021	0.045	0.008
		Umbriel_T	141.9	-6.7	0.123	0.017	0.054	0.008
		Oberon_T	261.9	-18.3	*0.025*	*0.021*	-	-
		Titania_L	290.3	-10.6	0.155	0.029	0.066	0.012
		Titania_T	291.6	-18.3	0.120	0.032	0.053	0.014
	Ch.4	Oberon_L	88.3	-14.6	0.101	0.043	0.079	0.034
		Umbriel_L	133.5	-10.7	0.114	0.020	0.085	0.015
		Umbriel_T	141.9	-6.7	*0.067*	-	-	-
		Oberon_T	261.9	-18.3	0.285	0.068	0.229	0.054
		Titania_L	290.3	-10.6	*0.104*	-	-	-
		Titania_T	291.6	-18.3	0.176	0.043	0.141	0.034

Italicized fluxes represent average background values.

Table 1.6. Mean leading and trailing IRAC geometric albedos.

Target	Hemisphere	IRAC Channel	Number of Observations	Mean Geometric Albedo	ΔMean Geometric Albedo
Ariel	Leading	1	5	0.188	0.003
		2	5	0.092	0.005
		3	4	0.067	0.009
		4	5	0.250	0.027
	Trailing	1	2	0.232	0.003
		2	2	0.124	0.005
		3	2	0.089	0.015
		4	2	0.361	0.048
Umbriel	Leading	1	4	0.153	0.002
		2	4	0.078	0.004
		3	4	0.052	0.011
		4	4	0.232	0.045
	Trailing	1	2	0.158	0.001
		2	2	0.077	0.003
		3	2	0.067	0.023
		4	2	0.287	0.040
Titania	Leading	1	1	0.160	0.001
		2	1	0.063	0.002
		3	1	0.044	0.006
		4	1	0.094	0.024
	Trailing	1	4	0.160	0.001
		2	4	0.066	0.001
		3	4	0.037	0.007
		4	4	0.142	0.019
Oberon	Leading	1	3	0.167	0.001
		2	3	0.067	0.001
		3	3	0.050	0.005
		4	2	0.082	0.019
	Trailing	1	3	0.168	0.001
		2	3	0.076	0.002
		3	2	0.060	0.009
		4	2	0.185	0.032

Table 1.7. Wavelength position of CO_2 ice bands and adjacent continua.

Band Name	Combination/Overtone Designation	Band Center (μm)	Band Width (μm)	Continua (μm)
CO_2 band 1	$2\upsilon_1 + \upsilon_3$	1.966	1.962 - 1.969	1.957 - 1.962, 1.969 - 1.974
CO_2 band 2	$\upsilon_1 + 2\upsilon_2 + \upsilon_3$	2.012	2.008 - 2.015	2.002 - 2.008, 2.015 - 2.020
CO_2 band 3	$4\upsilon_2 + \upsilon_3$	2.070	2.068 - 2.072	2.062 - 2.068, 2.072 - 2.078

Table 1.8. Summary of CO_2 ice band parameter analysis.

			CO_2 Band Area (10^{-4} μm)							
Satellite	Long. (°)	Lat. (°)	Band 1	ΔArea	Band 2	ΔArea	Band 3	ΔArea	Total Area	Total Δarea
Ariel	53.60	-16.00	1.36	0.64	1.42	1.19	0.23	0.59	3.02	1.47
	79.80	-19.40	1.34	0.44	-1.23	0.56	0.81	0.26	0.92	0.76
	87.80	24.00	1.26	0.31	0.43	0.44	0.49	0.23	2.17	0.59
	93.50	-18.10	0.87	0.56	1.11	0.72	-0.24	0.51	1.74	1.05
	159.90	-11.10	2.30	0.53	2.91	0.78	1.08	0.45	6.29	1.04
	200.00	-15.90	4.19	0.67	5.94	0.80	2.89	0.45	13.02	1.14
	219.80	-17.20	5.77	0.29	6.71	0.68	2.52	0.29	14.99	0.80
	233.80	-23.10	4.09	0.78	6.31	0.85	2.99	0.45	13.40	1.24
	257.60	-29.50	3.33	0.50	6.47	0.49	3.36	0.27	13.16	0.75
	278.30	24.80	6.06	0.83	6.48	1.02	2.83	0.60	15.37	1.45
	294.80	-19.30	6.26	0.40	5.56	0.47	3.08	0.25	14.90	0.66
	304.80	-23.20	5.12	0.76	6.29	0.96	3.35	0.61	14.76	1.36
	316.60	-18.20	4.52	0.58	6.72	0.82	2.32	0.46	13.56	1.11
Umbriel	38.40	20.30	-0.74	0.61	-0.66	0.72	0.14	0.37	-1.26	1.01
	75.20	-29.30	-0.04	0.75	-3.07	0.78	-0.37	0.50	-3.48	1.19
	92.10	-11.10	2.59	0.99	0.74	1.41	0.83	0.63	4.16	1.83
	131.30	17.50	0.23	0.37	1.18	0.44	0.07	0.22	1.48	0.61
	216.20	-10.90	1.09	0.92	1.54	1.22	2.56	0.74	5.19	1.69
	219.80	-23.00	0.65	0.92	1.42	1.10	1.11	1.03	3.18	1.77
	261.30	-9.40	2.11	0.52	3.13	0.52	1.67	0.29	6.92	0.79
	264.00	23.70	1.73	0.42	4.27	0.49	1.39	0.25	7.39	0.69
	317.60	-11.40	0.95	0.51	2.12	0.72	1.40	0.36	4.47	0.95
Titania	13.60	19.00	0.01	0.25	0.20	0.28	0.48	0.16	0.70	0.41
	86.50	23.60	0.40	0.21	1.24	0.27	-0.02	0.15	1.62	0.37
	98.00	-18.10	0.95	0.89	0.88	1.50	0.53	0.66	2.36	1.87
	160.00	18.20	-0.65	0.51	0.03	0.70	-0.12	0.39	-0.74	0.95
	213.90	-11.10	1.55	0.48	2.54	0.61	0.53	0.35	4.62	0.85
	237.00	-23.00	2.05	1.57	1.98	1.87	1.09	1.11	5.12	2.68
	258.90	-29.30	1.77	0.38	2.32	0.50	0.79	0.27	4.88	0.68
	277.80	-23.00	0.53	0.46	2.94	0.71	-0.11	0.89	3.36	1.22
	299.60	-10.20	1.68	0.38	1.40	0.54	1.30	0.27	4.37	0.71
	342.70	-29.40	0.90	0.44	0.43	0.59	0.07	0.28	1.41	0.78
Oberon	1.00	-29.40	1.83	0.49	-0.30	0.53	0.60	0.30	2.13	0.78
	64.80	18.10	-0.38	0.42	-0.19	0.49	0.22	0.27	-0.35	0.70
	85.90	-3.70	-3.75	0.95	-2.83	1.27	-0.31	0.64	-6.89	1.71
	91.00	23.70	0.31	0.75	0.40	0.79	0.23	0.62	0.94	1.26
	110.60	-10.20	0.08	0.38	0.48	0.47	-0.50	0.32	0.06	0.68

Table 1.8. Continued. Summary of CO_2 ice band parameter analysis.

Satellite	Long. (°)	Lat. (°)	Band 1	ΔArea	Band 2	ΔArea	Band 3	ΔArea	Total Area	Total Δarea
	164.00	-23.00	0.44	1.79	0.14	2.17	0.34	1.21	0.91	3.06
	216.20	-23.10	-0.35	0.50	-0.68	0.72	-0.45	0.57	-1.48	1.04
	223.70	18.90	0.61	0.28	0.97	0.36	0.23	0.16	1.81	0.49
	236.10	17.40	0.64	0.25	1.22	0.32	0.35	0.15	2.21	0.43
	266.50	20.20	1.62	0.72	1.15	0.86	0.74	0.51	3.51	1.23
	307.20	-29.30	0.84	0.38	0.79	0.27	0.68	0.22	2.31	0.52

Table 1.8. Continued. Summary of CO_2 ice band parameter analysis.

			Gauss Fit CO_2 Band Centers (μm)					
Satellite	Long. (°)	Lat. (°)	Band 1	Δcenter	Band 2	Δcenter	Band 3	Δcenter
Ariel	53.60	-16.00	-	-	-	-	-	-
	79.80	-19.40	-	-	-	-	-	-
	87.80	24.00	-	-	-	-	-	-
	93.50	-18.10	-	-	-	-	-	-
	159.90	-11.10	1.965	0.001	2.012	0.001	2.070	0.001
	200.00	-15.90	1.966	0.001	2.011	0.001	2.070	0.001
	219.80	-17.20	1.966	0.001	2.011	0.001	2.070	0.001
	233.80	-23.10	1.962	0.001	2.009	0.001	2.070	0.001
	257.60	-29.50	1.966	0.001	2.012	0.001	2.072	0.001
	278.30	24.80	1.966	0.001	2.011	0.001	2.070	0.001
	294.80	-19.30	1.966	0.001	2.012	0.001	2.070	0.001
	304.80	-23.20	1.965	0.001	2.012	0.001	2.070	0.001
	316.60	-18.20	1.966	0.001	2.012	0.001	2.070	0.001
Umbriel	38.40	20.30	-	-	-	-	-	-
	75.20	-29.30	-	-	-	-	-	-
	92.10	-11.10	-	-	-	-	-	-
	131.30	17.50	-	-	-	-	-	-
	216.20	-10.90	-	-	-	-	-	-
	219.80	-23.00	-	-	-	-	-	-
	261.30	-9.40	1.963	0.001	2.011	0.001	2.070	0.001
	264.00	23.70	1.963	0.001	2.015	0.001	2.070	0.001
	317.60	-11.40	1.968	0.001	2.013	0.001	2.068	0.001
Titania	13.60	19.00	-	-	-	-	-	-
	86.50	23.60	-	-	-	-	-	-
	98.00	-18.10	-	-	-	-	-	-
	160.00	18.20	-	-	-	-	-	-
	213.90	-11.10	-	-	-	-	-	-
	237.00	-23.00	-	-	-	-	-	-
	258.90	-29.30	-	-	-	-	-	-
	277.80	-23.00	-	-	-	-	-	-
	299.60	-10.20	-	-	-	-	-	-
	342.70	-29.40	-	-	-	-	-	-
Oberon	1.00	-29.40	-	-	-	-	-	-
	64.80	18.10	-	-	-	-	-	-
	85.90	-3.70	-	-	-	-	-	-
	91.00	23.70	-	-	-	-	-	-
	110.60	-10.20	-	-	-	-	-	-

Table 1.8. Continued. Summary of CO_2 ice band parameter analysis.

Satellite	Long. (°)	Lat. (°)	Band 1	Δcenter	Band 2	Δcenter	Band 3	Δcenter
			-	-	-	-	-	-
	216.20	-23.10	-	-	-	-	-	-
	223.70	18.90	-	-	-	-	-	-
	236.10	17.40	-	-	-	-	-	-
	266.50	20.20	-	-	-	-	-	-
	307.20	-29.30	-	-	-	-	-	-

Table 1.9. F-test analysis on leading and trailing hemispheres.

Satellite	Spectral Band Area	One Tailed F-test Ratio	Sample Size (n)	Mean Model Deg. Freedom (n - 1)	Sinusoidal Model Deg. Freedom (n - 3)	Probability (*p*)	Reject Null Hypothesis?
Ariel	Summed CO_2	152	13	12	10	1.10E-09	Yes
	1.52-μm H_2O	129	13	12	10	2.50E-09	Yes
	2.02-μm H_2O	50.6	13	12	10	2.50E-07	Yes
Umbriel	Summed CO_2	5.62	9	8	6	0.025	Yes
	1.52-μm H_2O	4.86	9	8	6	0.035	Yes
	2.02-μm H_2O	82.6	9	8	6	1.50E-05	Yes
Titania	Summed CO_2	6.91	10	9	7	9.00E-03	Yes
	1.52-μm H_2O	11.7	10	9	7	1.90E-03	Yes
	2.02-μm H_2O	23.8	10	9	7	2.00E-03	Yes
Oberon	Summed CO_2	6.81	11	10	8	6.00E-03	Yes
	1.52-μm H_2O	7.31	11	10	8	4.80E-03	Yes
	2.02-μm H_2O	3.86	11	10	8	0.034	Yes

Table 1.10. F-test analysis on leading and trailing quadrants

Satellite	Spectral Band Area	One Tailed F-test Ratio	Sample Size (n)	Mean Model Deg. Freedom (n - 1)	Sinusoidal Model Deg. Freedom (n - 3)	Probability (*p*)	Reject Null Hypothesis?
Ariel	Summed CO_2	247	9	8	6	5.50E-07	Yes
	1.52-μm H_2O	462	9	8	6	8.50E-08	Yes
	2.02-μm H_2O	194	9	8	6	1.10E-06	Yes
Umbriel	Summed CO_2	1.42	5	4	2	0.45	No
	1.52-μm H_2O	16.4	5	4	2	0.06	No
	2.02-μm H_2O	77.3	5	4	2	0.01	Yes
Titania	Summed CO_2	41.8	6	5	3	0.01	Yes
	1.52-μm H_2O	44.0	6	5	3	5.20E-03	Yes
	2.02-μm H_2O	65.3	6	5	3	2.90E-03	Yes
Oberon	Summed CO_2	5.63	7	6	4	0.06	No
	1.52-μm H_2O	4.43	7	6	4	0.09	No
	2.02-μm H_2O	0.374	7	6	4	0.86	No

Table 1.11. Radiolytic CO_2 saturation timescales

Satellite	Proton Fluence (cm^{-2})	Time to Proton Fluence Saturation (10^6 yrs)	Saturated over age of Solar System (4.5 Gyr)?
Ariel	100 - 200	4.75 - 9.50	Yes
Umbriel	50 - 100	9.50 - 19.0	Yes
Titania	0.1 - 1	950.0 - 9500.0	Maybe
Oberon	0.01 - 0.5	1900.0 - 95000.0	Maybe

Table 1.12. Summary of H_2O ice band parameter analysis.

			Integrated H_2O Band Area (10^{-2} μm)						H_2O Band Depth (μm)			
Target	Long. (°)	Lat. (°)	1.52-μm Band	ΔArea	2.02-μm Band	ΔArea	1.52-μm / 2.02-μm Band Ratio	Δband Ratio	1.52-μm Band	ΔDepth	2.02-μm Band	ΔDepth
Ariel	53.6	-16.0	4.73	0.02	8.66	0.05	0.546	0.002	0.274	0.002	0.456	0.005
	79.8	-19.4	4.99	0.01	9.20	0.04	0.542	0.001	0.292	0.002	0.481	0.003
	87.8	24.0	5.01	0.01	9.09	0.02	0.551	0.001	0.293	0.002	0.477	0.003
	93.5	-18.1	4.83	0.02	8.95	0.03	0.539	0.001	0.286	0.003	0.482	0.005
	159.9	-11.1	3.23	0.02	7.84	0.03	0.412	0.002	0.203	0.004	0.425	0.005
	200.0	-15.9	2.98	0.02	7.08	0.12	0.421	0.005	0.182	0.003	0.370	0.006
	219.8	-17.2	2.67	0.01	6.50	0.02	0.410	0.001	0.164	0.002	0.349	0.003
	233.8	-23.1	3.15	0.03	6.25	0.12	0.503	0.005	0.200	0.003	0.401	0.006
	257.6	-29.5	3.25	0.03	6.83	0.04	0.476	0.002	0.191	0.005	0.367	0.004
	278.3	24.8	2.95	0.02	6.74	0.04	0.437	0.002	0.183	0.004	0.371	0.007
	294.8	-19.3	2.90	0.02	6.84	0.04	0.423	0.002	0.178	0.002	0.392	0.003
	304.8	-23.2	3.02	0.03	6.74	0.18	0.449	0.007	0.185	0.003	0.391	0.006
	316.6	-18.2	3.21	0.02	6.71	0.03	0.478	0.002	0.191	0.003	0.378	0.006
Umbriel	38.4	20.3	1.74	0.02	4.33	0.03	0.402	0.002	0.116	0.004	0.263	0.005
	75.2	-29.3	1.87	0.03	4.38	0.08	0.427	0.004	0.122	0.007	0.274	0.007
	92.1	-11.1	1.48	0.04	4.30	0.06	0.346	0.005	0.097	0.005	0.284	0.012
	131.3	17.5	1.57	0.01	4.37	0.02	0.359	0.001	0.101	0.002	0.263	0.004
	216.2	-10.9	1.42	0.04	4.06	0.05	0.349	0.004	0.081	0.005	0.252	0.010
	219.8	-23.0	1.68	0.03	3.81	0.09	0.442	0.005	0.110	0.004	0.278	0.008
	261.3	-9.4	0.87	0.03	3.64	0.18	0.238	0.010	0.053	0.004	0.218	0.005
	264.0	23.7	1.26	0.01	3.90	0.02	0.323	0.002	0.090	0.003	0.228	0.004
	317.6	-11.4	1.04	0.02	3.89	0.04	0.269	0.003	0.069	0.004	0.230	0.006
Titania	13.6	19.0	3.60	0.01	7.85	0.01	0.459	0.001	0.217	0.001	0.437	0.002

Table 1.12. Continued. Summary of H_2O ice band parameter analysis.

Satellite	Long. (°)	Lat. (°)	1.52-µm Band	ΔArea	2.02-µm Band	ΔArea	1.52-µm / 2.02-µm Band Ratio	Δband Ratio	1.52-µm Band	ΔDepth	2.02-µm Band	ΔDepth
	86.5	23.6	4.43	0.01	8.72	0.01	0.507	0.000	0.264	0.001	0.467	0.002
	98.0	-18.1	4.44	0.03	8.70	0.04	0.511	0.002	0.270	0.004	0.477	0.007
	160.0	18.2	3.57	0.01	7.67	0.02	0.466	0.001	0.219	0.003	0.430	0.005
	213.9	-11.1	3.31	0.02	7.79	0.03	0.425	0.002	0.203	0.003	0.429	0.004
	237.0	-23.0	4.44	0.06	5.96	1.37	0.745	0.056	0.259	0.006	0.494	0.010
	258.9	-29.3	3.46	0.02	7.68	0.03	0.451	0.001	0.219	0.003	0.421	0.003
	277.8	-23.0	3.70	0.02	8.01	0.04	0.462	0.002	0.229	0.002	0.441	0.004
	299.6	-10.2	3.35	0.02	7.57	0.02	0.442	0.001	0.208	0.003	0.419	0.003
	342.7	-29.4	3.83	0.02	7.87	0.05	0.486	0.002	0.230	0.002	0.439	0.004
Oberon	1.0	-29.4	2.56	0.02	6.35	0.17	0.404	0.007	0.162	0.002	0.369	0.006
	64.8	18.1	2.63	0.01	6.18	0.02	0.425	0.001	0.170	0.002	0.350	0.003
	85.9	-3.7	2.73	0.05	6.03	0.16	0.453	0.007	0.177	0.006	0.366	0.008
	91.0	23.7	2.90	0.03	6.11	0.04	0.474	0.003	0.181	0.008	0.339	0.007
	110.6	-10.2	2.16	0.02	5.41	0.02	0.400	0.001	0.137	0.003	0.306	0.004
	164.0	-23.0	3.11	0.06	2.99	1.46	1.038	0.085	0.210	0.009	0.399	0.015
	216.2	-23.1	2.75	0.02	6.12	0.06	0.449	0.003	0.173	0.002	0.375	0.004
	223.7	18.9	2.21	0.01	5.77	0.01	0.382	0.001	0.141	0.002	0.327	0.003
	236.1	17.4	2.31	0.01	5.94	0.01	0.389	0.001	0.151	0.001	0.339	0.002
	266.5	20.2	2.46	0.02	5.43	0.04	0.453	0.002	0.153	0.005	0.309	0.007
	307.2	-29.3	2.49	0.01	5.92	0.02	0.421	0.001	0.162	0.001	0.330	0.002

Table 1.13. H_2O ice band area ratios.

Satellite Hemisphere	Mean 1.52-μm Band Area	ΔArea	Leading / Trailing Ratio	Δ Ratio	Mean 2.02-μm Band Area	Δ Area	Leading / Trailing Ratio	Δ Ratio	1.52-μm / 2.02-μm Band Ratio	ΔRatio
Ariel L	4.56	0.01			8.47	0.02			0.538	0.001
Ariel T	3.02	0.01	1.51	0.002	6.71	0.03	1.26	0.004	0.449	0.002
Umbriel L	1.67	0.02			4.35	0.03			0.384	0.004
Umbriel T	1.25	0.01	1.33	0.010	3.86	0.04	1.13	0.011	0.325	0.005
Titania L	4.01	0.01			8.24	0.01			0.487	0.001
Titania T	3.53	0.01	1.14	0.003	7.79	0.02	1.06	0.002	0.453	0.001
Oberon L	2.60	0.01			6.02	0.05			0.432	0.004
Oberon T	2.44	0.01	1.06	0.005	5.84	0.01	1.03	0.008	0.419	0.001

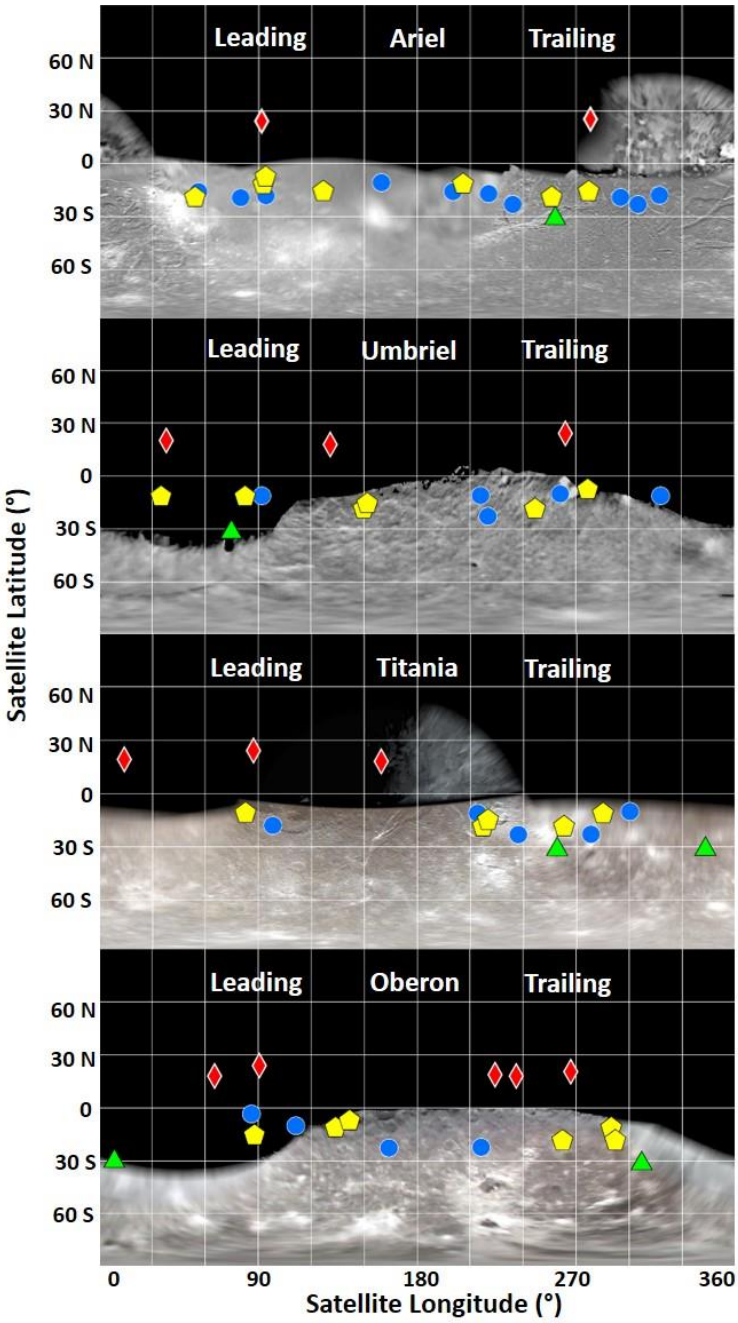

Figure 1.1. Position of the mid-observation satellite latitudes and longitudes observed by three different teams: PI Cartwright (red diamonds), PI Rivkin (green triangles), and PI Grundy (blue circles). IRAC mid-observation satellite latitudes and longitudes are also indicated (yellow pentagons). Base maps are Voyager 2 ISS mosaics (Courtesy NASA/JPL-Caltech/USGS, http://maps.jpl.nasa.gov/uranus.html), including night-side regions of Ariel and Titania (Stryk and Stooke, 2008).

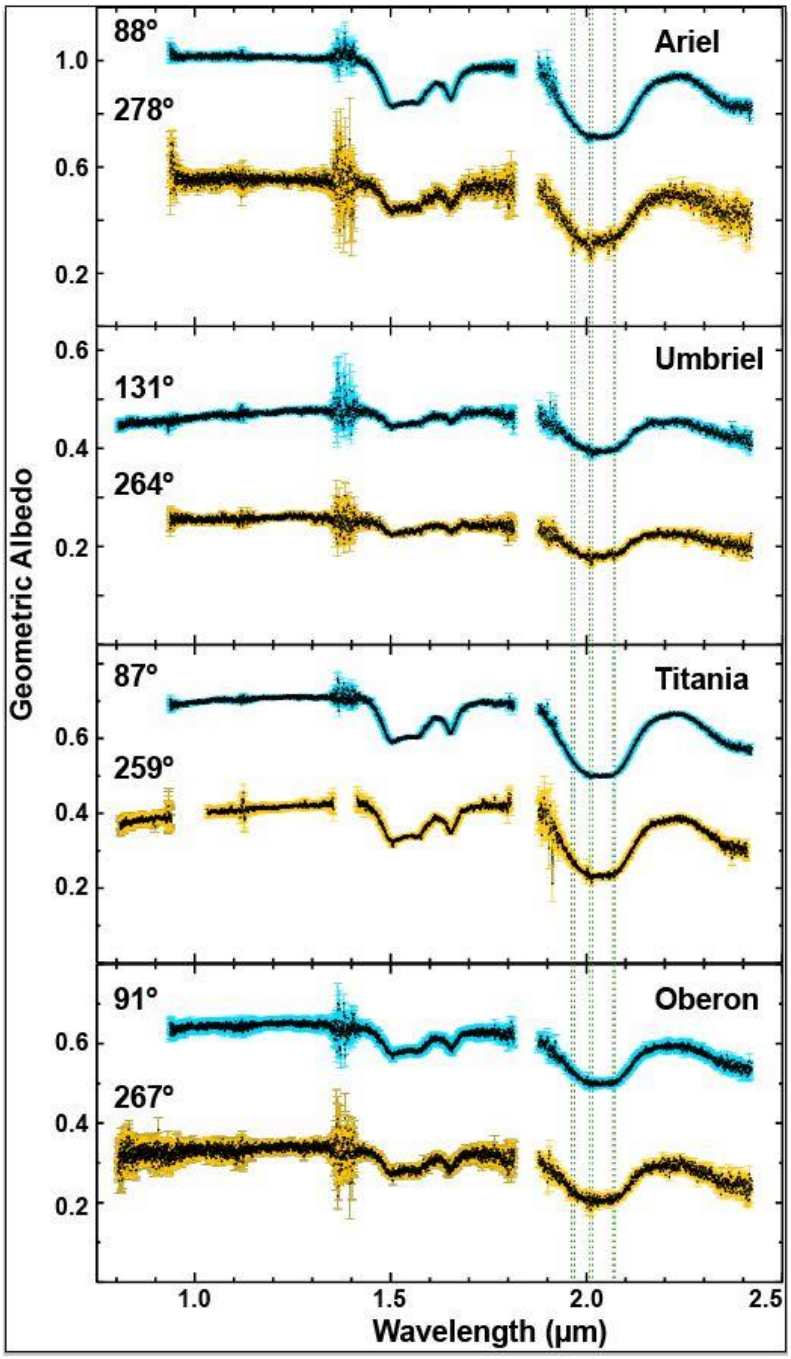

Figure 1.2. SpeX spectra of the leading (blue) and trailing (orange) hemispheres of Ariel, Umbriel, Titania, and Oberon, scaled to I band geometric albedos. Mid-observation satellite longitudes are listed in top left-hand corner of each plot. Position and width of the 1.966, 2.012, and 2.070 μm CO_2 ice bands are highlighted by the green dashed lines. For clarity, leading hemisphere spectra are offset upwards in each plot (Ariel +0.45, Umbriel +0.2, Titania +0.3, Oberon +0.3).

Figure 1.3. Mean geometric albedo as a function of satellite longitude in each IRAC channel. Ariel (a – d) , Umbriel (e – h) , Titania (i – l) , Oberon (m – p). Blue circles are leading hemisphere observations, orange circles are trailing hemisphere observations, and unfilled circles are data points not included in the analysis. The Ch.4 geometric albedos display more variation and lower S/N than the other three channels.

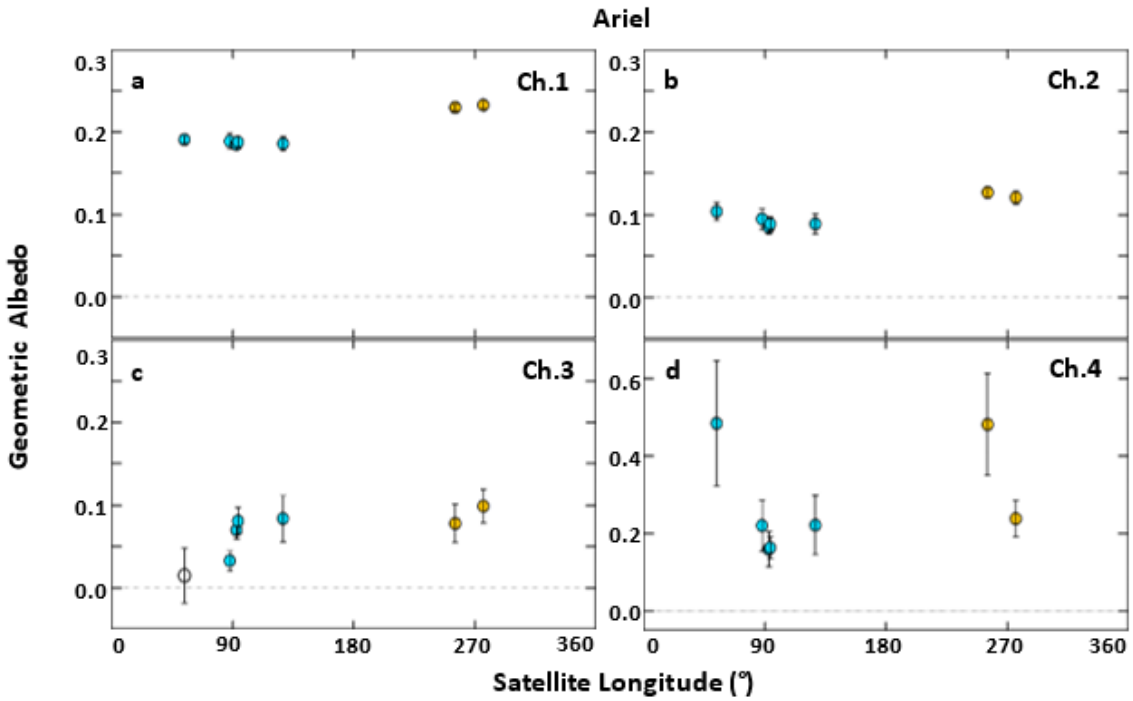

Figure 1.3. Continued.

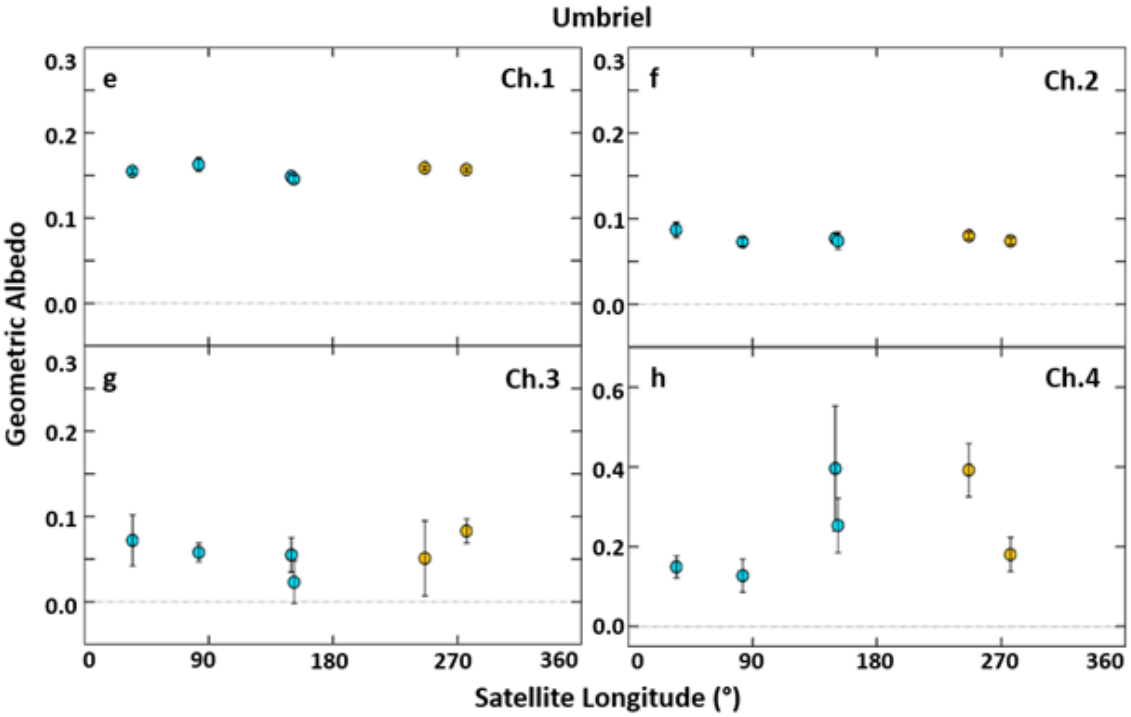

Figure 1.3. Continued.

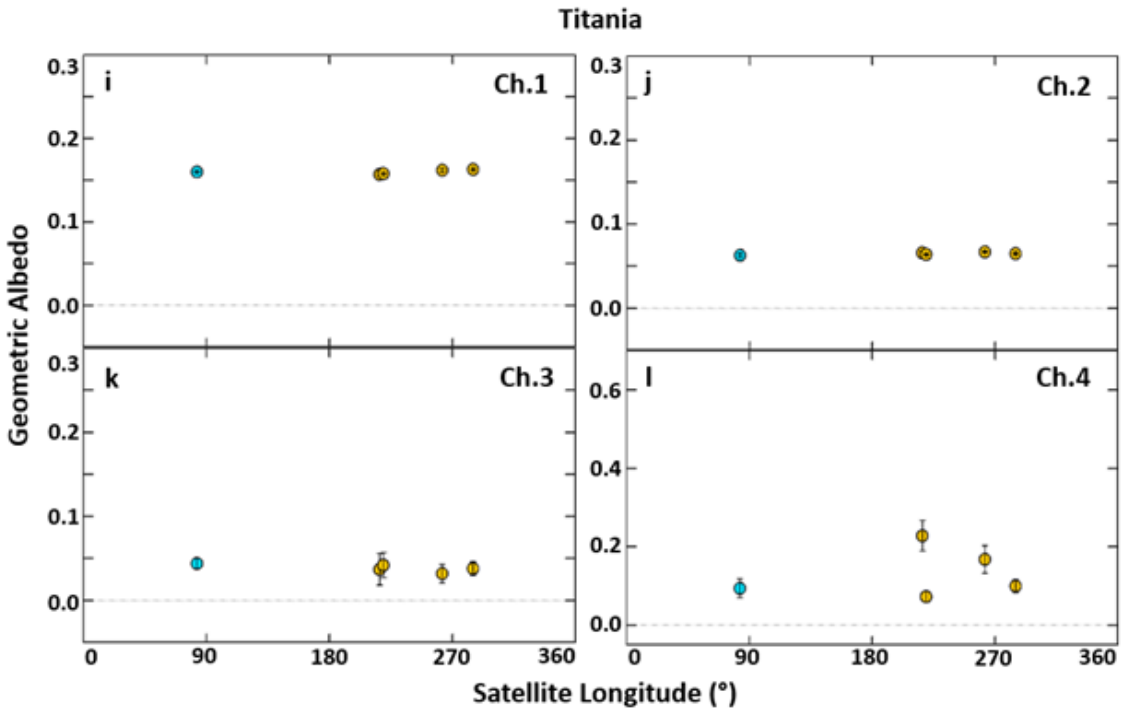

Figure 1.3. Continued.

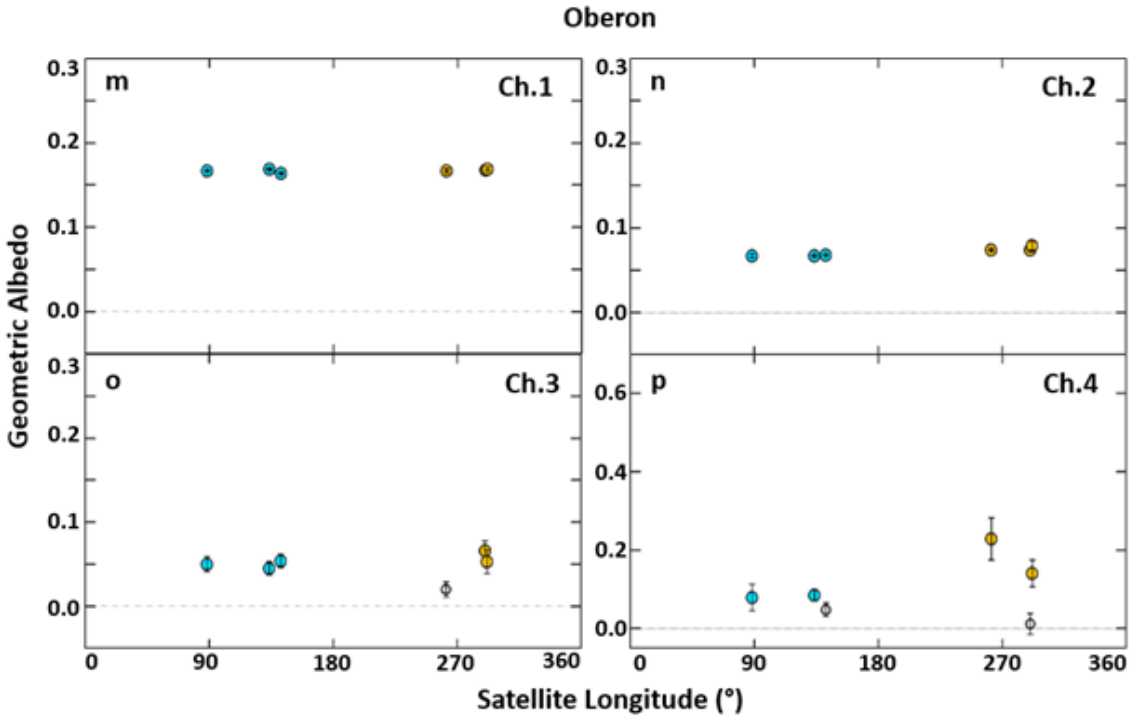

Figure 1.3. Continued.

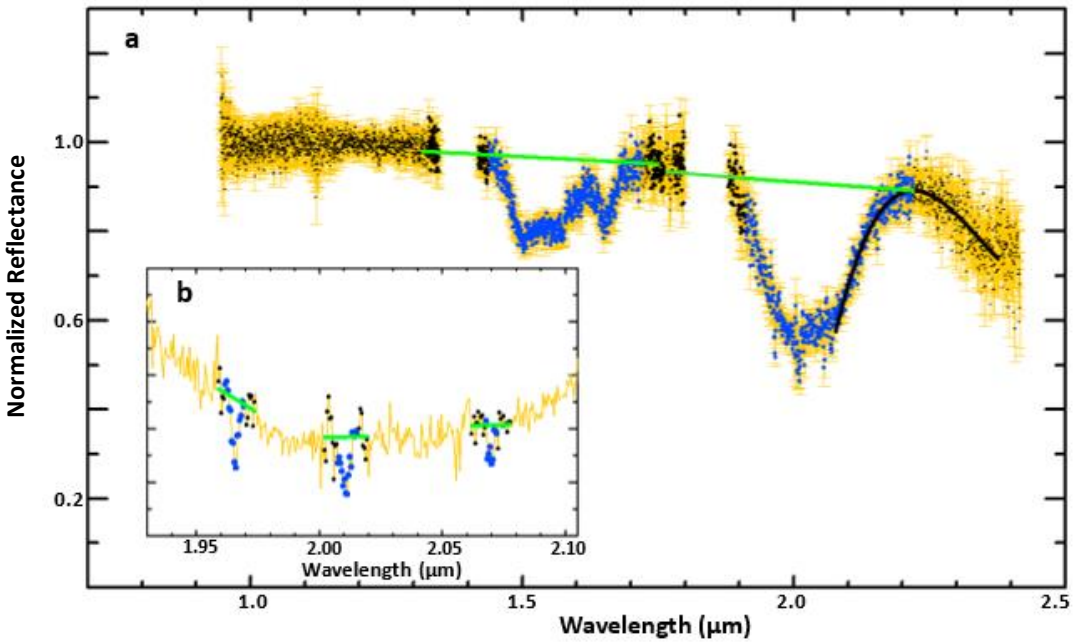

Figure 1.4. Examples of our H_2O and CO_2 ice band analyses. (**a**) Shows 1.52-μm and 2.02-μm H_2O ice bands (blue points) and their associated continua (larger black data points and peak of arch) connected with green lines. (**b**) Close up of same image shown in (a), focused on the positions of the detected CO_2 ice bands (blue points) and their associated continua (black points) connected with green lines. Error bars have been omitted in (b) for clarity.

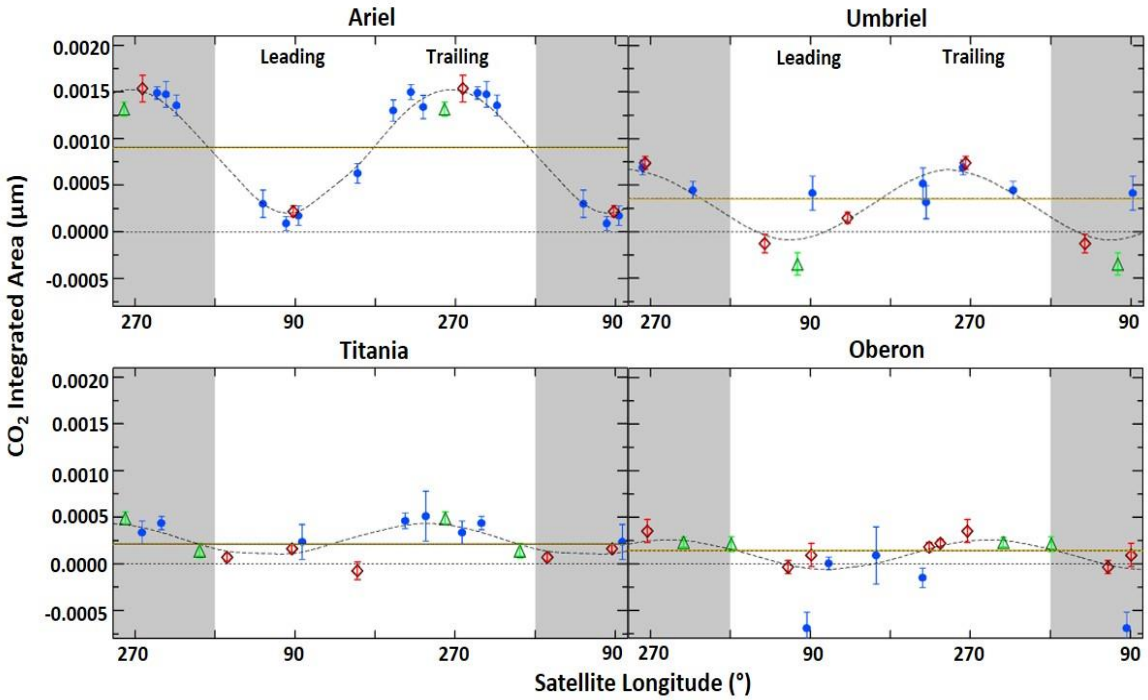

Figure 1.5. CO_2 integrated band areas as a function of satellite longitude: green triangles (Rivkin), blue filled circles (Grundy et al., 2003, 2006), and red diamonds (Cartwright). Duplicate longitudes are shown to highlight periodic trends in CO_2 ice abundance on each satellite (gray-toned regions). Black dashed lines in each plot represent sinusoidal model fits to the data, and yellow lines represent the mean integrated areas.

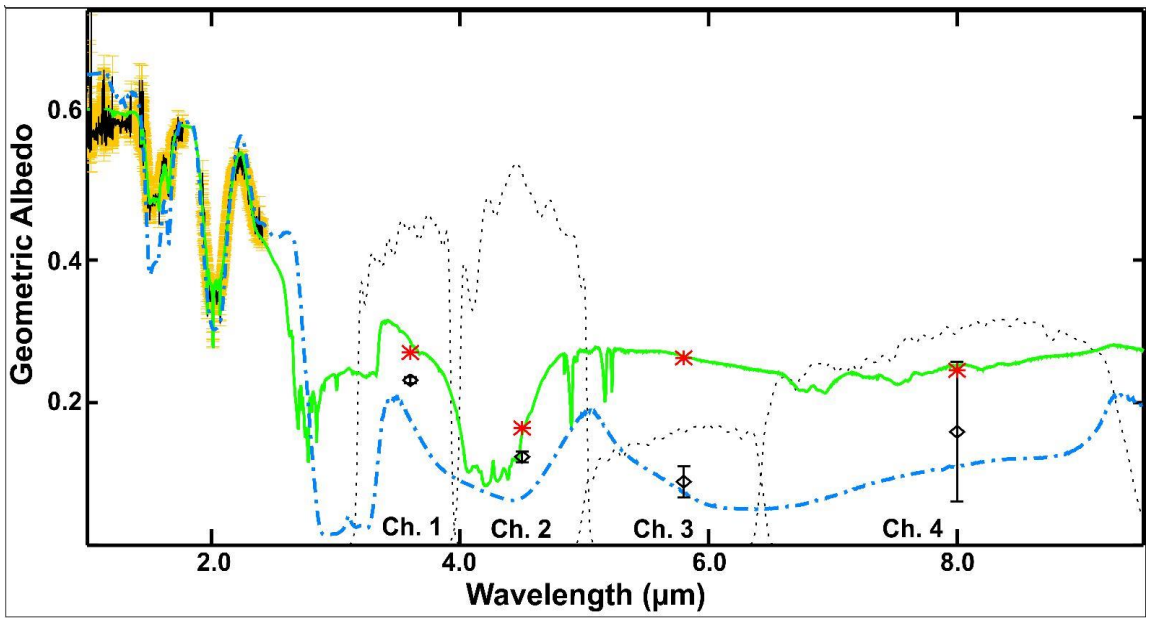

Figure 1.6. Best fit SpeX model for Ariel overprinting the mean Ariel trailing hemisphere spectrum (black with orange error bars), extrapolated over IRAC wavelengths (~3.1 – 9.5 μm). A synthetic spectrum of pure H_2O ice (blue dash-dot spectrum) is shown as well. The mean IRAC geometric albedos for the trailing hemisphere of Ariel (black diamonds with error bars) and the geometric albedos for the best fit SpeX model for Ariel extrapolated over IRAC wavelengths (red asterisks) are plotted along with these synthetic spectra. Spectral response curves shown to indicate width and position of IRAC channels (black dotted lines).

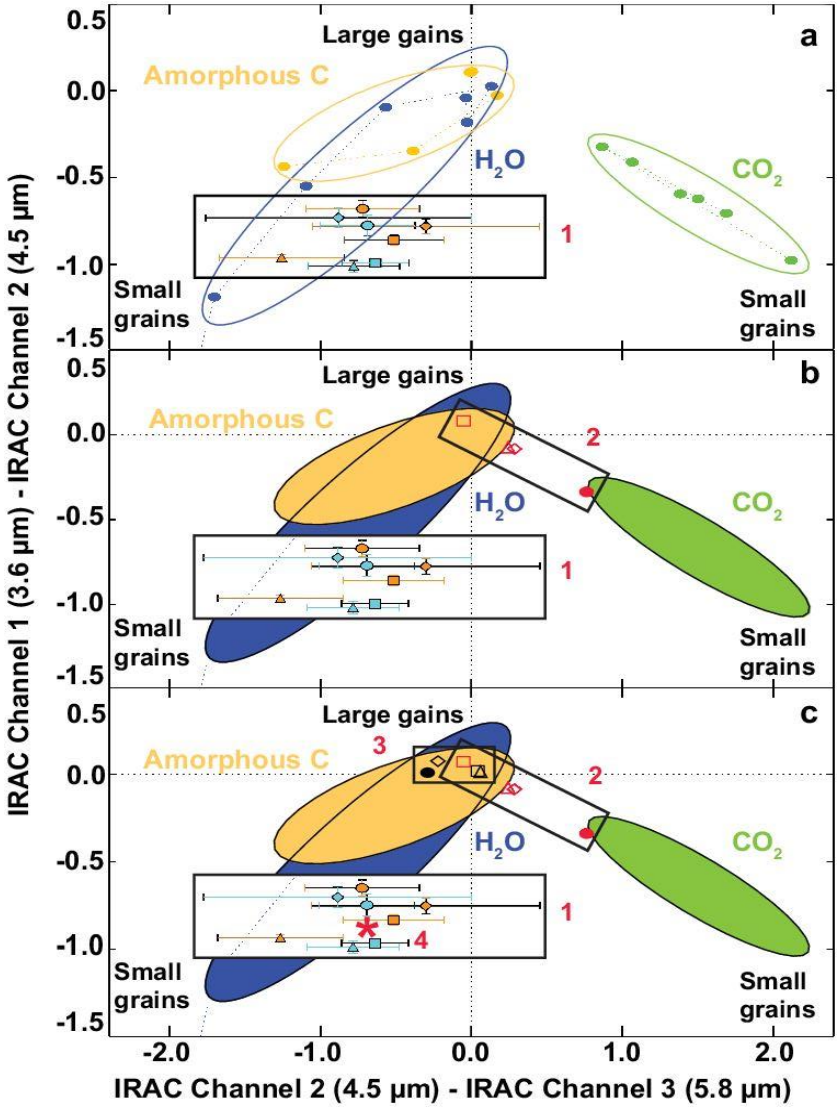

Figure 1.7. Color-color plots displaying IRAC data and compositional models. Position of the Uranian moon mean geometric albedos, converted into magnitudes, contained within box 1 in (a – c). Circles represent Ariel, diamonds Umbriel, triangles Titania, and squares Oberon in all three plots (blue symbols – leading hemisphere albedos, orange symbols – trailing hemisphere albedos). (**a**) This plot includes magnitudes for pure species: H_2O ice – blue circles, CO_2 ice – green circles, amorphous C – gold circles. (**b**) Same as (a) with best fit models for the mean trailing hemisphere SpeX spectra (box 2). (**c**) Same as (b) with a different set of best fit SpeX models composed of only H_2O ice and amorphous carbon (black colored shapes, box 3). The red asterisk in box 1 (labeled 4 in 7c) represents an IRAC best fit model.

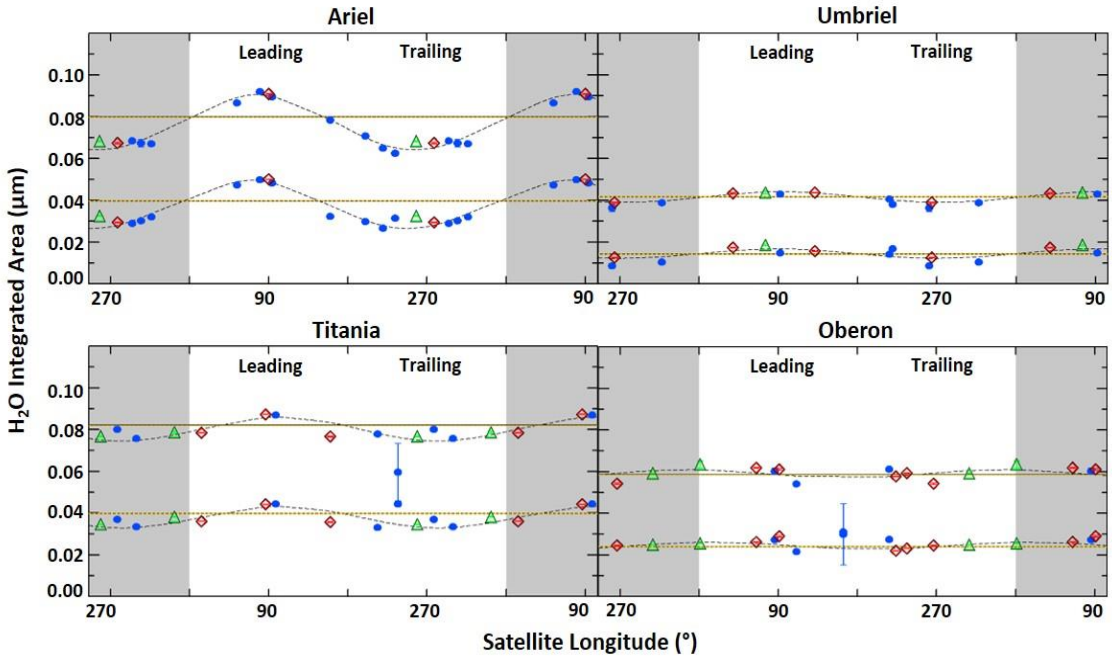

Figure 1.8. Areas for the 1.52-µm (bottom set of data points) and the 2.02-µm (top set of data points) H_2O ice bands, as a function of satellite longitude: green triangles (Rivkin), blue filled circles (Grundy et al., 2003, 2006), and red diamonds (Cartwright). Duplicate longitudes shown to highlight periodic trends in H_2O ice abundance (gray-toned regions). Black dashed lines represent sinusoidal model fits, and yellow lines represent the mean band area.

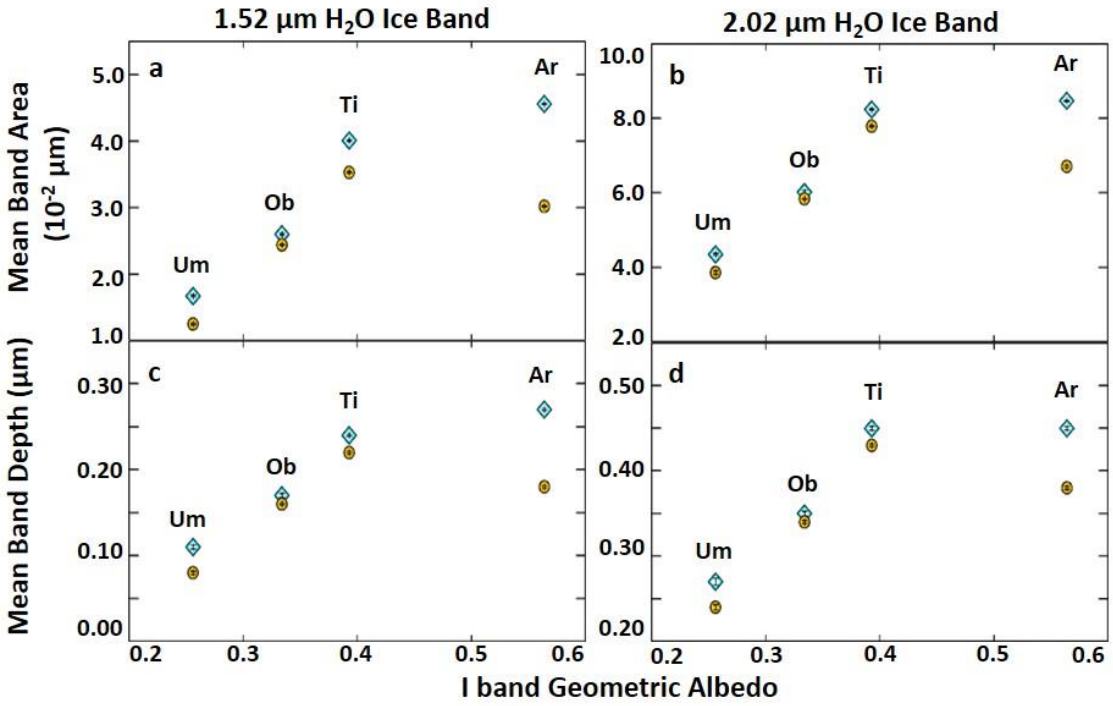

Figure 1.9. Mean leading (blue diamonds) and trailing (orange circles) H_2O band areas (**a, b**) and H_2O band depths (**c, d**) as a function of I band geometric albedos. Ar = Ariel, Um = Umbriel, Ti = Titania, and Ob = Oberon.

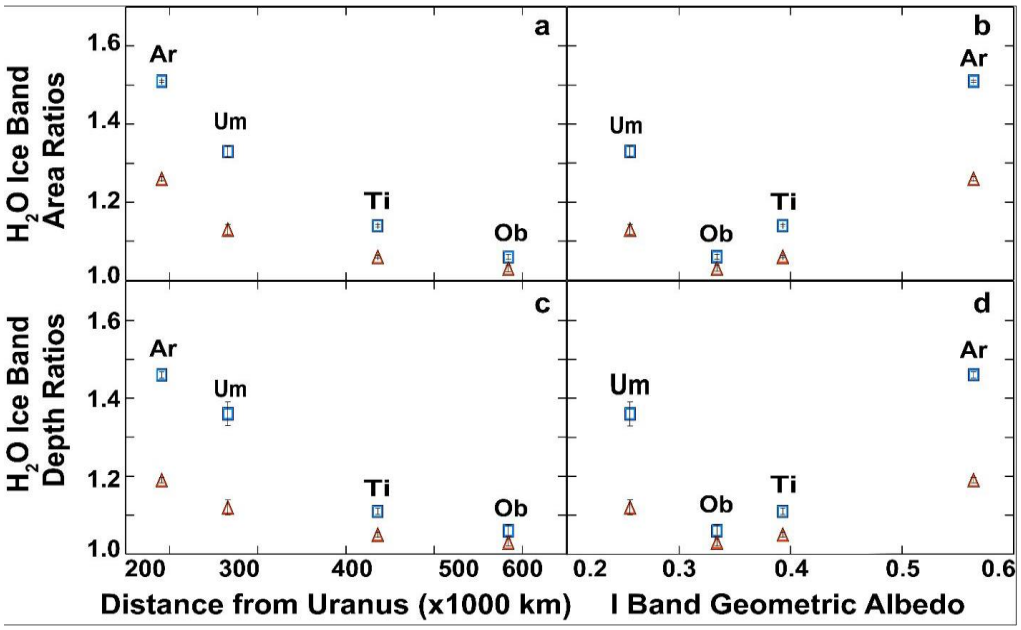

Figure 1.10. (**a**) Ratios between the mean leading and trailing H_2O ice band areas for the 1.52-µm (blue squares) and 2.02-µm (red triangles) bands, as a function of orbital radius. (**b**) Ratios between the mean leading and trailing H_2O ice band depths for the 1.52-µm (blue squares) and 2.02-µm (red triangles) bands, as a function of orbital radius. (**c**) Same H_2O band area data points shown in (**a**), but as a function of I band geometric albedo. (**d**) Same H_2O band depths shown in (**b**), but as a function of I band geometric albedo. Ar = Ariel, Um = Umbriel, Ti = Titania, and Ob = Oberon.

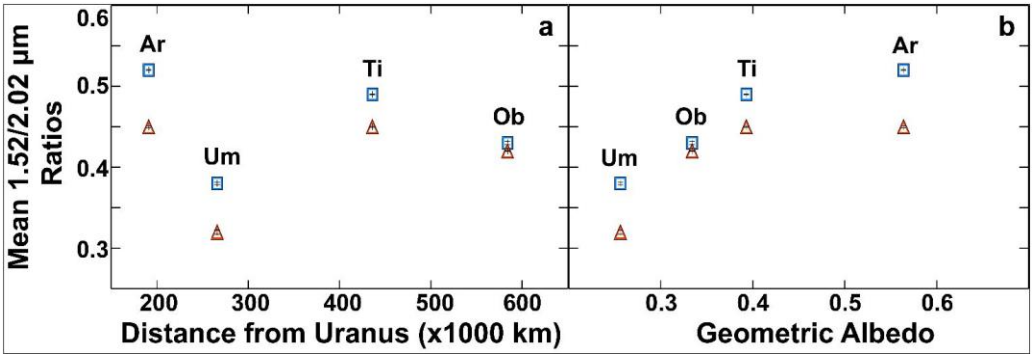

Figure 1.11. (a) Ratios of the mean 1.52-µm and 2.02-µm band areas on the leading (blue squares) and trailing (red triangles) hemispheres of the Uranian satellites as a function of geometric albedo. **(b)** Mean 1.52-µm / mean 2.02-µm band area ratios for the leading (blue squares) and trailing (red triangles) hemispheres of the Uranian satellites as a function of orbital radius. Ar = Ariel, Um = Umbriel, Ti = Titania, and Ob = Oberon.

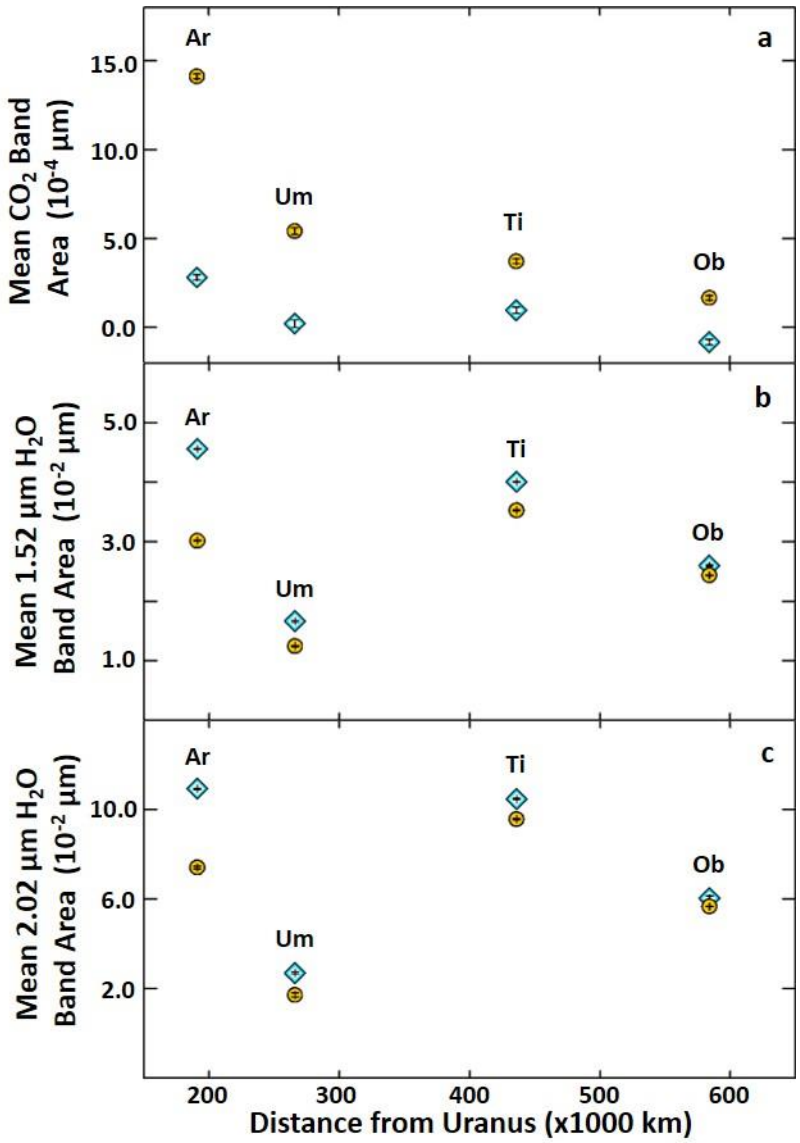

Figure 1.12. (**a**) Mean CO_2 band areas, (**b**) mean 1.52-µm H_2O band areas, and (**c**) mean 2.02-µm H_2O band areas as a function of orbital radius (blue diamonds – leading hemisphere, filled orange circles – trailing hemisphere). Ar = Ariel, Um = Umbriel, Ti = Titania, and Ob = Oberon.

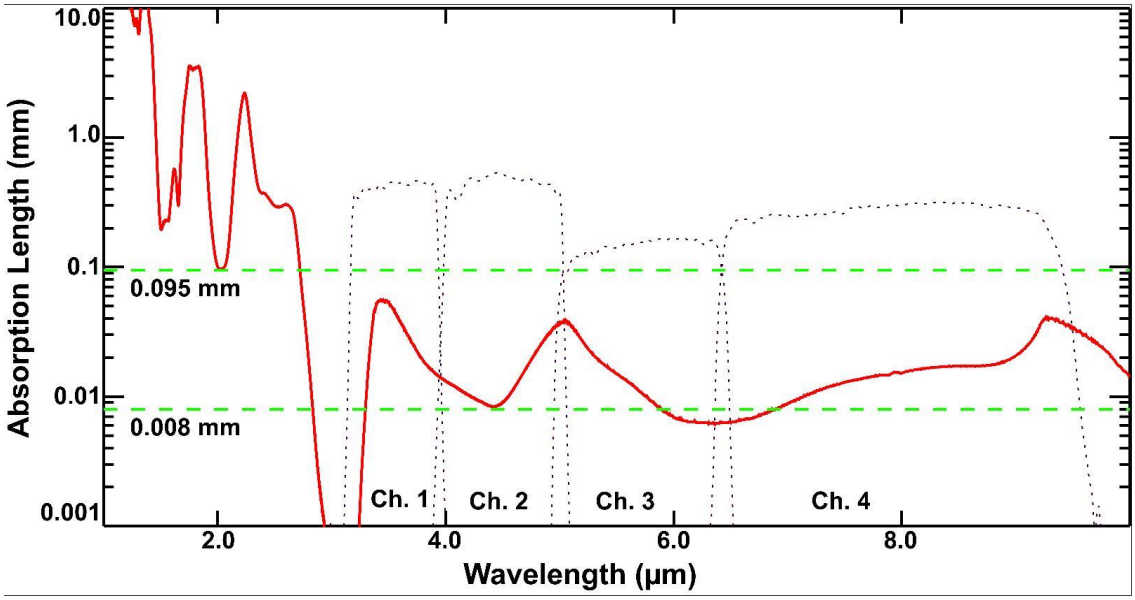

Figure 1.13. Red curve represents the e-folding absorption length for crystalline H_2O ice (80 K) as a function of wavelength. Green dashed lines highlight the H_2O penetration depths in the wavelength regions where CO_2 combination and overtone bands (~0.1 mm) and the CO_2 asymmetric stretch fundamental (~0.01 mm) are present. IRAC spectral response curves are indicated (black dotted lines).

Appendix 1-A: IRTF/SpeX spectra analyzed in this study

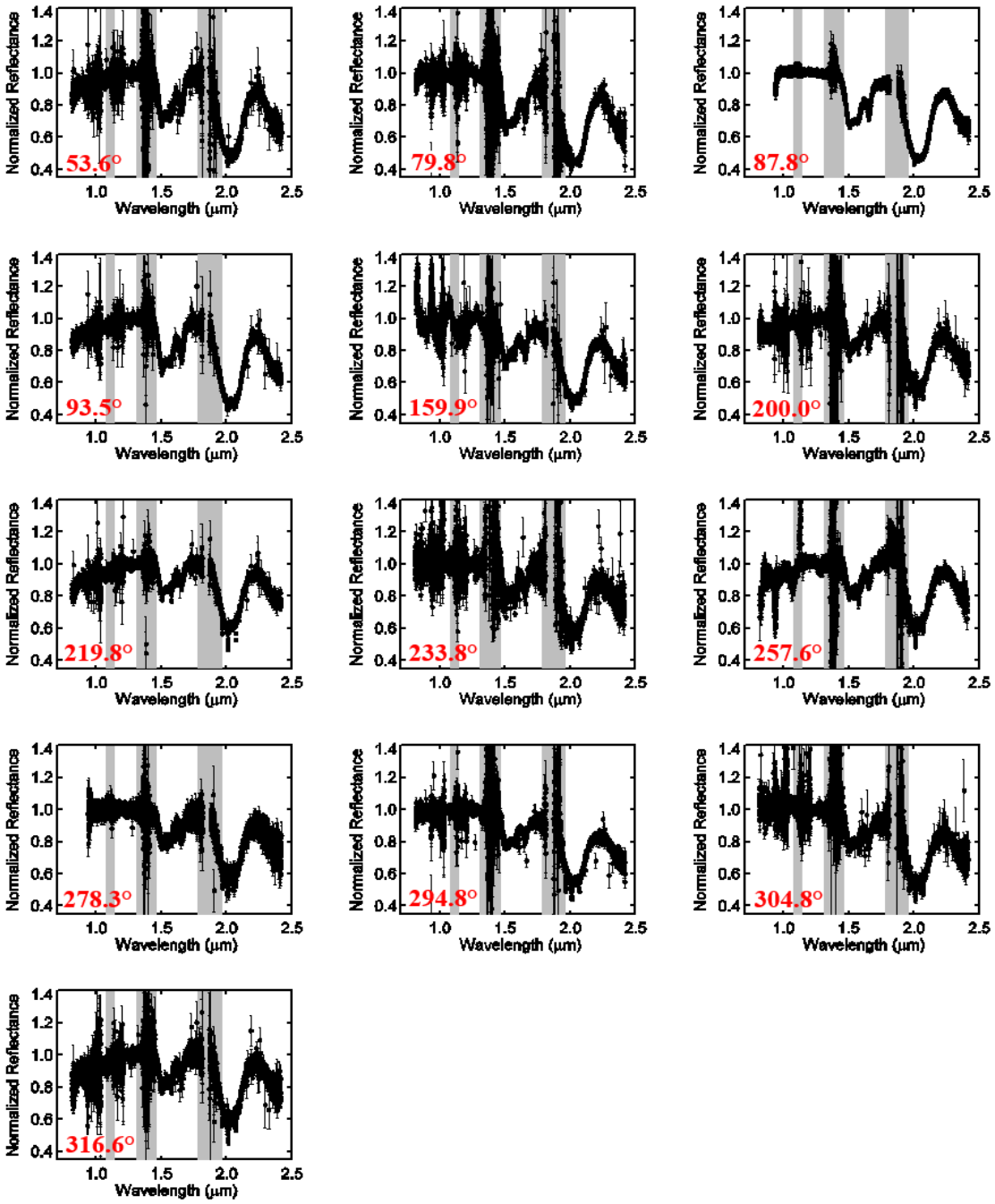

Figure 1-A.14. SpeX spectra of Ariel, organized by increasing mid-observation satellite longitude (listed in top right-hand corner of each plot). Each spectrum has been normalized to its mean reflectance between 1.2 and 1.3 μm. The wavelength ranges of strong telluric bands are indicated by the gray-toned regions (1.08 – 1.14 μm, 1.31 – 1.46 μm, and 1.78 – 1.96 μm).

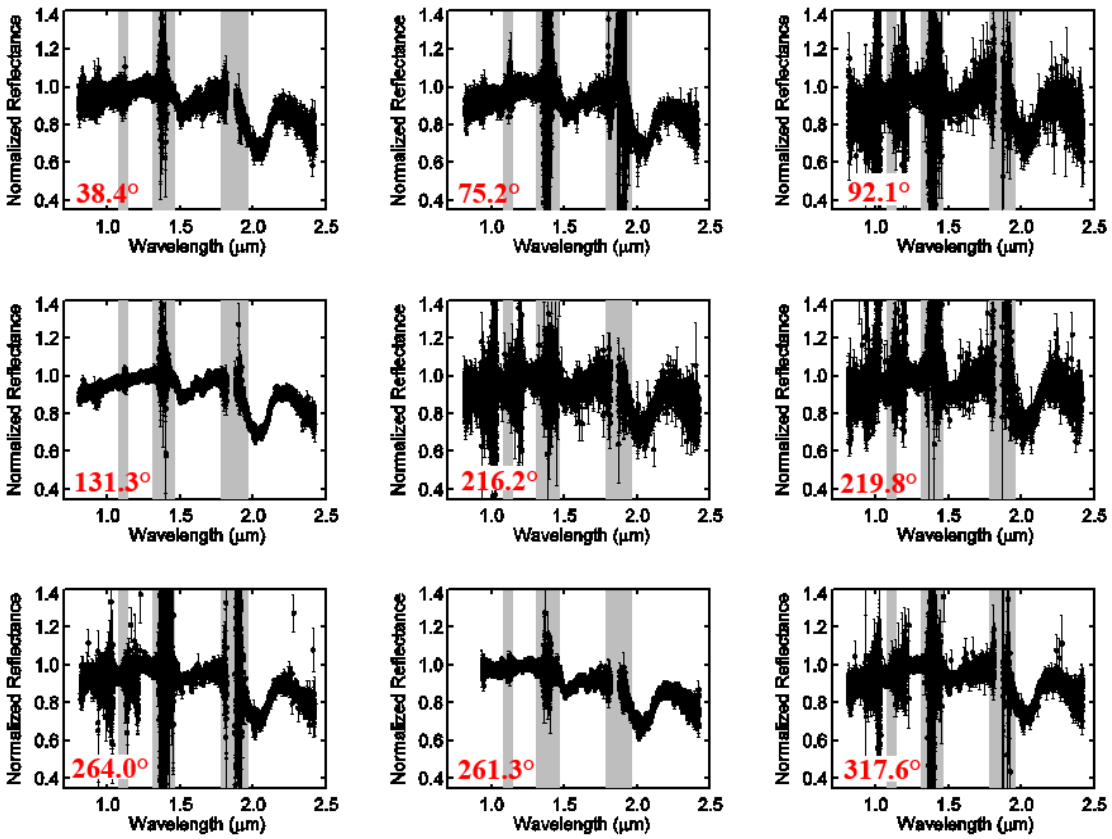

Figure 1-A.15. SpeX spectra of Umbriel, organized by increasing mid-observation satellite longitude (listed in top right-hand corner of each plot). Each spectrum has been normalized to its mean reflectance between 1.2 and 1.3 μm. The wavelength ranges of strong telluric bands are indicated by the gray-toned regions (1.08 –1.14 μm, 1.31 – 1.46 μm, and 1.78 – 1.96 μm).

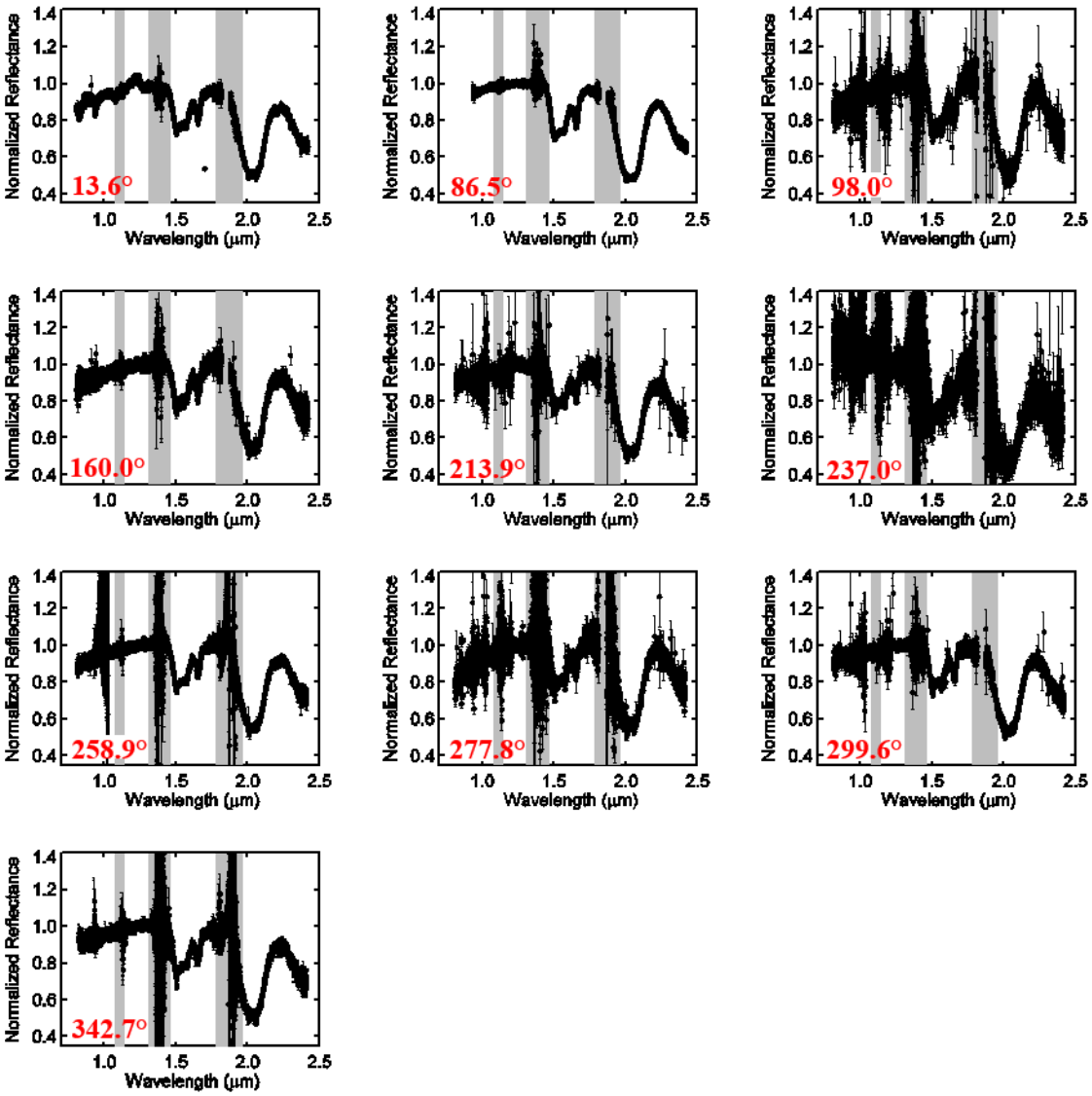

Figure 1-A.16. SpeX spectra of Titania, organized by increasing mid-observation satellite longitude (listed in top right-hand corner of each plot). Each spectrum has been normalized to its mean reflectance between 1.2 and 1.3 μm. The wavelength ranges of strong telluric bands are indicated by the gray-toned regions (1.08 –1.14 μm, 1.31 – 1.46 μm, and 1.78 – 1.96 μm).

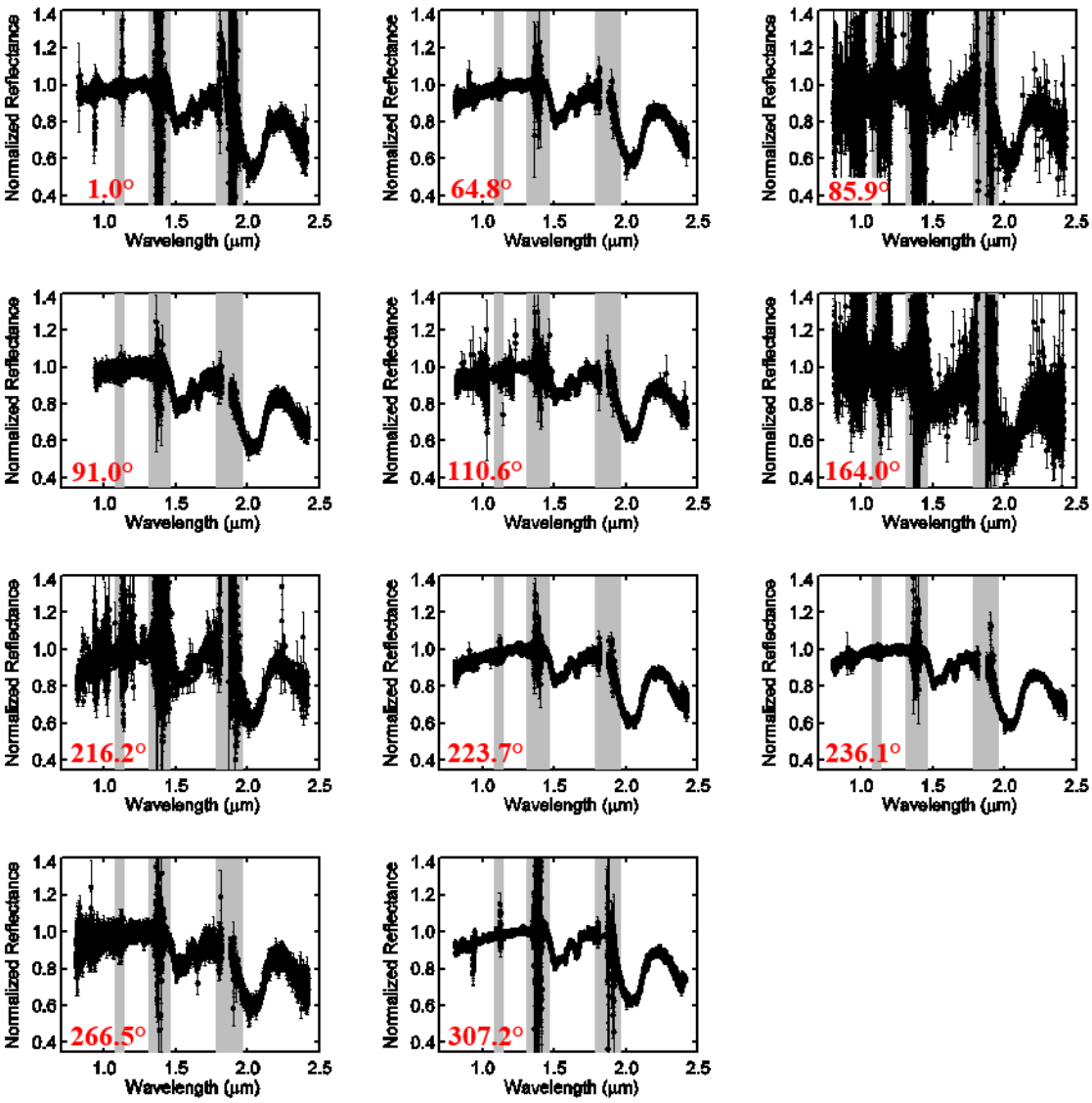

Figure 1-A.17. SpeX spectra of Oberon, organized by increasing mid-observation satellite longitude (listed in top right-hand corner of each plot). Each spectrum has been normalized to its mean reflectance between 1.2 and 1.3 μm. The wavelength ranges of strong telluric bands are indicated by the gray-toned regions (1.08 –1.14 μm, 1.31 – 1.46 μm, and 1.78 – 1.96 μm).

Appendix 1-B.1. Assessment of CO_2 band areas

Our band parameter code indicates that CO_2 ice is present in spectra collected over the trailing hemispheres of Ariel, Umbriel, Titania, and Oberon. Telluric CO_2 and higher noise levels in spectra with low S/N could be contaminating the measured CO_2 bands. In order to test for possible contamination of our CO_2 band area measurements, we compared them to the CO_2 band areas in a wide range of synthetic spectra generated using a Hapke-Mie numerical model. This hybrid numerical model utilizes Mie theory (e.g., Bohren and Huffman, 1983) to calculate the single scattering albedos for all species before passing these ratios to a Hapke equation that models scattering within a regolith (e.g., Hapke, 2002). This hybrid approach allows us to generate reliable synthetic spectra over a wider range of grain sizes than using Hapke-based codes alone (Moersch and Christensen, 1995).

In order to increase the S/N of the CO_2 bands, we averaged multiple trailing hemisphere spectra together, generating one spectrum to represent the trailing hemisphere of each moon (Figure 1-B.15). We used individual spectra with visibly identifiable CO_2 bands on Ariel (eight total spectra) and Umbriel (three spectra), along with the trailing hemisphere spectra with non-negative band areas on Titania and Oberon (three and four total spectra, respectively).

We then generated best fit models for these mean trailing hemisphere spectra using the Hapke-Mie model described above. The best fit spectral models (Figure 1-B.15) are a combination of intimately mixed H_2O ice and amorphous carbon and areally mixed CO_2 ice (Table 1-B.13). The relatively low albedos of the Uranian satellites, coupled with weak 1.52-μm and 2.02-μm H_2O ice bands (and the absence of shorter wavelength H_2O ice bands) suggests that their surfaces are covered by an intimate mixture of small H_2O ice grains and dark, presumably carbonaceous grains (e.g., Brown and Cruikshank, 1983). The absence of the ~2.134 μm CO_2 forbidden transition from our spectra, suggests that the detected CO_2 is predominantly segregated from other species (i.e., areally mixed). These best fit models are sufficient for characterization of the CO_2 bands present in the SpeX spectra; however, they only provide approximations of the H_2O ice band shapes and the spectral continuum levels.

Appendix 1-B.2. Analysis of mean spectra CO_2 band areas and best fit models

Gerakines et al. (2005) characterized the relative band strengths of pure CO_2 ice combination and overtone bands between 1.9 and 2.1 μm, finding that CO_2 band 2 (center near 2.012 μm) is the strongest band, followed by band 1 (centered near 1.966 μm), and finally band 3 (centered near 2.070 μm) is the weakest of the three. Therefore, if the observed spectral features on the Uranian satellites are dominated by pure CO_2 ice, as suggested by the absence of the ~2.134 μm CO_2 forbidden transition, they should display the same relative relationships. Consequently, the relative band area contributions of CO_2 bands 1, 2, and 3 can be used to test for the dominant CO_2 mixing regime (i.e., intimately mixed or segregated).

To this end, we measured CO_2 band areas in the mean trailing hemisphere spectra and in the best fit models. The models provide a 'control' measurement for this analysis because we know the contribution of CO_2 ice in each. We used two types of best fit

models: noise-free versions shown in Figure B1, and noise-added versions (example shown in Figure 1-B.16). Given that the detected CO_2 bands are weakest in our Oberon spectra, and therefore represent the CO_2 bands most likely to be obscured by noise, we chose to replicate the point-to-point variation of the mean Oberon spectrum (between 1.9 and 2.1 μm) in all of our noise-added models.

We measured the areas of the CO_2 bands in the mean trailing hemisphere spectra and their best fit models. Next, we normalized individual band areas by the total area of the three bands to determine their relative contributions (for example, CO_2 band 1 / (CO_2 band 1 + CO_2 band 2 + CO_2 band 3)). The relative CO_2 band ratios for the mean Ariel and Oberon spectra (Table 1-B.14) are within 2% and 3% of the noise-free models (Table 1-B.15) for these two moons, respectively. The ratios between the CO_2 bands in the mean spectra of Umbriel and Titania vary by up to 8% for CO_2 bands 1 and 2, but only 2% for CO_2 band 3. The CO_2 band area ratios for each mean spectrum display similar relationships with the band ratios in their corresponding best fit model. For example, CO_2 band 2 is strongest in the mean spectra of Ariel, Umbriel, and Oberon (but not Titania), and CO_2 band 3 is the weakest in all four spectra.

Appendix 1-B.3. Analysis of relative CO_2 band areas for synthetic spectra

To further test the dominant CO_2 mixing regime present in our spectra, we generated a range of noise-free and noise-added spectral models (1, 10, and 100 μm grain sizes), and investigated their relative CO_2 band area contributions (Table 1-B.16). We focus primarily on the noise-added synthetic spectra to highlight how point-to-point variations in spectra can alter CO_2 band strengths, in particular when only minor amounts of CO_2 are present (analogous to detected CO_2 levels on Titania and Oberon).
We first investigated the relative band strengths of pure CO_2 models using three different grain sizes (1, 10, and 100 μm): CO_2 band 1 (34 – 36% of total area), CO_2 band 2 (44 – 48%), and CO_2 band 3 (18 – 21%). The CO_2 band ratios for the mean spectra of Ariel (34 ± 2%, 45 ± 2%, 21 ± 1%, respectively) and Oberon (35 ± 11%, 44 ± 13%, 21 ± 7%, respectively) are nearly identical to those of pure CO_2 ice. Although the band area ratios for Umbriel (26 ± 4%, 51 ± 6%, 23 ± 3%, respectively) and Titania (41 ± 8%, 38 ± 10%, 21 ± 5%, respectively) display some variation compared to the relative band ratios for the pure CO_2 models, they are $\leq 2\sigma$ removed from the pure CO_2 models.

To test whether our band analysis code might incorrectly identify CO_2 in spectra of pure H_2O ice, we measured the 'CO_2 band areas' in both noise-free and noise-added pure H_2O ice models (1, 10, and 100 μm grain sizes). We found non-zero summed 'CO_2 band areas' in the pure H_2O ice models, but they are at least a factor of ~3 lower than the band areas in all four mean Uranian satellite spectra (Table 1-B.16). We also measured the 'CO_2 bands areas' of models composed of mixtures of different H_2O ice grain sizes (Table 1-B.17). We again found that the measured 'CO_2 bands' are much lower than the mean Uranian satellite spectra.

We also generated a wide range of models using areal and particulate mixtures of different H_2O and CO_2 grain sizes (along with amorphous C in our particulate mixtures) (Table 1-B.17). At the lowest CO_2 abundance levels we investigated (1% and 9% for areal and particulate mixtures, respectively), the measured band areas and relative CO_2

band ratios are similar to the pure H_2O ice models described above. At higher CO_2 levels ($\geq$ 5%), the measured band areas and relative band area ratios for the areal mixtures of H_2O and CO_2 are consistent with the best fit models for the mean Uranian satellite spectra. Much more CO_2 ice ($\geq$ 49%) is required before the CO_2 band areas in the particulate mixture models can approximate the best fit models. Additionally, the relative band area ratios of the particulate models are not consistent with the mean spectra or their best fit models at any of the tested CO_2 abundance levels. The particulate mixture shown in Figure 1-B.16 (10 μm grains of H_2O (9%), CO_2 (89%), and amorphous C (2%)) has a comparable summed CO_2 band area to the mean Ariel spectrum and its best fit model (Figure 1-B.16). It is apparent that the H_2O ice bands in the particulate mixture are much weaker than those in the mean Ariel spectrum.

Table B-1.14. Best fit synthetic spectra.

Particulate Mixture Model Components								
Satellite	Component 1	Mix (%)	Component 2	Mix (%)	Component 3	Mix (%)	Component 4	Mix (%)
Ariel	50 μm H_2O	50	10 μm H_2O	47	0.3 μm H_2O	0.8	12.5 μm amorph C	2.2
Umbriel	50 μm H_2O	25.05	10 μm H_2O	34.7	0.2 μm H_2O	0.25	5 μm amorph C	40
Titania	50 μm H_2O	47	10 μm H_2O	38.7	0.2 μm H_2O	0.3	10 μm amorph C	14
Oberon	50 μm H_2O	21.68	10 μm H_2O	52.9	0.2 μm H_2O	0.32	7 μm amorph C	25.1

Areal (Final) Mixture Model Components						
Satellite	Component 1	Mix (%)	Component 2	Mix (%)	Component 3	Mix (%)
Ariel	particulate model described above	73	10 μm CO_2	22.5	50 μm CO_2	4.5
Umbriel	particulate model described above	92	5 μm CO_2	5.2	10 μm CO_2	2.8
Titania	particulate model described above	95	5 μm CO_2	1.0	10 μm CO_2	4.0
Oberon	particulate model described above	97	5 μm CO_2	1.5	10 μm CO_2	1.5

Table B-1.15. CO_2 band areas for mean trailing hemisphere spectra.

	CO_2 Band Area (10^{-4} μm)								Relative CO_2 Band Ratios					
Satellite	Band 1	ΔArea	Band 2	ΔArea	Band 3	ΔArea	Total Area	Total Δarea	Band 1 (%)	ΔBand 1 (%)	Band 2 (%)	ΔBand 2 (%)	Band 3 (%)	ΔBand 3 (%)
Ariel	4.65	0.22	6.20	0.27	2.90	0.15	13.75	0.38	34	2	45	2	21	1
Umbriel	1.61	0.25	3.18	0.31	1.42	0.15	6.21	0.43	26	4	51	6	23	3
Titania	1.43	0.23	1.33	0.31	0.71	0.15	3.47	0.41	41	8	38	10	20	5
Oberon	0.84	0.23	1.07	0.25	0.50	0.15	2.41	0.37	35	11	44	13	21	7

Table B-1.16. CO_2 band areas for best fit synthetic spectra.

		CO_2 Band Area (10^{-4} μm)				Relative CO_2 Band Ratios		
Satellite	Noise Added ?	Band 1	Band 2	Band 3	Total Area	Band 1 (%)	Band 2 (%)	Band 3 (%)
Ariel	No	4.81	6.57	2.62	14.00	34	47	19
	Yes	4.64	6.56	2.68	13.88	34	47	19
Umbriel	No	1.79	2.65	1.23	5.67	32	47	22
	Yes	1.91	2.66	1.02	5.59	34	48	18
Titania	No	0.86	1.69	0.54	3.09	28	55	18
	Yes	1.18	1.69	0.68	3.55	33	48	19
Oberon	No	0.84	1.05	0.45	2.33	36	45	18
	Yes	0.73	1.04	0.42	2.18	33	48	19

Table B-1.17. CO_2 band areas for pure synthetic spectra.

Pure Model Component 1	Noise Added?	CO_2 Band Area (10^{-4} µm)				Relative CO_2 Band Ratios		
		Band 1	Band 2	Band 3	Total Area	Band 1 (%)	Band 2 (%)	Band 3 (%)
1 µm H_2O	No	0.035	0.072	0.045	0.152	23	47	30
10 µm H_2O	No	0.051	0.091	0.057	0.200	26	46	29
100 µm H_2O	No	0.195	0.173	0.114	0.482	40	36	24
1 µm H_2O	Yes	-0.035	-0.148	-0.013	-0.195	18	76	7
10 µm H_2O	Yes	-0.132	0.036	0.071	-0.025	535	-146	-289
100 µm H_2O	Yes	0.292	0.352	0.035	0.680	43	52	5
1 um CO_2	No	5.15	7.29	2.73	15.17	34	48	18
10 um CO_2	No	9.37	12.34	4.71	26.42	35	47	18
100 um CO_2	No	20.53	25.04	11.59	57.16	36	44	20
1 um CO_2	Yes	5.11	7.14	2.77	15.03	34	48	18
10 um CO_2	Yes	9.17	12.21	4.76	26.14	35	47	18
100 um CO_2	Yes	20.41	25.06	11.73	57.20	36	44	21

Table B-1.18. CO_2 band areas for mixed synthetic spectra.

Compositional Model Parameters								CO_2 Band Area (10^{-4} μm)				Relative CO_2 Band Ratios		
Mix. Reg.	Comp. 1	Mix (%)	Comp. 2	Mix (%)	Comp. 3	Mix (%)	Noise Added?	Band 1	Band 2	Band 3	Total Area	Band 1 (%)	Band 2 (%)	Band 3 (%)
Areal	1 μm H_2O	20	10 μm H_2O	80	-	-	Yes	0.388	0.250	0.097	0.736	53	34	13
Areal	1 μm H_2O	50	10 μm H_2O	50	-	-	Yes	-0.100	0.202	0.019	0.121	-83	167	15
Areal	1 μm H_2O	80	10 μm H_2O	20	-	-	Yes	-0.113	0.309	0.038	0.234	-48	132	16
Areal	1 μm H_2O	20	100 μm H_2O	80	-	-	Yes	0.112	0.222	0.130	0.465	24	48	28
Areal	1 μm H_2O	50	100 μm H_2O	50	-	-	Yes	0.086	0.127	0.178	0.391	22	32	46
Areal	1 μm H_2O	80	100 μm H_2O	20	-	-	Yes	0.425	0.017	0.112	0.555	77	3	20
Areal	10 μm H_2O	99	10 μm CO_2	1	-	-	Yes	0.443	0.043	0.198	0.684	65	6	29
Areal	10 μm H_2O	95	10 μm CO_2	5	-	-	Yes	0.595	1.084	0.580	2.258	26	48	26
Areal	10 μm H_2O	90	10 μm CO_2	10	-	-	Yes	1.402	1.899	0.791	4.092	34	46	19
Areal	10 μm H_2O	80	10 μm CO_2	20	-	-	Yes	2.685	3.837	1.280	7.801	34	49	16
Areal	10 μm H_2O	70	10 μm CO_2	30	-	-	Yes	3.787	5.268	2.086	11.141	34	47	19
Part.	10 μm H_2O	69	10 μm CO_2	29	10 μm a.C	2	Yes	0.932	1.350	0.173	2.455	38	55	7
Part.	10 μm H_2O	49	10 μm CO_2	49	10 μm a.C	2	Yes	0.932	2.323	0.444	4.408	21	53	10
Part.	10 μm H_2O	29	10 μm CO_2	69	10 μm a.C	2	Yes	2.556	4.252	0.988	7.795	33	55	13
Part.	10 μm H_2O	9	10 μm CO_2	89	10 μm a.C	2	Yes	4.582	6.582	1.181	12.345	37	53	10

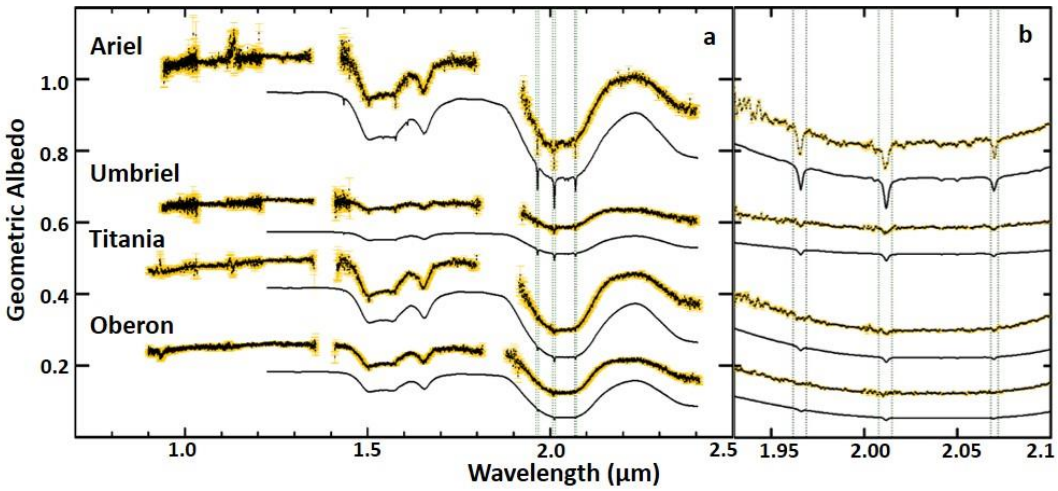

Figure 1-B.18. (a) Black spectra with orange error bars are the mean trailing hemisphere spectra of Ariel, Umbriel, Titania, and Oberon scaled to I band geometric albedos (Karkoschka 2001), offset by +0.47, +0.36, +0.07, -0.09, respectively. Black spectra are best fit models for these mean spectra. Green dashed lines indicate positions and widths of CO_2 ice bands 1, 2, and 3. (**b**) Close up of the same image shown in (a), focused on the three CO_2 bands.

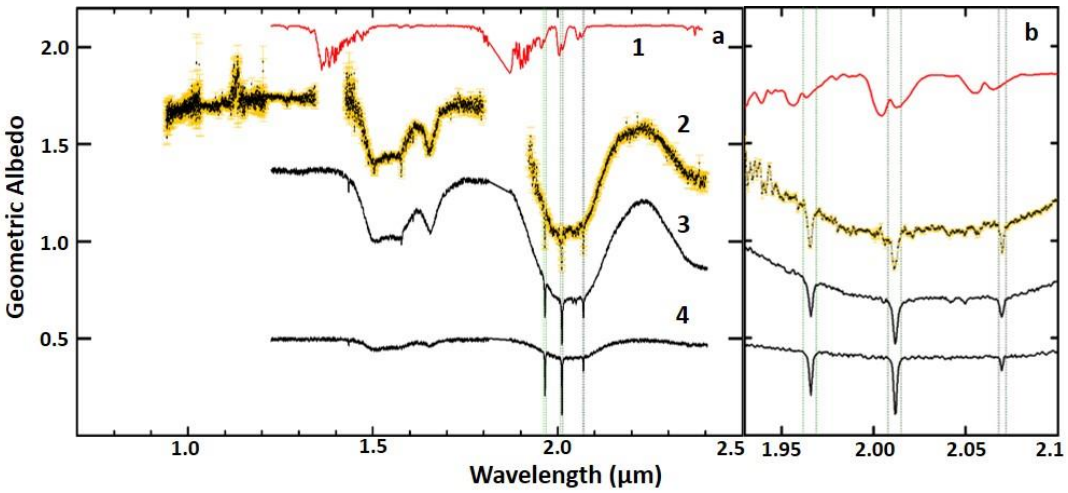

Figure 1-B.19. Atmospheric transmission spectrum taken at the IRTF (red, 1), mean trailing hemisphere spectrum of Ariel (black with orange error bars, 2), best fit model for the mean Ariel spectrum (black, 3), synthetic spectrum composed of a particulate mixture of CO_2 ice (89%), H_2O (9%), and amorphous C (2%) (black, 4). Green dashed lines indicate positions and widths of CO_2 ice bands 1, 2, and 3. (**b**) Close up of the same image shown in (a), focused on the three CO_2 bands. The shape and relative strength of the three CO_2 bands in the mean trailing hemisphere spectrum are most similar to the CO_2 bands in the best fit model that includes segregated CO_2 ice (black, 3).

Appendix 1-C.1. Impact and tectonically exposed CO_2

Native CO_2 ice buried beneath a protective regolith could be exposed by impact events and tectonic processes. Each moon has a large number of impact features over their spatially resolved southern hemispheres, and these impacts and ejecta are generally brighter than the surrounding terrain (e.g. Smith et al., 1986). The higher albedo of these craters is most likely due to the exposure of fresh material from beneath darker regoliths. Similarly, these moons display evidence for high albedo tectonic landforms. Ariel displays abundant evidence for global tectonism, including long grooves suggestive of extensional fractures (e.g. Jankowsky and Squyres, 1988). Titania and Oberon have localized clusters of chasmata and large scale fractures (Smith et al., 1986), and dark polygonal basins, which might be tectonic or cryovolcanic in origin, have been observed on Umbriel (Helfenstein et al., 1989). Therefore, each moon displays evidence for impact and tectonic resurfacing, and perhaps these processes could have exposed native CO_2 deposits.

Surface age estimates based on crater counting range from ~few 100 Ma for the younger tectonized terrains on Ariel, to > 4 Ga on the dark and ancient surface of Umbriel (Zahnle et al., 2003). Grundy et al. (2006) estimate that pure CO_2 ice might survive on the surfaces of the Uranian moons ranges from ~10 kyr to 1.0 Gyr. The large range in this sublimation timescale results from the assumed values of these satellites' bolometric Bond albedos (A_B 0.5 – 0.7), which are poorly constrained for the Uranian satellites. Therefore, any native CO_2 ice exposed by ancient tectonism and impacts has likely been removed, even from the youngest terrains on Ariel. Additionally, because the Uranian moons are tidally-locked, we would expect to find impact-exposed CO_2 deposits primarily on their leading hemispheres, which are preferentially bombarded by heliocentric impactors (e.g. Zahnle et al., 2001).

Appendix 1-C.2. Cryovolcanic CO_2 deposits

CO_2 could be produced in these satellites' interiors and deposited on their surfaces by cryovolcanism. Several studies have suggested that various surface features on each of these moons could represent cryovolcanic landforms (e.g. Smith et al., 1986; Schenk, 1991; Kargel, 1994). Long linear grooves at the center of chasmata floors have been interpreted as linear volcanic vents on Ariel (e.g. Jankowsky and Squyres, 1988), and trough-filling ridges with lobate edges and medial crests on Ariel have been interpreted as extrusive cryovolcanic flow deposits (e.g. Schenk, 1991). Numerous crater floors on Umbriel have albedos that are significantly higher than the surrounding terrains (Helfenstein and Veverka, 1988). In particular, the albedo of floor deposits in Wunda crater (~0.49), located at low southern latitudes near the antapex of motion, is over twice as bright as the surrounding terrain (~0.23). Smooth, low albedo regions on Titania have been interpreted as cryovolcanic deposits (Croft and Soderblom, 1991). Similar to Umbriel, crater floors on Oberon have smooth deposits that have been interpreted to be cryovolcanic in origin, albeit these deposits have a much lower albedo (< 0.1) than the surrounding terrains (~0.25), counter to the crater floor deposits on Umbriel. Consequently, each moon displays evidence for potential cryovolcanic structures and flow features, which might include large deposits of CO_2 ice.

Much like the observed tectonic features, however, most of the putative extrusive cryovolcanic flows and ridges are all fairly old according to crater age estimates (~few 100 Ma – 1 Ga, Zahnle et al., 2003), and exposed CO_2 should be effectively removed over these timescales. Furthermore, there is no obvious reason to expect a leading/trailing dichotomy in cryovolcanism, and therefore in emplaced CO_2, on these satellites. Even if emplaced CO_2 coincidently displayed a leading/trailing asymmetry on these satellites, perhaps due to global tidal forces enhanced by paleo-resonances (Tittemore and Wisdom, 1990), we would expect to find more CO_2 on the relatively younger surfaces of Titania and Oberon than the more ancient surface of Umbriel, counter to the observed CO_2 abundances on these moons. Therefore, CO_2-rich, extrusive cryolava deposits do not adequately fit the observed distribution of CO_2. However, the smooth crater floor deposits on Umbriel and Oberon appear to be devoid of over-printing impact features (albeit, at low spatial resolutions of ~5 – 6 km/pixel), and might represent young cryovolcanic deposits. In particular, Wunda crater is positioned near the antapex of Umbriel and at low southern latitudes where CO_2 bands are deepest. Additional observations at higher resolution than the available Voyager 2 data are needed to investigate the morphology and composition of putative cryovolcanic deposits further.

Appendix 1-C.3. Micrometeorite impacts

Micrometeorite impacts eject and vaporize buried material, mixing regolith materials and exposing fresh materials at the surface to irradiation sources. Furthermore, the kinetic energy imparted into surfaces by micrometeorite impacts can dissociate target molecules, even at relatively modest impact velocities of ~5 km/s (Borucki et al., 2002; Jaramillo-Botero et al., 2012). Thus, micrometeorite impacts might represent an important energy source for dissociating H_2O, CO_2, and others species on icy moons.

Gravitational focusing by planets increases impactor fluxes on the satellites closest to them (Shoemaker and Wolfe, 1982; Zahnle et al., 2003). Because the orbital velocities of the Uranian satellites (~3 – 7 km s^{-1}) are comparable to incoming heliocentric and planetocentric dust (~10 km s^{-1}), these particles should preferentially impact the leading hemispheres of the Uranian moons (Tamayo et al., 2013). It therefore seems unlikely that kinetic energy from micrometeorite impacts is a primary contributor to active CO_2 ice synthesis given that CO_2 is concentrated near the antapexes of these satellites, which are predicted to experience the fewest number of heliocentric impacts.

Appendix 1-C.4. Sublimation and cold trapping of CO_2

CO_2 deposits exposed on the surfaces of Uranian moons should sublimate away over timescales shorter than the age of the Solar System (*e.g.* Lebofsky, 1975). The large obliquity of the Uranian system leads to large seasonal disparities in heating that should drive CO_2 migration to low latitude cold traps (Grundy et al., 2006). Additionally, because maximum surface temperatures on airless bodies like the Uranian satellites are a strong function of rotation rate, CO_2 should be most resistant against sublimation at low latitudes on the fast rotating inner moons, Ariel and Umbriel – exactly where it has been detected. The absence of CO_2 at high latitudes on the Uranian moons has yet to be

confirmed, and subsequent observations of these satellites during northern summer will help constrain the abundance of CO_2 at high latitudes.

However, it seems unlikely that sublimation alone controls the observed hemispherical asymmetries in CO_2 band depths on the Uranian satellites. The time span of maximum subsolar heating should be the same on both their leading and trailing hemispheres, which over time, would drive sublimation on both hemispheres and homogenize the distribution of CO_2. It therefore seems unlikely that sublimation alone is responsible for the observed distribution of CO_2. As the Uranian system moves toward northern summer over the next two decades, subsequent observations of the Uranian satellites should provide insight into sublimation-driven seasonal migration of CO_2.

Appendix 1-C.5. UV photolysis

UV photons interact with icy surfaces, driving molecular dissociation of constituents and the synthesis of new species. Numerous laboratory studies have demonstrated that the absorption of UV photons ($\lesssim$ 227 nm, $h\upsilon \gtrsim$ 5.5 eV) by H_2O ice mixed with carbonaceous materials can synthesize CO_2 ice (e.g. Chakarov et al., 2001; Hudson and Moore, 2001; Loeffler et al., 2005; Mennella et al., 2006). Other laboratory experiments have demonstrated that CO_2 ice is readily dissociated by UV photon irradiation ($\lesssim$ 227 nm, $h\upsilon \gtrsim$ 5.5 eV) (e.g. Gerakines et al., 2001; Hudson and Moore, 2001; Schmidt et al., 2013).

An important consideration for investigating the efficiency of UV photolysis of CO_2 is the differences in penetration depths for chemistry-inducing UV photons ($\lambda \lesssim$ 227 nm) and the reflected NIR photons (λ ~0.8 – 9.5 μm) gathered by SpeX and IRAC. NIR photons penetrate ~100 μm into crystalline H_2O ice over the wavelength range relevant for detecting CO_2 ice combination and overtone bands (λ ~1.9 – 2.1 μm), but only penetrate ~10 μm into H_2O over the wavelength range relevant for detecting the CO_2 υ_3 band. Most of the UV photons that can utilize the highest probability pathway for dissociating CO_2 ($\lambda \lesssim$ 160 nm, $h\upsilon \gtrsim$ 7.7 eV) only interact with the top ~few microns of crystalline H_2O ice, while UV photons that utilize the much lower probability forbidden transition to dissociate CO_2 ($\lambda \lesssim$ 227 nm, $h\upsilon \gtrsim$ 5.5 eV) can interact with species in the top ~few meters of crystalline H_2O ice. Therefore, UV photons that can readily dissociate CO_2 ($\lambda \lesssim$ 160 nm) almost entirely affect the layer sensed by IRAC (~ 10 μm) and do not reach depths sensed by SpeX (~ 100 μm). This overlap between far-UV photons and IRAC penetration depths is consistent with our best fit IRAC models, which are dominated by small H_2O ice grains with only minor amounts of small grained CO_2 ($\lesssim$ 5%).

UV photons interact equally with both the leading and trailing hemispheres of synchronously-locked satellites. Hence, it seems unlikely that UV photolysis can account for the observed hemispherical asymmetries in CO_2 abundance on these satellites. Furthermore, UV photons should also interact equally with each satellite, which makes the observed planetocentric trend in CO_2 abundance difficult to explain with UV photolysis as well. While UV photons plausibly contribute to the production and destruction of CO_2 on the Uranian moons, as hypothesized for the detected CO_2 on

Iapetus (Palmer and Brown, 2011), it is unlikely to represent the primary controlling mechanism on the distribution of CO_2 ice in the Uranian system.

Appendix 1-C.6. Ion and electron radiolysis

Charged particle bombardment of icy surfaces leads to the destruction of constituent species, the synthesis of new species, the ejection of material, and amorphization of H_2O ice (Spinks and Wood, 1990). Synthesis of CO_2 via ion irradiation of carbon-rich and H_2O ice mixtures at cryogenic temperatures has been demonstrated to occur rapidly in laboratory settings, using a wide range of C and O rich constituents, substrate temperatures, and ion energies (e.g. Gerakines et al., 2001; Hudson and Moore, 2001; Mennella et al., 2004; Gomis and Strazzulla, 2005; Raut et al., 2012). Similarly, experimental work investigating electron irradiation of icy mixtures has demonstrated that electrons can readily synthesize CO_2 under a wide range of conditions and electron energy levels (e.g. Sedlacko et al., 2005; Jamieson et al., 2006; Kim and Kaiser, 2012).

Penetration depths of heavy ions and protons are significant larger than the ~few μm depths of near-UV photons. Hudson and Moore (2001) state that a 1 MeV proton, along with secondary electrons, can chemically alter the top 20 μm of an icy surface. Delitsky and Lane (1998) designate the top ~100 μm of icy surfaces as the "plasma deposition zone" where heavy ions and protons initiate chemical changes in the near-surface species. According to these authors, energetic electrons can penetrate much deeper than ions, on the order of ~5 mm. Penetration depths of NIR photons sensed by IRAC over the wavelengths covered by the CO_2 υ_3 band (~10 μm) clearly overlap with energetic ions and protons as well as electrons. However, only electrons have a high probability of penetrating to the depths probed by SpeX over the wavelength range covered by CO_2 bands 1 – 3 (~0.1 mm).

Similar to UV photons, solar wind particles ($\gtrsim$ 400 km s^{-1}) and cosmic rays ($\gtrsim$ 1% speed of light) interact with both the leading and trailing hemispheres of the synchronously locked Uranian moons (~3 – 7 km s^{-1} orbital velocities). Consequently, these radiation sources would tend to generate (and destroy) CO_2 molecules ubiquitously, without pronounced hemispherical asymmetries. In a simplified Offset Tilted Dipole (OTD) model of magnetospheric interactions with the surfaces of Uranus' tidally-locked moons, embedded charged particles should preferentially bombard their trailing hemispheres as the co-rotating field lines sweep over the satellites, similar to the Jovian and Saturnian systems. The observed distribution of CO_2 supports this simple model of magnetospheric-satellite surface interactions in the Uranian system.

Appendix 1-C.7. Charged particle sputtering

Impacts by charged particles, micrometeorites, and high energy photons can eject material from surfaces (e.g. Johnson et al., 1984). In the Uranian system, charged particle sputtering is estimated to be much lower than at Saturn because of lower ion fluxes in the Uranian satellite orbital plane, and the lower sputtering efficiency of protons compared to heavy ions (Lanzerotti et al., 1987). Grundy et al. (2006) estimate that charged particle sputtering rates for the more volatile CO_2 should be 50 – 100 times higher than H_2O. These authors determined that to remove a global surface layer of CO_2 (~0.5 cm thick)

using charged particle sputtering would take on the order of a few 100 Ma for the inner moons and longer than the age of the Solar System for the outer moons. Moreover, our CO_2 band parameter analysis indicates that the largest CO_2 band depths occur in spectra collected near the antapexes of these satellites, which likely represent the longitudes that experience the highest rates of charged particle sputtering. Therefore, charged particle sputtering does not appear to represent an important control on the distribution of CO_2.

Appendix 1-D.1. Uranian magnetic field and plasma environment

The magnetic dipole of Uranus is significantly offset from its rotational axis (58.6°), and its magnetic center is offset by ~0.3 Uranian radii (R_U) from the planetary center (Ness et al., 1986). The magnetopause is at a distance of ~18 R_U (~450,000 km), encompassing the orbits of Ariel, Umbriel, and Titania, but not entirely that of Oberon, which orbits upstream of the magnetopause on Uranus' Sun-facing hemisphere (< 50% of its orbital period). The rotation period of Uranus' magnetic field (~17.2 hours) is much shorter than the orbital periods of the large Uranian moons (~2.5 – 13.5 Earth days, Table 1.1). Due to this differential velocity, charged particles embedded in the Uranian magnetosphere bombard the trailing hemispheres of the satellites as the magnetic field lines sweep past them. While higher order multipole models are needed to adequately describe the structure of Uranus' magnetic field (Connerney et al., 1987), higher order terms die out faster than the dipole term and are negligible outwards of ~5 U_R and a simple OTD model provides a reasonable approximation at the radial distances of the classical satellites (Acuna et al., 1988). Subsequent discussion of the Uranian plasma environment relies on this simpler OTD model.

Analysis of data collected by the Low Energy Charge Particle (LECP) instrument onboard Voyager 2 demonstrated that the magnetosphere of Uranus is populated by protons and electrons (sourced by Uranus' ionosphere) with little evidence of heavier ions (< 1% of total ion population) (Krimigis et al., 1986). Voyager 2's Cosmic Ray System (CRS) measured a steep increase in the electron and proton counts interior to the orbit of Titania (Stone et al., 1986). Localized reductions in high energy (> 1 MeV) electron and proton counts coincide with the orbits of Miranda, Ariel, and Umbriel, indicating that these satellites are bombarded by high energy particles that intersect their orbits (Stone et al., 1986). The lack of heavy ions in the Uranian magnetosphere is likely due in part to the large offset between the orbital plane of the satellites and the magnetic equator, which results in heavy ions and (pre-cursor) neutrals occupying distinctly different volumes of the magnetosphere (Cheng et al., 1987). Consequently, implantation of heavy ions is unlikely to be an important driver of chemistry on the Uranian satellites.

Due to the large offset of the magnetic equator, the satellite orbital plane intersects a wide range of magnetic latitudes and L shells (measure of the magnetic field distance in Uranian radii, with lower L shell values typically corresponding to higher charged particle fluxes within radiation belts) (Stone et al., 1986). The net result is that electron and proton fluxes in the satellite orbital plane are low compared to the magnetic equator (Cheng et al., 1987). Laboratory experiments, informed by LECP measurements of proton and electron fluxes at each satellite, demonstrate that cryogenic H_2O ice is readily modified. Consequently, electrons and protons embedded in Uranus' magnetosphere should chemically alter the surfaces of these moons over short timescales (Lanzerotti et al., 1987). The large offset of Uranus' magnetic axis from its rotational axis makes predictions of the satellite latitudes where charged particle irradiation is greatest much more uncertain than in the Jovian or Saturnian systems. Detailed models simulating the interactions between Uranus' magnetic field and its satellites are therefore required to constrain the locations of peak radiation dose and fluence on these satellites.

CHAPTER 2:
USING SYNTHETIC APERTURE RADAR DATA OF TERRESTRIAL ANALOGS TO TEST ALLUVIAL FAN FORMATION MECHANISMS ON TITAN

This chapter is a reformatted version of a paper by the same name published in Icarus in 2017 by Richard Cartwright and Devon Burr. The work presented here includes additional changes not included in the published version of this manuscript. All data collection and analyses were performed by Richard Cartwright.

Cartwright, R.J., and Burr, D.M.., 2017. Using synthetic aperture radar data of terrestrial analogs to test alluvial fan formation mechanisms on Titan. *Icarus*, *284*, 183-205. http://dx.doi.org/10.1016/j.icarus.2016.11.013

Abstract

Landforms on Titan include features hypothesized to be alluvial fans. Analysis of possible alluvial fans on Titan could provide key insight into the regional hydrology and sedimentology where these features are present. Terrestrial alluvial fans form via two processes spurred by intense and infrequent precipitation: fluid-gravity flows (sheetfloods) and sediment-gravity flows (debris flows). Along the Panamint mountain Range in Death Valley, California, USA, seven fans formed primarily by debris flows are located adjacent to seven fans formed primarily by sheetfloods. The causal difference between these two groupings stems from their catchment lithologies; the debris flow fan catchments are clay-rich and sand-poor, and the sheetflood fan catchments are clay-poor and sand-rich. On Titan, the low and mid latitudes are dominated by sand seas, demonstrating that sand is available for transport. At high latitudes, these sand seas are absent, suggesting that transportable sand is scarce. Based on the sedimentology of the two Panamint Range fan types, we hypothesize that possible fans at lower latitudes on Titan are formed by sheetfloods, whereas those at higher latitudes formed primarily by debris flows. To test these hypotheses, we measured and analyzed the mean normalized radar cross sections (σ^0) and changes in σ^0 with downfan distance for debris flow and sheetflood fans along the Panamint Range. We then compared the results with the same measurements for possible fans on Titan. Because terrestrial alluvial fans have consistent sedimentologies at meter-scale depths, the greater penetration depths of radar signal into cryogenic water ice on Titan should still be dominated by backscatter from sediments deposited during possible fan formation. We find that, in the Panamint Range, debris flow fans are brighter than sheetflood fans and have greater change in σ^0 with downfan distance. On Titan, low-latitude possible fans are brighter than the fans at high latitudes with greater change in σ^0 with downfan distance, suggesting that the dominant range in grain sizes for sediments in high latitude fans is smaller than low- and mid-latitude fans. Consequently, our findings suggest that low-latitude possible fans on Titan are formed primarily by debris flows, whereas high-latitude possible fans on Titan are formed primarily by sheetfloods. Thus, our results do not support our hypotheses. Scenarios to explain these results include: (1) high-latitude possible fans are dominated by radar-dark debris flow deposits, (2) low and mid-latitude possible fans are dominated by radar-bright

sheetflood deposits, (3) sand-sized sediments were relatively scarce at the time of low and mid-latitude possible fan formation, (4) bedrock composition varies as a function of latitude on Titan, (5) alluvial fans form differently on Titan because of the lower gravity conditions, and (6) fan-like features may result from non-alluvial processes, such as distributary fluvial systems on Earth.

Introduction

Alluvial fans are sedimentary landforms that result from intense and infrequent atmospheric precipitation, transportable sediment, and topographic relief, whereby sediments are deposited in semi-conical or wedge shapes at changes in flow confinement. Two mechanisms dominate alluvial fan formation: sediment-gravity debris flows, in which gravity directly transports the sediment in a hyperconcentrated mass, and fluid-gravity sheetfloods, in which the movement of the fluid carries the sediment (*e.g.*, Blair and McPherson, 1994a). Identification of alluvial fans formed by these mechanisms can provide valuable insight into their sedimentology and catchment lithology (Blair, 1999). The distinctive planview morphology of alluvial fans makes them useful indicators of local sedimentological and regional hydrological conditions where *in situ* analyses are not possible.

Alluvial fans are readily identifiable in many imaging datasets collected by orbiting satellites and spacecraft. Terrestrial alluvial fans have been identified and morphologically analyzed using a wide range of visible/near-infrared (VIS/NIR) reflectance datasets (*e.g.*, Bull, 1991 and references therein; Crouvi et al., 2006), as well as thermal infrared (TIR) (Hardgrove et al., 2010) and synthetic aperture radar (SAR) images (Farr et al., 1996). On Mars, alluvial fans have been identified in multiple datasets with moderate to high spatial resolution (*e.g.*, Moore and Howard, 2005; Williams and Malin, 2008). The Cassini RADAR instrument (λ ~2.2 cm) can readily penetrate Titan's atmosphere to observe Titan's surface (*e.g.*, Elachi et al., 2005). Analysis of SAR images gathered by Cassini RADAR has led to the identification of hypothesized alluvial fans on Titan's surface (Moore and Howard, 2010; Radebaugh et al., 2016; Birch et al., 2016).

Identification of alluvial fans in remotely-sensed datasets can provide insight into regional hydrology and sedimentology where these landforms are present. Inference of specific fan formation mechanisms requires detailed analyses of high resolution VIS datasets, which may not be possible in lower resolution images at microwave wavelengths. Consequently, gaining insight into alluvial fan formation on Titan requires different techniques than have been applied to VIS data of terrestrial planets.

Analysis of terrestrial alluvial fans, formed by debris flows and sheetfloods, in high spatial resolution ($\gtrsim$ 10 m/pix) SAR data, provides an opportunity to infer diagnostic attributes for formation mechanisms. These attributes may then be applied to analysis of possible alluvial fans in SAR images gathered over Titan. Fans on Earth and features that may be fans on Titan have similar large-scale morphologies: confined upfan feeder channels, central wedge- or cone-shaped fan surfaces, and downfan terminal fan toes (*e.g.*, Blair and McPherson, 1994a, 1994b). Thus, by using terrestrial fans with well-characterized formation histories as analogs to similar landforms on Titan, we can gain insight into fan formation mechanisms on Titan.

In this work, we compare terrestrial alluvial fans, imaged by high-resolution SAR instruments, to possible alluvial fans in SAR images of Titan. We delineate the planform boundaries of alluvial fans on Earth and of possible alluvial fans on Titan and measure their mean, normalized radar cross sections (σ^0) and downfan σ^0 values. We analyze the radar signal returned from debris flow and sheetflood fans to determine whether these two fan types can be distinguished in terrestrial SAR datasets. We apply the same σ^0 analyses to SAR data of Titan to infer formation mechanisms for possible alluvial fans. From our results, we draw broader implications for the availability of sediment for fluvial transport at different latitudes on Titan. We precede the presentation of our work with some necessary background on alluvial fan formation, relevant Titan science, and SAR data collection and analysis.

Background

Alluvial fans: Sedimentary delivery mechanisms

Alluvial fans are aggradational landforms that commonly form along topographic discontinuities. In tectonic settings, these topographic discontinuities might exist at the boundaries between uplifted mountain blocks and down-dropped valley floors, such as in the Basin and Range province in the southwestern United States (Bull et al., 1977). In non-tectonic settings, fans often form where pre-existing sediment sources and relief are present, such as at the base of hanging valleys exposed by retreating glaciers (Harvey et al., 2005, and references therein). On Earth, alluvial fans are commonly associated with arid and semi-arid climates (*e.g.*, Denny, 1965; Bull, 1977; Blair and McPherson, 1994a, 1994b). However, alluvial fans have been identified in a wide range of environments, including: arctic (*e.g.*, Boothroyd and Nummendal, 1977), alpine (*e.g.*, Kostaschuk et al., 1986), and both humid temperate (*e.g.*, Kochel, 1990) and humid tropical (*e.g.*, Kesel and Spicer, 1985) climatic zones.

Alluvial fans develop as a result of catastrophic flows emerging from confining canyons to debouch onto valley floors, where they subsequently deposit sediment in a semi-conical pattern originating at the exit to the confining canyon (Bull, 1977). These catastrophic flows are generated by infrequent mass wasting and flashflood events that transport pulses of stored material out of fan catchments (*e.g.*, Baker et al., 1988). The steep reduction in sediment capacity of the flow, due to reduction in flow depth at the exit from the confining canyon, leads to rapid deposition of the material. Repeated catastrophic flow events build up alluvial fans over time. Consequently, the grain size range, roundness, and sorting properties of subsurface sediments are similar to sediments exposed on alluvial fan surfaces (*e.g.*, Blair and McPherson, 1994a, 1994b).

The two types of processes that drive alluvial fan development are sediment-gravity flows ($\gtrsim$ 40% sediment by volume of a given flow) and fluid-gravity flows ($\lesssim$ 40% sediment by volume) (Costa, 1988). Debris flows, a common type of sediment-gravity flow, are a mix of poorly-sorted materials that include fine-grained sediments, *i.e.*, silts and clays, moving downslope as a viscoplastic body (Johnson, 1970). Because of the viscoplastic nature of debris flows, their turbulence and inter-layer mixing tends to be low, and they tend toward more laminar flow conditions that can sustain the transport

of boulders and other large objects on top or near the front of the flow (*e.g.*, Blair and McPherson, 1994a). Sheetfloods, a common type of fluid-gravity flow, move as unconfined, low-viscosity flows, transporting more homogeneously-sized sand or larger sediments as bedload or suspended load (*e.g.*, Bull et al., 1972). Large alluvial fans and megafans on Earth are primarily formed by fluid-gravity flows (*e.g.*, Arzani, 2012), with surfaces that commonly include friable gravelly sandstone. Because of the greater viscosity and sediment grain size heterogeneity of debris flows over sheetfloods, debris flow-dominated fan surfaces are typically rougher (*i.e.*, mantled by relatively more coarse-grained sediments) and more indurated than sheetflood-dominated fans (Blair and McPherson, 1994a, 1994b). Alluvial fans dominated by debris flows include clast-rich and clast-poor lobes deposited across their surfaces, extending to their fan toes. Alluvial fans dominated by sheetfloods commonly exhibit minor to moderate reduction in sediment grain sizes with downfan distance (Blair and McPherson, 1994b). Consequently, the clast-rich deposits that comprise debris flow fans result in rougher surfaces, mantled with coarser sediments, than characterize sheetflood fan surfaces. Both fan types are subsequently modified by post-depositional processes that are common in arid environments like Death Valley, including, fluvial erosion, salt precipitation, and aeolian winnowing of fine-grained sediments (*e.g.*, Goudie, 2013).

Although other factors influence the development of alluvial fans (drainage basin size and shape, neighboring landforms, climate, and tectonism), investigation of alluvial fans along the Panamint Range in Death Valley suggests that fan formation mechanisms are most strongly affected by drainage basin lithology (Blair and McPherson, 1994a; Blair, 1999). These Panamint Range alluvial fans include seven debris flow fans and seven sheetflood fans that are geographically grouped together, separated by a lithologic contact between the two fan types. The surfaces of the Panamint debris flow fans are dominantly mantled by clast-rich lobes, with some clast-poor lobes.

Debris flow-dominated fans, of both clast-rich and clast-poor composition, have drainage basins underlain by bedrock materials that readily weather into clay- and silt-sized particles. These fine-grained sediments reduce the permeability of colluvium in fan catchments, leading to increased water retention in colluvium and subsequent increase in pore pressure. The enhanced pore pressure reduces shear strength along the sediment-rock interface, triggering the initiation of debris flows (*e.g.*, Iverson, 2005). In contrast, the sheetflood-dominated fans have catchments underlain by jointed/fractured granitic plutons or friable gravelly sandstone that weathers into medium to very coarse sand, pebbles, and cobbles, with only minor amounts of silt and clay (Blair and McPherson, 1994a). This comparison illustrates the general causal correlation that alluvial fan surfaces dominated by debris flows typically have catchments with substantial amounts of clay- and silt-sized sediments and relatively less sand-sized particles, whereas fan surfaces dominated by sheetfloods typically have catchments with substantial amounts of sand-sized and larger sediments, lacking finer grained particles. Additionally, the range of grain sizes and degree of sediment sorting in the near-surfaces of these fans are consistent with the sedimentology of their respective surfaces to at least a few meters depth (Blair, 1999).

Alluvial fans have also been identified in craters on Mars, where they are likely composed of impact comminuted material that was transported from high-standing crater rims and deposited on crater floors (Craddock and Howard, 2002). Alluvial fans on Mars, like most other Martian fluviatile landforms, most likely formed during wetter periods of Martian history. The morphology and gentle slopes of large Martian alluvial fans suggest that they were formed primarily by fluid-gravity (*e.g.*, sheetflood) processes, similar to terrestrial megafans (*e.g.*, Moore and Howard, 2005). The potential for an intermittent runoff-inducing climate on Mars suggests that alluvial fans took longer to form on Mars than equivalently sized terrestrial fans (Moore and Howard, 2005).

On Titan, radar-bright, wedge-shaped features have been observed at the termini of curvilinear features, which are interpreted to be fluvial in nature (*e.g.*, Elachi et al., 2005; Lorenz et al., 2008a; Burr et al., 2009; Cartwright et al., 2011; Langhans et al., 2012; Burr et al., 2013a, 2013b). Although the coarse spatial resolution of the SAR images, as well as the sparseness of local scale topographic data, hinders conclusive geomorphic interpretation of these wedge-shaped features, they have been interpreted by multiple teams to be alluvial fans (Moore and Howard, 2010; Radebaugh et al., 2016; Birch et al., 2016).

Titan science: The surficial sedimentary environment

Titan is the second largest satellite in the solar system and the only moon with a substantial aerosol-rich atmosphere. Titan's atmosphere is primarily composed of N_2 (~95%) and CH_4 (~5% near-surface abundance) (Niemann et al., 2005). At the temperature (~93.5 K at the Huygens landing site) and pressure (~1.5 bars) of Titan's surface, near-surface CH_4 is close to its triple point and is stable as a liquid. Both ground-based observations (*e.g.*, Brown et al., 2002) and images gathered by the Cassini spacecraft (Turtle et al., 2011) demonstrate that clouds can form and dissipate on short timescales, suggesting that liquid hydrocarbons, mixed with dissolved N_2, rain out of Titan's atmosphere (*e.g.*, Graves et al., 2008). Numerical modeling of these precipitation events suggests that rain reaches Titan's surface during infrequent and intense storms (*e.g.*, Roe et al., 2012 and references therein). Along with liquid hydrocarbons, organic aerosols, generated by UV photolysis and charged particle radiolysis of CH_4, slowly settle out of Titan's atmosphere onto its surface (*e.g.*, Yung et al., 1984). Due to super-rotating stratospheric winds, the organic aerosols are quickly spread throughout Titan's atmosphere (Anderson and Samuelson, 2011), generating a global layer of optically thick particulates that obscure the surface of Titan at visible wavelengths (Smith et al., 1981, 1982; Rages et al., 1983). Additionally, CH_4 in Titan's atmosphere strongly absorbs light over multiple large NIR bands, degrading the quality of images gathered by the Imaging Science Subsystem (ISS, λ ~0.38 – 1.1 μm) and Visible and Infrared Mapping Spectrometer (VIMS, λ ~0.35 – 5.1 μm) onboard Cassini (see Cornet et al. (2012) for comparison of Titan features in ISS, VIMS, and SAR images).

The Cassini RADAR instrument (SAR mode) has imaged the surface of Titan at a range of resolutions (~350 – 1700 m/pixel). These data reveal numerous types of geomorphic landforms, including drainage networks and fluvial and alluvial features with morphologies strikingly similar both to river-formed networks and features (Lorenz et al.,

2008a; Burr et al., 2009; Cartwright et al., 2011; Langhans et al., 2012; Burr et al., 2013a, 2013b) and to alluvial fans (Moore and Howard, 2010; Radebaugh et al., 2016; Birch et al., 2016) on Earth. Integrated fluvial networks are interpreted as evidence that liquid hydrocarbons reach Titan's surface where they become concentrated into channelized flow, forming the observed fluvial features (*e.g.*, Burr et al., 2013a) while entraining and transporting available sediments (*cf.*, Burr et al., 2006). In other locations, precipitation might infiltrate into Titan's subsurface, dissolving organic constituents like benzene to form dissected, karst-like landscapes (Malaska and Hodyss, 2014).

Titan's surface is most likely composed of a mixture of H_2O ice and a wide range of organic species (Clark et al., 2010; Neish et al., 2015; Janssen et al., 2016). The dielectric constants of H_2O ice and most organic materials are all much lower than common terrestrial materials (Zebker et al., 2008). Consequently, the intensity of radar echoes returned to the Cassini RADAR instrument is inferred to be dominated by sensor-facing slopes, subsurface volume scattering, and surface/near-surface roughness elements (Le Gall et al., 2010; Janssen et al., 2011). At least two fluvial features observed by the Cassini RADAR instrument have anomalously high σ^0 values that are unlikely to be the result of only incidence angle (θ) effects and/or volume scattering (Le Gall et al., 2010). Instead, the backscatter from these two fluvial features is hypothesized to result from a mantle of coarse, rounded sediments, which behave like retro-reflectors (Le Gall et al., 2010). The Huygens probe imaged numerous rounded cobbles ($\lesssim$ 20 cm diameter) at its landing site on Titan's surface (Tomasko et al., 2005), supporting this retro-reflection hypothesis. Thus, other radar-bright fluvial features, including radar-bright features that might be alluvial fans, could also be mantled with signal-enhancing cobbles. If alluvial fans on Titan form from similar processes to alluvial fans on Earth, then the range of grain sizes and degree of sorting observed in the near-surfaces of these features should reflect their sedimentologies to at least several meters depth (*e.g.*, Blair and McPherson, 1994a). Consequently, subsurface volume scattering from possible Titan fans would be dominated by sediments deposited during fan development.

In contrast to localized cobble deposits, fine grain particulates, comparable in size to terrestrial clay sediments (few μm diameter), should be present at all latitudes on Titan due to photometrically-produced aerosols settling out of Titan's atmosphere (*e.g.*, Raulin et al., 2012). It is unclear, however, whether deposits of organic particles, in the presence of liquid hydrocarbons, would mimic the impermeable properties of silicate-rich clays on Earth. If they do not, then this lack of an impermeable component would tend to limit the frequency of debris flows on Titan. Whereas these aerosols settle out globally, readily mobilized sand-sized particles appear to be latitudinally heterogeneous. The presence of vast sand seas straddling equatorial latitudes on Titan (*e.g.*, Lorenz et al., 2006; Lopes et al., 2010; Neish et al., 2010; Le Gall et al., 2011, 2012) indicates that sand available for transport is prevalent at low and mid latitudes. Given this sand availability, possible fans in Titan's equatorial regions could be dominantly mantled by sand-sized particles. In contrast, these sand seas are not apparent at high latitudes, suggesting a relative dearth of sand. Given the global distribution of atmospheric aerosols, possible fans at high latitudes could be dominantly mantled by fine-grained particles.

SAR observations

Operating at microwave (~cm scale) wavelengths, radar systems are able to penetrate clouds and atmospheric haze layers to observe planetary surfaces, with negligible atmospheric absorption. Therefore, radar instruments are ideal for observing the surfaces of Earth, Venus, and Titan, where thick atmospheres and/or variable cloud cover makes observations at shorter wavelengths more difficult. Radar imaging instruments are side-looking sensors that build up images by actively transmitting energy and receiving reflected radar echoes from a target surface as the radar platform moves along its flightpath (*e.g.*, Ulaby et al., 1982; Ulaby and Dobson, 1989; Ulaby et al., 2014). Each location imaged by a radar system is observed at multiple times in different sections of the radar beam footprint, which represent distinct radar "looks." The primary limit to the resolution of radar images is the physical size of the radar antenna. However, the resolution of radar images can be greatly enhanced during signal processing by utilizing Doppler shift and time delay information from each observed location to synthetically increase the effective aperture of the radar antenna, thus generating SAR images.

The intensity of radar echoes returned to a receiver is a function of radar wavelength, local incidence angle (*i.e.*, incidence angle and local slope effects), beam polarization (*i.e.*, orientation of outgoing and incoming radar signal), and the dielectric properties and roughness of the target. In general, radar "rough" surfaces are those with individual scattering elements comparable in scale ($\gtrsim \lambda/10$) to the wavelength of the radar instrument (Campbell, 2002 and references therein). The dielectric properties of a target surface help determine the intensity of returned radar echoes, with stronger echoes returned from surface materials that are easily polarized by applied electrical fields and materials that are good conductors (*i.e.*, materials with a large dielectric constant such as transition metals and salt water). In terms of beam polarization, horizontally-polarized backscatter is primarily composed of pure surface and double bounce scattering contributions, whereas vertically polarized backscatter is dominated by volume scattering (Cloude, 2009 and references therein).

Interpretation of SAR images is complicated by speckle noise. For a given resolution cell in a SAR image, returned echoes backscatter off a large number of individual scatterers, each of which reflects signal back to the receiver. These reflected signals interfere with each other, generating bright and dark spots (speckle) in the resulting image. Speckle noise can be greatly reduced by averaging multiple radar looks together. SAR sensors have gathered images of Earth's surface at wavelengths spanning ~3 to 70 cm, with multiple beam polarizations, and at a wide range of incidence angles (Ouchi et al., 2013, and references therein). The Cassini RADAR instrument operating in imaging mode (SAR) has observed Titan at only one central wavelength (~2.2 cm), with a single beam polarization and a more limited range in incidence angles (~20 – 35°) (West et al., 2009). The dielectric constants of terrestrial materials range from ~2 to 150, with dry, rock-forming silicate minerals, like those in Death Valley, having values in the range of 5 to 8 (*e.g.*, Parkhomenko, 2012). The estimated dielectric constants for Titan surface materials, based on scatterometry and radiometry data, are ~1.5 to 3.2, which are much lower, and have a more limited range, than the bulk dielectric constants of terrestrial rocks ($\gtrsim 3 – 9$) (Zebker et al., 2008).

Along with surface roughness, the penetration depths of radar signal are a strong function of the dielectric properties of a medium (*e.g.*, Campbell et al., 2002). The depths probed by radar signal propagating into a compositionally-homogenous surface can be estimated by (Ulaby et al., 1982): $Penetration\ Depth\ (cm) \approx (\lambda\sqrt{(\varepsilon')})/(2\pi\varepsilon'')$, where λ is the wavelength of the instrument, and ε' and ε'' are the real and imaginary components of the dielectric constant of a given material, respectively. For a surface composed of silicate-dominated rocks (with negligible water content or metal-rich inclusions), ε' and ε'' are commonly in the range of 5 – 8 and 0.05 – 0.2, respectively (Ulaby et al., 1988), leading to penetration depths on order of ~0.1 to 0.5 m for a 5.7 cm wavelength (C band) radar instrument and ~0.4 to 2 m for a 23.6 cm wavelength (L band) radar instrument. The 'bedrock' on Titan is likely composed of water ice and organics (*e.g.*, Lunine and Atreya, 2008). Laboratory measurements of the dielectric properties of these likely bedrock constituents found ε' and ε'' of 3.2 and 0.0013, respectively, for cryogenic water ice and ε' and ε'' of 2.38 and 0.0022, respectively, for benzene ice (Paillou et al., 2008). These low-loss materials lead to penetration depths on order of ~2.5 to 5 m into the surface of Titan by Cassini's Radar instrument (2.2 cm).

Consequently, the low-loss properties of cryogenic water ice and organic ices would allow radar signal to penetrate to greater depths into bedrock on Titan compared to silicate-dominated surfaces on Earth. Because alluvial fan sedimentologies are consistent to at least several meter depths, surface and volume scattering from possible fan substrates on Titan should be dominantly from sediments deposited during fan formation. Furthermore, the terrestrial and Titan penetration depth estimates given above assume negligible backscattering from roughness elements and dielectric interfaces (*i.e.*, radar signal propagating into smooth, compositionally-homogenous slabs), and therefore, these penetration depth estimates most likely represent upper limits to real surface depths probed by radar instruments.

Water ice exposed on the surfaces of the Galilean satellites strongly backscatters radar signal, likely from volume scattering in their near-surfaces (*e.g.*, Black et al., 2001). As on the icy Galilean satellites, volume scattering from Titan's subsurface likely dominates over dielectric response for structures at the scale sampled by the radiometry and scatterometry modes of Cassini's RADAR instrument (~50 km) (Zebker et al., 2008). Because of the more limited dielectric range of materials on Titan, differences in the intensity of backscatter from adjacent landforms are likely dominated by differences in surface and subsurface roughness elements, as opposed to differences in compositions.

Features observed in SAR images are inferred to be dominated by surface scattering, including retro-reflection from low-loss, rounded cobbles (Le Gall et al., 2010). If Titan fans are sedimentologically analogous to debris flow and sheetflood alluvial fans along the Panamint Range (*i.e.*, permeated with thick deposits of cobbles), then subsurface contributions to the radar signal returned from the Titan features are likely from sediments of the same size and roundness as those mantling their surfaces. On Earth, radar echoes from rough and desiccated landforms like alluvial fans are mostly dominated by surface scattering and slope effects, with negligible signal returned from subsurface scatterers (Campbell, 2002 and references therein). Thus, for both alluvial fans on Earth and possible fans on Titan, returned signal should be dominated by

scattering from sedimentary deposits on their surfaces, and, in particular for the possible fans on Titan, buried in their near-surfaces.

Direct comparison of backscatter from analogous Earth and Titan landforms is challenging because of the differences between the radar scattering properties of cryogenic water ice versus silicates, along with possible retro-reflection from low-loss icy and organic sediments. Laboratory measurements of radar backscatter from expected Titan materials at cryogenic temperatures, including measurements of backscatter from low-loss, icy, retro-reflective cobbles, and comparison of these measurements to the backscatter from common rock-forming materials on Earth would contribute greatly to the understanding necessary to directly compare sedimentary deposits on Earth and Titan. However, despite the issues with comparing *absolute* backscatter values, comparison of *relative* backscatter values between Titan and terrestrial fans is currently possible. Specifically, comparison of backscatter from different alluvial fan types on Earth, as well as comparison of the backscatter with distance downfan on these differentially-formed terrestrial fans, can provide insight into fan formation mechanisms at different latitudes on Titan.

Hypotheses

Complex organic aerosols settling out of Titan's atmosphere presumably provide fine-grained material to possible alluvial fans at all latitudes. The equatorial region of Titan is dominated by huge sand seas that are noticeably absent at high latitudes, suggesting that sand-sized particles available for transport could be relatively scarce at high latitudes.

Given the evidence for fine-grained sediment at all latitudes, the lower relative proportion of sand available for transport at high latitudes on Titan, and the effect of fine-grained sediment in promoting debris flows on Earth, we hypothesize that possible alluvial fans at high latitudes on Titan were formed primarily by debris flows. Conversely, given the voluminous presence of unconsolidated sand-sized particles at low latitudes, and the role of sand in promoting sheetfloods, we hypothesize that possible alluvial fans at low and mid latitudes on Titan were formed primarily by sheetfloods.

Data

For the comparison of debris flow and sheetflood fans on Earth with possible alluvial fans on Titan, we used SAR images of Titan collected by the Cassini RADAR instrument and SAR data of alluvial fans located along the Panamint Range in Death Valley, California. The Panamint Range SAR data were gathered by two terrestrial platforms: the Canadian Space Agency's (CSA) Radarsat-1 (RS1) and the Japan Aerospace Exploration Agency and Ministry of Economy Trade and Industry (JAXA/METI) Advanced Land Observation Satellite (ALOS-1). These three SAR datasets are described in greater detail in the following subsections. All datasets were analyzed in linear scale units (as shown in Figures 2.1-2.8 and 2.12-2.14). Where each

radar instrument's radiometric calibration was required to compare measurements, we utilized decibel units (dB) (Figures 2.9-2.11).

Cassini RADAR

The Cassini spacecraft began imaging Titan with its radar instrument in October 2004. The K_u band radar onboard the Cassini spacecraft gathers data in four modes: imaging (SAR), radiometry, scatterometry, and altimetry (Elachi et al., 2004). The SAR imaging mode of this instrument gathers SAR images with five overlapping beams that generate an image swath across the target of interest. Titan SAR swaths are commonly ~4000 to 5000 km long (covering over 100° of longitude and/or latitude), and they range from ~150 km wide at closest approach to ~700 km wide near the start and end of each swath. These data are characterized by a wide range of incidence and polarization angles across each swath (Stofan et al., 2010). The Cassini SAR data products used in this study (Table 2.1) were normalized to 30° incidence angle prior to analysis (see Cassini RADAR Users Guide for details). The possible fans we analyzed display a range of orientations relative to the look direction of the Cassini Radar instrument (mean azimuth angle listed in Table 2.1). We conducted our analysis using these incidence angle-normalized data products in order to account for likely differences in radar return from the possible fans located on different SAR swaths, collected under different viewing geometry conditions. These data are absolutely calibrated to ~1.3 dB (3σ), with smaller relative uncertainties between SAR swaths of ~0.9 dB (3σ) (West et al., 2009). All radar data calibration was performed by the Cassini RADAR science team prior to data release on the Planetary Data System, from which we downloaded the data.

Radarsat-1

RS1 was launched into a Sun-synchronous orbit around Earth in 1994, gathering continuous data for 17 years. The C band radar instrument onboard RS1 operates solely in SAR mode (central wavelength ~5.7 cm, HH polarization), with five different imaging options, allowing for a wide variety of incidence angles (~20 – 50°), spatial resolutions (~10 – 100 m/pixel), and image footprints (~50 – 500 km swath widths) (Raney et al., 1991). The long lifespan of RS1 allowed for a large number of data collection passes over Death Valley, in multiple imaging modes, covering a wide range of viewing geometries. All CSA RS1 data used in this study (gathered between 1997 and 2003) are level 1.0 image products processed by the Alaska Satellite Facility (ASF) and downloaded using ASF's data portal, Vertex, between April 19th and July 13th, 2015 (individual image download dates listed in Table 2.2). ASF is NASA's Distributed Active Archive Center (DAAC) for terrestrial SAR datasets. Conversion of DN values to σ^0, and map projection of RS1 images, was done using ASF's MapReady tool (https://www.asf.alaska.edu/data-tools/mapready/). Our σ^0 measurements were made using eight different standard beam RS1 images (all have ~30 m/pixel resolution). These images span an incidence angle range of ~20 – 40°, for both ascending and descending orbits (Table 2.3). The imaged alluvial fans are semi-perpendicular to the look direction of RS1. RS1 images are absolutely calibrated to ~0.6 dB (3σ) (Luscombe, 2001).

ALOS-1 PALSAR

Complementary to our analysis of the Panamint Range fans using RS1 SAR images, this study utilizes two images gathered by the Phased-Array L-Band SAR (PALSAR) onboard ALOS-1 (Table 2.2) to investigate possible wavelength- and polarization-dependent backscatter effects. JAXA/METI ALOS-1 was launched into a Sun-synchronous orbit in March, 2006 and remained in service until 2011. The SAR onboard ALOS-1 (central wavelength ~23.6 cm, with single, dual, or quad polarization modes) gathered images over a wide range of incidence angles (~10 – 60°), spatial resolutions (10 – 100 m/pixel), and swath widths (30 – 350 km) (Rosenqvist et al., 2007). PALSAR imaged alluvial fans in Death Valley over a wide range of viewing geometries and in all three polarization modes. Both JAXA/METI ALOS-1 PALSAR images used in this study (gathered in 2006 and 2010) are level 1.5 image products processed by ASF and accessed through ASF DAAC using Vertex on September 13th, 2015. We converted the PALSAR images DN values to σ^0, and map projected them using ASF's MapReady tool (https://www.asf.alaska.edu/data-tools/mapready/). The imaged alluvial fans are semi-perpendicular to the look direction of PALSAR. PALSAR swaths are absolutely calibrated to ~0.6 dB (3σ) (Shimada and Tadono, 2010).

Methods

In our analysis of σ^0 for fans on Earth and possible fans on Titan, we first delineated fan boundaries using a GIS software suite. Then we placed profile lines along each fan surface, parallel to the downfan direction. Next, we extracted the DN values for pixels within each fan's boundaries to calculate their mean σ^0, as well as the DN values for the pixels of the profile lines to sample the downfan σ^0 of each fan. Finally, we classified the changes in DN values, or 'slopes,' of the downfan σ^0 profile lines.

Fan boundary delineation

Fan boundaries were delineated in order to define the area from which to extract σ^0 data. Because distinct changes in sediment transport occur at the toes of alluvial fans (*e.g.*, Blair and McPherson, 1994a, 1994b) the bounded fan area was then divided into the large fan surface and the fan toe. We mapped the fan boundaries using vector graphics in Environmental Systems Research Institute's ArcGIS software package. The boundaries of fans on Earth and possible fans on Titan were mapped using the same planform criteria, which include three components (Figure 2.1): (1) a discernable upfan confined (feeder) channel, (2) a central wedge-shaped fan surface, and (3) a downfan termination or fan toe. For both the Panamint fans (Figures 2.2 and 2.3) and possible Titan fans (Figure 2.4), the confined feeder channels and central fan surfaces are relatively radar-bright compared to the fan toes, and all three fan components are typically brighter than the surrounding terrain (but see caveats below). We used the same fan boundary delinations for the Panamint fans in the RS1 and PALSAR images.

Where possible, fan boundaries were placed along visually apparent σ^0 differences or discontinuities between the fans and the surrounding terrain (*i.e.*, bright fans surrounded by relatively darker terrain). In some locations, the putative deposits appear to

have merged, forming elongated, radar-bright landforms suggestive of bajadas. For these locations, we used σ^0 discontinuities within the radar-bright unit and between adjacent confined channels to define the (possible) fan boundaries. Where merged fans are not separated by clear σ^0 discontinuities, we separated them along the approximate mid-point between adjacent confined channels. For some merged fan surfaces, σ^0 discontinuities between the fans become less clear with distance downfan. In these cases, we completed the boundary between the merged fans using the upfan σ^0 discontinuity as a guide (Figure 2.4a). These poorly constrained boundaries are indicated with yellow-black dashed lines on our Titan fan maps (Figure 2.4).

For many of the possible Titan fans, σ^0 remains constant or only gradually decreases with distance downfan from their confined channels, with no apparent terminal boundary, making the location of fan toes more uncertain. In these cases, we placed fan toes where we noted an increase in the gradual reduction of σ^0 with distance downfan, or where a fan surface is proximal to a SAR swath edge (examples shown in Figure 2.4a). Like the uncertain boundaries between adjacent fans, we indicated uncertain terminal fan toes using yellow-black dashed lines on our Titan maps.

For the Titan fans, we used the locations of hypothesized fans presented in Birch et al. (2016) and Radebaugh et al. (2016) to initiate our mapping. For the Death Valley fans, we used the schematic outlines presented in Blair (1999, Fig. 1) as a rough guide for the placement of boundaries. Additionally, we utilized Landsat 7 mosaics (VIS/NIR wavelengths, 15 m/pixel resolution) to aid in the placement of Panamint fan toes.

Sampling downfan σ^0

We placed seven profile lines across the Panamint and possible Titan fan surfaces, sampling σ^0 in the downfan direction for each fan. These seven lines originate at a shared vertex, with one central line and three peripheral lines on either side (Figure 2.1c). For the Titan fans, we assigned the locations of these shared vertices proximal to the estimated location of each fan's apex (*i.e.*, the point where flow capacity and competence decreases rapidly and sediment deposition increases). The shared vertices were placed at the boundary between each delineated fan's confined channel and fan surface, near the location of the Panamint fan apices. Although the locations of the Panamint Range fan apices could be more accurately mapped on the basis of *in situ* field data, we utilized the same planform mapping technique for the placement of profiles lines on those fans as for the Titan fans in order to make our resultant data as comparable as possible.

Calculation of mean σ^0 and downfan σ^0

Once the fan delineation and profile line mapping procedures were completed, we extracted the DN values of the pixels within the fan boundaries and used these data to calculate the mean σ^0 of each Panamint fan and possible Titan fan. We also extracted the pixels along each profile line, sampling σ^0 as a function of distance downfan. The lengths of these profile lines were then normalized to distance downfan, where the shared vertex and the toe represent 0% and 100% distance downfan, respectively. Finally, the seven profile lines for each fan were averaged together, generating one mean σ^0 profile line per fan.

Fan classification using downfan σ^0 profile lines

Our visual observations show that in SAR data, fans commonly exhibit two regions of different brightness: a brighter upfan zone and a darker terminal zone. We therefore split the normalized profile line of each Panamint fan into two regions: fan body and fan terminus. The location of the transition between the two regions was made from a visual assessment of where a noticeable break in the slope of the σ^0 (DN) values occurs, approximately 85% of the distance downfan. For consistency, we used the same relative downfan distances to define the fan body and fan terminus for all of the possible Titan fans (including those with no noticeable break in σ^0 slope).

We modeled the σ^0 slope for each fan body and terminus by fitting a line (see example of line fits in Figure 2.5), and estimated slope uncertainties. We then classified the σ^0 slopes of each fan region: slope values < 2σ of the corresponding slope uncertainty were not considered to be statistically significant, and thus, were classified as 'neutral,' whereas slope values > 2σ were considered to be significant, and thus, classified as 'positive' (increase in σ^0 with downfan distance), or 'negative' (decrease in σ^0 with downfan distance).

We also provide a visual assessment of the shape of each fan terminus, which show clear differences between each fan. Fan termini that display a negligible change in σ^0 are classified as 'small ΔDN,', fan termini that display a moderate change in σ^0 are classified as 'medium ΔDN,' and fan termini that display a large change in σ^0 are classified as 'large ΔDN' (examples shown in Figure 2.6). A summary of our σ^0 profile line classifications is provided in Table 2.3.

Results

Fan boundary delineation

Earth: The delineated fan boundaries (RS1 and PALSAR images, respectively) and the size of their enclosed areas (Tables 2.4 and 2.5) differ somewhat in the descending and ascending orbit images. These differences are primarily due to increased radar foreshortening of the Panamint Range mountains in the descending orbit images that truncates the confined channels and toes of these alluvial fans, reducing their measured areas.

Because we emphasized consistency between our terrestrial and Titan mapping techniques over reproduction of published Death Valley maps, the Panamint Range fan boundaries and areas reported here are somewhat different from those in Blair (1999). Because the seven debris flow fans and seven sheetflood fans are geographically clustered together (see Figures 2.2 and 2.3), the σ^0 values of these two fan types are easy to isolate and compare.

Titan: Fan boundaries are most apparent for the fans in the high-latitude SAR swath T30 and in the low-latitude swath T44 (Figure 2.2a and 2.2e, respectively, areas summarized in Table 2.6). Because of the ambiguity in radar brightness between the fans and the surrounding terrain on the other three SAR swaths, those other boundary delineations include a larger number of uncertain boundaries, in particular for the fan toes

in T03 (Figure 2.2b). Additionally, many of the mid- and low-latitude fans include discontinuous confined channels, separated into segments by radar-dark 'gaps' (for example fans 1 and 2 on TA, Figure 2.2d). Furthermore, some of these same fans include low radar albedo 'patches' on their fan surfaces, or bordering their fan toes (Figure 2.2b and 2.2c, respectively). The pervasiveness of the radar-dark gaps and patches suggests these fans surfaces have been modified by post-depositional processes. Given the coarse spatial resolution of the data, the precision of our mapping of the fan toe locations is likely variable.

Mean σ^0

Earth: The mean σ^0 of each fan is summarized in Tables 2.4 and 2.5 (descending and ascending orbits, respectively). In general, the mean σ^0 of the debris flow fans (in particular, fans 2-5 and 7) are higher than the sheetflood fans (in particular, fans 8-9 and 11-13). This finding is consistent for both terrestrial datasets. Trends in σ^0 are fairly consistent for both RS1 and PALSAR images, with many of the same fans representing the darkest and brightest examples in each RS1 and PALSAR image. As HH polarization is more sensitive to surface scattering (*e.g.*, Cloude et al., 2009 and references therein), the much lower mean σ^0 values of the fans in the HV polarized PALSAR image, compared to the HH polarized PALSAR image (Tables 2.4 and 2.5) are consistent with radar return dominated by mostly pure surface scattering from these fans, with minimal subsurface contributions. Azimuth effects are most likely minimal given that the alluvial fans are quasi-parallel with the illumination direction of the SAR instruments.

Titan: The mean σ^0 of each possible Titan fan is summarized in Table 2.6. In general, mean σ^0 values tend to decrease with increasing latitude, with a significant difference in mean σ^0 between the high-latitude and the mid- and low-latitude fans ($> 2\sigma$). The mean σ^0 values of the low-latitude fans in T44 and T03 are somewhat brighter than the mid-latitude fans in TA and T39, but we do not detect a statistically significant difference in σ^0 between the possible fans in these latitude bands. Furthermore, we do not observe significant intra-swath variations between the mean σ^0 of fans proximal to each other. Azimuth effects could increase backscatter from some of the possible fans on SAR swaths TA, T03, and T39, which are quasi-perpendicular to the illumination direction.

Downfan σ^0

Earth: The downfan σ^0 profile lines for each Panamint fan were generated using RS1 image 55279 (Figure 2.7). These profile lines are generally consistent with the mean σ^0 of each fan, with darker profile lines for the sheetflood fans and brighter profile lines for the debris flow fans. The σ^0 slopes of the fan body and terminus regions, along with the qualitative assessment of the shape of each fan terminus, is summarized in Table 2.7.

Debris flow fans 1, 2, 3, and 4 have fan bodies with positive slopes and large ΔDN, negatively sloped fan termini. Debris flow fan 7 also has a large ΔDN, negatively sloped terminus, but it has a negatively sloped fan body. Debris flow fans 5 and 6 both have medium ΔDN, negatively sloped fan termini, and negative and positive fan bodies, respectively. Sheetflood fans 9, 10, 11, 13, and 14 all have medium ΔDN, negatively

sloped fan termini. The fan bodies of these five sheetflood fans include positive, neutral, and negative slope classifications. Fan 12 has a negatively sloped fan body and a small ΔDN, positively sloped fan terminus. Fan 8 has a negatively sloped fan body and is the only sheetflood fan with a large ΔDN, negatively sloped fan termini.

Titan: We present the profile lines for each possible Titan fan in Figure 2.8. These profile lines are consistent with our results for the mean σ^0 of each fan, with clearly darker profile lines for the high-latitude fans observed in T30, and brighter profile lines for the low- and mid-latitude fans.

The σ^0 slope classifications for each Titan fan body and terminus, as well as the shape of each fan terminus, is summarized in Table 2.8. Most of the fan bodies are classified as either neutral or negative, with a small number of positive slopes (T39 fans 3, 4, and 6). The fan termini are mostly neutral or negatively sloped as well, with two examples of positive slopes (TA fan 2 and T39 fans 4). The shapes of the fan termini display some latitude-dependent differences. The three possible high-latitude fans in T30 have fan termini that are either medium ΔDN or small ΔDN. Five of the seven possible low-latitude fans in swath T03 have small ΔDN fan termini (with one large ΔDN and one medium ΔDN fan termini). Four of the eight mid-latitude possible fans in T39 have large ΔDN fan termini, with the other four displaying medium ΔDN fan termini. The possible mid-latitude and low-latitude fans in TA and T44, respectively, do not display discernable trends in fan terminus shape.

Analysis

Mean σ^0

Earth: Our results indicate that the majority of the Panamint debris flow fans are brighter than the sheetflood fans, for both RS1 and PALSAR descending and ascending orbits, over a wide range of incidence angles. Using their mean σ^0 values, we divided the Panamint fans into three radar brightness groups (from lowest to highest mean σ^0): 'dark,' 'intermediate,' and 'bright' (Table 2.9, Figure 2.9). All fans in the bright group are at least 2σ brighter than all of the seven sheetflood fans. Conversely, all fans in the dark group are at least 2σ darker than all of the seven debris flow fans. All sheetflood and debris flow fans with mean σ^0 separated by less than 2σ are included in the intermediate group.

To further investigate differences in radar brightness between the two fan types, we averaged the mean σ^0 values for the seven debris flow fans and the mean σ^0 values for the seven sheetflood fans together, generating one σ^0 value for each fan type (Table 2.10). The debris flow fans, as a group, are significantly brighter ($> 2\sigma$) than the sheetflood fans in all of the RS1 and PALSAR images, except for RS1 image 22474, where they are $> 1\sigma$ brighter (Figure 2.8). Given the complementary characteristics of the RS1 and PALSAR data, these results show that the debris flow fans are clearly brighter than the sheetflood fans over a range of incidence angles (~20 – 40°) for both descending and ascending orbit images gathered at both C band (λ ~5.7 cm) and L band (λ ~23.6 cm) wavelengths.

The SAR data characteristics influence the analysis results. Our analysis of the mean σ^0 for each fan type indicates that the brightness difference between the debris flow and sheetflood fans increases with incidence angle (Table 12.0, Figure 2.10). Furthermore, the brightness difference between these fan types increases with wavelength, with 1 to 5σ difference in σ^0 between the fan types in the eight RS1 images and > 6σ difference in σ^0 for the two PALSAR images. Both fan types are dramatically darker in the HV polarized PALSAR image compared to the other PALSAR and RS1 images (all HH polarized). Given that vertically polarized backscatter is dominated by volume scattering (*e.g.*, Cloude, 2009), the radar signal returned from both debris flow and sheetflood fans along the Panamint Range is likely dominated by surface scattering, with minimal subsurface contributions.

Titan: Our results indicate that the possible high-latitude fans in T30 are significantly darker than the mid- and possible low-latitude fans in the other four Cassini SAR swaths. To further investigate differences in radar brightness between the possible Titan fans, as a function of latitude, we averaged all the fans in each latitude zone together (high-northern, mid-northern, low-northern, low-southern, mid-southern latitudes), generating one mean σ^0 value per latitude zone (Table 2.11). The mean σ^0 value for the possible high-latitude fans in T30 is significantly darker (> 2σ) than the mean σ^0 for the other four latitude zones. The mean σ^0 of the equatorial possible fans in TA is > 1σ brighter than the possible mid-latitude fans in swaths T03 and T39 (Figure 2.11). Consequently, both the mean σ^0 of individual fans, and the mean σ^0 of the latitude-aggregated fans demonstrate clear latitudinal trends in radar brightness, with relatively dark near-polar fans and bright mid-latitude and equatorial fans. Given the small range in the effective dielectric constant for materials at all latitudes on Titan (*e.g.*, Janssen et al., 2016), the clear latitudinal differences in σ^0 indicates that possible fans at high latitudes have relatively smooth surfaces compared to the brighter, and presumably rougher, surfaces of fans at low and mid latitudes. This difference in roughness suggests possible fans at high latitudes are composed of sediments with a more homogenous range in grain sizes compared to the sediments forming possible fans at low and mid latitudes.

The dark near-polar fans on Titan show significantly greater radar return than do any of the Panamint fans we have analyzed. Whereas both the Titan and terrestrial materials produce surface scattering, backscatter from possible Titan fans is likely enhanced by volume scattering and retro-reflective additions (Janssen et al., 2009; Le Gall et al., 2010). Volume scattering and retro-reflective effects are absent from silicate-dominated, radar-rough surfaces on Earth (Campbell et al., 2002 and references therein). Thus, the discrepancy between the absolute mean σ^0 values of Panamint fans and possible Titan fans likely results from enhanced volume scattering and retro-reflectors on the possible fan surfaces.

Downfan σ^0

Earth: Similar to the mean σ^0 trends described in the preceding section, the Panamint profile lines demonstrate clear differences in downfan σ^0 between the two fan types, with darker sheetflood and brighter debris flow profile lines. The slope and termini shape classifications divide the Panamint fans in a similar fashion to the mean σ^0 radar

brightness classifications (bright, intermediate, dark). Aggregating the classifications of the mean σ^0 radar brightness groups and the profile line slope/shape groups demonstrates that fans 2, 3, and 4 represent a debris flow fan endmember for both analyses. Additionally, fans 11 and 13 represent a sheetflood fan endmember. Fans 5 and 7 are similar to the debris flow endmember, but lack the positively sloped fan bodies and large ΔDN fan termini that are characteristic of this group. Although fan 1 (debris flow) and fan 8 (sheetflood) have large ΔDN, negatively sloped termini, their mean σ^0 are consistently lower than the debris flow endmember group. The classification of fans 6, 9, 10, 12 and 14 is more ambiguous, but in terms of mean σ^0, they are more similar to the sheetflood group than the debris flow group.

In order to isolate diagnostic differences in downfan σ^0 between the two fan types, we combined the profile lines of the seven debris flow and seven sheetflood fans into one mean profile line per fan type (Figure 2.12). Similar to the σ^0 of individual fan profile lines, the mean debris flow profile line is brighter than the mean sheetflood profile line. We classified the fan body and termini slopes of these two mean fan type profile lines using the same techniques utilized for the individual fan profile lines (Table 2.12). The slope classification of the mean debris flow fan body is positive, and the sheetflood fan body is negative. Both mean fan type profile lines display negatively sloped fan termini. However, the shape of the mean debris flow profile line terminus is large ΔDN, whereas the fan terminus of the mean sheetflood profile line is medium ΔDN. This mean fan type profile line analysis suggests that positive fan bodies with large ΔDN, negatively sloped fan termini are representative of Panamint debris flow fans, and negative fan surfaces with medium ΔDN, negatively sloped fan termini are representative of Panamint sheetflood fans.

Titan: As in the mean fan type profile line analysis, we combined the profile lines for all of the possible Titan fans into one mean profile line per latitude zone (high-northern, mid-northern, low-northern, low-southern, and mid-southern latitudes) (Figure 2.13). The latitude-aggregated profile lines display the same relative brightness as the profile lines for individual possible fans, with a clearly darker high-northern profile line compared to the other four latitude zones. We classified the fan body and terminus slopes of these five latitude-aggregated profile lines using the same techniques utilized for the individual possible fan profile lines (Table 2.13). Four of the five latitude-aggregated profile lines have negative fan bodies (low-northern is neutral), and three of the five latitude-aggregated profile lines have negative fan termini (high- and mid-northern are neutral). Additionally, the shapes of the latitude-aggregated profile lines' fan termini are medium ΔDN (high-northern), small ΔDN (mid-northern, low-northern), and large ΔDN (low-southern, mid-southern). Thus, by aggregating the possible fan profile lines, trends in σ^0 slope for each latitude zone become clearer. For example, four of the eight possible mid-southern fans in T39 have profile lines with large ΔDN, negatively sloped termini, and their latitude-aggregated profile line also has a large ΔDN, negatively sloped fan terminus.

Discussion

Sedimentological interpretation of relative σ^0 values for Panamint fans

The debris flow fans along the Panamint Range are dominated by poorly-sorted, clast-rich lobes, some of which extend nearly to their fan toes. These clast-rich lobes are characterized by large amounts of coarse sediments embedded in a clay-rich matrix, including boulders that are transported along the front and on top of debris flows (Blair and McPherson, 1994a, 1994b; Blair, 1999). Panamint sheetflood fans, on the other hand, are mantled by well-sorted layers of stratified sediment. Like other landforms developed by fluid-gravity flows, sheetflood fans exhibit relatively more downfan fining of sediments than features formed by sediment-gravity flows like debris flow fans. Consequently, the coarsest fraction of sediments transported in sheetfloods is commonly deposited on the upfan surfaces of sheetflood fans, where flow capacity and competence begin to decrease rapidly. Because of this downfan fining, sheetflood fans commonly develop distal skirts of fine-grained sand proximal to their fan toes (*e.g.*, Blair and McPherson, 1994a, 1994b).

The radar reflectivities of these two fan types are consistent with their disparate sedimentary surfaces. As a group, Panamint debris flow fans have higher mean σ^0 values than sheetflood fans. These higher σ^0 values are consistent with rough surfaces mantled by poorly-sorted, coarse sediments that generate backscatter from surface roughness elements of a similar size to the radar wavelength. Conversely, the more well-sorted and finer-grained sediments mantling Panamint sheetflood fans, being mantled by roughness elements much smaller than radar wavelength, generate less surface scattering. Furthermore, the σ^0 values of most of the Panamint debris flow fans slightly increase in the downfan direction before decreasing rapidly toward their fan toes. Using the terminology from Table 2.3, this group of debris flow fans is represented by a σ^0 profile line with a positively sloped fan body and a large ΔDN, negatively sloped fan terminus. These changes in downfan σ^0 are consistent with clast-rich debris flow lobes, extending nearly to their fan toes, where they abut clast-poor lobes that are relatively smooth and radar-dark. In contrast, most of the sheetflood fans display a slight reduction in downfan σ^0 values across their surfaces, which then decreases steadily toward their fan toes. Using the terminology from Table 2.3, this group of sheetflood fans are represented by a σ^0 profile line with a negatively sloped fan body and a medium ΔDN, negatively sloped fan terminus. This gradual reduction in downfan σ^0 is consistent with the downfan fining of sediments on sheetflood fan surfaces. Thus, our σ^0 results and analyses clearly reflect the sedimentological environments of these two fan types.

Post-depositional salt weathering aids in breaking down coarse sediments at the toes of Death Valley alluvial fans (Goudie and Day, 1980). Such salt-driven sediment disintegration could be steepening the fan termini of both debris flow and sheetflood fan σ^0 profile lines. It is unclear whether salt weathering occurs on Titan, nor whether it would breakdown sediments as efficiently as in Death Valley.

Comparing relative σ^0 values for Panamint fans and possible Titan fans

Comparison of our mean σ^0 analyses for the Panamint Range fans and possible Titan fans shows that the possible low-latitude fans are more similar to debris flow-dominated fans, and the relatively dark high-latitude deposits are more similar to sheetflood-dominated fans. Additionally, comparison of the mean Panamint fan type and Cassini latitude-aggregated σ^0 profile lines reveals similarities in downfan σ^0 for the Panamint and Titan fans. Both the high northern latitude σ^0 profile line for the Titan fans and the mean σ^0 profile line for the Panamint sheetflood fans have negatively sloped fan bodies and medium ΔDN fan termini, with neutral and negative slopes, respectively. The low- and mid-southern latitude σ^0 profile lines have large ΔDN, negatively sloped fan termini, analogous to the mean debris flow σ^0 profile line. However, the Panamint debris flow fan σ^0 profile line has a positively sloped fan body, whereas the low- and mid-southern latitude σ^0 profile lines have negatively sloped fan bodies.

Thus, both our mean σ^0 and σ^0 slope analyses show that the possible high-latitude fans are more similar to Panamint sheetflood fans, whereas the possible low- and mid-southern latitude fans are more similar to Panamint debris flow fans. We hypothesized that sheetfloods dominate possible fan formation at low and mid latitudes, and debris flows dominate possible fan formation at high latitudes. Our findings show an opposite relationship between latitude and the dominant fan formation mechanism. Thus, our hypotheses are not supported by our analyses.

Implications

In the following subsections, we offer six possible reasons to explain why our results and analyses do not support our hypotheses. (1) Enhanced sedimentation and limited availability of coarse-grained sediments at high latitudes could spur alluvial fan formation via clast-poor debris flows (*8.3.1*). (2) Post-depositional processes like aeolian winnowing could enhance retro-reflection from coarse-grained pavement layers, masking sheetflood deposits on Titan (*8.3.2*). (3) Sand-sized grains are relatively scarce in low- and mid-latitude possible fan catchments (*8.3.3*). (4) Titan's bedrock composition is different at different latitudes, promoting possible fan formation by debris flows at low and mid latitudes and sheetfloods at high latitudes (*8.3.4*). (5) Alluvial fan formation processes could operate differently on Titan compared to Earth (*8.3.5*). (6) The possible Titan fans are not alluvial fans and instead are landforms formed by non-alluvial processes (*8.3.6*).

Radar-dark debris flow deposits at high latitudes on Titan

The cobble-sized sediments that have been imaged (Tomasko et al., 2005), and inferred (Le Gall et al., 2010) at low latitudes could be relatively scarce at high latitudes. Examples of crenulated terrains, isolated ridges, and other high standing, radar-bright terrains, similar in morphology and radar texture to Xanadu, are fairly common at low latitudes on Titan (Lopes et al., 2010). However, far fewer examples of these radar-bright 'basement outcrops' are observed at high latitudes (Moore et al., 2014), and radar-bright crater rims are also absent from high latitudes (Neish and Lorenz, 2014). Additionally, Titan's poles are topographically depressed by ~1 km compared to low- and mid-latitude

regions (Zebker et al., 2009). The lack of basement outcrops and depressed topography suggest that high-latitude landscapes have undergone enhanced sedimentation, as unconsolidated sediment, from low- and mid-latitude crustal sources as well as atmospheric aerosols, migrated poleward (Moore et al., 2014; Lopes et al., 2016). This enhanced sedimentation could have buried radar-bright basement outcrops, reducing the availability of coarse-grained, transportable sediments in high-latitude possible fan catchments. Consequently, the surfaces of possible high-latitude fans could be mantled by thick deposits of fine-grained material, leading to sediment transport dominated by clast-poor debris flows, perhaps similar to mudflows on Earth (*e.g.*, Blair and McPherson, 1994b), although it is unclear whether clay-sized organic aerosols on Titan expand in the presence of liquid hydrocarbons like silicate-rich clays do in water on Earth. Because our terrestrial analog site does not include alluvial fans dominated by clast-poor debris flows, our analysis techniques are not sensitive to this mud-dominated fan type if present on Titan. In this scenario, our hypotheses are correct, but the high-latitude debris flows are clast poor.

Radar-bright sheetflood deposits at low and mid latitudes on Titan

Differential radar response to terrestrial and Titan materials could also explain our results. Retro-reflection effects have been hypothesized for fluvial cobbles on Titan (Le Gall et al., 2010), but such effects are likely absent for silicate materials on Earth. It has been inferred that low-latitude, radar-bright fluvial landforms are mantled by gravel-rich lag deposits, where finer-grained material has been removed by aeolian winnowing and is incorporated into equatorial sand seas (Moore et al., 2014; Howard et al., 2016). The resulting lag of low-loss pebbles on the possible fan surfaces could provide an ideal substrate for retro-reflection.

Additionally, gravel-rich lag deposits could armor possible fan surfaces, forming a pavement layer, which makes fluvial entrainment and transport of substrate sediments in response to atmospheric precipitation a relatively infrequent and inefficient process (Howard et al., 2016). Consequently, post-depositional winnowing of sand-sized sediments from the possible fans could mask possible fan formation by sheetfloods because of enhanced retro-reflection from gravel- and cobble-rich pavements. In this scenario, as in the previous, our hypotheses are correct, but the radar dark signature has been modified by post-depositional processes.

Sand unavailable in low- and mid-latitude possible fan catchments

Possible low- and mid-latitude fans are located adjacent to radar-bright basement outcrops and crater rims, which must have been high-standing relative to possible fan deposits at the time of formation. This relative elevation difference would imply that the fan catchments are sedimentologically disconnected from the equatorial sand seas. Consequently, sediments available for transport in low and mid-latitude possible fan catchments could be dominated by coarse clasts, sourced by mass-wasting of materials off highland slopes, along with clay-sized sediments, sourced from globally distributed aerosols. The presence of unconsolidated coarse-grained and clay-sized sediments in these possible fan catchments could provide ideal conditions for clast-rich debris flows.

Along with this inferred geographic separation, possible low- and mid-latitude fans could be temporally separated from equatorial sand seas. Numerical modeling suggests that Titan's climate at low and mid latitudes has progressively become more arid (Rannou et al., 2006; Mitchell et al., 2008). Geomorphic mapping demonstrates that there are no unambiguous examples where dunes are cross cut by fluvial valleys (Lopes et al., 2010; Moore et al., 2014). Furthermore, the presence of low albedo 'gaps' and 'patches' on some of the low- and mid-latitude possible fans (Figure 2.4) could suggest that these fans' surfaces have been reworked, perhaps by aeolian processes. Therefore, low- and mid-latitude deposits could be paleo-features that formed during a wetter period in Titan's history. In this scenario, equatorial sand was relatively scarce in possible low- and mid-latitude fan catchments at the time of their formation.

Variation in bedrock composition as a function of latitude on Titan

Possible fan formation mechanisms on Titan may be influenced by the composition of the bedrock located at different latitudes. Combination of water ice, hydrocarbons, and nitriles likely varies across different regions (*e.g.*, Soderblom et al., 2009). Analogous to the different catchment substrates for the Panamint fan types, the composition of the bedrock underlying the possible fans may be different at different latitudes on Titan. In this scenario, the substrate material underlying low- and mid-latitude possible fan catchments is dominated by "sedimentary rocks" that weather readily into clay-sized particles, similar to debris flow fan catchments. In contrast, high latitude possible fan catchments would be underlain by material that weathers readily into sand-sized particles, similar to the sandstones underlying Panamint sheetflood fan catchments.

Alluvial fan formation processes different on Titan

Sedimentological landforms likely develop differently on other planetary bodies. For example, numerical modeling of paleo-delta formation on Mars suggests that relatively more sediment is transported beyond the mouth of Martian rivers compared to Earth rivers due to the lower gravity on Mars (9.8 m s^{-2} and 3.7 m s^{-2} for Earth and Mars, respectively) (Hoke et al., 2014). Consequently, Martian deltas could form more slowly than similarly-sized deltas on Earth because Martian delta deposition zones are more spatially extended in the low gravity environment of Mars.

Likewise, conditions on Titan likely increase alluvial sediment dispersion. Numerical modeling suggests that for a given flow depth, larger icy sediments can be entrained and transported in liquid hydrocarbon flows under the low gravity of Titan compared to silicate sediments in liquid water on Earth (Burr et al., 2006). Furthermore, the presence of large amounts of fine-grained aerosols in hydrocarbon flows could decrease settling velocities and increase transport of coarse sediments (Burr et al., 2006). Thus, both the formation timescales and sizes of alluvial fans on Titan may be greater than on Earth. The possible fans investigated in this study are areally larger than the Panamint alluvial fans, and are closer in areal extent to large distributary fluvial systems (Hartley et al., 2010; Weissmann et al., 2010), including terrestrial megafans formed via

fluvial processes (*e.g.*, Shukla et al., 2001; Arzani et al., 2012) and terrestrial submarine fans formed by turbidity flows (Shanmugam, 2016 and references therein).

The likely extensive areal distribution of sediments under Titan gravity could help explain why some of the possible fans do not have well-defined fan toes, and instead, exhibit gradual reductions in σ^0 along their fan termini (for examples, see profile lines for T03 possible fans 1, 2, 3, 4, 5, and 7 in Figure 2.8 part 2). This steady reduction in fan termini σ^0 could be the result of longer sediment transport distances, extending the terminal boundaries of possible fans on Titan. In this scenario, our hypotheses are correct, but not supported by the data, because of the spatially extended sedimentation processes that occur under Titan conditions.

Possible Titan fans not alluvial fans

The Cassini RADAR instrument has provided tantalizing views of a wide range of geomorphic landforms on Titan's surface. However, the coarse spatial resolution of this dataset (~350 – 1700 m/pixel) obscures local scale features (~10's of meters in size). It has been suggested that the coarse resolution of the Cassini SAR dataset could mislead assessments of landforms on Titan's surface, in particular, the identification of cryovolcanic features (Moore and Pappalardo, 2011). An important consideration for geomorphic analysis of landforms observed in remotely sensed datasets is equifinality, where landforms that look similar are, in fact, formed by different processes (Zimbelman, 2001). For example, analysis of Mariner 6 and 7 images of Olympus Mons led to the origin conclusion that this bright, > 500 km diameter feature with a bright central region was a large impact basin (Leighton et al., 1969). Subsequent imaging campaigns at higher resolutions revealed that Olympus Mons was not an impact feature but the largest volcano in the Solar System. By analogy to the early period of Martian image analysis, many of the landforms observed on Titan, including possible alluvial fans, could be misidentified due to the coarse resolution of the Cassini SAR dataset.

On Earth, distributary fluvial systems can readily generate non-alluvial, fan-shaped deposits (Nichols and Fisher et al., 2007; Hartley et al., 2010; Weissmann et al., 2010). These features are characterized by rivers that exit confining valleys as a radial network of channels (Weismann et al., 2010). The gross-scale morphologies of these features are similar to alluvial fans, and they can be difficult to distinguish from one another in low resolution datasets. As an example of how coarse resolution data can obscure landforms, we provide an RS1 image of the Panamint fans at both its native resolution (30 m/pixel) and at the highest Cassini SAR-equivalent resolution (350 m/pixel), with speckle noise added (Figure 2.14). The Panamint alluvial fans are readily identifiable in the native resolution SAR image (Figure 2.14a, 2.14b), but are much harder to discern from the surrounding landscape at Cassini SAR-equivalent resolution (Figure 2.14c, 2.14d). Consequently, the low resolution of the Cassini SAR dataset likely reduces the accuracy of landform assessment on Titan. In this scenario, the possible fans are not alluvial fans, and instead, are fan-shaped features formed by non-alluvial processes, such as those that form distributary fluvial systems on Earth.

Summary and Future Work

We used measurements of mean σ^0 and changes in downfan σ^0 for terrestrial alluvial fans along the Panamint Range in Death Valley, CA, to infer possible fan formation mechanisms at different latitudes on Titan. We found that Panamint fans formed by debris flows are significantly brighter those formed by sheetfloods, over a wide range of incidence angles (~20 – 45°), for both descending and ascending orbits at C and L band wavelengths (λ ~5.7 and 23.6 cm, respectively), and for both HH and HV polarizations. The σ^0 profile lines for most of the Panamint debris flow fans include positive fan bodies and large ΔDN, negatively sloped fan termini, whereas the Panamint sheetflood fans are mostly characterized by negative fan bodies and medium ΔDN, negatively sloped fan termini. Furthermore, the mean sheetflood fan σ^0 profile line has a negative fan body and a medium ΔDN, negatively sloped fan terminus and the mean debris flow fan σ^0 profile line has a positive fan body and a large ΔDN, negatively sloped terminus, consistent with many of the individual σ^0 profile lines for these two fan types.

Possible Titan fans located at low and mid latitudes are significantly brighter than at high latitudes. These clear latitudinal differences in σ^0 suggest a smaller range in grain sizes for sediments in possible fans at high latitudes compared to sediments in possible fans at low and mid latitudes. The σ^0 profile lines of the possible Titan fans display a wide range of σ^0 slope classifications for their fan body and terminus regions, with some apparent latitudinal trends. Possible low- and mid-latitude fans include numerous examples of large ΔDN fan termini, in particular fans at mid-southern latitudes, whereas all of the possible high-latitude fans have medium ΔDN or small ΔDN fan termini. The mean, latitude-aggregated σ^0 profile lines more clearly reveal latitude-dependent trends than the individual σ^0 profile lines. The northern high-latitude σ^0 profile line has a medium ΔDN, neutral terminus, the northern mid- and low-latitude σ^0 profile lines have small ΔDN, neutral and negatively sloped termini, and the southern low- and mid-latitude σ^0 profile lines have large ΔDN, negatively sloped termini. Thus, the mean σ^0 measurements and σ^0 profile line analyses demonstrate that high-latitude possible fans are more similar to Panamint sheetflood fans, whereas low- and mid-latitude possible fans are more similar to Panamint debris flow fans. These conclusions are not consistent with our hypotheses that possible fans at low latitudes are formed primarily by sheetfloods, whereas possible fans at high latitudes are formed primarily by debris flows.

We presented multiple explanations for why our results and analyses do not support our hypotheses, including: (1) radar-dark debris flow deposits at high latitudes on Titan, (2) radar-bright sheetflood deposits at low and mid latitudes on Titan (3) lack of sand-sized sediments where/when low- and mid-latitude fans formed, (4) composition of bedrock different at different latitudes on Titan, (5) more spatially extended alluvial deposits than those that develop on Earth due to the lower Titan gravity, and (6) formation of the deposits by non-alluvial, fluvial processes. Future work that explores the radar reflectivities of clast-poor debris flows, as well as fan-shaped, non-alluvial landforms on Earth (like fluvial fans and distributary networks), could provide additional ground-truth for analysis of Titan data. Modeling of sedimentary deposition from hydrocarbon flows under Titan gravity could shed light on the surface sedimentology and stratigraphy of alluvial deposits. Subsequent studies that correlate radar return with the

sedimentology of terrestrial alluvial fans would provide further data to understand the radar return in terms of the sedimentology of possible Titan fans. Reanalysis of the possible fans using despeckled images (Lucas et al., 2014) could shed light on whether the possible fans were formed by alluvial processes or other geologic mechanisms. Lastly, new modeling studies that quantify and analyze the radar backscattering properties of cryogenic water ice cobbles (*e.g.*, Le Gall et al., 2010) and silicates would support inter-comparison of these materials.

References

Arzani, N., 2012. Catchment lithology as a major control on alluvial megafan development, Kohrud Mountain range, central Iran. *Earth Surface Processes and Landforms*, *37* (7), p.726-740.

Baker, V., Kochel, R.C. and Patton, P.C., 1988. Flood geomorphology. In *Wiley-Interscience*.

Barnes, J.W., Brown, R.H., Soderblom, L., Buratti, B.J., Sotin, C., Rodriguez, S., Le Mouèlic, S., Baines, K.H., Clark, R. and Nicholson, P., 2007. Global-scale surface spectral variations on Titan seen from Cassini/VIMS. *Icarus*, *186* (1), p.242-258.

Barnes, J.W., Brown, R.H., Soderblom, L., Sotin, C., Le Mouèlic, S., Rodriguez, S., Jaumann, R., Beyer, R.A., Buratti, B.J., Pitman, K. and Baines, K.H., 2008. Spectroscopy, morphometry, and photoclinometry of Titan's dunefields from Cassini/VIMS. *Icarus*, *195* (1), p.400-414.

Birch, S.P.D., Hayes, A.G., Howard, A.D., Moore, J.M. and Radebaugh, J., 2016. Alluvial Fan Morphology, distribution and formation on Titan. *Icarus*. *270*, p.238-247.

Black, G.J., Campbell, D.B. and Ostro, S.J., 2001. Icy Galilean satellites: 70 cm radar results from Arecibo. *Icarus*, *151* (2), p.160-166.

Blair, T.C., 1999. Cause of dominance by sheetflood vs. debris-flow processes on two adjoining alluvial fans, Death Valley, California.*Sedimentology*, *46* (6), p.1015-1028.

Blair, T.C. and McPherson, J.G., 1994a. Alluvial fan processes and forms. In *Geomorphology of desert environments*, p. 354-402. Springer, Netherlands.

Blair, T.C. and McPherson, J.G., 1994b. Alluvial fans and their natural distinction from rivers based on morphology, hydraulic processes, sedimentary processes, and facies assemblages. *Journal of sedimentary research*, *64* (3).

Boothroyd, J.C. and Nummedal, D., 1978. Proglacial braided outwash: a model for humid alluvial-fan deposits. In *Fluvial Geomorphology*, p.641-688. Canadian Society of Petroleum Geologists.

Brown, M.E., Bouchez, A.H. and Griffith, C.A., 2002. Direct detection of variable tropospheric clouds near Titan's south pole. *Nature*, *420* (6917), p.795-797.

Burr, D.M., Emery, J.P., Lorenz, R.D., Collins, G.C. and Carling, P.A., 2006. Sediment transport by liquid surficial flow: Application to Titan. *Icarus*, *181* (1), p.235-242.

Burr, D.M., Jacobsen, R.E., Roth, D.L., Phillips, C.B., Mitchell, K.L. and Viola, D., 2009. Fluvial network analysis on Titan: Evidence for subsurface structures and west-to-east wind flow, southwestern Xanadu. *Geophysical Research Letters*, *36* (22).

Burr, D.M., Perron, J.T., Lamb, M.P., Irwin, R.P., Collins, G.C., Howard, A.D., Sklar, L.S., Moore, J.M., Ádámkovics, M., Baker, V.R. and Drummond, S.A., 2013a. Fluvial features on Titan: Insights from morphology and modeling. *Geological Society of America Bulletin*, *125* (3-4), p.299-321.

Burr, D.M., Drummond, S.A., Cartwright, R., Black, B.A. and Perron, J.T., 2013b. Morphology of fluvial networks on Titan: Evidence for structural control. *Icarus*, *226* (1), p.742-759.

Bull, W.B., 1972. Recognition of alluvial fan deposits in the stratigraphic record. *Society of Economic Paleontologists and Mineralogists* (SP16).

Bull, W.B., 1977. The alluvial-fan environment. *Progress in physical geography*, *1* (2), p.222-270.

Bull, W.B., 1991. Geomorphic responses to climatic change. Oxford University Press, New York.

Campbell, B.A., 2002. Radar remote sensing of planetary surfaces. Cambridge University Press, New York.

Cartwright, R., Clayton, J.A. and Kirk, R.L., 2011. Channel morphometry, sediment transport, and implications for tectonic activity and surficial ages of Titan basins. *Icarus*, *214* (2), p.561-570.

Clark, R.N., Curchin, J.M., Barnes, J.W., Jaumann, R., Soderblom, L., Cruikshank, D.P., Brown, R.H., Rodriguez, S., Lunine, J., Stephan, K. and Hoefen, T.M., 2010. Detection and mapping of hydrocarbon deposits on Titan. *Journal of Geophysical Research: Planets*, *115* (E10).

Cloude, S., 2009. *Polarisation: applications in remote sensing*. OUP, Oxford.

Collins, G.C., Polito, P.J., Litwin, K.L. and Sklar, L.S., 2011, March. Resistance of water ice to fluvial abrasion and implications for erosion on Titan. In *Lunar and Planetary Science Conference*, Vol. 42, p. 2781.

Cornet, T., Bourgeois, O., Le Mouélic, S., Rodriguez, S., Gonzalez, T.L., Sotin, C., Tobie, G., Fleurant, C., Barnes, J.W., Brown, R.H. and Baines, K.H., 2012. Geomorphological significance of Ontario Lacus on Titan: Integrated interpretation of Cassini VIMS, ISS and RADAR data and comparison with the Etosha Pan (Namibia). *Icarus*, *218* (2), p.788-806.

Costa, J.E., 1988. Rheologic, geomorphic, and sedimentologic differentiation of water floods, hyperconcentrated flows, and debris flows. In *Flood Geomorphology.* John Wiley & Sons New York. 1988. p 113-122.

Craddock, R.A. and Howard, A.D., 2002. The case for rainfall on a warm, wet early Mars. *Journal of Geophysical Research: Planets*, *107* (E11).

Crouvi, O., Ben-Dor, E., Beyth, M., Avigad, D. and Amit, R., 2006. Quantitative mapping of arid alluvial fan surfaces using field spectrometer and hyperspectral remote sensing. *Remote sensing of environment*, *104* (1), p.103-117.

Davidson, S.K., Hartley, A.J., Weissmann, G.S., Nichols, G.J. and Scuderi, L.A., 2013. Geomorphic elements on modern distributive fluvial systems. *Geomorphology*, *180*, p.82-95.

Denny, C.S., 1965. Alluvial fans in the Death Valley region, California and Nevada (No. 466). US Govt. Print. Off.

Elachi, C., Allison, M.D., Borgarelli, L., Encrenaz, P., Im, E., Janssen, M.A., Johnson, W.T.K., Kirk, R.L., Lorenz, R.D., Lunine, J.I. and Muhleman, D.O., 2004. Radar: the Cassini Titan radar mapper. *Space Science Reviews*, *115* (1-4), p.71-110.

Elachi, C., Wall, S., Allison, M., Anderson, Y., Boehmer, R., Callahan, P., Encrenaz, P., Flamini, E., Franceschetti, G., Gim, Y. and Hamilton, G., 2005. Cassini radar views the surface of Titan. *Science*, *308* (5724), p.970-974.

Farr, T.G. and Chadwick, O.A., 1996. Geomorphic processes and remote sensing signatures of alluvial fans in the Kun Lun Mountains, China. *Journal of Geophysical Research: Planets*, *101* (E10), p.23091-23100.

Goudie, A.S. and Day, M.J., 1980. Disintegration of fan sediments in Death Valley, California, by salt weathering. *Physical Geography*, *1* (2), p.126-137.

Goudie, A.S., 2013. Arid and semi-arid geomorphology. Cambridge University Press, New York, p.42-113.

Graves, S.D.B., McKay, C.P., Griffith, C.A., Ferri, F. and Fulchignoni, M., 2008. Rain and hail can reach the surface of Titan. *Planetary and Space Science*, *56* (3), p.346-357.

Hardgrove, C., Moersch, J. and Whisner, S., 2010. Thermal imaging of sedimentary features on alluvial fans. *Planetary and Space Science*, *58* (4), p.482-508.

Hartley, A.J., Weissmann, G.S., Nichols, G.J. and Warwick, G.L., 2010. Large distributive fluvial systems: characteristics, distribution, and controls on development. *Journal of Sedimentary Research*, *80* (2), p.167-183.

Howard, A.D., Breton, S. and Moore, J.M., 2016. Formation of gravel pavements during fluvial erosion as an explanation for persistence of ancient cratered terrain on Titan and Mars. *Icarus*, *270*, p.100-113.

Iverson, R.M., 2005. Debris-flow mechanics. In *Debris-flow hazards and related phenomena*. Springer, Berlin Heidelberg.

Janssen, M.A., Lorenz, R.D., West, R., Paganelli, F., Lopes, R.M., Kirk, R.L., Elachi, C., Wall, S.D., Johnson, W.T.K., Anderson, Y. and Boehmer, R.A., 2009. Titan's surface at 2.2-cm wavelength imaged by the Cassini RADAR radiometer: Calibration and first results. *Icarus*, *200* (1), p.222-239.

Janssen, M.A., Le Gall, A. and Wye, L.C., 2011. Anomalous radar backscatter from Titan's surface?. *Icarus*, *212* (1), p.321-328.

Janssen, M.A., Le Gall, A., Lopes, R.M., Lorenz, R.D., Malaska, M.J., Hayes, A.G., Neish, C.D., Solomonidou, A., Mitchell, K.L., Radebaugh, J., Keihm, S.J., Choukroun, M., Leyrat, C., Encrenaz, P.J., Mastrogiuseppe, M., 2016. Titan's surface at 2.18-cm wavelength imaged by Cassini RADAR radiometer: Results and interpretations through the first ten years of observation. *Icarus*, *270*, p.443-459.

Johnson, A.M., 1970. Physical processes in geology: A method for interpretation of natural phenomena; intrusions in igneous rocks, fractures, and folds, flow of debris and ic*e*. Freeman, Cooper.

Kesel, R.H. and Spicer, B.E., 1985. Geomorphologic relationships and ages of soils on alluvial fans in the Rio General Valley, Costa Rica. *Catena*, *12* (1), p.149-166.

Kochel, R.C., 1990. Humid fans of the Appalachian Mountains. Alluvial Fans: A Field Approach. Wiley, New York, pp.109-129.

Kostaschuk, R.A., MacDonald, G.M. and Putnam, P.E., 1986. Depositional process and alluvial fan-drainage basin morphometric relationships near Banff, Alberta, Canada. *Earth Surface Processes and Landforms*, *11* (5), p.471-484.

Langhans, M.H., Jaumann, R., Stephan, K., Brown, R.H., Buratti, B.J., Clark, R.N., Baines, K.H., Nicholson, P.D., Lorenz, R.D., Soderblom, L.A. and Soderblom, J.M., 2012. Titan's fluvial valleys: Morphology, distribution, and spectral properties. *Planetary and Space Science*, *60* (1), p.34-51.

Le Gall, A., Janssen, M.A., Paillou, P., Lorenz, R.D. and Wall, S.D., 2010. Radar-bright channels on Titan. *Icarus*, *207* (2), p.948-958.

Le Gall, A., Janssen, M.A., Wye, L.C., Hayes, A.G., Radebaugh, J., Savage, C., Zebker, H., Lorenz, R.D., Lunine, J.I., Kirk, R.L. and Lopes, R.M.C., 2011. Cassini SAR, radiometry, scatterometry and altimetry observations of Titan's dune fields. *Icarus*, *213* (2), p.608-624.

Le Gall, A., Hayes, A.G., Ewing, R., Janssen, M.A., Radebaugh, J., Savage, C. and Encrenaz, P., 2012. Latitudinal and altitudinal controls of Titan's dune field morphometry. *Icarus*, *217* (1), p.231-242.

Leighton, R.B., Horowitz, N.H., Murray, B.C., Sharp, R.P., Herriman, A.G., Young, A.T., Smith, B.A., Davies, M.E. and Leovy, C.B., 1969. Mariner 6 television pictures: First report. *Science*, *165* (3894), p.685-690.

Litwin, K.L., Zygielbaum, B.R., Polito, P.J., Sklar, L.S. and Collins, G.C., 2012. Influence of temperature, composition, and grain size on the tensile failure of water ice: Implications for erosion on Titan. *Journal of Geophysical Research: Planets*, *117* (E8).

Lopes, R.M.C., Stofan, E.R., Peckyno, R., Radebaugh, J., Mitchell, K.L., Mitri, G., Wood, C.A., Kirk, R.L., Wall, S.D., Lunine, J.I. and Hayes, A., 2010. Distribution and interplay of geologic processes on Titan from Cassini radar data. *Icarus*, *205* (2), p.540-558.

Lopes, R.M.C., Kirk, R.L., Mitchell, K.L., LeGall, A., Barnes, J.W., Hayes, A., Kargel, J., Wye, L., Radebaugh, J., Stofan, E.R. and Janssen, M.A., 2013. Cryovolcanism on Titan: New results from Cassini RADAR and VIMS. *Journal of Geophysical Research: Planets*, *118* (3), p.416-435.

Lopes, R.M., Malaska, M.J., Solomonidou, A., Le Gall, A., Janssen, M.A., Neish, C.D., Turtle, E.P., Birch, S.P.D., Hayes, A.G., Radebaugh, J. and Coustenis, A., 2016. Nature, distribution, and origin of Titan's Undifferentiated Plains. *Icarus*, *270*, p.162-182.

Lorenz, R.D., Wall, S., Radebaugh, J., Boubin, G., Reffet, E., Janssen, M., Stofan, E., Lopes, R., Kirk, R., Elachi, C. and Lunine, J., 2006. The sand seas of Titan: Cassini RADAR observations of longitudinal dunes. *Science*, *312* (5774), p.724-727.

Lorenz, R.D., Wood, C.A., Lunine, J.I., Wall, S.D., Lopes, R.M., Mitchell, K.L., Paganelli, F., Anderson, Y.Z., Wye, L., Tsai, C. and Zebker, H., 2007. Titan's young surface: Initial impact crater survey by Cassini RADAR and model comparison. *Geophysical Research Letters*, *34* (7).

Lorenz, R.D., Lopes, R.M., Paganelli, F., Lunine, J.I., Kirk, R.L., Mitchell, K.L., Soderblom, L.A., Stofan, E.R., Ori, G., Myers, M. and Miyamoto, H., 2008a. Fluvial channels on Titan: initial Cassini RADAR observations. *Planetary and Space Science*, *56* (8), p.1132-1144.

Lorenz, R.D., Mitchell, K.L., Kirk, R.L., Hayes, A.G., Aharonson, O., Zebker, H.A., Paillou, P., Radebaugh, J., Lunine, J.I., Janssen, M.A. and Wall, S.D., 2008b. Titan's inventory of organic surface materials. *Geophysical Research Letters*, *35* (2).

Lorenz, R.D. and Radebaugh, J., 2009. Global pattern of Titan's dunes: radar survey from the Cassini prime mission. *Geophysical Research Letters*, *36* (3).

Lucas, A., Aharonson, O., Deledalle, C., Hayes, A.G., Kirk, R. and Howington-Kraus, E., 2014. Insights into Titan's geology and hydrology based on enhanced image processing of Cassini RADAR data. *Journal of Geophysical Research: Planets*, *119* (10), p.2149-2166.

Lunine, J.I. and Atreya, S.K., 2008. The methane cycle on Titan. *Nature Geoscience*, *1* (3), p.159-164.

Luscombe, A.P., 2001, April. Radiometric calibration information from RADARSAT-1 Amazon measurements. In *Proceedings of the CEOS SAR Workshop 2001, CEOS Working Group on Calibration and Validation, SAR Subgroup*, p. 68-71.

Luspay-Kuti, A., Chevrier, V.F., Wasiak, F.C., Roe, L.A., Welivitiya, W.D.D.P., Cornet, T., Singh, S. and Rivera-Valentin, E.G., 2012. Experimental simulations of CH4 evaporation on Titan. *Geophysical Research Letters*, *39* (23).

Malaska, M.J. and Hodyss, R., 2014. Dissolution of benzene, naphthalene, and biphenyl in a simulated Titan lake. *Icarus*, *242*, p.74-81.

Mitchell, J.L., 2008. The drying of Titan's dunes: Titan's methane hydrology and its impact on atmospheric circulation. *Journal of Geophysical Research: Planets*, *113* (E8).

Moore, J.M. and Howard, A.D., 2005. Large alluvial fans on Mars. *Journal of Geophysical Research: Planets*, *110* (E4).

Moore, J.M. and Howard, A.D., 2010. Are the basins of Titan's Hotei Regio and Tui Regio sites of former low latitude seas?. *Geophysical Research Letters*, *37* (22).

Moore, J.M. and Pappalardo, R.T., 2011. Titan: An exogenic world?. *Icarus*, *212* (2), p.790-806.

Moore, J.M., Howard, A.D. and Morgan, A.M., 2014. The landscape of Titan as witness to its climate evolution. *Journal of Geophysical Research: Planets*, *119* (9), p.2060-2077.

Neish, C.D., Lorenz, R.D., Kirk, R.L. and Wye, L.C., 2010. Radarclinometry of the sand seas of Africa's Namibia and Saturn's moon Titan. *Icarus*, *208* (1), p.385-394

Neish, C.D. and Lorenz, R.D., 2014. Elevation distribution of Titan's craters suggests extensive wetlands. *Icarus*, *228*, p.27-34.

Neish, C.D., Barnes, J.W., Sotin, C., MacKenzie, S., Soderblom, J.M., Le Mouelic, S., Kirk, R.L., Stiles, B.W., Malaska, M.J., Le Gall, A., Brown, R.H., Baines, K.H., Buratti, B., Clark, R.N., Nicholson, P.D., 2015. Spectral properties of Titan's impact craters imply chemical weathering of its surface. *Geophysical Research Letters*, *42* (10), p.3746-3754.

Nichols, G.J. and Fisher, J.A., 2007. Processes, facies and architecture of fluvial distributary system deposits. *Sedimentary Geology*, *195* (1), p.75-90.

Niemann, H.B., Atreya, S.K., Bauer, S.J., Carignan, G.R., Demick, J.E., Frost, R.L., Gautier, D., Haberman, J.A., Harpold, D.N., Hunten, D.M. and Israel, G., 2005. The abundances of constituents of Titan's atmosphere from the GCMS instrument on the Huygens probe. *Nature*, *438* (7069), p.779-784.

Ouchi, K., 2013. Recent trend and advance of synthetic aperture radar with selected topics. *Remote Sensing*, *5* (2), p.716-807.

Paillou, P., Lunine, J., Ruffié, G., Encrenaz, P., Wall, S., Lorenz, R. and Janssen, M., 2008. Microwave dielectric constant of Titan-relevant materials. *Geophysical Research Letters*, 35 (18).

Parkhomenko, E.I., 2012. Electrical properties of rocks. Springer Science & Business Media.

Radebaugh, J., Lorenz, R.D., Kirk, R.L., Lunine, J.I., Stofan, E.R., Lopes, R.M. and Wall, S.D., 2007. Mountains on Titan observed by Cassini RADAR. *Icarus*, *192* (1), p.77-91.

Radebaugh, J., Ventra, D., Lorenz, R.D., Farr, T., Kirk, R., Hayes, A., Malaska, M.J., Birch, S., Liu, Z.Y.C., Lunine, J. and Barnes, J., 2016. Alluvial and fluvial fans on Saturn's moon Titan reveal processes, materials and regional geology. *Geological Society, London, Special Publications*, *440*, p. SP440-6.

Rages, K., Pollack, J.B. and Smith, P.H., 1983. Size estimates of Titan's aerosols based on Voyager high-phase-angle images. *Journal of Geophysical Research: Space Physics*, *88* (A11), p.8721-8728.

Raney, R.K., Luscombe, A.P., Langham, E.J. and Ahmed, S., 1991. Radarsat [sar imaging]. *Proceedings of the IEEE*, *79* (6), p.839-849.

Rannou, P., Montmessin, F., Hourdin, F. and Lebonnois, S., 2006. The latitudinal distribution of clouds on Titan. *Science*, *311* (5758), p.201-205.

Raulin, F., Brassé, C., Poch, O. and Coll, P., 2012. Prebiotic-like chemistry on Titan. *Chemical Society Reviews*, *41* (16), p.5380-5393.

Rosenqvist, A., Shimada, M., Ito, N. and Watanabe, M., 2007. ALOS PALSAR: A pathfinder mission for global-scale monitoring of the environment. *Geoscience and Remote Sensing, IEEE Transactions on*, *45* (11), p.3307-3316.

Shanmugam, G., 2016. Submarine fans: A critical retrospective (1950-2015). *Journal of Palaeogeography*, *5*, p.2-76.

Shimada, M., Tadono, T. and Rosenqvist, A., 2010. Advanced Land Observing Satellite (ALOS) and monitoring global environmental change. *Proceedings of the IEEE, 98* (5), p.780-799.

Sklar, L.S., Collins, G.C., Litwin, K.L., Polito, P.J. and Zygielbaum, B.R., 2012, December. Erodibility of Titan ice bedrock constrained by laboratory measurements of ice strength and erosion by sediment impacts. In *AGU Fall Meeting Abstracts* (Vol. 1, p. 06).

Smith, B.A., Soderblom, L., Beebe, R., Boyce, J., Briggs, G., Bunker, A., Collins, S.A., Hansen, C.J., Johnson, T.V., Mitchell, J.L. and Terrile, R.J., 1981. Encounter with Saturn: Voyager 1 imaging science results. *Science, 212* (4491), p.163-191.

Smith, B.A., Soderblom, L., Batson, R., Bridges, P., Inge, J.A.Y., Masursky, H., Shoemaker, E., Beebe, R., Boyce, J., Briggs, G. and Bunker, A., 1982. A new look at the Saturn system: The Voyager 2 images. *Science, 215* (4532), p.504-537.

Soderblom, L.A., Barnes, J.W., Brown, R.H., Clark, R.N., Janssen, M.A., McCord, T.B., Niemann, H.B. and Tomasko, M.G., 2009. Composition of Titan's surface. In *Titan from Cassini-Huygens*, p. 141-175. Springer, Netherlands.

Stofan E.R., Lopes, R., Mitchell, K.L., Wall, S.D., Mitri, G., Janssen, M., Ostro, S., Kirk, R.L., Hayes, A.G., Stofan, E.R., Lunine, J.I. and Lorenz, R.D., 2007. The lakes and seas of Titan. *EOS, Transactions American Geophysical Union, 88* (51), p.569-570.

Stofan E.R., Wall, S.D., Stiles, B.W., Kirk, R.L., West, R.D., and Callahan, P.S., 2010. Cassini RADAR Users Guide. http://pds-imaging.jpl.nasa.gov/documentation/Cassini_RADAR_Users_Guide.pdf

Tomasko, M.G., Archinal, B., Becker, T., Bézard, B., Bushroe, M., Combes, M., Cook, D., Coustenis, A., deBergh, C., Dafoe, L.E. and Doose, L., 2005. Results from the descent imager/spectral radiometer (DISR) instrument on the Huygens probe of Titan. *Nature, 438*, p.765-778.

Tomasko, M.G., Doose, L.R., Dafoe, L.E. and See, C., 2009. Limits on the size of aerosols from measurements of linear polarization in Titan's atmosphere. *Icarus, 204* (1), p.271-283.

Tomasko, M.G. and Smith, P.H., 1982. Photometry and polarimetry of Titan: Pioneer 11 observations and their implications for aerosol properties. *Icarus, 51* (1), p.65-95.

Turtle, E.P., Perry, J.E., Hayes, A.G., Lorenz, R.D., Barnes, J.W., McEwen, A.S., West, R.A., Del Genio, A.D., Barbara, J.M., Lunine, J.I. and Schaller, E.L., 2011. Rapid and extensive surface changes near Titan's equator: Evidence of April showers. *Science, 331* (6023), p.1414-1417.

Ulaby, F.T., Bengal, T., East, J., Dobson, M.C., Garvin, J. and Evans, D., 1988. Microwave dielectric spectrum of rocks.

Ulaby, F.T., Moore, R.K. and Fung, A.K., 1982. Microwave remote sensing: Active and passive. Volume 2-Radar remote sensing and surface scattering and emission theory. Artech House, London.

Ulaby, F.T., Long, D.G., Blackwell, W.J., Elachi, C., Fung, A.K., Ruf, C., Sarabandi, K., Zebker, H.A. and Van Zyl, J., 2014. Microwave radar and radiometric remote sensing. University Michigan Press, Ann Arbor.

Ulaby, F.T. and Dobson, M.C., 1989. Handbook of Radar Scattering Statistics for Terrain. Artech House, London.

Waite, J.H., Young, D.T., Cravens, T.E., Coates, A.J., Crary, F.J., Magee, B. and Westlake, J., 2007. The process of tholin formation in Titan's upper atmosphere. *Science*, *316* (5826), p.870-875.

Weissmann, G.S., Hartley, A.J., Nichols, G.J., Scuderi, L.A., Olson, M., Buehler, H. and Banteah, R., 2010. Fluvial form in modern continental sedimentary basins: Distributive fluvial systems. *Geology*, *38* (1), p.39-42.

West, R.A., Lane, A.L., Hart, H., Simmons, K.E., Hord, C.W., Coffeen, D.L., Esposito, L.W., Sato, M. and Pomphrey, R.B., 1983. Voyager 2 photopolarimeter observations of Titan. *Journal of Geophysical Research: Space Physics*, *88* (A11), p.8699-8708.

West, R.D., Anderson, Y., Boehmer, R., Borgarelli, L., Callahan, P., Elachi, C., Gim, Y., Hamilton, G., Hensley, S., Janssen, M.A. and Johnson, W.T., 2009. Cassini RADAR sequence planning and instrument performance. *Geoscience and Remote Sensing, IEEE Transactions on*, *4 7*(6), p.1777-1795.

Wilford, D.J., Sakals, M.E., Innes, J.L. and Sidle, R.C., 2005. Fans with forests: contemporary hydrogeomorphic processes on fans with forests in west central British Columbia, Canada. *Special Publication Geological Society of London*, *251*, p.25.

Williams, R.M. and Malin, M.C., 2008. Sub-kilometer fans in Mojave crater, Mars. *Icarus*, *198* (2), p.365-383.

Yung, Y.L., Allen, M. and Pinto, J.P., 1984. Photochemistry of the atmosphere of Titan-Comparison between model and observations. *The Astrophysical Journal Supplement Series*, *55*, p.465-506.

Zebker, H.A., Stiles, B., Hensley, S., Lorenz, R., Kirk, R.L. and Lunine, J., 2009. Size and shape of Saturn's moon Titan. *Science*, *324* (5929), p.921-923.

Zimbelman, J.R., 2001. Image resolution and evaluation of genetic hypotheses for planetary landscapes. *Geomorphology*, *37* (3), p.179-199.

Appendix 2

Table 2.1. Titan SAR data summary.

Cassini swath	Obser. Date	*Mean Azimuth Angle (°)	*Mean Polar. Angle (°)	Number of Fans	Fan Lat. Range (°)	Fan Long. Range (°)
T39	12/20/2007	110.1	179.5	8	56.5 - 58.8 S	146.0 - 151. E
T44	5/28/2008	248.7	178.7	3	15.2 - 20.5 S	160.2 - 167.0 W
T03	2/15/2005	275.8	176.8	7	17.5 - 20.6 N	54.0 - 60.2 E
TA	10/26/2004	93.7	172.2	2	50.3 - 51.5 N	54.8 - 56.3 E
T30	5/12/2007	217.4	11.7	3	68.0 - 69.4 N	81.3 - 85.5 W

**Azimuth and polarization angles change across each swath. We refer the reader to the Cassini RADAR Users Guide (Stofan et al., 2010) for more details.*

Table 2.2. Panamint Range SAR data summary.

Instrument	Orbit Number	Obser. Date	θ (°)	Orbit	Look Direction	Polarization	ASF Download Date
RS1	06117	1/5/1997	~19.6	Descend.	West	HH	4/19/2015
	06460	1/29/1997	~19.6	Descend.	West	HH	4/19/2015
	42332	12/14/2003	~30.5	Descend.	West	HH	7/13/2015
	52279	11/9/2005	~30.5	Descend.	West	HH	4/19/2015
	64827	4/5/2008	~41.5	Descend.	West	HH	6/18/2015
	06310	1/19/1997	~19.6	Ascend.	East	HH	4/19/2015
	22474	2/24/2000	~36.5	Ascend.	East	HH	6/18/2015
	28205	3/31/2001	~41.5	Ascend.	East	HH	6/18/2015
PALSAR	04488	11/27/2006	~34.3	Descend.	West	HH	10/13/2015
	25705	11/21/2010	~34.3	Ascend.	East	HV	10/13/2015

Table 2.3. Classification scheme summary.

Fan Region	Classification Scheme	Classification Types	Quantitative or Qualitative?
Body: 0-85% downfan distance	Slope	Slope > 2σ: **Positive** or **Negative** Slope < 2σ: **Neutral**	Quantitative
Terminus: 86-100% downfan distance	Slope	Slope > 2σ: **Positive** or **Negative** Slope < 2σ: **Neutral**	Quantitative
	Shape	Large change in σ^0: **Large ΔDN** Moderate change in σ^0: **Medium ΔDN** Negligible change in σ^0: **Small ΔDN**	Qualitative

Table 2.4. Areas and mean σ^0 for Panamint fans (descending orbits).

			RS1 06117 (θ ~19.6°)		**RS1 06460 (θ ~19.6°)**		**RS1 42332 (θ ~30.5°)**		**RS1 52279 (θ ~30.5°)**		**RS1 64827 (θ ~41.5°)**		**PALSAR 4488 (θ ~34.3°)**	
Fan	**Fan Type**	**Area (Km^2)**	**Mean σ^0**	**Std. Dev. σ^0**	**Mean σ^0**	**Std. Dev. σ^0**	**Mean σ^0**	**Std. Dev. σ^0**	**Mean σ^0**	**Std. Dev. σ^0**	**Mean σ^0**	**Std. Dev. σ^0**	**Mean σ^0**	**Std. Dev. σ^0**
1	DF	33.3	**0.172**	0.092	**0.172**	0.096	**0.108**	0.054	**0.108**	0.055	**0.089**	0.046	**0.078**	0.059
2	DF	42.3	**0.235**	0.125	**0.230**	0.137	**0.133**	0.062	**0.133**	0.069	**0.124**	0.060	**0.081**	0.061
3	DF	23.5	**0.264**	0.128	**0.255**	0.137	**0.151**	0.071	**0.157**	0.081	**0.140**	0.067	**0.105**	0.078
4	DF	11.5	**0.238**	0.138	**0.239**	0.126	**0.135**	0.069	**0.143**	0.071	**0.118**	0.061	**0.106**	0.068
5	DF	3.0	**0.276**	0.118	**0.260**	0.112	**0.156**	0.067	**0.153**	0.071	**0.133**	0.055	**0.116**	0.092
6	DF	7.4	**0.196**	0.093	**0.205**	0.120	**0.119**	0.058	**0.116**	0.057	**0.095**	0.044	**0.084**	0.065
7	DF	34.4	**0.199**	0.103	**0.209**	0.174	**0.119**	0.059	**0.121**	0.059	**0.102**	0.052	**0.083**	0.071
8	SF	25.3	**0.144**	0.085	**0.157**	0.102	**0.098**	0.054	**0.089**	0.053	**0.072**	0.041	**0.065**	0.050
9	SF	17.5	**0.161**	0.077	**0.162**	0.074	**0.111**	0.049	**0.099**	0.047	**0.078**	0.039	**0.055**	0.038
10	SF	4.8	**0.178**	0.077	**0.187**	0.090	**0.124**	0.054	**0.119**	0.055	**0.091**	0.040	**0.007**	0.004
11	SF	5.9	**0.139**	0.071	**0.152**	0.106	**0.096**	0.043	**0.082**	0.039	**0.066**	0.032	**0.004**	0.002
12	SF	3.5	**0.134**	0.061	**0.164**	0.149	**0.099**	0.044	**0.079**	0.036	**0.065**	0.028	**0.039**	0.024
13	SF	11.7	**0.121**	0.064	**0.121**	0.064	**0.083**	0.044	**0.070**	0.034	**0.055**	0.026	**0.045**	0.039
14	SF	7.5	**0.169**	0.080	**0.156**	0.088	**0.116**	0.054	**0.116**	0.053	**0.087**	0.042	**0.073**	0.047

Table 2.5. Areas and mean σ^0 for Panamint fans (ascending orbits).

Fan Number	Fan Type	Area (Km^2)	RS1 06310 (θ ~19.6°) Mean σ^0	RS1 06310 (θ ~19.6°) Std. Dev. σ^0	RS1 22474 (θ ~36.5°) Mean σ^0	RS1 22474 (θ ~36.5°) Std. Dev. σ^0	RS1 28205 (θ ~41.5°) Mean σ^0	RS1 28205 (θ ~41.5°) Std. Dev. σ^0	PALSAR 7588 (θ ~34.3°) Mean σ^0	PALSAR 7588 (θ ~34.3°) Std. Dev. σ^0
1	Debris Flow	38.1	0.150	0.078	0.098	0.052	0.106	0.054	0.009	0.006
2	Debris Flow	52.1	0.188	0.096	0.110	0.063	0.126	0.070	0.009	0.007
3	Debris Flow	27.9	0.215	0.102	0.139	0.075	0.207	0.107	0.013	0.009
4	Debris Flow	11.4	0.186	0.088	0.125	0.061	0.134	0.065	0.011	0.007
5	Debris Flow	5.1	0.201	0.091	0.126	0.065	0.137	0.066	0.012	0.006
6	Debris Flow	9.5	0.167	0.079	0.114	0.058	0.108	0.060	0.009	0.005
7	Debris Flow	36.3	0.172	0.089	0.125	0.065	0.122	0.070	0.010	0.006
8	Sheetflood	29.9	0.124	0.067	0.104	0.057	0.080	0.044	0.006	0.004
9	Sheetflood	15.3	0.120	0.055	0.109	0.049	0.080	0.035	0.005	0.002
10	Sheetflood	5.6	0.135	0.059	0.127	0.055	0.098	0.042	0.007	0.004
11	Sheetflood	8.1	0.098	0.046	0.103	0.046	0.068	0.031	0.004	0.002
12	Sheetflood	3.1	0.097	0.042	0.102	0.044	0.065	0.028	0.004	0.002
13	Sheetflood	13.8	0.092	0.045	0.096	0.048	0.061	0.031	0.005	0.002
14	Sheetflood	7.4	0.130	0.059	0.139	0.063	0.097	0.052	0.009	0.004

Table 2.6. Areas and mean σ^0 for possible Titan fans.

Latitude Zone	SAR swath	Fan Number	Area (Km^2)	Mean σ^0	Std. Dev. σ^0
High N.	T30	1	404.0	**0.347**	0.278
		2	610.0	**0.380**	0.299
		3	928.9	**0.403**	0.333
Mid N.	TA	1	464.3	**0.998**	0.658
		2	291.0	**0.817**	0.541
Low N.	T03	1	788.1	**1.246**	0.787
		2	2993.9	**1.141**	0.698
		3	1602.2	**1.124**	0.704
		4	1745.1	**1.275**	0.750
		5	687.1	**1.176**	0.750
		6	863.0	**1.238**	0.830
		7	2112.7	**1.112**	0.669
Low S.	T44	1	479.9	**1.185**	0.743
		2	836.0	**0.671**	0.405
		3	740.0	**1.126**	0.923
Mid S.	T39	1	248.0	**0.833**	0.722
		2	177.5	**0.844**	0.746
		3	39.5	**0.776**	0.636
		4	42.1	**0.807**	0.658
		5	219.5	**0.805**	0.659
		6	149.1	**0.797**	0.697
		7	415.9	**0.776**	0.690
		8	68.5	**1.001**	0.816

Table 2.7. Analysis of σ^0 profile lines for Panamint fans.

Fan Number	Fan Type	Fan Body Slope	Fan Body Slope (stdev)	Fan Body Slope Classification	Fan Terminus Slope	Fan Terminus Slope (stdev)	Fan Terminus Slope Classification	Fan Terminus Shape
1	Debris Flow	0.00010	0.00003	positive	-0.0061	0.0003	negative	large ΔDN
2	Debris Flow	0.00042	0.00004	positive	-0.0073	0.0005	negative	large ΔDN
3	Debris Flow	0.00029	0.00005	positive	-0.0064	0.0006	negative	large ΔDN
4	Debris Flow	0.00016	0.00005	positive	-0.0035	0.0004	negative	large ΔDN
5	Debris Flow	-0.00042	0.00007	negative	-0.0029	0.0006	negative	medium ΔDN
6	Debris Flow	0.00014	0.00004	positive	-0.0013	0.0003	negative	medium ΔDN
7	Debris Flow	-0.00040	0.00006	negative	-0.0029	0.0005	negative	large ΔDN
8	Sheetflood	-0.00015	0.00004	negative	-0.0060	0.0002	negative	large ΔDN
9	Sheetflood	-0.00015	0.00003	negative	-0.0017	0.0003	negative	medium ΔDN
10	Sheetflood	-0.00025	0.00005	negative	-0.0011	0.0005	negative	medium ΔDN
11	Sheetflood	0.00013	0.00003	positive	-0.0015	0.0003	negative	medium ΔDN
12	Sheetflood	-0.00017	0.00003	negative	0.0005	0.0003	positive	small ΔDN
13	Sheetflood	0.00027	0.00003	positive	-0.0018	0.0002	negative	medium ΔDN
14	Sheetflood	-0.00003	0.00004	neutral	-0.0014	0.0003	negative	medium ΔDN

Table 2.8. Analysis of σ^0 profile lines for possible Titan fans.

Latitude Zone	SAR Swath	Fan Number	Fan Body Slope	Fan Body Slope (stdev)	Fan Body Slope Classification	Fan Terminus Slope	Fan Terminus Slope (stdev)	Fan Terminus Slope Classification	Fan Terminus Shape
High N.	T30	1	-0.00135	0.00043	negative	-0.0029	0.0038	neutral	medium ΔDN
		2	0.00034	0.00030	neutral	-0.0120	0.0030	negative	medium ΔDN
		3	-0.00316	0.00030	negative	-0.0020	0.0030	neutral	small ΔDN
Mid N.	TA	1	-0.00316	0.00049	negative	-0.0222	0.0064	negative	medium ΔDN
		2	-0.00608	0.00047	negative	0.0217	0.0056	positive	large ΔDN
Low N.	T03	1	0.00009	0.00009	neutral	-0.0103	0.0067	neutral	small ΔDN
		2	-0.00305	0.00049	negative	-0.0131	0.0074	neutral	small ΔDN
		3	0.00084	0.00047	neutral	-0.0056	0.0055	neutral	small ΔDN
		4	-0.00309	0.00054	neutral	0.0087	0.0046	neutral	small ΔDN
		5	-0.00085	0.00084	neutral	-0.0115	0.0086	neutral	medium ΔDN
		6	-0.00554	0.00100	negative	-0.0140	0.0063	negative	large ΔDN
		7	0.00051	0.00041	neutral	0.0064	0.0056	neutral	small ΔDN
Low S.	T44	1	-0.00493	0.00085	negative	-0.0104	0.0079	neutral	large ΔDN
		2	0.00091	0.00058	neutral	-0.0076	0.0044	neutral	medium ΔDN
		3	-0.00038	0.00049	neutral	-0.0025	0.0035	neutral	small ΔDN
Mid S.	T39	1	-0.00682	0.00083	negative	-0.0054	0.0067	neutral	medium ΔDN
		2	0.00001	0.00077	neutral	-0.0025	0.0043	neutral	medium ΔDN
		3	0.00317	0.00144	positive	0.0072	0.0067	neutral	medium ΔDN
		4	0.00279	0.00138	positive	0.0218	0.0109	positive	medium ΔDN
		5	-0.00482	0.00081	negative	-0.0040	0.0096	neutral	large ΔDN
		6	0.00345	0.00109	positive	-0.0525	0.0085	negative	large ΔDN
		7	-0.00325	0.00080	negative	-0.0253	0.0062	negative	large ΔDN
		8	-0.00246	0.00163	neutral	-0.0005	0.0072	neutral	large ΔDN

Table 2.9. Mean σ^0 Brightness Groups for Panamint Range Fans.

	Descending RS1 Orbits					Ascending RS1 Orbits			Des. PALSAR	Asc. PALSAR
Fan	**06117**	**06460**	**42332**	**52279**	**64827**	**06310**	**22474**	**28205**	**4488**	**7588**
1	Intermed.	Intermed.	Intermed.	Intermed.	Intermed.	Intermed.	Intermed.	Intermed.	Intermed.	Intermed.
2	bright	bright	Intermed.	Intermed.	bright	bright	Intermed.	bright	Intermed.	Intermed.
3	bright	bright	bright	bright	bright	bright	Intermed.	bright	bright	bright
4	bright	bright	Intermed.	Intermed.	bright	bright	Intermed.	bright	bright	bright
5	bright	bright	bright	bright	bright	bright	Intermed.	bright	bright	bright
6	Intermed.	Intermed.	Intermed.	Intermed.	Intermed.	bright	Intermed.	Intermed.	Intermed.	Intermed.
7	Intermed.	Intermed.	Intermed.	Intermed.	Intermed.	bright	Intermed.	bright	Intermed.	Intermed.
8	dark	Intermed.	Intermed.	dark	dark	dark	Intermed.	dark	dark	dark
9	Intermed.	Intermed.	Intermed.	Intermed.	Intermed.	dark	Intermed.	dark	dark	dark
10	Intermed.	Intermed.	Intermed.	Intermed.	Intermed.	Intermed.	Intermed.	Intermed.	dark	dark
11	dark	Intermed.	Intermed.	dark	dark	dark	Intermed.	dark	dark	dark
12	dark	Intermed.	Intermed.	dark	dark	dark	Intermed.	dark	dark	dark
13	dark	dark	dark	dark	dark	dark	Intermed.	dark	dark	dark
14	Intermed.	Intermed.	Intermed.	Intermed.	Intermed.	Intermed.	Intermed.	Intermed.	Intermed.	Intermed.

Table 2.10. Mean σ^0 for Panamint Fan Types.

Radar Platform	Orbit	Image Number (Incidence Angle)	Debris Flow		Sheetflood	
			Mean σ^0	Std. Dev. σ^0	Mean σ^0	Std. Dev. σ^0
RS1	Descending	06117 (θ ~19.6°)	**0.226**	0.114	**0.149**	0.074
RS1	Descending	06460 (θ ~19.6°)	**0.225**	0.129	**0.157**	0.096
RS1	Descending	42332 (θ ~30.5°)	**0.132**	0.063	**0.104**	0.049
RS1	Descending	52279 (θ ~30.5°)	**0.133**	0.066	**0.094**	0.045
RS1	Descending	64827 (θ ~41.5°)	**0.114**	0.055	**0.073**	0.035
PALSAR	Descending	4488 (θ ~34.3°)	**0.093**	0.071	**0.041**	0.029
RS1	Ascending	06310 (θ ~19.6°)	**0.183**	0.089	**0.114**	0.053
RS1	Ascending	22474 (θ ~36.5°)	**0.120**	0.063	**0.112**	0.052
RS1	Ascending	28205 (θ ~41.5°)	**0.134**	0.070	**0.078**	0.037
PALSAR	Ascending	7588 (θ ~34.3°)	**0.010**	0.007	**0.006**	0.003

Table 2.11. Mean σ^0 for Latitude-Aggregated Possible Fans on Titan.

Latitude Zone	SAR swath	Number of Fans	Mean σ^0	Std. Dev. σ^0
High N.	T30	3	**0.377**	0.303
Mid N.	TA	2	**0.908**	0.599
Low N.	T03	7	**1.187**	0.741
Low S.	T44	3	**0.994**	0.690
Mid S.	T39	8	**0.830**	0.703

Table 2.12. Analysis of Averaged σ^0 Profile Lines for Panamint Fan Types.

Fan Type	Fan Body Slope	Fan Body Slope (stdev)	Fan Body Slope Classification	Fan Terminus Slope	Fan Terminus Slope (stdev)	Fan Terminus Slope Classification	Fan Terminus Shape
Debris Flow	0.000043	0.000018	positive	-0.004	0.0002	negative	large ΔDN
Sheetflood	-0.000052	0.000017	negative	-0.002	0.0001	negative	medium ΔDN

Table 2.13. Analysis of σ^0 Profile Lines for Latitude-Aggregated Possible Fans on Titan.

Latitude Zone	SAR Swath	Fan Body Slope	Fan Body Slope (stdev)	Fan Body Slope Classification	Fan Terminus Slope	Fan Terminus Slope (stdev)	Fan Terminus Slope Classification	Fan Terminus Shape
High N.	T30	-0.0014	0.0002	negative	-0.0028	0.0022	neutral	medium ΔDN
Mid N.	TA	-0.0046	0.0003	negative	0.0001	0.0033	neutral	small ΔDN
Low N.	T03	-0.0016	0.0002	negative	-0.0014	0.0002	negative	small ΔDN
Low S.	T44	-0.0014	0.0004	negative	-0.0074	0.0034	negative	large ΔDN
Mid S.	T39	-0.0009	0.0003	negative	-0.0075	0.0028	negative	large ΔDN

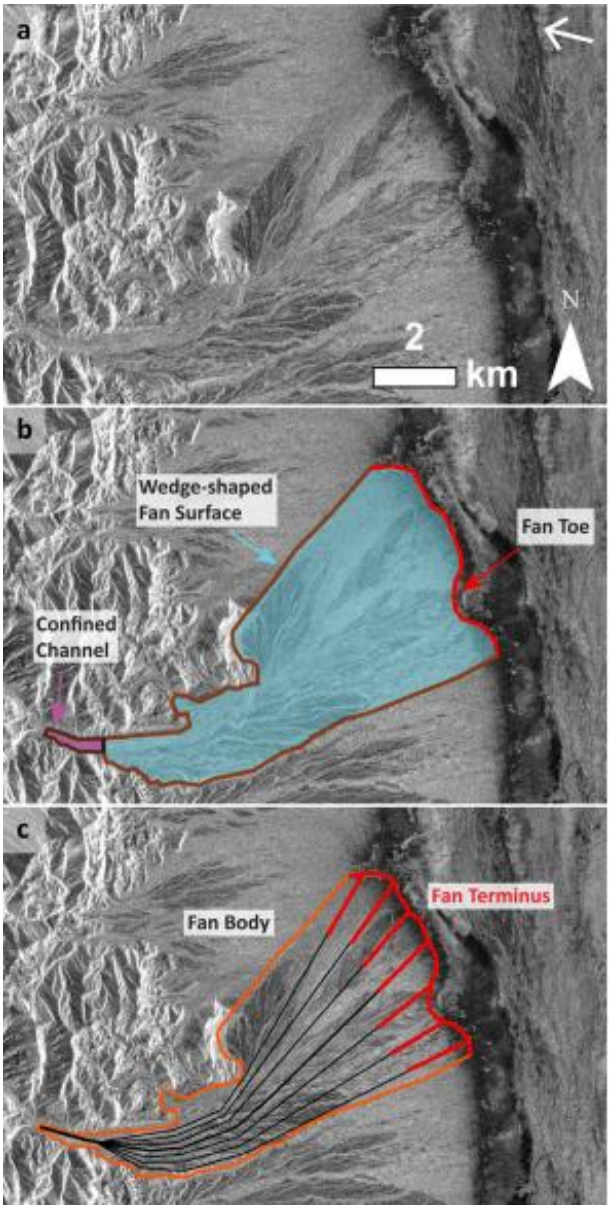

Figure 2.1. Alluvial fans along the Panamint Range in Death Valley, CA. White arrow in top right-hand corner indicates radar look direction. (**a**) Panamint fans observed in PALSAR image #04488. (**b**) Same image as shown in (a) with fan boundary delineation and labels for Panamint Range fan 1: confined channel (purple zone), fan surface (semi-transparent blue zone), and fan toe (red colored boundary). (**c**) Same fan delineation as shown in (b) with downfan σ^0 profile lines separated into two regions: fan body (black lines) and fan terminus (red lines).

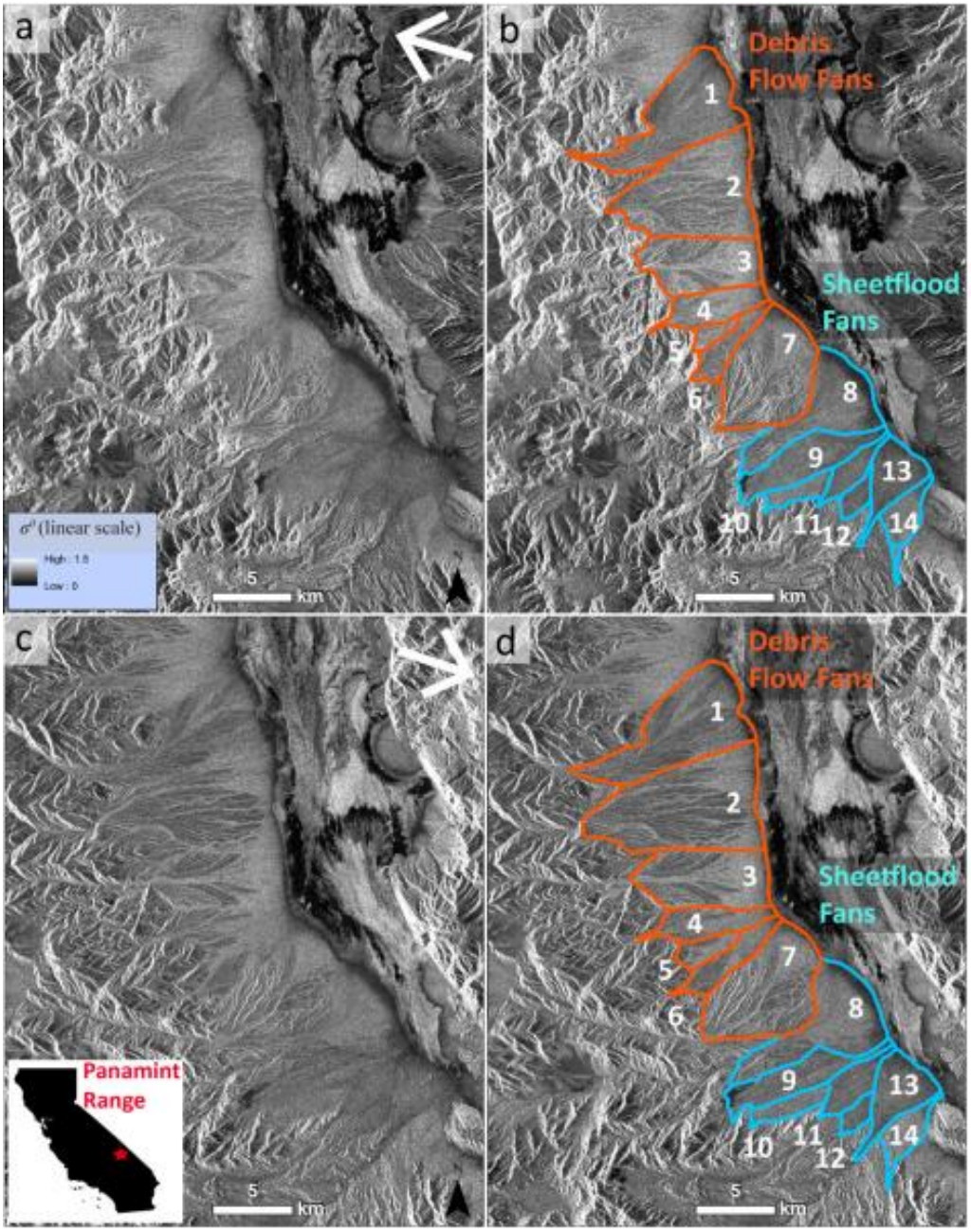

Figure 2.2. RS1 images and mapping of Panamint Range alluvial fans. Insert map of California indicating the location of Death Valley is shown in bottom left hand corner. (**a**) Descending orbit image (52279) with illumination direction indicated by white arrow, (**b**) same image as shown in (a) with delineated fan boundaries, (**c**) ascending orbit image (22474) with illumination direction indicated by white arrow, (**d**) same image as shown in (c) with delineated fan boundaries. Numbers correspond to fan numbers in Tables 2.4, 2.5, and 2.7. DN values for pixels in each image scaled from 0 – 1.5.

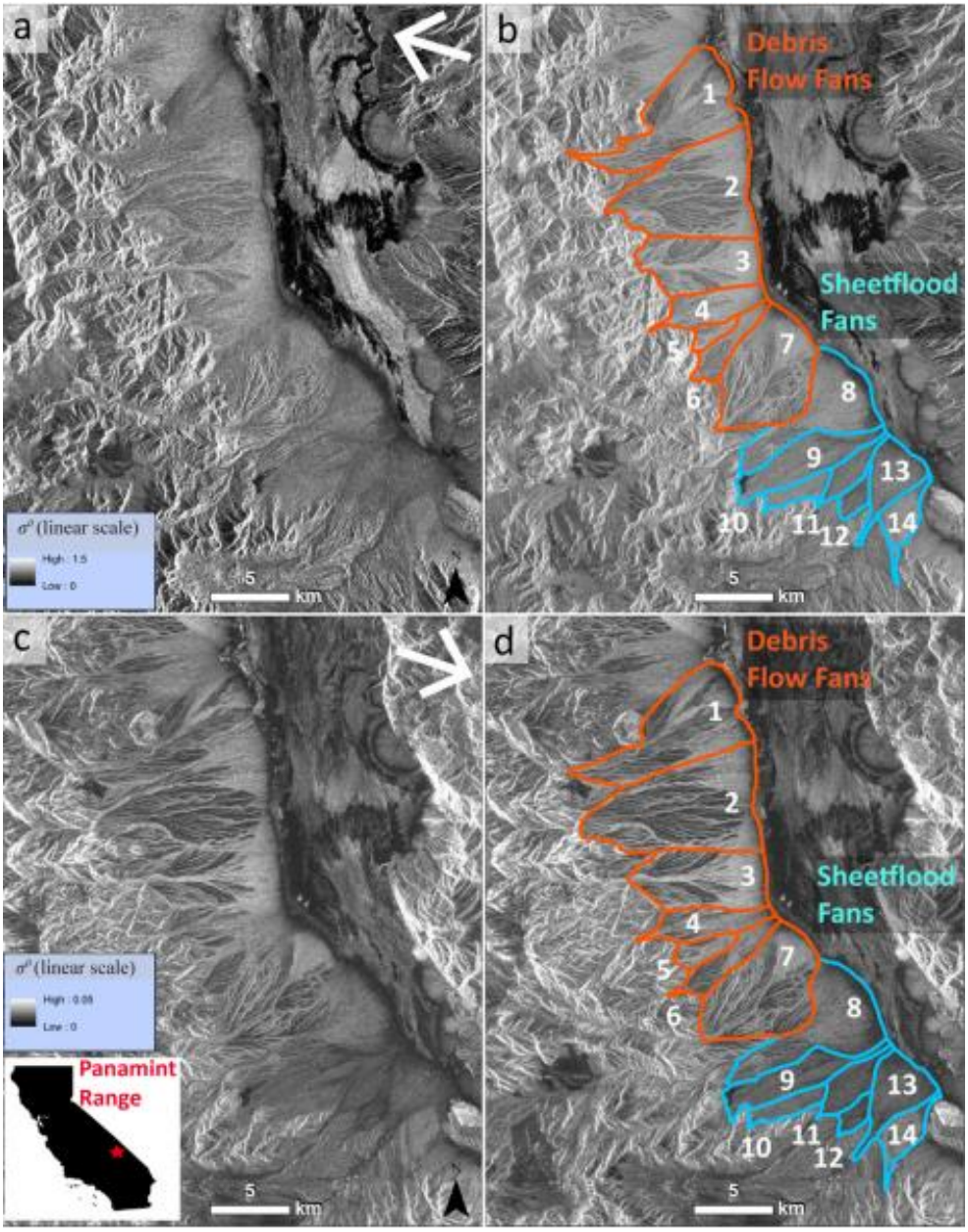

Figure 2.3. PALSAR images and mapping of Panamint Range alluvial fans. Insert map of California indicating the location of Death Valley is shown in bottom left hand corner. (**a**) HH polarized, descending orbit image (04488), with illumination direction indicated by white arrow, (**b**) same image as shown in (a) with delineated fan boundaries, (**c**) HV polarized, ascending orbit image (25705), with illumination direction indicated by white arrow, (**d**) same image as shown in (c) with delineated fan boundaries. Numbers in each image correspond to fan numbers in Tables 2.4, 2.5, and 2.7. DN values for pixels scaled from 0 – 0.5 (a and b) and from 0 – 0.05 (c and d).

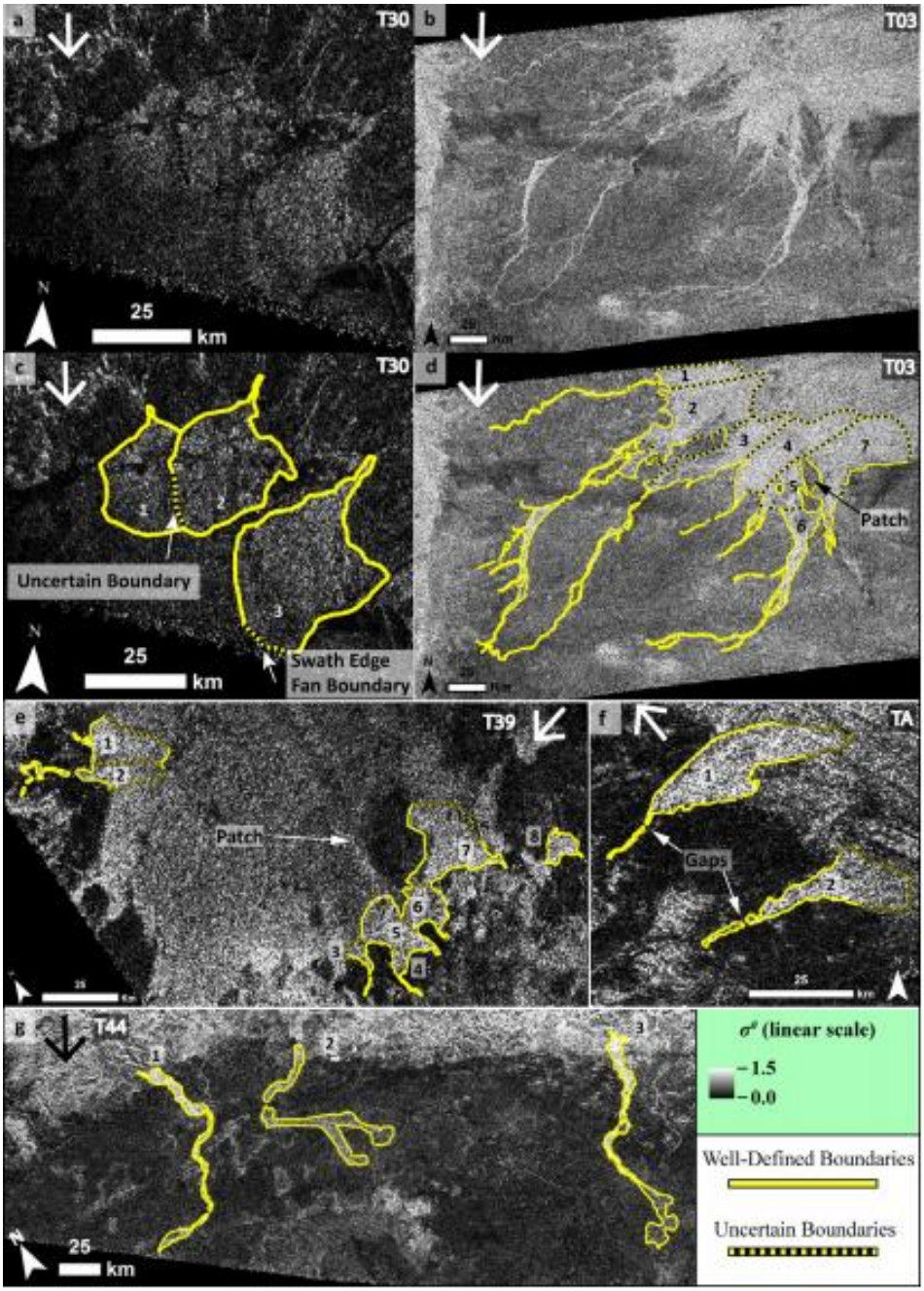

Figure 2.4. Possible fans on Titan analyzed by this study. Arrow in top left-hand corner of each image (top right-hand corner of (e)) indicates illumination direction. (**a**) and (**b**) show examples of fans. Possible fans with delineated boundaries are shown in: (**c**) SAR swath T30, (**d**) T03, (**e**) T39, (**f**) TA, and (**g**) T44 (previously delineated by *e.g.*, Lorenz et al., 2008a; Radebaugh et al., 2016; Birch et al., 2016). Fan numbers on each image correspond to fan numbers in Table 2.6 and 2.8. DN values for pixels in each image scaled from 0 – 1.5. Differences in the radar brightness of the relatively dark possible fans in the near polar swath (T30) compared to the brighter potential fans in the mid- and low-latitude swaths (TA, T03, T44, and T39) are qualitatively apparent in these images. Examples of discontinuous σ^0 regions labeled as 'gaps' and 'patch' are highlighted in 2.4b-d.

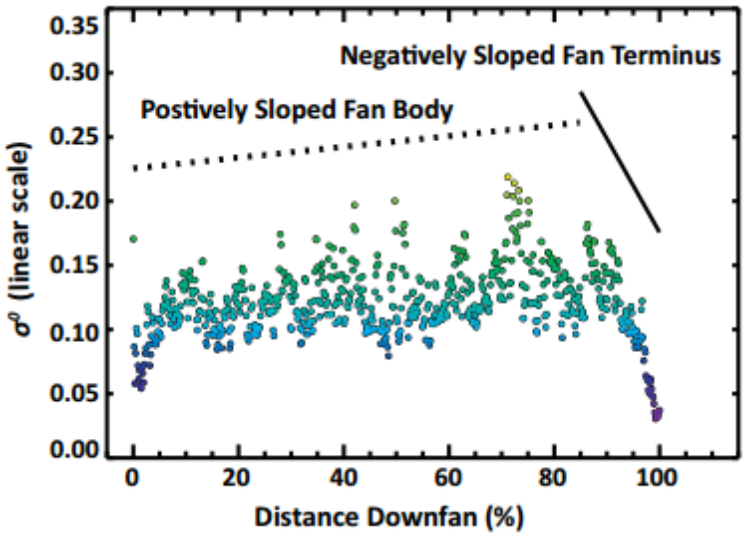

Figure 2.5. Downfan σ^0 profile line for Panamint Range fan 2, with the line fits to the fan body (0 to 85% downfan distance, black dashed line) and fan terminus (86 to 100% downfan distance, black solid line). In this example, σ^0 of the fan body region increases with downfan distance (positive slope), whereas σ^0 of the fan terminus decreases with downfan distance (negative slope), as summarized in Table 2.7.

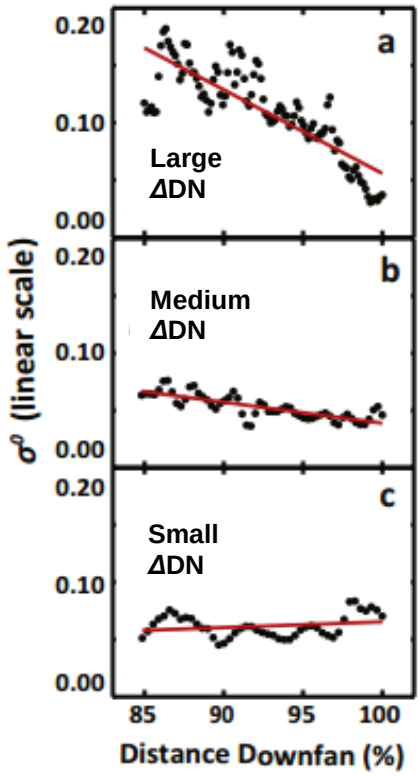

Figure 2.6. Fan terminus shape classifications: (**a**) large *Δ*DN (fan 2), (**b**) medium *Δ*DN (fan 13), and (**c**) small *Δ*DN (fan 12) (Table 2.3 for description of classifications). Line fits to termini (red) show shapes of each region.

Figure 2.7. (part 1). Mean downfan σ^0 profile lines for seven Panamint debris flow fans (observed in descending RS1 image 52279) (colorized data points). Warm colors represent larger values of σ^0. Smoothed versions of each profile line (offset upwards) included to highlight the slope and shape of each profile line fan body (black dashed lines) and fan terminus (solid black lines). Fan numbers in top right-hand corner of each plot correspond to fan numbers in Table 2.7. **(part 2)** Mean downfan σ^0 profile lines for the seven Panamint sheetflood fans (observed in descending RS1 55279) (colorized data points). Warm colors represent larger values of σ^0. Smoothed versions of each profile line (offset upwards) included to highlight the slope and shape of each profile line fan body (black dashed lines) and fan terminus (solid black lines). Fan numbers in top right-hand corner of each plot correspond to fan numbers in Table 2.7.

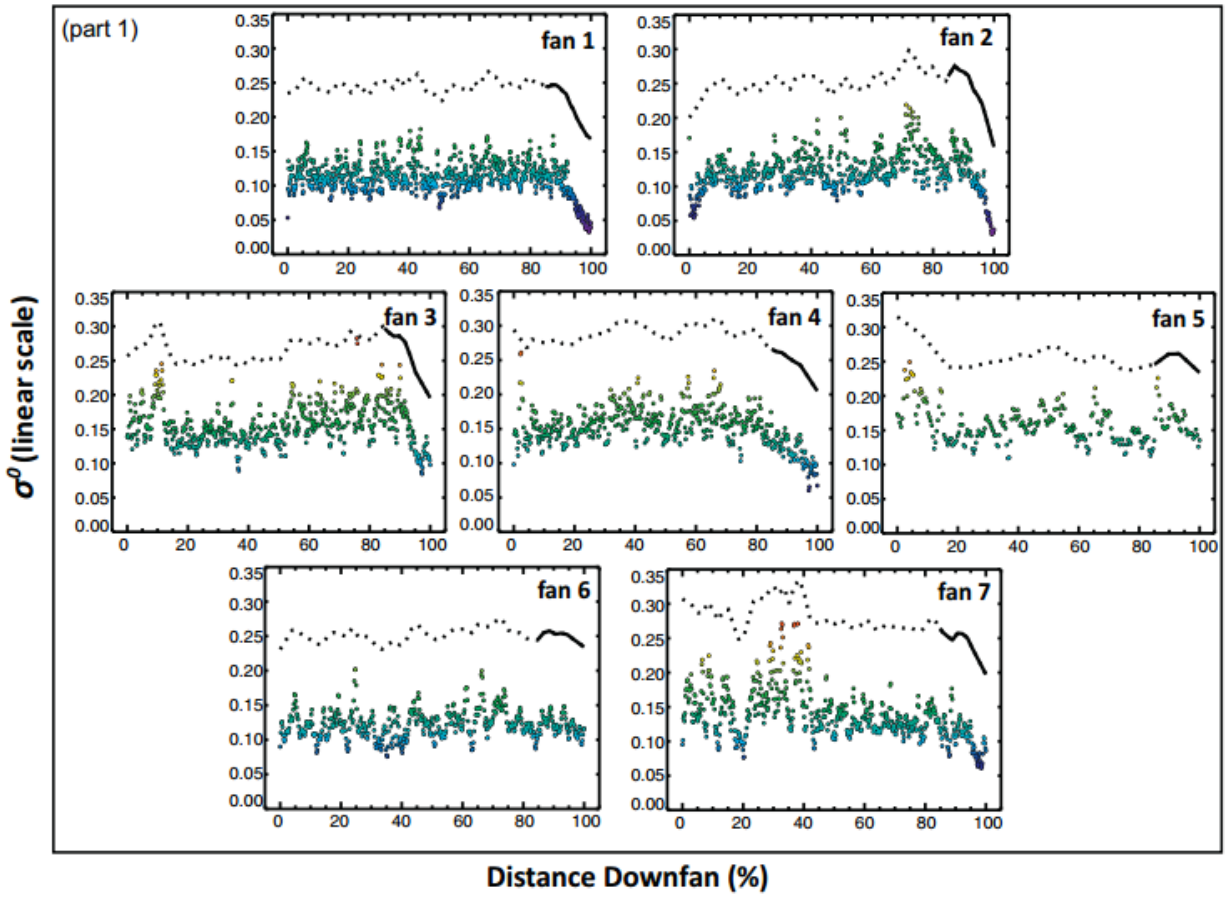

Figure 2.7. Continued.

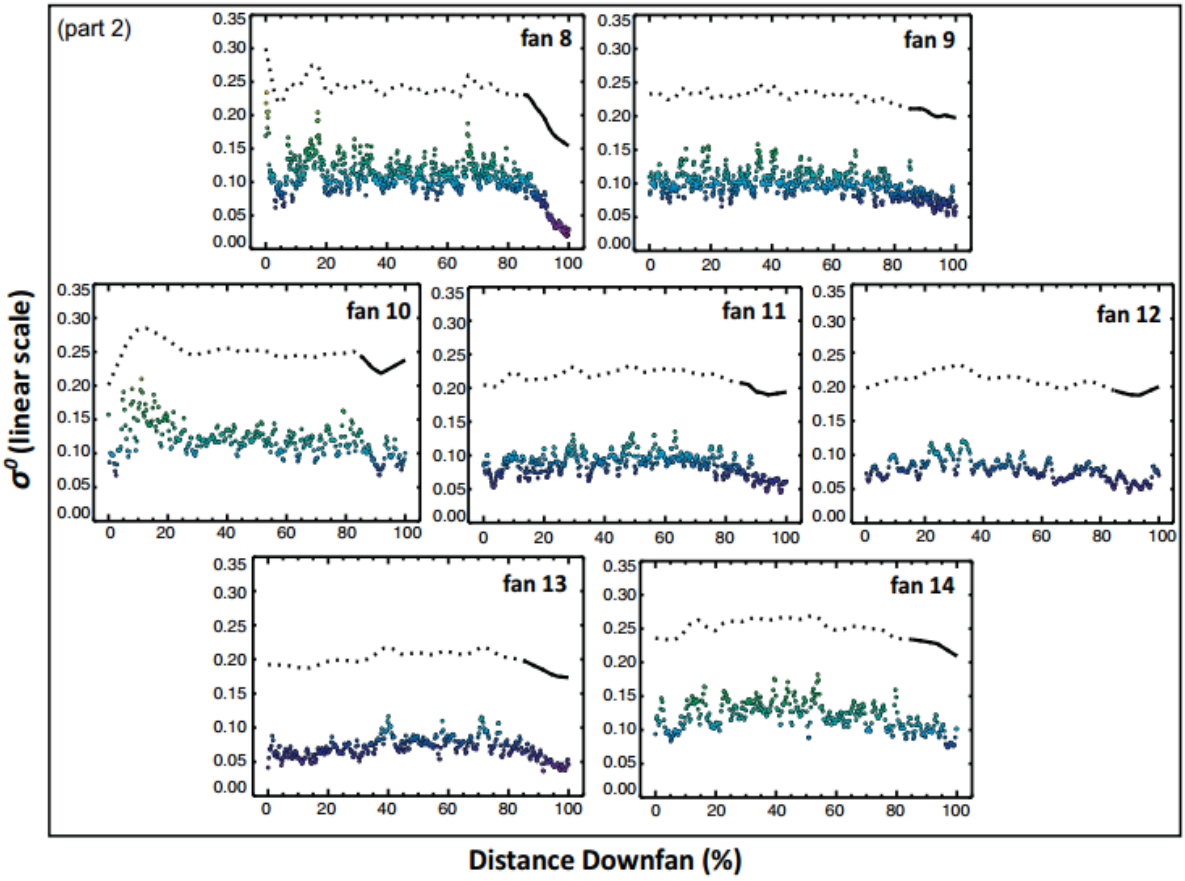

Figure 2.7. Continued.

Figure 2.8. (part 1) Mean downfan σ^0 profile lines for Titan possible fans observed in SAR swaths T30 (high-northern latitudes), TA (mid-northern latitudes), and T44 (low-southern latitudes) (colorized data points). Warm colors represent larger values of σ^0. Smoothed versions of each profile line (offset upwards) included to highlight the slope and shape of each profile line fan body (black dashed lines) and fan terminus (solid black lines). Fan numbers in top right-hand corner of each plot correspond to fan numbers in Table 2.8. (**part 2)** Mean downfan σ^0 profile lines for Titan possible fans observed in SAR swath T03 (low- northern latitudes) (colorized data points). Warm colors represent larger values of σ^0. Smoothed versions of each profile line (offset upwards) included to highlight the slope and shape of each profile line fan body (black dashed lines) and fan terminus (solid black lines). Fan numbers in top right-hand corner of each plot correspond to fan numbers in Table 2.8. (**part 3**) Mean downfan σ^0 profile lines for Titan possible fans observed in SAR swath T39 (mid-southern latitudes) (colorized data points). Warm colors represent larger values of σ^0. Smoothed versions of each profile line (offset upwards) included to highlight the slope and shape of each profile line fan body (black dashed lines) and fan terminus (solid black lines). Fan numbers in top right-hand corner of each plot correspond to fan numbers in Table 2.8.

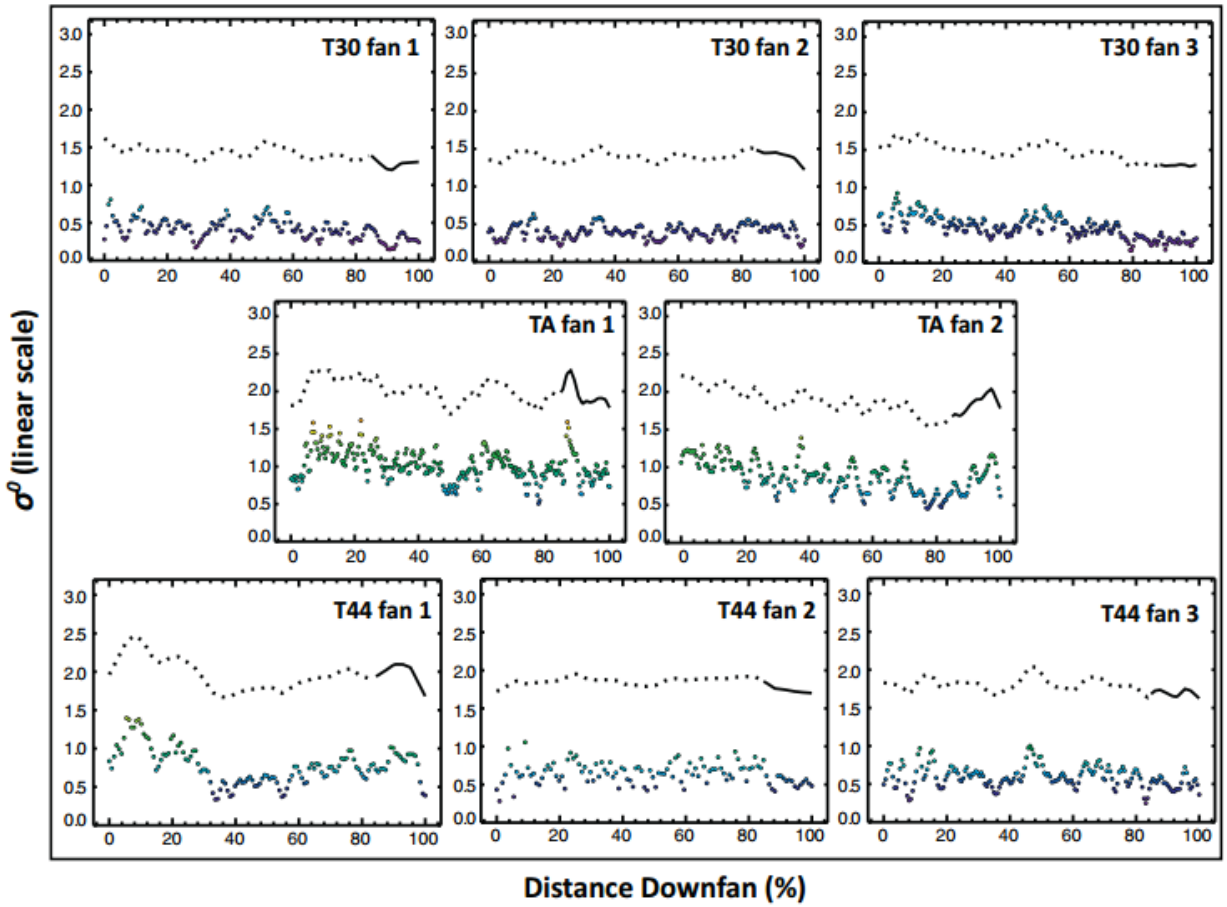

Figure 2.8. Continued.

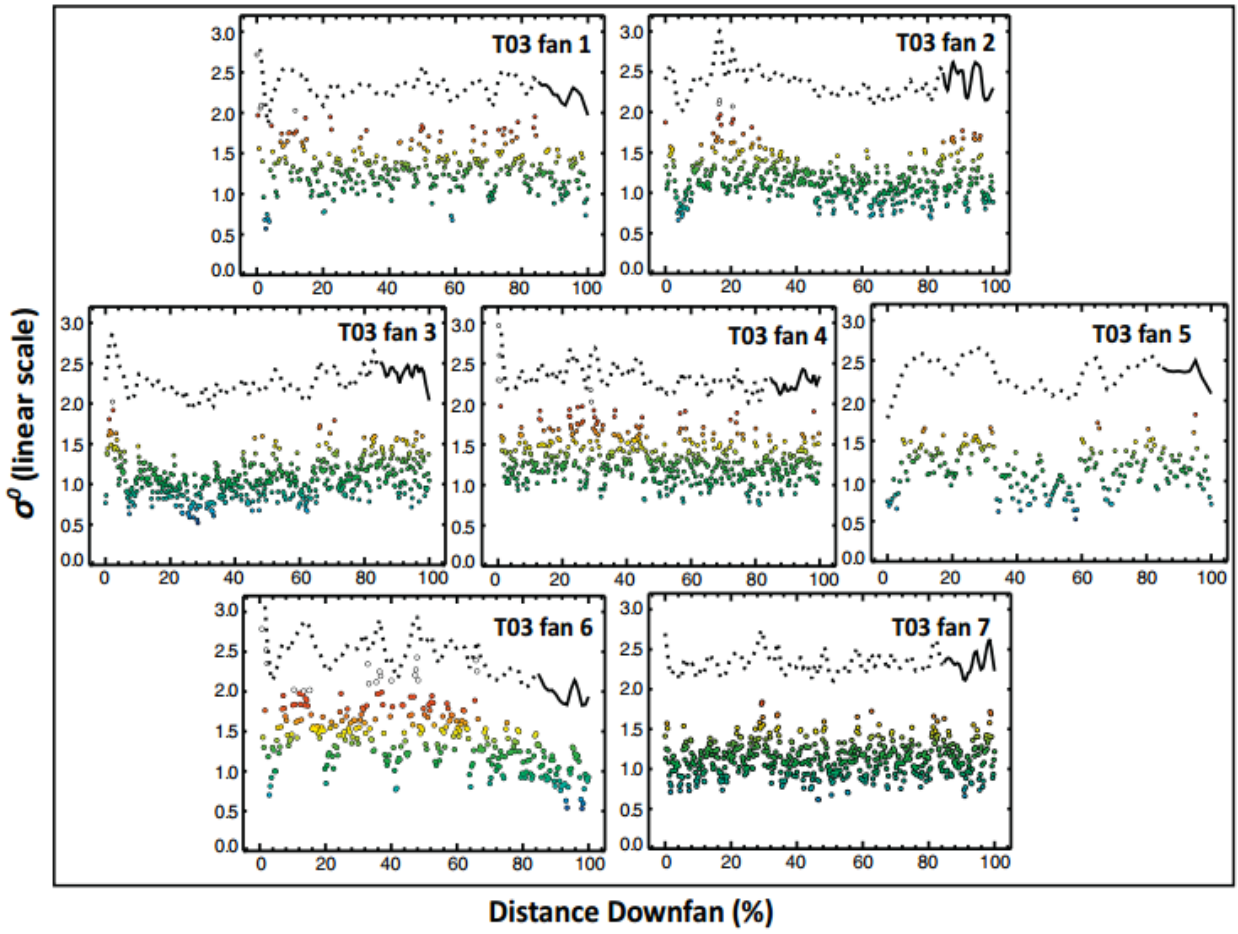

Figure 2.8. Continued.

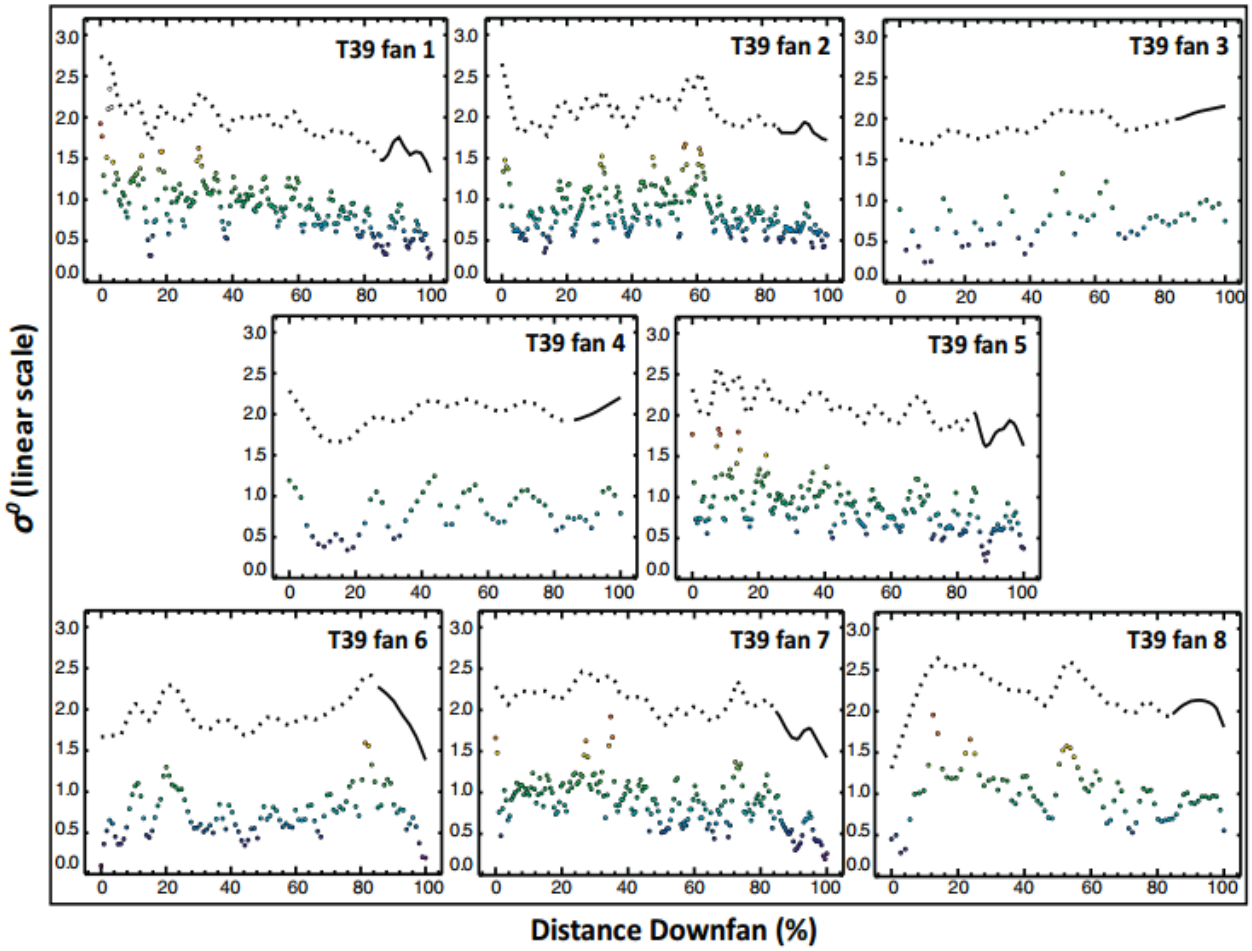

Figure 2.8. Continued.

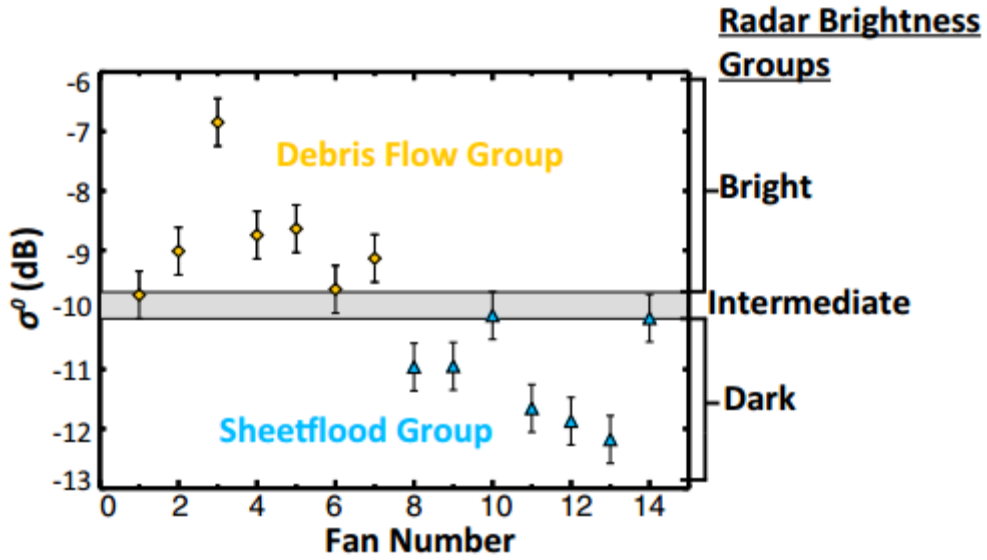

Figure 2.9. Mean σ^0 for the seven debris flow fans (orange diamonds) and seven sheetflood fans (blue triangles) in RS1 image 28205. Error bars represent 2σ radiometric uncertainties for each fan. Debris flow fans with mean σ^0 significantly brighter ($> 2\sigma$) than the brightest sheetflood fan are classified as 'bright', whereas all sheetflood fans with mean σ^0 significantly darker ($> 2\sigma$) than the darkest debris flow fans are classified as 'dark.' Fans that overlap these two groups are classified as 'intermediate.' Fan classification for each RS1 and PALSAR image is summarized in Table 2.9.

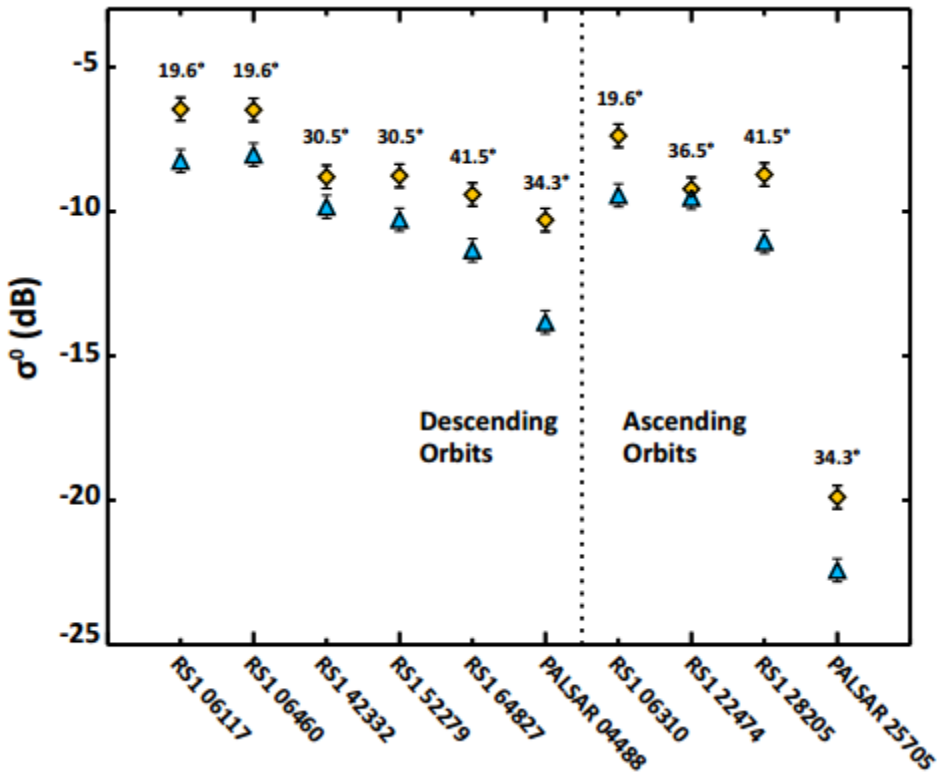

Figure 2.10. Mean σ^0 for the debris flow fan type (orange diamonds) and sheetflood fan type (blue triangles) for ten terrestrial SAR images. Error bars represent 2σ radiometric uncertainties. Incidence angle for each image is shown above each orange diamond/blue triangle pair. PALSAR image 25705 is cross-polarized whereas the other SAR images are all like-polarized. For all ten SAR images, the debris flow fans, as a group, are brighter than the sheetflood fans. Mean σ^0 for both fan types for each image is summarized in Table 2.10

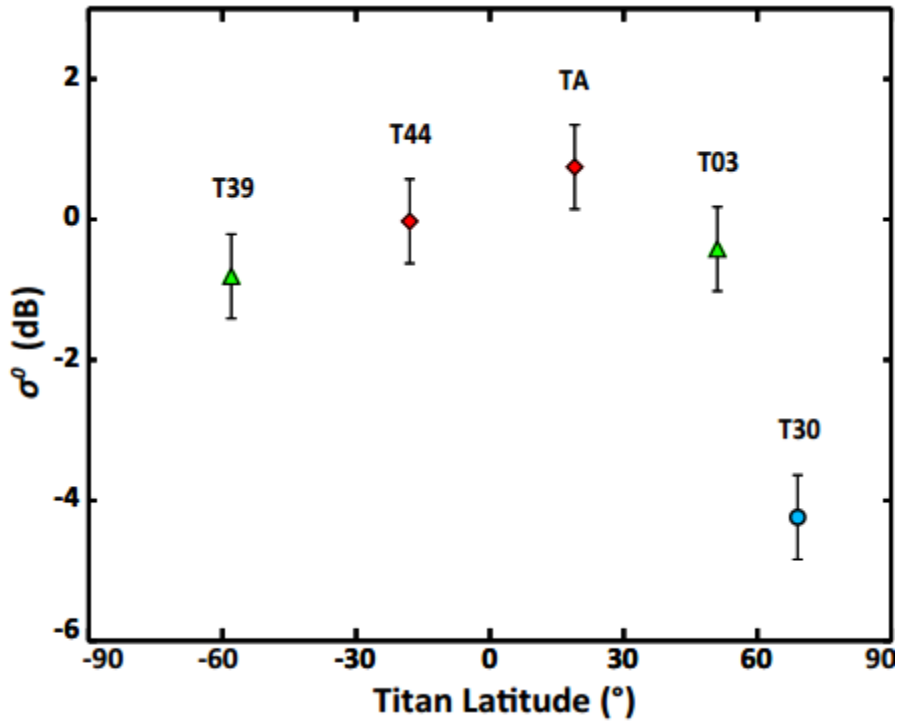

Figure 2.11. Latitude-aggregated mean σ^0 for low latitude (red diamonds), mid latitude (green triangles), and high latitude (blue circle) zones on Titan (Cassini SAR flyby designation indicated above each symbol). Error bars represent 2σ radiometric uncertainties. Latitude-aggregated mean σ^0 for each latitude zone summarized in Table 2.11.

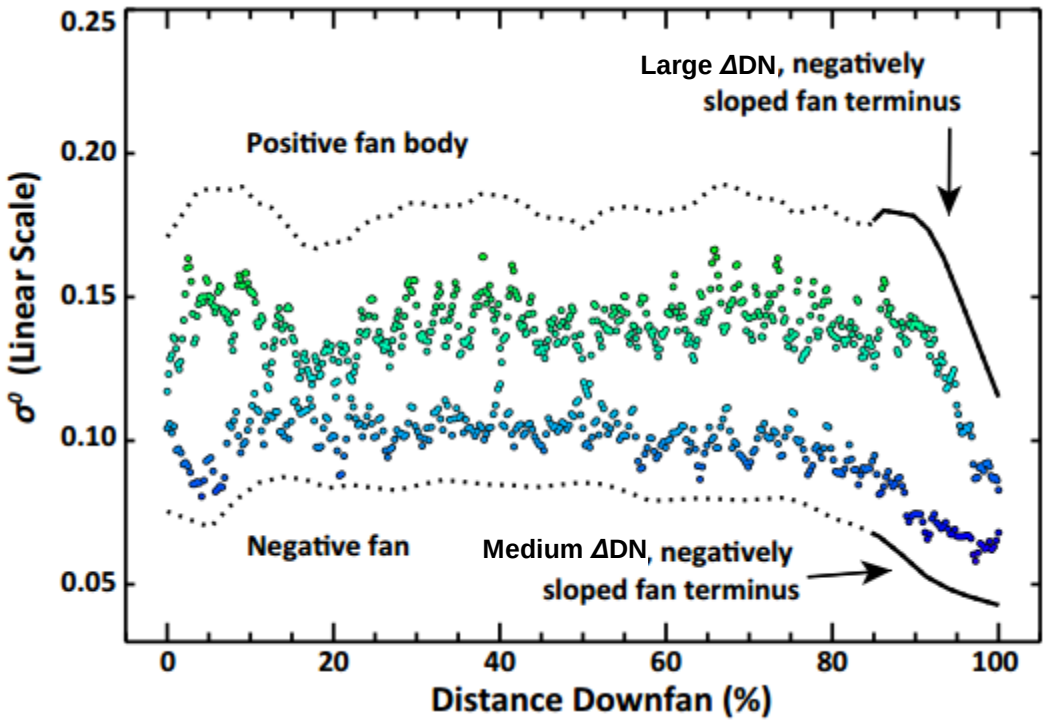

Figure 2.12. Mean σ^0 profile lines for both Panamint fan types (colorized data points). Warm colors represent larger values of σ^0. Smoothed versions of the profile lines (offset upward for debris flow fan and downward for sheetflood fan) are included to highlight the slope and shape of their fan body regions (black dashed lines) and fan terminus regions (solid black lines). Slope classifications for these fan regions are included on the plot and summarized in Table 2.12.

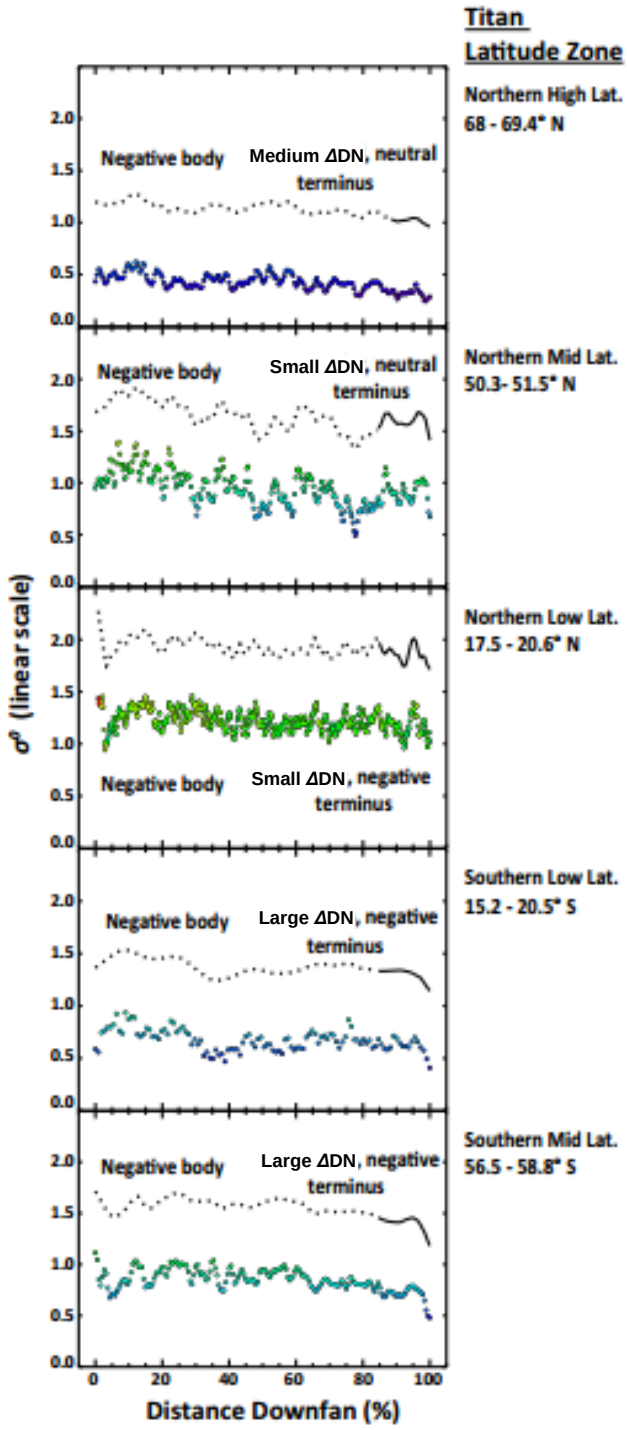

Figure 2.13. Latitude-aggregated profile lines for each latitude zone on Titan (colorized data points). Warm colors represent larger values of σ^0. Smoothed versions of the profile lines (offset upwards) are included to highlight the slope and shape of each profile line fan body (black dashed lines) and fan terminus (solid black lines). Latitude-aggregated profile lines are summarized in Table 2.13.

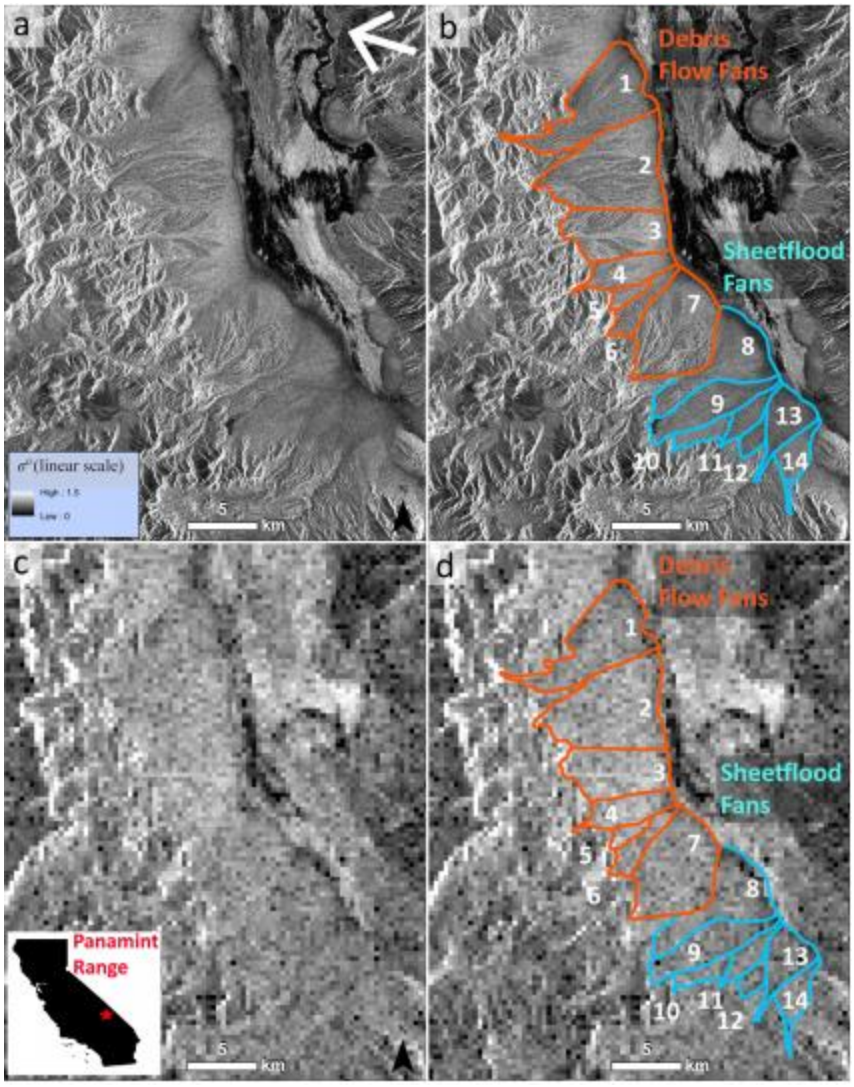

Figure 2.14. RS1 images and mapping of Panamint Range alluvial fans. Insert map of California indicating the location of Death Valley is shown in bottom left hand corner. (**a**) Descending orbit image (06117), with illumination direction indicated by white arrow, (**b**) same image as shown in (a) with delineated fan boundaries, (**c**) same image modified to match spatial resolution (350 m/pixel) and speckle level of Cassini SAR images of Titan, (**d**) same modified image as shown in (c) with the same delineated fan boundaries shown in (b). Numbers correspond to fan numbers in Tables 2.4, 2.5 and 2.8. DN values for pixels in each image scaled from 0 – 1.5. Speckle model designed with input from Bryan Stiles (JPL/Caltech).

CHAPTER 3:

DARK, SPECTRALLY RED MATERIAL ON THE LARGE MOONS OF URANUS: WHAT IS IT AND WHERE DID IT COME FROM?

This chapter is a reformatted version of a paper by the same name in preparation for submission to Icarus by Richard J. Cartwright, Joshua P. Emery, Noemi Pinilla-Alonso, Michael P. Lucas, Andy S. Rivkin, and David E. Trilling. All data collection and analyses were performed by Richard Cartwright.

Abstract

The classical Uranian satellites display clear longitudinal and planetocentric trends in their surface compositions. Spectrally red material has been detected primarily on the leading hemispheres of the outermost moon, Oberon. Furthermore, detected H_2O ice bands are stronger on the leading hemispheres of the classical satellites, and the leading/trailing asymmetry in H_2O ice band strengths decreases with distance from Uranus. We hypothesize that the observed distribution of red material and trends in H_2O ice band strengths results from infalling dust from Uranus' irregular satellites, orbiting beyond the classical moons. These dust particles migrate inward on slowly decaying orbits, eventually reaching the classical satellite zone, where they collide primarily with the outer moons. The latitudinal distribution of dust swept up by these moons should be fairly even across their southern and northern hemispheres. However, red material has only been detected over the southern hemispheres of these moons, during the Voyager 2 flyby of the Uranian system (subsolar latitude ~81ºS). Consequently, to test whether planetocentric dust impacts drive the observed enhancement in reddening, we have gathered new ground-based data, of the now observable northern hemispheres of these moons (sub-observer latitudes ~17 – 35ºN). Additionally, we present spectra that span L/L' bands (~2.9 – 4.1 μm), a previously unexplored wavelength range for these moons, in terms of spectroscopy, and compare the shape and albedo of the spectral continua in these L/L' band data to other icy moons in the Jovian and Saturnian systems. Our results and analyses indicate that longitudinal and planetocentric trends in reddening and H_2O ice band strengths in our new data gathered over the northern latitudes of these moons are similar to the trends observed previously over southern latitudes, thereby supporting our hypothesis. Utilizing a suite of numerical best fit models, we investigate the composition of the reddening agent detected on these moons, finding that both complex organics and amorphous pyroxene match the spectral slopes of our data. We discuss the probable role of space weathering processes in 'graying' the Uranian moons over the age of the Solar System, inferring that the red material was refreshed in the recent past. Finally, we explore possible localized enhancement of reddening on Titania, subtle differences in H_2O ice band strengths between the southern and northern hemispheres of these satellites, the distribution of constituents on Miranda, and the possible presence of NH_3-hydrates on these moons. In closing, we briefly discuss potential directions for future observational and numerical modeling work in the Uranian system.

Introduction

Ground-based observations of the large and tidally-locked Uranian satellites Miranda, Ariel, Umbriel, Titania, and Oberon (Table 3.1) have revealed that the surfaces of these 'classical' moons are dominated by H_2O ice, intimately mixed with a low albedo and spectrally neutral constituent (*e.g.*, Cruikshank, 1980; Cruikshank and Brown, 1981; Soifer et al., 1981; Brown and Cruikshank, 1983; Brown and Clark, 1984). Laboratory experiments suggest that this low albedo material is carbonaceous in composition, spectrally similar to charcoal (*e.g.*, Clark and Lucey, 1984). More recent ground-based observations have detected pure CO_2 ice, segregated from other constituents, primarily on the trailing hemispheres of the moons closest to Uranus (Grundy et al., 2003, 2006; Cartwright et al., 2015). The combination of H_2O ice-rich regions intimately mixed with dark material and regions of pure, segregated CO_2 ice makes this group of moons compositionally distinct from other icy objects in the outer Solar System.

The Imaging Science System (ISS, ~0.4 – 0.6 μm) onboard Voyager 2 collected spatially-resolved images of these satellites during its brief encounter with the Uranian system (*e.g.*, Smith et al., 1986; Stone and Miller, 1986) (Figure 3.1). Analysis of those ISS images demonstrated that the leading hemispheres (1 – 180º longitude) of the Uranian moons are spectrally redder than their trailing hemispheres (181 – 360º longitude) (Bell and McCord, 1991; Buratti and Mosher, 1991; Helfenstein et al., 1991). Furthermore, the detected longitudinal asymmetry in reddening increases with distance from Uranus, peaking on the farthest classical satellite, Oberon (Buratti and Mosher, 1991).

The observed longitudinal and planetocentric trends in reddening on these moons likely result from system-wide surface modification processes. There are three broad types of system-wide mechanisms that operate in giant planet systems: charged particle bombardment, *inter*planetary (heliocentric) dust impacts, and *intra*planetary (planetocentric) dust impacts. Although all three of these processes can redden surfaces (*e.g.*, Bennett et al., 2013 and references therein), the observed longitudinal and planetocentric trends for each process should be distinct. Greater magnetic field densities closer to Uranus (Ness et al., 1986) should increase charged particle bombardment (and enhance the reddening of) the trailing hemispheres of the moons closest to Uranus. Due to gravitational focusing by Uranus, heliocentric dust should preferentially impact (and enhance the reddening of) the leading hemispheres of the moons closest to Uranus (Zahnle et al., 2003). Planetocentric dust particles infalling toward Uranus on decaying orbits should preferentially impact (and enhance the reddening of) the leading hemispheres of the outer classical moons (Tamayo et al., 2013). Furthermore, the nine known irregular satellites of Uranus are all redder than the five classical moons (*e.g.*, Gladman et al., 1998; Grav et al., 2003, 2004; Maris et al., 2002, 2007). Thus, dust from the Uranian irregular satellites represents the most plausible source of red material that can generate planetocentric and longitudinal trends consistent with the observed trends in reddening on the classical moons.

Measurements of the 1.52-μm and 2.02-μm H_2O ice band complexes present in Uranian satellite spectra indicate that H_2O ice bands are stronger on the leading hemispheres of these moons compared to their trailing hemispheres. Furthermore, the

longitudinal asymmetry in H_2O band strengths decreases with distance from Uranus (greatest on Ariel, lowest on Oberon) (Grundy et al., 2006; Cartwright et al., 2015). This longitudinal trend is consistent with greater accumulation of dark, spectrally red dust, which could help mask the spectral signature of H_2O ice on the leading hemispheres of these satellites, in particular the outer moons. Thus, based on the longitudinal and planetocentric trends in reddening and H_2O band strengths, we hypothesize that the red material observed on the classical moons originated on the surfaces of retrograde irregular satellites. The degree of reddening with this mechanism should be similar over southern and northern latitudes of the classical moons, without latitudinal preference.

To test this hypothesis, we have gathered new spectral data of the now observable northern hemispheres of the classical Uranian satellites (sub-observer latitudes ~17 – 35°N). The Voyager 2 encounter with Uranus occurred near southern summer solstice, when the subsolar point was ~81°S, and ISS almost exclusively imaged the southern hemispheres of the Uranian satellites (Figures 3.1 and 3.2). Additionally, previous analyses of H_2O ice band strengths were made using ground-based, NIR spectra collected over the southern hemispheres of these moons (~6 – 30°S) (Grundy et al., 2006). Irregular satellite dust should mantle both the southern and northern hemispheres of the classical moons (Tamayo et al., 2013). Therefore, measurement of spectral slopes and H_2O ice band strengths in our northern hemisphere data, and comparison to these same measurements in previously collected southern hemisphere data, will enable us to constrain the origin of the red material. We precede the presentation of our work with some necessary background on heliocentric and planetocentric dust and other red, icy objects in the outer Solar System.

Background

Planetocentric and heliocentric dust entering the Uranian system

Impact events on irregular satellites eject dust particles off their surfaces and into orbit around their giant planet primary. These ejected dust particles initially have the same orbital elements (semi-major axes, eccentricities, inclinations, etc) as the irregular moon they originated on. However, over ~5 to 500 Myr timescales (for 10 and 1000 μm grain sizes, respectively), the semi-major axes of these dust particles decay due to Poynting-Robertson drag (*i.e.*, loss of forward momentum due to isotropic re-radiation of solar flux) (Burns et al., 1979), and the dust slowly migrates inward. For low obliquity planets like Jupiter and Saturn, almost all of this planetocentric dust collides with the outermost classical satellite in each system (Callisto and Iapetus, respectively).

For high obliquity ($\gtrsim 70^{o}$) planetary systems like Uranus, the inward migration of planetocentric dust is more complicated. In the Uranian system, infalling planetocentric dust particles encounter an unstable 'chaotic' region as their semi-major axes decay (*e.g.*, Tremaine et al., 2009), causing their inclinations and eccentricities to experience large amplitude oscillations over short timescales (~10^4 yrs). Numerical simulations by Tamayo et al. (2013) indicate that the fates of the dust particles depend on their initial orbits (*i.e.*, the orbits of the irregular satellite from which they originate) and the size of

the dust grains. Large dust grains (> 50 μm) with low initial eccentricity ($e_o \lesssim 0.20$) impact Ariel, Umbriel, Titania, and Oberon with fairly even probabilities. In all other cases (small grains and all grain sizes with $e_o \gtrsim 0.20$), the collision probabilities decrease with decreasing planetocentric distance (*i.e.*, are higher at Oberon and decrease systematically to Ariel). This latter situation is most applicable to the Uranus system. Seven of the nine known irregular moons have orbital eccentricities > 0.20. This includes the largest irregular, Sycorax, with an eccentricity of 0.52. Furthermore, Tamayo et al. (2017) find from Cassini imaging of the Phoebe dust ring that the size distribution of that dust is very steep, strongly dominated by small grains (< 20 μm). It is reasonable to assume a similar dust production mechanism in the Uranus system and therefore a similar dominance by small grains. Taking these considerations into account, the numerical simulations by Tamayo et al. (2013) predict that the amount of irregular satellite dust deposition scales inversely with planetocentric distance, with Oberon receiving the most dust.

A leading/trailing dichotomy in dust collisions is also expected. Eight of the nine known Uranian irregular satellites have retrograde orbits. The Tamayo et al. (2013) simulations demonstrate that dust particles from retrograde irregular satellites collide with the leading hemispheres of the classical moons at a higher frequency (factor of ~2 – 3) than their trailing hemispheres. This dust mantle should display a fairly homogenous distribution across both the southern and northern latitudes of these moons. The net result of the Tamayo et al. (2013) models is that dust from retrograde irregular satellites should collide primarily with the leading hemispheres of Oberon, Titania, Umbriel, and Ariel in order of decreasing probability, respectively.

The Uranian moons have likely accumulated substantial amounts of irregular satellite dust over the age of the Solar System. Dynamical simulations indicate that when the irregular satellite swarms of the giant planets were initially captured and/or experienced subsequent orbital perturbations, these objects frequently collided, generating large amounts of dust (Bottke et al., 2010). Much of this primordial dust would have collided with the classical Uranian moons early on in Solar System history. However, recent impacts and collisions between irregular satellites can also generate substantial amounts of dust, as evidenced by the torus of material detected around the Saturnian moon Phoebe (Verbiscer et al., 2009). Dust from Phoebe, and the other Saturnian irregular satellites, is swept up primarily by the leading hemisphere of the outer classical moon, Iapetus, with a small amount reaching the orbits of Titan and Hyperion (*e.g.*, Tamayo et al., 2011).

Unlike planetocentric dust particles, heliocentric dust is not gravitationally bound to Uranus on slowly decaying orbits. Instead, heliocentric micrometeorites enter the Uranian system as high velocity 'bullets,' heading for collisions primarily with Uranus and the leading hemispheres of the inner moons due to gravitational focusing (Tamayo, private communication). The larger leading/trailing asymmetries in H_2O ice band strengths for the moons closer to Uranus are consistent with enhanced regolith overturn by heliocentric dust grains (*e.g.*, Bennett et al., 2013, and references therein). The likely lower velocity of planetocentric dust impacts compared to heliocentric dust impacts (few km s^{-1} and ~10 – 30 km s^{-1}, respectively) should reduce regolith overturn and promote the

accumulation of a layer of planetocentric dust, primarily on the outer moons. Therefore, the combination of fewer heliocentric dust impacts, and more planetocentric dust impacts, on the outer moons should reduce leading/trailing H_2O band asymmetries compared to the inner moons.

Red objects in the outer Solar System

Numerous objects in the outer Solar System have dark, red surfaces, including the north pole of Pluto's moon Charon (Grundy et al., 2016), the leading hemisphere of Iapetus (*e.g.*, Veeder and Matson, 1980), asteroids in the outer Main Belt and in the Jupiter Trojan swarms (*e.g.*, Gaffey et al., 1993; Barucci et al., 1994; Luu et al., 1994), irregular satellites of the jovian planet systems (including those that orbit Uranus) (*e.g.*, Maris et al., 2007), and asteroids in the Kuiper Belt (KBOs) (*e.g.*, Jewitt et al., 1998). Red material exposed on the surfaces of airless bodies becomes less spectrally red (and more spectrally 'gray') over time due to space weathering processes, including charged particle and photon irradiation and micrometeorite dust impacts (*e.g.*, Moroz et al., 2004; Kanuchova et al., 2012; Pieters and Noble, 2016 and references therein). Additional surface modification is required to (re)enhance spectrally red regions by exposing native, or delivering exogenic, 'fresh' material, which is subsequently modified by continued space weathering mechanisms (*e.g.*, Bennett et al., 2013 and references therein).

Many of the red objects observed in the outer Solar System are likely primitive asteroids with ancient and relatively unprocessed surfaces. These primitive asteroids likely experienced sufficient space weathering (via UV photolysis) to generate refractory organic residues, like tholins, from simple hydrocarbon ices (*e.g.*, Cruikshank et al., 2005). Subsequent space weathering of these primitive objects has not yet processed the reddish organic residues exposed on their surfaces into gray carbonaceous species, suggesting that space weathering rates could be relatively low.

Implicit in this interpretation is that simple hydrocarbon ices (like CH_4) were exposed on the primordial surfaces of red objects like the Uranian satellites and primitive asteroids. These simple hydrocarbons were processed into more refractory organics over relatively short timescales, consistent with the rapid generation of tholins from hydrocarbon ices that has been observed in the laboratory (*e.g.*, Sagan and Khare, 1979). The Uranian moon surfaces then grayed much faster than the primitive asteroids due to enhanced space weathering rates. Laboratory experiments have demonstrated that organic residues, left from the irradiation of simple hydrocarbon ices, preferentially lose H atoms when exposed to continued irradiation, making the sample increasingly carbonaceous, and reducing the sample's spectral slope in reflectance spectra (*e.g.*, Cruikshank et al., 1998). Furthermore, the rate of H atom removal from organic residues decreases with continued irradiation (*e.g.*, Lanzerotti et al., 1987), and thus, irradiated organics become spectrally gray more slowly.

Observations and Data Reduction

Uranian satellite observations were made using the NIR SpeX spectrograph/imager at NASA's Infrared Telescope Facility (IRTF) on Mauna Kea

(Rayner et al., 1998, 2003). SpeX spectra were collected by four different teams (summarized in Tables 3.2 and 3.3 and displayed in Figure 3.2). In total, we have analyzed 90 SpeX spectra of the classical Uranian moons (28 collected over their southern hemispheres and 62 over their northern hemispheres). Observing details for each reduced spectrum, including mid-observation satellite latitudes and longitudes are summarized in Table 3.3. Observations made by Grundy were presented in Grundy et al. (2003, 2006), observations made by Gourgeot were presented in Gourgeot et al. (2014), and spectra collected by Rivkin and Cartwright (2012 – 2013) were presented in Cartwright et al. (2015). We refer the reader to these three papers for more information pertaining to each team's data reduction routines. Here, we present 41 new SpeX spectra of the Uranian satellites gathered in PRISM (low resolution, single order) and SXD (moderate resolution, dispersed across multiple orders) modes, with wavelength ranges spanning ~0.7 to 2.5 μm. We also present six new SpeX spectra gathered in LXD "short" mode (moderate resolution, dispersed across multiple orders) that covers a wavelength range of ~1.7 to 4.2 μm (spectral resolution and wavelength range of each mode is summarized in Table 3.2).

Observing setup and data reduction

Prior to 2014, SpeX included a 1024 x 1024 InSb detector and a 512 x 512 InSb array that imaged the slit. The SpeX spectrograph was upgraded in 2014 with a Teledyne 2048 x 2048 H2RG array, and the 1024 x 1024 InSb array was moved to the slit imager (only a 512 x 512 quadrant of the chip is used). All data were collected utilizing the 'AB' nodding mode of SpeX, where the target spectrum is measured in two different positions on the array ('A' and 'B'), separated by 7.5 arcsec along the 15 arcsec slit. First order sky emission correction was performed by subtracting the 'A' position frame from the 'B' position frame. Each team limited individual frame exposure times to a maximum of 120 seconds for SXD and PRISM mode spectra, and 20 seconds for LXD mode spectra, to minimize the impact of atmospheric variability on gathered data. Flat field and wavelength calibration frames were generated using a quartz lamp and argon lamp, respectively, with SpeX's internal integrating sphere. Because argon emission lines are quite weak at wavelengths > 2.5 μm, night sky emission lines are also used to calibrate the longer wavelength orders of LXD mode spectra.

Spectra collected by Rivkin (2000) and Cartwright (2012 – 2017) were extracted, calibrated, and background subtracted using a combination of custom codes and the Spextool data reduction package (Cushing et al., 2004; Vacca et al., 2003). To boost signal-to-noise (S/N), all frames for each object observed on a given night, collected using the same mode of SpeX, were co-added during reduction. Selected analog stars (Table 3.4) were observed at multiple times throughout the night, over a range of airmasses. Satellite spectra were divided by solar analog spectra from the same night, observed at similar airmasses (within ± 0.1 airmasses in most cases), to remove the solar spectrum and correct for telluric absorptions. These reduced spectra were combined using custom programs and the Spextool program suite (Cushing et al., 2004).

To remove residual telluric contamination, we performed subpixel shifting of star and object spectra using custom codes. Additional correction routines were applied to

some of the reduced spectra collected by Cartwright (2012 – 2017), including, interpolation of star airmasses to more precisely match object airmasses and division by an appropriately scaled atmospheric transmission spectrum collected over Mauna Kea. To correct for scattered light from Uranus between ~0.7 and 1.5 μm in some spectra of Ariel and Umbriel, and all Miranda spectra, we used a scaled SpeX spectrum of Uranus gathered each night we observed these moons.

We present 'grand average' PRISM mode spectra for each moon, along with the six longer wavelength LXD mode spectra we have gathered for Ariel, Titania, and Oberon in Figure 3.3. We compare these LXD spectra to broadband geometric albedos calculated using images gathered by the Infrared Array Camera (IRAC, 4 channels spanning ~3.1 to 9.5 μm) (Fazio et al., 2004) onboard the Spitzer Space Telescope (Werner et al., 2004) in the Analysis section of this paper (IRAC geometric albedos were originally presented in Cartwright et al., 2015).

Methods

Leading and trailing hemisphere reflectance ratios

With these new NIR spectra, we quantified the degree of reddening by hemisphere on each moon. Although the SXD and PRISM modes of SpeX cover similar wavelength ranges (~0.7 – 2.5 μm), the cross-dispersed SXD mode spectra have significantly lower S/N at wavelengths $\lesssim$ 1.2 μm compared to PRISM mode spectra, and we therefore conducted our slope analyses using only PRISM spectra. We selected 0.724 μm as the short wavelength end for our reflectance ratio measurements, ensuring high S/N and avoiding any possible 'edge effects' at the short wavelength end of the spectra (~0.67 μm). The analyzed PRISM spectra display an increase in reflectance with wavelength (*i.e.*, spectral reddening) up to ~1.25 μm, and then at longer wavelengths, the spectral continua display neutral slopes until absorption by the 1.52 H_2O ice band starts near 1.4 μm. Consequently, we set the long wavelength end of our reflectance ratio measurements to 1.260 μm, capturing the entire wavelength range where reddening is apparent (~0.72 – 1.25 μm). We averaged an equal number of reflectance data points together at either end of the selected wavelength range: between 0.724 and 0.740 μm ($R_{0.72\ \mu m}$) and 1.230 and 1.260 μm ($R_{1.26\ \mu m}$).

To estimate the uncertainties for these mean reflectances, we calculated the mean error by adding the 1σ instrument errors in quadrature and dividing by the sample size (n). We then calculated the standard deviation of the mean ($\sigma_{\bar{x}} = \sigma/\mathrm{sqrt}(n)$) to estimate the point-to-point variation for both ends of the selected wavelength range. Next, we added the mean error and $\sigma_{\bar{x}}$ in quadrature for both ends ($\Delta R_{0.72\ \mu m}$ and $\Delta R_{1.26\ \mu m}$). Finally, we divided the mean $R_{1.26\ \mu m}$ by the mean $R_{0.72\ \mu m}$ ($R_{1.26\ \mu m}/ R_{0.72\ \mu m}$) for each PRISM spectrum and propagated the errors for these mean reflectances (*e.g.*, Taylor, 1982). The wavelength range of the reflectance ratio measurements is illustrated in Figure 3.4. Because of substantial Uranian scattered light contamination in the Miranda spectra over this wavelength range, we did not calculate reflectance ratios for this innermost classical moon.

Leading and trailing H_2O band area and depth measurements

The spectral signature of H_2O ice includes multiple overlapping combination and overtone band complexes in the NIR region covered by SpeX spectra, centered near 0.81, 0.90, 1.04, 1.25, 1.52, and 2.02 μm, with an additional absorption feature present in crystalline ice-rich surfaces, centered near 1.65 μm (*e.g.*, Mastrapa et al., 2008). Spectral analysis of H_2O ice intimately mixed with dark material (both silicate and carbonaceous species) demonstrates that the strengths of these H_2O ice bands are greatly reduced by relatively minor amounts of dark contaminants (*e.g.*, Clark and Lucey, 1984). Spectra collected over the low albedo, ice-rich surfaces of the Uranian satellites provide clear evidence of the 1.52-μm band, including the crystalline H_2O feature centered near 1.65 μm, and the 2.02-μm band, with no evidence for the weaker H_2O bands between ~0.8 and 1.25 μm. We therefore focused our analysis on the 1.52-μm and 2.02-μm band complexes.

Following Cartwright et al. (2015), we measured the areas and depths of the 1.52-μm and 2.02-μm bands using a modified version of the Spectral Analysis Routine for Asteroids program (SARA, Lindsay et al., 2015). We first defined the continuum on either side of both bands (Table 3.5), taking particular care on the short wavelength end of both H_2O band complexes to avoid any residual telluric contributions. The long wavelength end of the 2.02-μm band was defined using a third order polynomial to fit the 'arched' H_2O ice continuum between 2.215 and 2.230 μm. We then connected the short and long wavelength ends of the bands' continua with a line, and divided both bands by their associated continuum (see example in Figure 3.4). Using the trapezoidal rule, we calculated the integrated 1.52-μm and 2.02-μm H_2O band areas for each spectrum. We estimated the 1σ errors for our band area measurements by running Monte Carlo simulations, resampling from within a Gaussian distribution, represented by the 1σ error bars for each spectral channel. This process was iterated 20,000 times. (for more details on this technique, see Lindsay et al., 2015).

To measure the depths of these two bands, we calculated the mean, continuum-divided reflectance ($R_{band}/R_{continuum}$) between 1.515 and 1.525 μm and 2.015 and 2.025 μm (for the 1.52-μm and 2.02-μm bands, respectively), and subtracted these mean values from 1.0 (wavelength ranges for these band center measurements are shown in Figure 3.4). To estimate uncertainties for these depth measurements, we calculated a mean error by adding the 1σ instrument errors in quadrature and dividing by the sample size (n), and then we calculated $\sigma_{\bar{x}}$ to estimate point-to-point variation for the band center data points. Next, we added the mean error and $\sigma_{\bar{x}}$ in quadrature for each band center measurement.

Results

Detected absorption features and spectral slopes

We clearly detect the 1.52-μm and 2.02-μm H_2O ice band complexes in all of the 41 new SXD and PRISM spectra presented here (see Figs 3.3, 3.4, and Appendix 3-A). We do not detect the H_2O bands between ~0.8 and 1.25 μm because of strong absorption by intimately-mixed dark material that masks the relatively weak H_2O bands in this

wavelength range (*e.g.*, Clark and Lucey, 1984). The absence of these weak H_2O bands is consistent with previous analyses of NIR reflectance spectra of these moons (*e.g.*, Grundy et al., 2006; Cartwright et al., 2015). There is strong evidence for the three CO_2 ice combination and overtone absorption bands centered near 1.966, 2.012, and 2.070 μm in the moderate resolution SXD spectra collected over the trailing hemispheres of these moons (in particular for Ariel), consistent with prior work (Grundy et al., 2003, 2006; Cartwright et al., 2015). We note subtle, but apparent, spectral reddening between ~0.7 and 1.3 μm for Ariel, Umbriel, Titania, and Oberon. For all five moons, we see evidence of spectral 'blueing' (*i.e.*, reduction in reflectance with wavelength) between ~1.4 and 2.5 μm, consistent with the presence of H_2O ice (*e.g.*, Clark et al., 2013, and references therein).

Some of the spectra analyzed in this study hint at the presence of an absorption feature centered near 2.2 μm (Figure 3.5). The spectral characteristics of this feature are (qualitatively) consistent with the position and shape of the 2.2 μm feature detected on Charon, which has been attributed to NH_3-hydrates (*e.g.*, Buie and Grundy, 2000; Brown and Calvin, 2000; Dumas et al., 2001; Cook et al., 2007; Grundy et al., 2016, Cook et al., 2017). A previous study has attributed a similar feature centered near 2.2 μm in spectra of Miranda to NH_3-hydrates as well (Bauer et al., 2002). We consider the implications of the possible detection of NH_3-hydrates on these moons in the Discussion section.

The native S/N of the LXD spectra in L/L' bands (~2.9 – 4.1 μm) are quite low (~1.5 – 3), and thus, we binned these spectra (factor of 50), increasing their S/N up to the ~10 – 20 range, which is sufficient to characterize the shapes and albedos of the continua over this wavelength range. We detect clear evidence for the 3-μm H_2O ice band (Mastrapa et al., 2009) in all six LXD spectra. Additionally, the spectra of Titania and the trailing hemisphere of Oberon hint at the presence of a subtle Fresnel peak centered near 3.1 μm, consistent with the presence of crystalline H_2O ice (Mastrapa et al., 2009). The LXD spectrum of Oberon's leading hemisphere also hints at the presence of an H_2O ice Fresnel peak, but this feature is centered closer to 3.05 μm, which is more consistent with amorphous H_2O ice (Mastrapa et al., 2009). Evidence for a Fresnel peak in the LXD spectra of Ariel is less clear, albeit, the S/N of the Ariel spectra are lower than the S/N of the Titania and Oberon spectra. All six LXD spectra display a steep increase in reflectance on the long wavelength end of the 3-μm H_2O ice band, peaking between ~3.5 to 3.6 μm. The reflectance of the spectra then steadily decreases toward the long wavelength edge of each spectrum (~4.1 μm), presumably due to absorption by the H_2O ice combination band centered near 4.5 μm. We compare these LXD spectra to channel 1 IRAC geometric albedos (presented in Cartwright et al., 2015) in the Analysis section.

Reflectance ratios

The $R_{1.26\ \mu m}/ R_{0.72\ \mu m}$ results indicate an increase in reddening with distance from Uranus, with more pronounced reddening on the outer moons, Titania and Oberon. The leading and trailing hemispheres of Ariel and Umbriel do not display discernable asymmetries in their reflectance ratios, with similar levels of reddening on both their leading and trailing hemispheres. In contrast, the reflectance ratios for the outer moons Titania and Oberon show that their leading hemispheres are significantly redder than their

trailing hemispheres (> 2σ for most of the reflectance ratios). We present further analysis of our reflectance ratio results in the Analysis section.

H_2O ice band areas and depths

Our H_2O ice band parameter measurements (with 1σ uncertainties) are summarized in Table 3.7. Consistent with previous analyses of H_2O ice bands on these moons (Grundy et al., 2006; Cartwright et al., 2015), our band parameter results indicate that the detected H_2O bands are generally stronger (*i.e.*, larger band areas and depths) on the leading hemispheres of these moons, compared to their trailing hemispheres. Our measurements indicate that the strongest H_2O bands are in spectra of the leading hemisphere of Ariel, and the weakest bands are in spectra of Umbriel. When considering only the trailing hemispheres of the Uranian satellites, the Titania spectra display the strongest H_2O bands, with the weakest bands in the Umbriel spectra. Furthermore, the asymmetry in H_2O band strengths between the leading and trailing hemispheres of these moons decreases with distance from Uranus. Unlike the planetocentric and longitudinal trends in H_2O band strengths for Ariel, Umbriel, Titania, and Oberon, the measured H_2O ice bands appear to be slightly stronger on the trailing hemisphere of Miranda. We explore our H_2O ice band measurements further in Analysis section. Because our H_2O band area and depth measurements display the same trends, we focus our subsequent analyses on only the H_2O band area results.

Analysis

In order to constrain the distribution of red material on the classical Uranian satellites, we conducted statistical analyses of our reflectance ratio and H_2O band area results. We focused these analyses on the distribution of these constituents as a function of satellite longitude and as a function of planetocentric distance.

Longitudinal and planetocentric trends in reflectance ratios

To test whether the leading and trailing hemispheres of these moons display statistically significant differences in spectral reddening, we compared our reflectance ratio results (weighted by their uncertainties) to two different models: mean and sinusoidal (solid purple and black dashed lines in Figure 3.6). The mean model is an average reflectance ratio for each moon, representing a surface without statistically significant variations in spectral reddening. The sinusoidal model (utilizing three coefficients: amplitude, phase shift, and vertical offset) represents longitudinal asymmetries in the distribution of spectrally red material on these moons. To statistically compare these models, we used an *F*-test (*e.g.*, Speigel et al., 1992), with the null hypothesis that there is no statistically significant difference between the fits provided by the mean and sinusoidal models.

The results of this *F*-test analysis demonstrate that there is no significant difference between these two models for the inner moons, Ariel and Umbriel, supporting the null hypothesis (Table 3.8). For Titania and Oberon, on the other hand, the *F*-test results indicate that the sinusoidal model is a significantly better fit (> 2σ) for the

reflectance ratio measurements, and we reject the null hypothesis for these two satellites (Table 3.8).

To explicitly look for longitudinal-scale variations of red material on these moons, we also calculated mean reflectance ratios for the leading and trailing hemisphere of each moon, reported in Table 3.9 and Figure 3.7a with 2σ uncertainties. To highlight the trends in reddening on these satellites, we divided the mean reflectance ratios of their leading hemispheres by the mean reflectance ratios of their trailing hemispheres (Figure 3.7b). Similar to our *F*-test analyses of the individual reflectance ratios, the mean reflectance ratios reveal that there is no significant difference in reddening between the leading and trailing hemispheres of the inner moons, Ariel and Umbriel, but a clear difference ($> 2\sigma$) between the leading and trailing hemispheres of the outer moons, Titania and Oberon.

When comparing the mean reflectance ratios for the trailing hemispheres of Umbriel, Titania, and Oberon, we find that these ratios are all statistically similar ($< 2\sigma$ difference), whereas the trailing hemisphere of Ariel is clearly less red than the other moons (Figure 3.7a). Thus, planetocentric trends in reddening are only apparent on the leading hemispheres of these moons. Unlike the analysis of Voyager 2/ISS spectral colors, our mean reflectance ratio analysis demonstrates that the leading hemisphere of Titania is significantly redder ($> 2\sigma$) than the leading hemisphere of the farthest classical satellite, Oberon.

Overall, the results of our PRISM reflectance ratio analyses are consistent with the analysis of Voyager 2/ISS spectral colors. Both datasets show that the leading and trailing hemispheres of the inner moons do not display significant differences in reddening, whereas the leading hemispheres of the outer moons are significantly redder than their trailing hemispheres, and the distribution of spectrally red material is similar over both northern and southern latitudes. Consequently, our reflectance ratio analyses support the hypothesis that spectrally red dust from Uranus' irregular satellites preferentially accumulates on the leading hemispheres of the outer moons.

Longitudinal and planetocentric trends in H_2O band strengths

We investigated the areas of the 1.52-μm and 2.02-μm H_2O ice bands as a function of satellite longitude for all five satellites (Figure 3.8). We used an *F*-test to compare mean and sinusoidal models fit to the H_2O band area data points for each moon (solid purple and black dashed lines in Figure 3.8). The results of this *F*-test analysis (Table 3.8) indicate that there is a significant difference ($> 2\sigma$) for the 1.52-μm and 2.02-μm H_2O band areas between the leading and trailing hemispheres of Ariel, Umbriel, Titania, and Oberon. Unlike the other moons, Miranda appears to display a significant difference ($> 2\sigma$) in H_2O band strength between its anti-Uranus (135 – 225º longitude) and Uranus-facing (315 – 45º longitude) quadrants for the 1.52-μm H_2O ice band (but not the 2.02-μm band). Curiously, the one available data point near the predicted peak at 180º longitude (mid-observation longitude 165.0º) falls well below the model fit. We intend to follow up with additional observations of Miranda to gain a better understanding of the distribution of H_2O band strengths for this moon.

Using the individual H_2O band area measurements reported in the Results section, we calculated mean H_2O band areas (and 2σ uncertainties) for the leading and trailing hemispheres of these moons (Table 3.10, Figure 3.9a and 3.9b). We found a significant difference ($> 2\sigma$) for the 1.52-μm and 2.02-μm H_2O ice bands between the leading and trailing hemispheres of Ariel and Titania. The mean 2.02-μm H_2O ice bands for the leading and trailing hemispheres of Umbriel and Oberon also display significant differences, whereas the 1.52-μm H_2O bands for these two moons does not display significant differences ($> 1\sigma$). We also calculated mean leading/trailing H_2O band area ratios for each moon (Table 3.11, Figure 3.9c). These leading/trailing H_2O band area ratios demonstrate that both H_2O ice band complexes are significantly stronger on the leading hemispheres of Ariel, Umbriel, Titania, and Oberon, but not on the innermost classical moon, Miranda.

Thus, both the *F*-test and mean H_2O band area analyses indicate that H_2O ice bands are stronger on the leading hemispheres of Ariel, Umbriel, Titania, and Oberon (statistically significant differences in band areas in most cases). Furthermore, our analyses show that the difference in H_2O band areas between the leading and trailing hemispheres of these moons tends to decrease with distance from Uranus, consistent with enhanced planetocentric dust accumulation on the leading hemispheres of the outer moons.

Latitudinal variations in H_2O band strengths

Along with mapping longitudinal variations in H_2O band strengths, we compared H_2O ice bands in spectra collected over southern and northern hemispheres for Ariel, Umbriel, Titania, and Oberon. We separated the SpeX spectra into two groups: the southern hemisphere spectra, which were collected by Rivkin and Grundy (sub-observer latitudes ~4 – 30°S) and northern hemisphere spectra, which were gathered by Cartwright (sub-observer latitudes ~17 – 35°N). We further split the southern and northern latitude groups of spectra into leading and trailing quadrants, and then calculated the mean H_2O band areas for all four groups: southern-leading (SL), southern-trailing (ST), northern-leading (NL), and northern-trailing (NT) quadrants (Table 3.12). Next, we divided the mean leading quadrant H_2O band areas by the mean trailing quadrant H_2O band areas ($H_2O_{SL/ST}$ and $H_2O_{NL/NT}$ for southern and northern latitude spectra, respectively) and compared the resulting ratios (Table 3.11, Figure 3.10).

We note visibly apparent, but non-significant ($< 2\sigma$), differences between the $H_2O_{SL/ST}$ and $H_2O_{NL/NT}$ ratios for the mean 1.52-μm and 2.02-μm H_2O ice band areas. The leading/trailing H_2O band area ratios for Ariel, Umbriel, and the 1.52-μm H_2O band area ratio for Titania appear to be larger in the southern latitude dataset compared to the northern latitude dataset. These subtle latitudinal differences in H_2O band areas suggest that more H_2O ice is exposed on the NT quadrants of these moons compared to the ST quadrants. Unlike Ariel, Umbriel, and Titania, the mean H_2O ice band areas for the southern latitude dataset appear to be stronger on the trailing hemisphere of Oberon compared to its leading hemisphere ($> 1\sigma$ difference). This flipped hemispherical asymmetry in the mean H_2O band strengths of Oberon does not hold for the northern latitude spectra of this moon, which have larger mean H_2O band areas on its leading

hemisphere, like the other classical moons (> 2σ difference). Because we only analyzed one spectrum collected over the southern hemisphere of Miranda, we excluded this moon from our analysis of latitudinal variation in H_2O band strengths on the classical Uranian satellites. We discuss the implications of these latitudinal differences in H_2O ice band areas in greater detail in the Discussion section.

Analysis of LXD and IRAC albedos and comparison to other icy moons

We compared broadband L/L' geometric albedos (A_0), calculated using the LXD spectra, to broadband IRAC channel 1 geometric albedos, spanning the same wavelength range (~3.1 – 4.0 μm) (for IRAC image reduction and geometric albedo calculation details, see Cartwright et al., 2015). To do this, we convolved the binned versions of the LXD spectra shown in Figure 3.3 with the IRAC channel 1 filter response curves. The resulting LXD geometric albedos and 1σ uncertainties are summarized, and compared to the mean IRAC geometric albedos previously reported in Cartwright et al. (2015), in Table 3.13. The LXD geometric albedos and their 1σ uncertainties are consistent with the mean IRAC geometric albedos and uncertainties for these moons, adding to our confidence in both datasets.

The Uranian moons are dark over VNIR wavelengths (A_0 ranging from ~0.23 – 0.56 at ~0.96 μm, Table 3.1) compared to H_2O ice-rich moons like Tethys and Rhea (VNIR A_0 of 1.23 and 0.949 at 0.55 μm, respectively, Verbiscer et al., 2007), but are brighter than dark material-rich moons like Iapetus and Callisto (VNIR A_0 of 0.05 and 0.19 at 0.55 μm, respectively, Dalton et al., 2010, and references therein). The LXD and IRAC albedos indicate that the Uranian moons are brighter than these H_2O ice-rich and dark material-rich moons over L/L' band wavelengths. We provide a visual comparison of the LXD spectrum of Oberon's leading hemisphere to LXD spectra of Rhea and Tethys (Emery et al., 2005), an LXD spectrum of Callisto (gathered by our team in 2015), and a Visual Imaging Mapping Spectrometer (VIMS) spectrum of average dark material on Iapetus (Pinilla-Alonso et al., 2011) (Figure 3.11). This comparison demonstrates that ice-rich (Rhea and Tethys) and dark material-rich (Callisto and Iapetus) moons in the Jovian and Saturnian systems have lower albedos in L/L' bands than Oberon. In particular, the peak of the H_2O ice continuum (~3.6 μm) is much more pronounced in the Oberon spectrum compared to these ice-rich and dark material-rich Jovian and Saturnian moons (the other Uranian moons show a similar bright peak in reflectance between ~3.4 and 3.7 μm). Although the albedo of Oberon's spectrum is higher than the ice-rich moons Rhea and Tethys, the shape of the spectral continuum is similar. This 'peaked' continuum shape for Oberon is distinctly different from the spectra of dark material-rich moons Iapetus and Callisto, which steadily increase in reflectance with increasing wavelength.

The similarity of Oberon's continuum shape to Rhea and Tethys in L/L' bands suggests that the Uranian satellites are dominated by the scattering properties of H_2O ice grains over this wavelength range, as opposed to the intimately mixed dark material. Furthermore, the relatively high L/L' band geometric albedos of Oberon and the other Uranian moons suggests that the top veneer of their surfaces are dominated by small H_2O ice grains that promote backscattering and enhance their reflectances. The Uranian moons

therefore represent a compositionally distinct group of icy objects, with relatively dark surfaces in the VIS and NIR (~0.4 – 2.5 μm), and relatively bright surfaces in L/L' bands (~2.9 – 4.1 μm), compared to other H_2O ice-rich moons.

Spectral modeling

Analysis of reflectance spectra (*e.g.*, Brown and Cruikshank, 1983) and laboratory analog studies (*e.g.*, Clark and Lucey, 1984) suggest that the dark material present on the Uranian moons is likely carbonaceous in origin. In this section, we present some of the numerical models we have made to investigate the composition of the Uranian moon surfaces and the range in grain sizes for detected constituents.

Modeling procedure

The numerical models were generated using a Hapke-Mie hybrid modeling program. This hybrid approach utilizes Mie theory (*e.g.*, Bohren and Huffman, 1983) to calculate single scattering albedos for each modeled constituent, and then passes these albedos to Hapke equations (*e.g.*, Hapke, 2002) to model the scattering properties of the selected constituents. The Hapke-Mie codes allow us to generate robust numerical models over a wider range of grain sizes than are permissible using Hapke-based scattering codes alone (Moersch and Christensen, 1995). The numerical models presented here represent a starting point for more comprehensive modeling runs in future work. We focused this analysis on spectra of Oberon's leading and trailing hemispheres.

Previous spectral modeling work of Uranian satellite spectra, using the same Hapke-Mie hybrid codes, demonstrated that best fit spectra between ~1.0 and 2.5 μm generated poor fits to longer wavelength broadband geometric albedos (spanning ~3.1 to 6.5 μm) calculated using Spitzer/IRAC images (Cartwright et al., 2015). Similarly, best fit models that match the IRAC geometric albedos are poor matches to the wavelength region covered by IRTF/SpeX (for more details, see Cartwright et al., 2015).

With the results of previous Uranian moon spectral modeling efforts in mind, we generated synthetic spectra for three different wavelength regions of Oberon: 0.7 – 1.3 μm, 1.2 – 2.5 μm, and 2.9 – 4.1 μm, which from hereon we refer to as 'short,' 'mid,' and 'long' wavelength regions, respectively. Because of the relatively low S/N for SXD spectra at shorter wavelengths (< 1.2 μm), and varying wavelength coverage of these data (Table 3.2), we used the grand average PRISM spectra (shown in Figure 3.3) to generate best fit models for the short wavelength region. For the mid region, we modeled grand average SXD spectra, and for the long region, we modeled the two Oberon LXD spectra presented here (shown in Figures 3.3g and 3.3h).

Modeling results

We used intimate mixtures of crystalline H_2O ice (0.2, 10, and 50 μm grain sizes) and amorphous carbon (7 μm grain size) to match the H_2O ice bands in the mid wavelength region, and added areally mixed CO_2 ice (5 and 10 μm grain sizes) to the models of Oberon's trailing hemisphere, consistent with previous modeling efforts of this moon (Cartwright et al., 2015). To fit the red-sloped continua of the short wavelength region, we included Triton tholins or iron-rich (Fe_{40}) amorphous "pyroxene" (9 μm grain

sizes) in intimate mixtures of crystalline H_2O ice and amorphous C (best fit models summarized in Table 3.14 and shown in Figure 3.12).

Our modeling efforts reveal clear differences between the best fit synthetic spectra for the short, mid, and long wavelength ranges. In the short wavelength region, the reflectance levels of our best fit models are sensitive to the abundance and grain size of amorphous carbon, as well as Triton tholins and pyroxene. However, the short wavelength region models are relatively insensitive to changes in H_2O ice abundance, and they do not display the weak H_2O bands centered near 0.81, 0.90, 1.04, and 1.25 μm, consistent with the absence of these shorter H_2O bands in the spectra we have presented. The insensitivity of our short wavelength region models to changing H_2O ice abundance is a result of the small absorption coefficients, and therefore long penetration depths, of H_2O ice over these wavelengths (Mastrapa et al., 2008). The modeled reddening agents, Triton tholins and pyroxene, represent a smaller fraction of our best fit mid wavelength region synthetic spectra, which are dominated by intimate mixtures of H_2O ice and amorphous C. The long wavelength region synthetic spectra are clearly different than the best fit models for either the short or mid wavelength regions, with much smaller grain sizes (primarily 1 μm diameters) and different abundances for all included components. The small grain size-dominated best fit models we generated for the long wavelength region LXD spectra are consistent with previous spectral models, generated using IRAC channel 1 geometric albedos (Cartwright et al., 2015). Although our best fit models fit the shape and albedo of the long wavelength region, they provide poor fits to the possible Fresnel peaks hinted at in the LXD spectra of Titania and Oberon.

Thus, the spectral signature of our selected reddening agents (Triton tholins and amorphous pyroxene) and amorphous C dominate our models in the short wavelength region, H_2O ice and amorphous C dominate our models in the mid region, and H_2O ice dominates the synthetic spectra in the long region. Our short wavelength region models require a larger fraction of reddening agents (pyroxene and Triton tholins) to match the leading hemisphere spectrum of Oberon compared to its trailing hemisphere spectrum. However, the required fraction of reddening agents in the mid and long region models is not clear cut, with comparable abundance of pyroxene and Triton tholins required for both the leading and trailing hemisphere of Oberon.

Discussion

Our reflectance ratio and H_2O ice band area results and analyses indicate that longitudinal and planetocentric trends in composition are present on the classical Uranian satellites, with more spectrally red material on the leading hemispheres of the outer moons. These results and analyses are supported by our short wavelength region best fit models, which require a larger fraction of reddening agents to match the leading hemisphere spectra of Oberon compared to spectra of its trailing hemisphere. In the following sections, we discuss the implications of our results and analyses and compare the Uranian moons to other red, icy moons. We also explore the implications of our spectral modeling work, the different distribution of constituents on Miranda compared to

the other classical satellites, and the implications of the possible presence of NH_3-hydrates on these moons.

Implications of the observed trends in spectrally reddening

Unlike the unprocessed surfaces of spectrally-reddened, primitive asteroids in the outer Solar System, the classical Uranian satellites have experienced extensive space weathering from bombardment by charged particles embedded in Uranus' magnetic field (*e.g.*, Stone et al., 1986; Lanzerotti et al., 1987), as well as from more frequent heliocentric dust impacts due to gravitational focusing by Uranus (*e.g.*, Zahnle, 2003; Tamayo et al., 2013). This enhancement in space weathering rates for the Uranian moons likely grayed their surfaces relatively fast compared to more primitive red objects, in particular for the inner moons, where charged particle and heliocentric dust impacts are far more frequent than on the outer moons. Consequently, the presence of red material on the four largest classical moons indicates recent replenishment of this constituent, most likely due to the accumulation of irregular satellite dust particles generated by recent impacts, analogous to the dust torus around Phoebe that is slowly mantling the leading hemisphere of Iapetus.

Unlike the Voyager 2/ISS results, our analyses indicate that the leading hemisphere of Titania is significantly redder than Oberon, largely due to the reflectance ratios of two spectra with mid-observation longitudes of 21.3º and 29.0º. The mid-observation longitudes of these two spectra are clearly separated from Titania's apex (the location predicted to experience the most heliocentric dust impacts, *e.g.*, Zahnle et al., 2003). Furthermore, the reflectance ratios for these two spectra are significantly larger than the reflectance ratio for the one spectrum collected near Titania's apex (113.8° longitude) (Table 3.6). Analysis of the Voyager 2/ISS dataset did not lead to the detection of enhanced reddening on Titania (relative to Oberon). It therefore appears that a locally enhanced red spot exists on the northern hemisphere of Titania, between 20-30º longitude. Additionally, slightly weaker H_2O band strengths in spectra collected over the SL quadrant of Oberon and the NL quadrant of Titania coincide with the regions of enhanced reddening on these two moons, demonstrating a possible connection between enhanced reddening and weaker H_2O bands.

Evidence of dark, red, and smooth regions mantling crater floors are present in the Voyager 2/ISS images of Oberon's southern hemisphere (Smith et al., 1986). These crater floor deposits have been interpreted as cryovolcanically-emplaced units, possibly of organic-rich materials (*e.g.*, Croft and Soderblom, 1991 and references therein). Alternatively, the red material might have originated in Titania's subsurface and has been recently exposed by tectonic activity, mass wasting, and/or impact events. Consequently, along with mantling by planetocentric red dust, geologic processes could be enhancing the red spectral color of this region. The absence of spatially-resolved images of the northern hemispheres of the classical Uranian moons limits our ability to search for crater-filling deposits, and other signs of localized geologic activity, in this region of Titania.

Possible influence of charged particle bombardment on H_2O ice band strengths

Along with heliocentric and planetocentric dust impacts, bombardment by charged particles trapped in Uranus' magnetic field could contribute to the observed longitudinal asymmetries in H_2O ice band strengths (Cartwright et al., 2015). It has been hypothesized that charged particle radiolysis drives the generation of the detected CO_2 ice, converting native H_2O ice and C-rich materials into CO_2 (Grundy et al., 2006; Cartwright et al., 2015). This process could enhance leading/trailing asymmetries in H_2O band strengths by reducing the amount of exposed H_2O ice on the trailing hemispheres of these satellites, in particular on the inner moons, where charged particles densities are higher (*e.g.*, Ness et al., 1986, Stone et al., 1986).

The observed differences in SL and NL mean H_2O bands could be the result of enhanced magnetospheric bombardment of either northern or southern latitudes on these moons, driving enhanced generation of CO_2 ice and replacing native H_2O ice deposits. The large angular offset (~60°) observed during the Voyager 2 flyby between Uranus' rotational and magnetic field axes (*e.g.*, Ness et al., 1986) appears to qualitatively support preferential charged particle bombardment of the northern hemispheres of these moons. Furthermore, dynamical modeling of charged particle bombardment trajectories demonstrates that low and high energy electrons preferentially impact different latitude and longitude zones of the tidally-locked Galilean moon, Europa (*e.g.*, Cassidy et al., 2013). By analogy to the Jovian system, perhaps low and high energy charged particles in Uranus' magnetosphere also bombard different longitudinal and latitudinal zones of the classical satellites, generating differences in H_2O band strengths on their southern and northern hemispheres. Detailed numerical modeling of magnetic field interactions with the classical Uranian satellites (for example, building on the work of Cao and Paty, 2017) would provide key insight into possible latitudinal preferences of charged particle irradiation and represents critical future work for understanding radiolytic chemistry in the Uranian system.

Implications of the best fit spectral models of Oberon

The e-folding absorption lengths of photons into H_2O ice are a steep function of wavelength (see Figure 3.13 in Cartwright et al., 2015), with photons in the short and mid wavelength regions penetrating much further (~0.1 to > 10 mm depths) compared to photons in the long wavelength range (< 0.001 to ~0.05 mm depths). Additionally, our estimates of the MOPL, calculated using the best fit spectral models of these moons' trailing hemispheres, indicate similar penetration depths for photons in these two wavelength ranges (~0.15 to > 10 mm between 0.7 and 2.5 μm and ~0.001 to 0.05 mm between 2.9 and 4.1 μm). Consequently, comparison of our short/mid and long wavelength region spectral models suggest that we are probing two distinct compositional layers.

Over the short and mid wavelength regions, where H_2O ice absorption is quite weak, photons probe much greater depths into the near-surface of Oberon, and are primarily absorbed by the intimately mixed dark material. The enhancement of dark material absorption leads to a reduction in albedo over this wavelength range, weakens the 1.52-μm and 2.02-μm H_2O ice bands, and effectively masks the weaker H_2O ice

bands between ~0.8 and 1.3 μm. Whereas, over the long wavelength region, where H_2O ice absorbs strongly, the spectra likely probe only the top veneer of Oberon's regolith, where small H_2O ice grains appear to dominate. These small H_2O ice grains enhance backscatter and increase the reflectance of the L/L' band spectra, in particular for the spectral continuum region between ~3.4 and 3.7 μm (on the long wavelength end of the 3-μm H_2O ice band).

Comparing the distribution of constituents on Miranda to the other classical moons

The subtly stronger H_2O ice bands on the trailing hemisphere of Miranda might be the result of ring particle bombardment, driving enhanced regolith overturn of its trailing hemisphere. In this scenario, ring particles become electrically charged, experience a Lorentz force as magnetic field lines sweep past them, and then slowly spiral outward until their orbits intersect Miranda (Grundy et al., 2006). However, the impact velocities between electrically-charged ring material and Miranda are likely low (Grundy et al., 2006), which would tend to spur mantling of Miranda's trailing hemisphere with dark, non-ice ring material, as opposed to regolith overturn and refreshment of H_2O ice.

CO_2 ice has not been detected on Miranda (Bauer et al., 2002; Grundy et al., 2006; Gourgeot et al., 2014; Cartwright et al., 2015). Although the low S/N (~5 – 20) of the available Miranda spectra could be obscuring low levels of CO_2 ice (band depths $\lesssim$ 5% of the continuum), this small amount of CO_2 is much less than the abundance of CO_2 on Ariel (band depths ~15% of the continuum). It is plausible that the lower mass of Miranda compared to the other classical moons (Table 3.1) allows more CO_2 molecules to escape into space, decreasing CO_2 molecule retention timescales on Miranda (Grundy et al., 2006).

Possible presence of NH_3-hydrates on the Uranian moons

Some of the spectra presented here display a subtle absorption feature centered near 2.2 μm (Figure 3.5), similar to the NH_3-hydrate feature identified on Charon in ground-based (*e.g.*, Brown and Calvin, 2000) and New Horizons (*e.g.*, Grundy et al., 2016) reflectance spectra. The potential presence of this constituent on the Uranian moons is a tantalizing possibility given that this volatile should be efficiently removed by a combination of space weathering processes and sublimation (estimated peak surface temperatures of Miranda and Ariel, 83 to 87 K, Hanel et al., 1986). This possible NH_3-hydrate absorption feature does not appear to display longitudinal trends (*i.e.*, preferentially on the leading or trailing hemispheres of these moons), suggesting that the distribution of this constituent could be controlled by geologic processes.

Numerous geologic features on these moons, including long linear grooves in chasmata on Ariel and smooth plains and crater deposits on the other moons, have been interpreted as cryovolcanic in origin (*e.g.*, Smith et al., 1986; Jankowski and Squyres, 1988; Schenk, 1991; Kargel, 1994). The subtle 2.2 μm absorption feature could therefore result from cryovolcanic emplacement of NH_3-hydrates, and other volatiles, on the surfaces of these satellites. The 2.2 μm absorption feature could also result from exposure of subsurface NH_3-hydrate deposits by tectonic processes, which have likely modified the

surfaces of these moons (*e.g.*, Smith et al., 1986; Helfenstein et al., 1989; Pappalardo et al., 1997; Beddingfield et al., 2015). Alternatively, NH_3-hydrates could be exposed and/or delivered by impactors, possibly analogous to the spatial association between spectra with strong NH_3-hydrate features and some of the craters on Charon (Grundy et al., 2016).

Summary and Future Work

We measured the reflectance ratios ($R_{1.26\ \mu m}$/ $R_{0.72\ \mu m}$) and 1.52-µm and 2.02-µm H_2O band areas and depths of 84 SpeX spectra to test the hypothesis that the spectrally red material observed on the classical Uranian moons originated on Uranus' retrograde irregular satellites. Our results indicate that the leading hemispheres of these moons are redder than their trailing hemispheres, and that the outer moons are significantly redder than the inner moons (subsolar latitudes ~17 to 35°N), consistent with the Voyager 2/ISS spectral colors (subsolar latitude ~81°S), demonstrating that spectrally red material is present at all observed latitudes of the classical Uranian satellites. The fairly homogenous distribution of red material across the leading hemispheres of (primarily) the outer moons is broadly consistent accumulation of dust particles that originated on retrograde irregular satellites. Our analysis of H_2O band areas demonstrates that H_2O ice bands are stronger on the leading hemispheres of Ariel, Umbriel, Titania, and Oberon than on their trailing hemispheres, and leading/trailing longitudinal asymmetries in H_2O band strengths decrease with distance from Uranus. The reduction in longitudinal asymmetries in H_2O ice band strengths with distance from Uranus is consistent with increased accumulation of planetocentric dust on the leading hemispheres of (primarily) the outer moons. Therefore, our results and analyses support the hypothesis that the spectrally red material, observed in Voyager 2/ISS images and detected in ground-based spectra of the classical moons, originated on retrograde irregular satellites.

Miranda, the innermost classical moon, does not display the same compositional trends, with no evidence for CO_2 ice (at the > 5% level of the continuum), no red material, and possibly stronger H_2O ice bands on its trailing hemisphere, unlike the other moons. Furthermore, some of the spectra for all five of these moons hint at the presence of NH_3-hydrates. Given the short lifespan of NH_3-hydrates on airless bodies at the estimated surface temperatures of the Uranian moons, this volatile constituent could represent evidence of recent geologic resurfacing, by an emplacement (cryovolcanism) and/or exposure mechanism (impacts, mass wasting, tectonism).

We have observed the classical Uranian satellites for the past five years using IRTF/SpeX (subsolar latitudes ~17 – 35ºN). Analysis of the NIR spectra we have collected indicates that the surfaces of these objects are predominantly composed of H_2O ice intimately mixed with a spectrally neutral, dark constituent, with stronger H_2O ice bands on their leading hemispheres. Intimately mixed, spectrally-reddened material is also present, primarily on the leading hemispheres of the outer moons Titania and Oberon. CO_2 ice is present primarily on the trailing hemispheres of the inner moons, Ariel and Umbriel, but has not been detected on the innermost classical moon, Miranda. Our relative band area measurements and spectral models indicate that the detected CO_2

ice is pure (*i.e.*, molecularly bound to other CO_2 ice molecules) and segregated (*i.e.*, surrounded primarily by other CO_2 ice grains).

The longitudinal and planetocentric trends in the distribution of red material, CO_2 ice, and H_2O ice band strengths suggest that space weathering mechanisms operate differently throughout the Uranian system, thereby modifying the compositions of these moons with different efficiencies and at non-uniform rates. For the inner moons, Ariel and Umbriel, where charged particle irradiation is more intense and heliocentric dust impacts occur more frequently, CO_2 ice abundance and longitudinal asymmetries in H_2O ice band strengths are greater. For the outer moons, Titania and Oberon, where planetocentric dust impacts are more frequent, red material is more abundant.

The classical Uranian satellites are located at a heliocentric "crossroads" between the warmer Jovian and Saturnian satellite systems, where the detected CO_2 ice is molecularly bound to more refractory components (*e.g.*, Clark et al., 2013, and references therein), and the colder Neptunian satellite, Triton, where CO_2 ice is pure and segregated, but displays no longitudinal asymmetries in its distribution and is non-mobile (Holler et al., 2016), unlike the CO_2 ice on the Uranian moons. Thus, these moons represent a distinct group of dark, icy objects with different spectral characteristics from the icy moons of the closer in gas giants and icy objects beyond the Uranian system.

New ground- and space-based telescopic observations of the classical Uranian moons would complement and build on the data presented here. Additional observations of Titania could provide key insight into the extent of the localized red spot we have identified on its leading hemisphere. New, high S/N, NIR spectra of Miranda would improve our understanding of the distribution of constituents on the innermost moon. Similarly, additional spectra with high S/N in the 2.1 to 2.3 μm wavelength range would help us search for and characterize the subtle absorption feature centered near 2.2 μm, which hints at the presence of NH_3-hydrates on these moons. Investigation of these moons at wavelengths > 2.5 μm is still at an early stage, and additional L/L' band spectra, gathered using ground-based telescopes and NASA's James Webb Space Telescope (scheduled to launch in 2018), would provide us with critical new data to constrain the compositions of the dark material on the Uranian moons. In particular, new, high S/N, L/L' band spectra could determine whether organic species are exposed on the surfaces of these moons by searching for C-H stretching features centered between ~3.3 and 3.4 μm, which could be present in the data we analyzed here but obscured by their low S/N. Additionally, a dedicated mission to the Uranian system would provide critical data for understanding the compositions of these satellites, the origin of their surface constituents, and the system-wide processes that modify their surfaces.

Along with follow up observations, new modeling work of Uranus' plasma environment would provide key insight into interactions between magnetospherically-embedded charged particles and the surfaces of the classical Uranian satellites. These charged particle-satellite surface simulations would dramatically improve our understanding of the resulting radiolytic chemistry on these moons, especially regarding the origin of CO_2 ice, and whether the subtle latitudinal asymmetries in H_2O ice band strengths that we have detected are the result of charged particle bombardment. Finally, spectral modeling codes that can accommodate multiple, distinct regolith layers could

help future investigations of whether the near-surfaces of the Uranian satellites are compositionally-stratified.

References

Barucci, M.A., Lazzarin, M., Owen, T., Barbieri, C. and Fulchignoni, M., 1994. Near-infrared spectroscopy of dark asteroids. *Icarus*, *110* (2), p.287-291.

Bauer, J.M., Roush, T.L., Geballe, T.R., Meech, K.J., Owen, T.C., Vacca, W.D., Rayner, J.T. and Jim, K.T., 2002. The near infrared spectrum of Miranda: Evidence of crystalline water ice. *Icarus*, *158* (1), p.178-190.

Beddingfield, C.B., Burr, D.M., Emery, J.P., 2015. Fault geometries on Uranus' satellite Miranda: Implications for internal structure and heat flow. *Icarus 247*, 35–52. http://dx.doi.org/10.1016/j.icarus.2014.09.048.

Bell III, J.F. and McCord, T.B., 1991. A search for spectral units on the Uranian satellites using color ratio images. In *Lunar and Planetary Science Conference Proceedings*, Vol. 21, p. 473-489.

Bennett, C.J., Pirim, C. and Orlando, T.M., 2013. Space-weathering of solar system bodies: a laboratory perspective. *Chemical reviews*, *113* (12), p.9086-9150.

Bohren, C.F. and Huffman, D.R., 1983. Absorption and scattering by a sphere. *Absorption and Scattering of Light by Small Particles*, p.82-129.

Bottke, W.F., Nesvorný, D., Vokrouhlický, D. and Morbidelli, A., 2010. The irregular satellites: The most collisionally evolved populations in the Solar System. *The Astronomical Journal*, *139* (3), p.994.

Brown, M.E. and Calvin, W.M., 2000. Evidence for crystalline water and ammonia ices on Pluto's satellite Charon. *Science*, *287* (5450), p.107-109.

Brown, R.H. and Clark, R.N., 1984. Surface of Miranda: Identification of water ice. *Icarus*, *58* (2), p.288-292.

Brown, R.H. and Cruikshank, D.P., 1983. The Uranian satellites: Surface compositions and opposition brightness surges. *Icarus*, *55* (1), p.83-92.

Buie, M.W. and Grundy, W.M., 2000. The distribution and physical state of H_2O on Charon. *Icarus*, *148* (2), p.324-339.

Buratti, B.J. and Mosher, J.A., 1991. Comparative global albedo and color maps of the uranian satellites. *Icarus*, *90* (1), p.1-13.

Burns, J.A., Lamy, P.L. and Soter, S., 1979. Radiation forces on small particles in the solar system. *Icarus*, *40* (1), p.1-48.

Cao, X. and Paty, C., Diurnal and Seasonal Variability of Uranus' Magnetosphere. *Journal of Geophysical Research: Space Physics*, *122*, p.6318-6331.

Cartwright, R.J., Emery, J.P., Rivkin, A.S., Trilling, D.E. and Pinilla-Alonso, N., 2015. Distribution of CO_2 ice on the large moons of Uranus and evidence for compositional stratification of their near surfaces. *Icarus*, *257*, p.428-456.

Cassidy, T.A., Paranicas, C.P., Shirley, J.H., Dalton III, J.B., Teolis, B.D., Johnson, R.E., Kamp, L. and Hendrix, A.R., 2013. Magnetospheric ion sputtering and water ice grain size at Europa. *Planetary and Space Science*, *77*, p.64-73.

Clark, R.N., Carlson, R., Grundy, W. and Noll, K., 2013. Observed ices in the Solar System. In *The Science of Solar System Ices*, p. 3-46. Springer New York.

Clark, R.N. and Lucey, P.G., 1984. Spectral properties of ice-particulate mixtures and implications for remote sensing: 1. Intimate mixtures. *Journal of Geophysical Research: Solid Earth*, *89* (B7), p.6341-6348.

Cook, J.C., Desch, S.J., Roush, T.L., Trujillo, C.A. and Geballe, T.R., 2007. Near-infrared spectroscopy of Charon: Possible evidence for cryovolcanism on Kuiper belt objects. *The Astrophysical Journal*, *663* (2), p.1406.

Cook et al. [In Prep]. Composition of Pluto's small satellites: Analysis of New Horizons Spectral Images.

Croft, S.K. and Soderblom, L.A., 1991. Geology of the Uranian satellites. *Uranus*, p.561-628.

Cruikshank, D.P., Morrison, D. and Pilcher, C.B., 1977. Identification of a new class of satellites in the outer solar system. *The Astrophysical Journal*, *217*, p.1006-1010.

Cruikshank, D.P., 1980. Near-infrared studies of the satellites of Saturn and Uranus. *Icarus*, *41* (2), p. 246-258.

Cruikshank, D.P., Roush, T.L., Bartholomew, M.J., Geballe, T.R., Pendleton, Y.J., White, S.M., Bell, J.F., Davies, J.K., Owen, T.C., De Bergh, C. and Tholen, D.J., 1998. The composition of centaur 5145 Pholus. *Icarus*, *135* (2), p.389-407.

Cruikshank, D.P., Imanaka, H. and Dalle Ore, C.M., 2005. Tholins as coloring agents on outer Solar System bodies. *Advances in Space Research*, *36* (2), p.178-183.

Cruikshank, D.P. and Brown, R.H., 1981. The uranian satellites: Water ice on Ariel and Umbriel. *Icarus*, *45* (3), p.607-611.

Cushing, M.C., Vacca, W.D. and Rayner, J.T., 2004. Spextool: a spectral extraction package for SpeX, a 0.8-5.5 micron cross-dispersed spectrograph. *Publications of the Astronomical Society of the Pacific*, *116* (818), p.362.

Dalton, J.B., Cruikshank, D.P., Stephan, K., McCord, T.B., Coustenis, A., Carlson, R.W. and Coradini, A., 2010. Chemical composition of icy satellite surfaces. *Space science reviews*, *153* (1-4), p.113-154.

Dumas, C., Terrile, R.J., Brown, R.H., Schneider, G. and Smith, B.A., 2001. Hubble Space Telescope NICMOS spectroscopy of Charon's leading and trailing hemispheres. *The Astronomical Journal*, *121* (2), p.1163.

Emery, J.P., Burr, D.M., Cruikshank, D.P., Brown, R.H. and Dalton, J.B., 2005. Near-infrared (0.8–4.0 μm) spectroscopy of Mimas, Enceladus, Tethys, and Rhea. *Astronomy & Astrophysics*, *435* (1), p.353-362.

Emery, J.P., Cruikshank, D.P. and Van Cleve, J., 2006. Thermal emission spectroscopy (5.2–38 μm) of three Trojan asteroids with the Spitzer Space Telescope: Detection of fine-grained silicates. *Icarus*, *182* (2), p.496-512.

Fazio, G.G., Hora, J.L., Allen, L.E., Ashby, M.L.N., Barmby, P., Deutsch, L.K., Huang, J.S., Kleiner, S., Marengo, M., Megeath, S.T. and Melnick, G.J., 2004. The infrared array camera (IRAC) for the spitzer space telescope. *The Astrophysical Journal Supplement Series*, *154* (1), p.10.

Gaffey, M.J., Burbine, T.H. and Binzel, R.P., 1993. Asteroid spectroscopy: Progress and perspectives. *Meteoritics*, *28* (2), p.161-187.

Gladman, B.J., Nicholson, P.D., Burns, J.A., Kavelaars, J.J., Marsden, B.G., Williams, G.V. and Offutt, W.B., 1998. Discovery of two distant irregular moons of Uranus. *Nature*, *392* (6679), p.897-899.

Gourgeot, F., Dumas, C., Merlin, F., Vernazza, P. and Alvarez-Candal, A., 2014. Near-infrared spectroscopy of Miranda. *Astronomy & Astrophysics*, *562*, p. A46.

Grav, T., Holman, M.J., Gladman, B.J. and Aksnes, K., 2003. Photometric survey of the irregular satellites. *Icarus*, *166* (1), p.33-45.

Grav, T., Holman, M.J. and Fraser, W.C., 2004. Photometry of irregular satellites of Uranus and Neptune. *The Astrophysical Journal Letters*, *613* (1), p.L77.

Grundy, W.M. and Schmitt, B., 1998. The temperature-dependent near-infrared absorption spectrum of hexagonal ice. *Journal Geophysical Research, 103*, p.25809-25822.

Grundy, W.M., Young, L.A. and Young, E.F., 2003. Discovery of CO_2 ice and leading–trailing spectral asymmetry on the uranian satellite ariel. *Icarus*, *162* (1), p.222-229.

Grundy, W.M., Young, L.A., Spencer, J.R., Johnson, R.E., Young, E.F. and Buie, M.W., 2006. Distributions of H 2 O and CO 2 ices on Ariel, Umbriel, Titania, and Oberon from IRTF/SpeX observations. *Icarus*, *184* (2), p.543-555.

Grundy, W.M., Binzel, R.P., Buratti, B.J., Cook, J.C., Cruikshank, D.P., Dalle Ore, C.M., Earle, A.M., Ennico, K., Howett, C.J.A., Lunsford, A.W. and Olkin, C.B., 2016. Surface compositions across Pluto and Charon. *Science*, *351* (6279), p.9189.

Hanel et al., 1986. Infrared observations of the Uranian System. *Science*, *233* (4759), p.70-74.

Hapke, 2002. Theory of Reflectance and Emittance Spectroscopy. Cambridge University Press.

Hapke, 2012. Theory of Reflectance and Emittance Spectroscopy (2nd Ed.). Cambridge University Press.

Helfenstein, P., Thomas, P.C., Veverka, J., 1989. Evidence from Voyager II photometry for early resurfacing of Umbriel. *Nature 338*, p.324–326.

Helfenstein, P. et al., 1991. Oberon color photometry from Voyager and its geological implications. *Icarus 90*, p.14–29.

Holler, B.J., Young, L.A., Grundy, W.M. and Olkin, C.B., 2016. On the surface composition of Triton's southern latitudes. *Icarus*, *267*, p.255-266.

Jankowski, D.G. and Squyres, S.W., 1988. Solid-state ice volcanism on the satellites of Uranus. *Science*, *241* (4871), p.1322.

Jewitt, D., Luu, J. and Trujillo, C., 1998. Large Kuiper belt objects: the Mauna Kea 8K CCD survey. *The Astronomical Journal*, *115* (5), p.2125.

Kargel, J.S., Kirk, R.L., Fegley, B. and Treiman, A.H., 1994. Carbonate-sulfate volcanism on Venus?. *Icarus*, *112* (1), p.219-252.

Lanzerotti, L.J., Brown, W.L., Maclennan, C.G., Cheng, A.F., Krimigis, S.M. and Johnson, R.E., 1987. Effects of charged particles on the surfaces of the satellites of Uranus. *Journal of Geophysical Research*, *92*, p.14949-14957.

Lindsay, S.S., Marchis, F., Emery, J.P., Enriquez, J.E. and Assafin, M., 2015. Composition, mineralogy, and porosity of multiple asteroid systems from visible and near-infrared spectral data. *Icarus*, *247*, p.53-70.

Luu, J., Jewitt, D. and Cloutis, E., 1994. Near-infrared spectroscopy of primitive Solar System objects. *Icarus*, *109* (1), p.133-144.

Maris, M., Carraro, G., Cremonese, G. and Fulle, M., 2002. Multicolor photometry of the Uranus irregular satellites Sycorax and Caliban. *The Astronomical Journal*, *121* (5), p.2800.

Maris, M., Carraro, G. and Parisi, M.G., 2007. Light curves and colours of the faint Uranian irregular satellites Sycorax, Prospero, Stephano, Setebos, and Trinculo. *Astronomy & Astrophysics*, *472* (1), p.311-319.

Mastrapa, R.M., Bernstein, M.P., Sandford, S.A., Roush, T.L., Cruikshank, D.P. and Dalle Ore, C.M., 2008. Optical constants of amorphous and crystalline H_2O ice in the near infrared from 1.1 to 2.6 μm. *Icarus*, *197* (1), p.307-320.

Mastrapa, R.M., Sandford, S.A., Roush, T.L., Cruikshank, D.P. and Dalle Ore, C.M., 2009. Optical Constants of Amorphous and Crystalline H_2O ice: 2.5-22 μm (4000-455 cm^{-1}) Optical Constants of H_2O ice. *The Astrophysical Journal*, *701* (2), p.1347.

Ness, N.F., et al., 1986. Magnetic fields at Uranus. *Science*, *233*, p.85-90.

Pappalardo, R.T., Reynolds, S.J., Greeley, R., 1997. Extensional tilt blocks on Miranda: Evidence for an upwelling origin of Arden Corona. J. Geophys. Res.: Planets 102 (E6), p.13369–13379.

Pinilla-Alonso, N., Roush, T.L., Marzo, G.A., Cruikshank, D.P. and Dalle Ore, C.M., 2011. Iapetus surface variability revealed from statistical clustering of a VIMS mosaic: The distribution of CO_2. *Icarus*, *215* (1), p.75-82.

Rayner, J.T. et al., 1998. SpeX: A medium-resolution IR spectrograph for IRTF. Proc. SPIE 3354, p.468–479.

Rayner, J.T. et al., 2003. SpeX: A medium-resolution 0.8–5.5 micron spectrograph and imager for the NASA Infrared Telescope Facility. Astron. Soc. Pacific 115, p.362.

Sagan, C. and Khare, B.N., 1979. Tholins-organic chemistry of interstellar grains and gas. *Nature, 277*, p.102-107.

Schenk, P.M., 1991. Fluid volcanism on Miranda and Ariel: Flow morphology and composition. *Journal of Geophysical Research: Solid Earth*, *96* (B2), p.1887-1906.

Smith, B.A. et al., 1986. Voyager 2 in the uranian system: Imaging science results. Science 233, p.43–64.

Soifer, B.T., Neugebauer, G. and Matthews, K., 1981. Near-infrared spectrophotometry of the satellites and rings of Uranus. *Icarus*, *45*(3), p.612-617.

Spiegel, M.R., 1992. Theory and Problems of Probability and Statistics. McGraw-Hill, New York, p.117–118.

Stone, E.C., Miller, E.D., 1986. The Voyager-2 encounter with the uranian system. Science 233, p.39–43.

Stone, E.C. et al., 1986. Energetic charged particles in the uranian magnetosphere. Science 233, p.93–97.

Tamayo, D., Burns, J.A., Hamilton, D.P. and Hedman, M.M., 2011. Finding the trigger to Iapetus' odd global albedo pattern: Dynamics of dust from Saturn's irregular satellites. *Icarus*, *215*(1), p.260-278.

Tamayo, D., Burns, J.A. and Hamilton, D.P., 2013. Chaotic dust dynamics and implications for the hemispherical color asymmetries of the Uranian satellites. *Icarus, 226* (1), p.655-662.

Tamayo, D., Marcham, S.R., Hedman, M.M., Burns, J.A., Hamilton, D.P. 2016. Radial profiles of the Phoebe ring: A vast debris disk around Saturn. *Icarus* 275, p.117-131.

Taylor, J.R., 1982. An introduction to error analysis: Mill Valley.

Tremaine, S., Touma, J. and Namouni, F., 2009. Satellite dynamics on the Laplace surface. *The astronomical journal*, *137* (3), p.3706.

Vacca, W.D., Cushing, M.C. and Rayner, J.T., 2003. A Method of Correcting Near-Infrared Spectra for Telluric Absorption Based on observations obtained with the Infrared Telescope Facility, which is operated by the University of Hawaii under contract to the National Aeronautics and Space Administration. *Publications of the Astronomical Society of the Pacific*, *115* (805), p.389.

Veeder, G.J. and Matson, D.L., 1980. The relative reflectance of Iapetus at 1.6 and 2.2 microns. *The Astronomical Journal*, *85*, p.969-972.

Verbiscer, A., French, R., Showalter, M. and Helfenstein, P., 2007. Enceladus: Cosmic graffiti artist caught in the act. *Science*, *315* (5813), p.815-815.

Verbiscer, A.J., Skrutskie, M.F. and Hamilton, D.P., 2009. Saturn's largest ring. *Nature*, *461* (7267), p.1098.

Werner, M.W., Roellig, T.L., Low, F.J., Rieke, G.H., Rieke, M., Hoffmann, W.F., Young, E., Houck, J.R., Brandl, B., Fazio, G.G. and Hora, J.L., 2004. The Spitzer space telescope mission. *The Astrophysical Journal Supplement Series*, *154* (1), p.1.

Zahnle, K., Schenk, P., Levison, H. and Dones, L., 2003. Cratering rates in the outer Solar System. *Icarus*, *163* (2), p.263-289.

Appendix 3

Table 3.1. Classical Uranian satellites.

Satellite	Orbital Radius (km)	Orbital Radius (R_{Uranus})	Orbital Period (days)	Radius (km)	Mass (x 10^{20} kg)	Density (g cm^{-3})	*Geo. Albedo (A_0) (λ ~0.96 μm)
Miranda	129,900	5.12	1.41	236	0.66	1.21	0.45
Ariel	190,900	7.53	2.52	579	13.53	1.59	0.56
Umbriel	266,000	10.5	4.14	585	11.72	1.46	0.26
Titania	436,300	17.2	8.71	789	35.27	1.66	0.39
Oberon	583,500	23.0	13.46	762	30.14	1.56	0.33

**Geometric albedos from Figure 7 in Karkoschka (2001).*

Table 3.2. IRTF/SpeX observing modes.

Observing PI	Years	SpeX Mode	MORIS?	Wavelength Range (μm)	Slit Width (")	Spectral Resolution ($\lambda/\Delta\lambda$)	Total Number of Spectra	References
Rivkin	2000	SXD	No	~0.81 - 2.42	0.8	~750	7	Cartwright et al. (2015)
Grundy	2001 - 2002	SXD	No	~0.81 - 2.42	0.5	~ 1400	6	Grundy et al. (2003)
Grundy	2003 - 2006	SXD	No	~0.81 - 2.42	0.3	~1700	15	Grundy et al. (2006)
Gourgeot	2014	SXD	No	~0.81 - 2.42	0.8	~750	2	Gourgeot et al. (2014)
Cartwright	2012	SXD	No	~0.81 - 2.42	0.8	~750	8	Cartwright et al. (2015)
Cartwright	2013	SXD	Yes	~0.94 - 2.42	0.8	~750	5	Cartwright et al. (2015)
Cartwright	2014 - 2015	SXD	Yes	~0.94 - 2.55	0.8	~750	11	This work
Cartwright	2014 - 2016	LXD	Yes	~1.67 - 4.2	0.8	~938	6	This work
Cartwright	2014 - 2017	PRISM	No	~0.70 - 2.52	0.8	~94	30	This work

Table 3.3. IRTF/SpeX observations.

Object	Obser. PI	SpeX Mode	Long. (°)	Lat. (°)	Lead/ Trail	UT Date	UT Time	t_{int} (min)
Miranda	Rivkin	SXD	36.3	-35.4	Interm. (L)	9/7/2000	9:30	37
	Cartwright	PRISM	92.1	30.4	Leading	9/12/2015	11:10	28
	Gourgeot	SXD	165.0	21.4	Interm. (T)	9/26/2012	10:40	64
	Cartwright	PRISM	236.2	30.4	Trailing	9/11/2015	14:50	16
	Gourgeot	SXD	277.3	21.4	Trailing	9/25/2012	10:30	92
	Cartwright	SXD	279.4	24.7	Trailing	11/30/2014	6:30	120
	Cartwright	PRISM	280.3	30.2	Trailing	9/17/2015	10:40	32
Ariel	Cartwright	PRISM	9.2	31.8	Interm. (L)	9/18/2015	10:05	7.5
	Cartwright	SXD	15.3	27.8	Interm. (L)	9/15/2014	11:35	88
	Cartwright	LXD	28.0	31.8	Interm. (L)	9/18/2015	13:15	93.3
	Cartwright	PRISM	38.8	35.8	Interm. (L)	9/20/2016	14:15	7.5
	Grundy	SXD	53.6	-16.0	Leading	8/9/2003	12:15	156
	Grundy	SXD	79.8	-19.4	Leading	7/17/2002	13:25	108
	Cartwright	SXD	87.8	24.0	Leading	9/5/2013	11:10	92
	Grundy	SXD	93.5	-18.1	Leading	10/4/2003	5:45	108
	Cartwright	SXD	110.1	32.0	Leading	9/11/2015	13:30	44
	Cartwright	SXD	132.2	28.5	Interm. (L)	8/24/2014	14:05	40
	Cartwright	PRISM	137.6	34.6	Interm. (L)	10/21/2016	12:40	7.5
	Grundy	SXD	159.9	-11.1	Interm. (L)	7/15/2004	12:00	112
	Grundy	SXD	200.0	-15.9	Interm. (T)	8/5/2003	12:00	84
	Grundy	SXD	219.8	-17.2	Interm. (T)	9/7/2003	9:35	90
	Cartwright	PRISM	224.8	31.8	Interm. (T)	9/17/2015	9:40	10
	Cartwright	PRISM	233.6	32.0	Trailing	9/12/2015	10:15	8
	Cartwright	LXD	253.0	32.0	Trailing	9/12/2015	13:30	66.6
	Cartwright	PRISM	253.9	29.2	Trailing	12/2/2015	5:25	9
	Rivkin	SXD	257.6	-29.5	Trailing	9/6/2000	7:35	76
	Cartwright	SXD	278.3	24.8	Trailing	8/7/2013	13:20	44
	Grundy	SXD	294.8	-19.3	Trailing	7/16/2002	13:10	140
	Grundy	SXD	304.8	-23.2	Trailing	7/8/2001	14:40	48
	Grundy	SXD	316.6	-18.2	Interm. (T)	10/8/2003	7:55	132
Umbriel	Cartwright	PRISM	14.4	28.8	Interm. (L)	12/2/2015	5:50	14
	Cartwright	SXD	38.4	20.3	Interm. (L)	8/13/2012	13:55	60
	Rivkin	SXD	75.2	-29.3	Leading	9/6/2000	10:00	80

Table 3.3. Continued.

Object	Obser. PI	SpeX Mode	Long. (°)	Lat. (°)	Lead/ Trail	UT Date	UT Time	t_{int} (min)
	Cartwright	SXD	81.7	27.4	Leading	9/15/2014	14:20	100
	Grundy	SXD	92.1	-11.1	Leading	7/16/2004	14:25	74
	Cartwright	PRISM	101.6	34.2	Leading	10/21/2016	11:30	7.5
	Cartwright	PRISM	105.9	31.7	Leading	9/11/2015	9:50	16
	Cartwright	SXD	131.3	17.5	Leading	11/1/2012	9:30	78
	Cartwright	PRISM	195.5	31.6	Interm. (T)	9/12/2015	10:35	10
	Grundy	SXD	216.2	-10.9	Interm. (T)	7/5/2004	14:10	80
	Grundy	SXD	219.8	-23.0	Interm. (T)	7/7/2001	14:10	52
	Grundy	SXD	261.3	-9.4	Trailing	9/18/2005	9:21	196
	Cartwright	SXD	264.0	23.7	Trailing	9/5/2013	13:55	52
	Cartwright	PRISM	268.0	31.5	Trailing	9/17/2015	10:00	12.5
	Grundy	SXD	317.6	-11.4	Interm. (T)	7/27/2004	11:30	184
	Cartwright	PRISM	323.6	32.8	Interm. (T)	1/23/2017	5:10	12
	Cartwright	SXD	345.8	27.5	Interm. (T)	9.14.2014	11:45	100
	Cartwright	PRISM	355.8	31.4	Interm. (T)	9/18/2015	10:20	10
Titania	Cartwright	SXD	13.6	19.0	Interm. (L)	9/21/2012	11:25	32
	Cartwright	PRISM	21.3	28.8	Interm. (L)	12/2/2015	4:55	7.5
	Cartwright	PRISM	29.0	32.7	Interm. (L)	1/23/2017	6:10	7.5
	Cartwright	SXD	37.2	27.4	Interm. (L)	9/14/2014	14:15	60
	Cartwright	SXD	86.5	23.6	Leading	9/6/2013	10:50	60
	Grundy	SXD	98.0	-18.1	Leading	10/8/2003	5:45	64
	Cartwright	LXD	106.5	32.2	Leading	10/21/2016	8:30	73.3
	Cartwright	PRISM	113.8	34.2	Leading	10/21/2016	12:45	7.5
	Cartwright	PRISM	126.2	31.4	Leading	9/17/2015	9:00	7.5
	Cartwright	SXD	160.0	18.2	Interm. (L)	10/12/2012	10:15	60
	Cartwright	PRISM	168.4	31.4	Interm. (L)	9/18/2015	9:30	7.5
	Grundy	SXD	213.9	-11.1	Interm. (T)	7/15/2004	14:25	64
	Cartwright	SXD	242.0	31.6	Trailing	9/11/2015	11:30	60
	Rivkin	SXD	258.9	-29.3	Trailing	9/5/2000	9:55	60
	Cartwright	LXD	270.3	35.4	Trailing	9/20/2016	11:45	80
	Cartwright	PRISM	274.3	35.4	Trailing	9/20/2016	14:00	7.5
	Grundy	SXD	277.8	-23.0	Trailing	7/7/2001	13:10	36
	Cartwright	PRISM	280.8	31.6	Trailing	9/12/2015	9:45	8
	Cartwright	SXD	282.7	27.2	Trailing	9/20/2014	13:00	28

Table 3.3. Continued.

Object	Obser. PI	SpeX Mode	Long. (°)	Lat. (°)	Lead/ Trail	UT Date	UT Time	t_{int} (min)
	Grundy	SXD	299.6	-10.2	Trailing	10/13/2005	9:05	106
	Rivkin	SXD	342.7	-29.4	Interm. (T)	9/7/2000	10:35	44
Oberon	Rivkin	SXD	1.0	-29.4	Interm. (L)	9/7/2000	8:30	32
	Cartwright	LXD	26.9	27.8	Interm. (L)	8/28/2014	13:40	80
	Cartwright	PRISM	30.8	35.2	Interm. (L)	9/20/2016	14:30	7.5
	Cartwright	SXD	64.8	18.1	Leading	10/12/2012	11:05	98
	Cartwright	PRISM	78.0	31.5	Leading	9/11/2015	10:15	10
	Grundy	SXD	87.0	-3.7	Leading	8/4/2006	13:22	92
	Cartwright	SXD	91.0	23.7	Leading	9/1/2013	11:40	56
	Cartwright	PRISM	104.5	28.6	Leading	12/2/2015	5:10	7.5
	Cartwright	PRISM	104.5	31.4	Leading	9/12/2015	10:00	8
	Grundy	SXD	110.6	-10.2	Leading	10/13/2005	6:30	124
	Cartwright	PRISM	123.2	32.6	Leading	1/23/2017	6:00	7.5
	Cartwright	PRISM	131.5	24.5	Leading	12/18/2014	5:05	16
	Grundy	SXD	216.2	-23.1	Interm. (T)	7/8/2001	13:10	48
	Cartwright	SXD	223.7	18.9	Trailing	9/21/2012	10:20	64
	Cartwright	SXD	236.1	17.4	Trailing	11/1/2012	6:55	40
	Cartwright	PRISM	237.3	31.3	Trailing	9/17/2015	9:25	7.5
	Cartwright	LXD	242.3	31.3	Trailing	9/17/2015	13:40	66.6
	Cartwright	PRISM	264.6	31.2	Trailing	9/18/2015	9:45	7.5
	Cartwright	SXD	266.5	20.2	Trailing	8/13/2012	15:15	28
	Cartwright	SXD	279.2	27.9	Trailing	8/24/2014	13:05	100
	Rivkin	SXD	307.2	-29.3	Trailing	9/5/2000	8:10	60

Table 3.4. Local standard and solar analog stars.

Observing PI	UT Date	Solar Analogs
Rivkin	9/5/2000	SAO 164, 16 Cygni A
	9/6/2000	SAO 164, 16 Cygni Q
	9/7/2000	SAO 164
Cartwright	8/13/2012	SAO 109348, SA 115-271
	9/21/2012	SAO 109182, SAO 110201, SA 115-271
	10/12/2012	SAO 109182, SA 115-271, Hyades 64
	11/1/2012	SAO 109182, SAO 126133, Hyades 64
	8/7/2013	SAO 109426, SAO 109450
	9/1/2013	SAO 109426, SAO 109450, SAO 109348
	9/5/2013	SAO 109426, SAO 109450, SAO 109348
	9/6/2013	SAO 109426, SAO 109450, SAO 109348
	8/24/2014	SAO 110201, SAO 109567
	8/28/2014	SAO 110201, SAO 109567, SAO 109182
	9/14/2014	SAO 110201, SAO 109567
	9/15/2014	SAO 110201, SAO 109567
	9/20/2014	SAO 110201, SAO 109567
	11/30/2014	SAO 110201, SAO 109567
	12/18/2014	SAO 110201, SAO 109567
	9/11/2015	SAO 110201, BD+08 205
	9/12/2015	SAO 110201, BD+08 205
	9/17/2015	SAO 110201, BD+08 205
	9/18/2015	SAO 110201, BD+08 205
	12/2/2015	SAO 110201, SAO 109567
	9/20/2016	SAO 110201, SAO 146253, SAO 109905
	10/21/2016	SAO 110201, SAO 109690
	1/23/2017	SAO 110201, SAO 109690

Table 3.5. Wavelength range of H_2O ice bands and continua.

H_2O Band Complex	Short Wave. Continuum (μm)	Long Wave. Continuum (μm)	Band Wave. Range (μm)	Band Width (μm)
1.52-μm	1.318 - 1.440	1.720 - 1.750	1.44 - 1.72	0.280
2.02-μm	1.720 - 1.907	2.215 - 2.230	1.907 - 2.215	0.308

Table 3.6. Reflectance ratios.

Object	Satellite Long. (°)	Reflect. Ratio	Δreflect. Ratio (1σ)
Ariel	9.2	1.039	0.022
	38.8	1.013	0.006
	137.6	1.035	0.005
	224.8	1.002	0.005
	233.6	1.014	0.005
	253.9	1.066	0.003
Umbriel	14.4	1.064	0.006
	101.6	1.062	0.008
	105.9	1.084	0.007
	195.5	1.077	0.006
	268.0	1.053	0.005
	323.6	1.021	0.006
	355.8	1.075	0.006
Titania	21.3	1.142	0.003
	29.0	1.134	0.006
	113.8	1.075	0.008
	168.4	1.093	0.005
	274.3	1.060	0.003
	280.8	1.085	0.011
Oberon	30.8	1.083	0.011
	78.0	1.085	0.005
	104.5	1.064	0.007
	104.5	1.093	0.005
	123.2	1.115	0.005
	131.5	1.082	0.005
	237.3	1.057	0.005
	264.6	1.065	0.004

Table 3.7. H_2O ice band areas and depths.

			Integrated H_2O Band Area (10^{-2} μm)				H_2O Band Depth (μm)			
Target	Long. (°)	Lat. (°)	1.52-μm Band	Δarea (1σ)	2.02-μm Band	Δarea (1σ)	1.52-μm Band	Δdepth (1σ)	2.02-μm Band	Δdepth (1σ)
Miranda	36.3	-35.4	2.62	0.02	6.61	0.15	0.169	0.005	0.360	0.007
	92.1	30.4	4.43	0.06	9.06	0.15	0.256	0.011	0.501	0.051
	165.0	21.4	3.32	0.79	8.00	0.39	0.226	0.015	0.433	0.040
	236.2	30.4	4.24	0.12	8.90	0.24	0.243	0.023	0.517	0.044
	277.3	21.4	3.32	0.79	8.07	0.22	0.226	0.015	0.433	0.040
	279.4	24.7	3.34	0.06	8.04	0.10	0.209	0.014	0.451	0.022
	280.3	30.2	3.89	0.05	8.13	0.08	0.229	0.010	0.446	0.025
Ariel	9.2	31.8	4.19	0.04	8.45	0.07	0.247	0.009	0.455	0.016
	15.3	27.8	4.05	0.01	8.58	0.02	0.235	0.002	0.446	0.003
	38.8	35.8	4.63	0.02	9.19	0.03	0.265	0.004	0.471	0.009
	53.6	-16.0	4.73	0.02	9.29	0.05	0.274	0.003	0.473	0.006
	79.8	-19.4	4.99	0.01	10.03	0.04	0.290	0.002	0.504	0.003
	87.8	24.0	4.92	0.01	9.27	0.02	0.291	0.002	0.480	0.003
	93.5	-18.1	4.83	0.02	9.66	0.03	0.286	0.003	0.503	0.004
	110.1	32.0	4.68	0.01	8.95	0.02	0.275	0.002	0.481	0.004
	132.2	28.5	4.31	0.01	8.44	0.02	0.258	0.002	0.441	0.005
	137.6	34.6	3.96	0.03	8.59	0.04	0.234	0.010	0.435	0.009
	159.9	-11.1	3.23	0.02	8.57	0.03	0.202	0.005	0.448	0.005
	200.0	-15.9	2.98	0.02	7.48	0.12	0.182	0.003	0.395	0.006
	219.8	-17.2	2.67	0.01	6.84	0.02	0.166	0.002	0.360	0.004
	224.8	31.8	3.18	0.01	7.30	0.02	0.195	0.002	0.394	0.008

Table 3.7. Continued.

Target	Long. (°)	Lat. (°)	1.52-µm Band	Δarea (1σ)	2.02-µm Band	Δarea (1σ)	1.52-µm Band	Δdepth (1σ)	2.02-µm Band	Δdepth (1σ)
	233.6	32.0	3.16	0.02	7.01	0.05	0.196	0.003	0.374	0.010
	253.9	29.2	2.88	0.02	7.38	0.02	0.187	0.004	0.400	0.008
	257.6	-29.5	3.25	0.03	7.18	0.09	0.188	0.005	0.375	0.005
	278.3	24.8	2.90	0.02	7.15	0.04	0.177	0.005	0.383	0.010
	294.8	-19.3	2.90	0.02	6.74	0.04	0.177	0.002	0.388	0.004
	304.8	-23.2	3.02	0.03	6.55	0.19	0.184	0.004	0.384	0.007
	316.6	-18.2	3.21	0.02	7.19	0.03	0.194	0.004	0.387	0.008
Umbriel	14.4	28.8	1.69	0.03	5.04	0.04	0.108	0.005	0.296	0.012
	38.4	20.3	1.74	0.02	4.64	0.03	0.116	0.004	0.274	0.005
	75.2	-29.3	1.87	0.03	5.05	0.17	0.120	0.006	0.285	0.007
	81.7	27.4	1.43	0.01	4.59	0.05	0.092	0.003	0.272	0.007
	92.1	-11.1	1.48	0.04	4.50	0.06	0.097	0.005	0.291	0.012
	101.6	34.2	1.82	0.04	4.85	0.06	0.118	0.009	0.277	0.021
	105.9	31.7	2.05	0.03	5.22	0.10	0.122	0.006	0.274	0.015
	131.3	17.5	1.57	0.01	4.74	0.02	0.102	0.003	0.276	0.004
	195.5	31.6	1.75	0.02	4.60	0.05	0.107	0.009	0.237	0.011
	216.2	-10.9	1.42	0.04	4.31	0.05	0.091	0.006	0.266	0.011
	219.8	-23.0	1.68	0.03	3.36	0.10	0.114	0.005	0.270	0.010
	261.3	-9.4	0.87	0.03	3.99	0.18	0.057	0.004	0.232	0.005
	264.0	23.7	1.26	0.01	4.22	0.01	0.093	0.002	0.238	0.003
	268.0	31.5	1.54	0.03	4.40	0.04	0.096	0.006	0.264	0.016
	317.6	-11.4	1.04	0.02	4.18	0.04	0.071	0.004	0.240	0.007

Table 3.7. Continued.

Target	Long. (°)	Lat. (°)	1.52-µm Band	Δarea (1σ)	2.02-µm Band	Δarea (1σ)	1.52-µm Band	Δdepth (1σ)	2.02-µm Band	Δdepth (1σ)
	323.6	32.8	1.53	0.03	4.43	0.05	0.100	0.006	0.245	0.010
	345.8	27.5	1.31	0.01	4.35	0.02	0.086	0.002	0.249	0.005
	355.8	31.4	1.73	0.02	4.46	0.05	0.118	0.004	0.253	0.010
Titania	13.6	19.0	3.67	0.01	8.41	0.01	0.221	0.002	0.452	0.002
	21.3	28.8	4.14	0.01	9.24	0.02	0.257	0.006	0.481	0.005
	29.0	32.7	4.47	0.02	9.49	0.03	0.258	0.007	0.500	0.009
	37.2	27.4	4.16	0.01	8.85	0.01	0.249	0.002	0.470	0.003
	86.5	23.6	4.43	0.01	9.07	0.01	0.265	0.001	0.477	0.002
	98.0	-18.1	4.44	0.03	9.05	0.05	0.270	0.004	0.484	0.007
	113.8	34.2	4.06	0.02	8.80	0.03	0.240	0.004	0.474	0.006
	126.2	31.4	4.26	0.01	8.92	0.02	0.257	0.005	0.466	0.005
	160.0	18.2	3.63	0.01	8.24	0.02	0.223	0.003	0.449	0.003
	168.4	31.4	4.00	0.02	8.27	0.02	0.242	0.004	0.434	0.006
	213.9	-11.1	3.31	0.02	8.17	0.03	0.203	0.004	0.441	0.004
	242.0	31.6	3.77	0.01	6.70	0.03	0.240	0.002	0.407	0.003
	258.9	-29.3	3.46	0.02	8.04	0.04	0.217	0.003	0.431	0.003
	274.3	35.4	3.67	0.02	7.89	0.04	0.223	0.002	0.420	0.013
	277.8	-23.0	3.70	0.02	8.10	0.04	0.225	0.003	0.443	0.004
	280.8	31.6	3.66	0.04	8.27	0.09	0.223	0.007	0.442	0.017
	282.7	27.2	3.50	0.01	7.53	0.03	0.215	0.002	0.414	0.003
	299.6	-10.2	3.35	0.02	8.05	0.02	0.207	0.003	0.434	0.004
	342.7	-29.4	3.83	0.02	9.01	0.29	0.231	0.002	0.452	0.004
Oberon	1.0	-29.4	2.56	0.02	7.18	0.32	0.162	0.003	0.383	0.007

Table 3.7. Continued.

Target	Long. (°)	Lat. (°)	1.52-µm Band	Δarea (1σ)	2.02-µm Band	Δarea (1σ)	1.52-µm Band	Δdepth (1σ)	2.02-µm Band	Δdepth (1σ)
	30.8	35.2	2.86	0.06	6.83	0.06	0.167	0.012	0.389	0.015
	64.8	18.1	2.63	0.01	6.52	0.02	0.172	0.003	0.363	0.004
	78.0	31.5	3.06	0.01	6.90	0.03	0.193	0.004	0.381	0.008
	87.0	-3.7	2.73	0.05	6.29	0.16	0.178	0.006	0.375	0.010
	91.0	23.7	2.90	0.03	6.78	0.04	0.181	0.006	0.353	0.007
	104.5	28.6	2.84	0.02	6.80	0.03	0.179	0.006	0.371	0.009
	104.5	31.4	2.86	0.01	7.11	0.02	0.185	0.005	0.383	0.005
	110.6	-10.2	2.16	0.02	5.71	0.02	0.140	0.003	0.318	0.004
	123.2	32.6	3.15	0.02	7.18	0.03	0.181	0.006	0.384	0.007
	131.5	24.5	2.87	0.02	6.85	0.03	0.188	0.004	0.376	0.010
	216.2	-23.1	2.75	0.02	6.12	0.06	0.173	0.003	0.375	0.005
	223.7	18.9	2.21	0.01	6.09	0.01	0.143	0.002	0.338	0.003
	236.1	17.4	2.31	0.01	6.30	0.01	0.150	0.002	0.350	0.003
	237.3	31.3	2.81	0.02	6.35	0.03	0.169	0.004	0.342	0.007
	264.6	31.2	2.76	0.01	6.32	0.03	0.177	0.003	0.345	0.006
	266.5	20.2	2.46	0.02	6.07	0.03	0.157	0.005	0.335	0.008
	279.2	27.9	2.67	0.01	6.10	0.01	0.159	0.002	0.336	0.003
	307.2	-29.3	2.46	0.01	6.35	0.04	0.157	0.002	0.347	0.002

Table 3.8. *F*-test analysis of reflectance ratios and H_2O ice band areas.

Satellite	Analyzed Measurement	One Tailed F test Ratio	Sample Size (n)	Mean Model Deg. Freedom (n - 1)	Sinusoidal Model Deg. Freedom (n - 3)	Probability (*p*)	Reject Null Hypothesis?
Miranda	Reflect. ratio	-	-	-	-	-	-
	1.52-μm H_2O	44.274	7	6	4	$1.3*10^{-3}$	Yes
	2.02-μm H_2O	3.642	7	6	4	$1.16*10^{-1}$	No
Ariel	Reflect. ratio	0.436	6	5	3	$8.05*10^{-1}$	No
	1.52-μm H_2O	134.243	21	20	18	<< 0.0001	Yes
	2.02-μm H_2O	89.713	21	20	18	<< 0.0001	Yes
Umbriel	Reflect ratio	1.474	7	6	4	$3.69*10^{-1}$	No
	1.52-μm H_2O	5.471	18	17	15	$9.31*10^{-4}$	Yes
	2.02-μm H_2O	23.845	18	17	15	<< 0.0001	Yes
Titania	Reflect ratio	11.619	6	5	3	$3.53*10^{-2}$	Yes
	1.52-μm H_2O	14.241	19	18	16	<< 0.0001	Yes
	2.02-μm H_2O	25.928	19	18	16	<< 0.0001	Yes
Oberon	Reflect ratio	33.959	8	7	5	$6.38*10^{-4}$	Yes
	1.52-μm H_2O	6.399	19	18	16	$2.53*10^{-4}$	Yes
	2.02-μm H_2O	8.939	19	18	16	$2.95*10^{-5}$	Yes

Table 3.9. Mean reflectance ratios.

Object	Number of PRISM Spec.	Leading/ Trailing	Reflect. Ratio	Δreflect. Ratio (2σ)
Ariel	3	L	1.029	0.016
	3	T	1.029	0.011
Umbriel	3	L	1.070	0.010
	4	T	1.058	0.010
Titania	4	L	1.118	0.010
	2	T	1.072	0.012
Oberon	6	L	1.092	0.008
	2	T	1.064	0.008

Table 3.10. Mean leading and trailing H_2O ice band areas.

			Integrated H_2O Band Area (10^{-2} μm)			
Satellite	Leading/ Trailing	Number of Spectra	1.52-μm Band	Δarea (2σ)	2.02-μm Band	Δarea (2σ)
Miranda	L	3	3.46	1.18	7.89	1.45
	T	4	3.70	0.70	8.29	0.45
Ariel	L	11	4.41	0.32	9.00	0.32
	T	10	3.02	0.12	7.08	0.19
Umbriel	L	8	1.71	0.15	4.83	0.19
	T	10	1.41	0.19	4.23	0.23
Titania	L	10	4.13	0.19	8.81	0.29
	T	9	3.58	0.12	7.97	0.42
Oberon	L	11	2.78	0.16	6.74	0.27
	T	8	2.55	0.16	6.21	0.09

Table 3.11. Mean leading/trailing H_2O band area ratios.

		All Latitudes		Southern Latitudes		Northern Latitudes	
Satellite	H_2O Band	Lead./Trail. Band Area Ratio	Δband Ratio (2σ)	Lead//Trail. Band Area Ratio	Δband Ratio (2σ)	Lead./Trail. Band Area Ratio	Δband Ratio (2σ)
Miranda	1.52-μm	0.94	0.36	-	-	-	-
	2.02-μm	0.95	0.18	-	-	-	-
Ariel	1.52-μm	1.46	0.12	1.48	0.285	1.45	0.119
	2.02-μm	1.27	0.06	1.34	0.105	1.22	0.047
Umbriel	1.52-μm	1.21	0.192	1.34	0.502	1.21	0.197
	2.02-μm	1.14	0.076	1.13	0.17	1.11	0.052
Titania	1.52-μm	1.15	0.066	1.26	0.074	1.13	0.065
	2.02-μm	1.11	0.068	1.09	0.053	1.16	0.109
Oberon	1.52-μm	1.09	0.093	0.953	0.168	1.142	0.101
	2.02-μm	1.09	0.046	1.025	0.148	1.089	0.035

Table 3.12. Mean leading and trailing H_2O band areas at southern and northern latitudes.

				Integrated H_2O Band Area (10^{-2} μm)			
Satellite	Leading/ Trailing	Southern/ Northern	Number of Spectra	1.52-μm Band	Δarea (2σ)	2.02-μm Band	Δarea (2σ)
Ariel	L	S	4	4.45	0.82	9.39	0.62
		N	7	4.39	0.27	8.78	0.27
	T	S	6	3.01	0.18	7.00	0.29
		N	4	3.03	0.16	7.21	0.17
Umbriel	L	S	2	1.68	0.39	4.78	0.58
		N	6	1.72	0.18	4.85	0.20
	T	S	4	1.25	0.37	3.96	0.44
		N	6	1.52	0.17	4.37	0.09
Titania	L	S	1	4.44	0.06	9.05	0.10
		N	9	4.09	0.20	8.81	0.29
	T	S	5	3.53	0.20	8.27	0.39
		N	4	3.61	0.11	7.60	0.67
Oberon	L	S	3	2.48	0.34	6.39	0.89
		N	8	2.90	0.11	6.76	0.18
	T	S	2	2.61	0.29	6.24	0.24
		N	6	2.54	0.20	6.21	0.11

Table 3.13. Mean leading and trailing Spitzer/IRAC ans SpeX/LXD geometric albedos.

		Spitzer/IRAC		SpeX/LXD	
Target	Leading/ Trailing	Mean Geometric Albedo	ΔMean Geometric Albedo (1σ)	Geometric Albedo	ΔGeometric Albedo (1σ)
Ariel	L	0.188	0.004	0.203	0.005
	T	0.232	0.005	0.229	0.007
Umbriel	L	0.153	0.006	-	-
	T	0.158	0.002	-	-
Titania	L	0.160	0.002	0.148	0.002
	T	0.160	0.003	0.162	0.002
Oberon	L	0.167	0.002	0.166	0.003
	T	0.168	0.001	0.167	0.003

Table 3.14. Best fit synthetic spectra of Oberon.

Leading/Trailing	"Short" Model (0.6 - 1.3 μm) Model Components	Mix (%)	"Mid" Model (1.3 - 2.5 μm) Model Components	Mix (%)	"Long" Model (2.9 - 4.2 μm) Model Components	Mix (%)
Oberon Leading	50 μm H_2O	23.4	50 μm H_2O	26.0	10 μm H_2O	14.0
Organic-rich model	10 μm H_2O	31.7	10 μm H_2O	35.7	1 μm H_2O	60.0
	0.2 μm H_2O	0.3	0.2 μm H_2O	0.3	0.2 μm H_2O	1.0
	7 μm amorphous C	17.6	7 μm amorphous C	21.0	1 μm amorphous C	15.0
	9 μm Triton tholin	27.0	9 μm Triton tholin	17.0	1 μm Triton tholin	10.0
Silicate-rich model	50 μm H_2O	24.0	50 μm H_2O	19.9	10 μm H_2O	14.0
	10 μm H_2O	33.7	10 μm H_2O	41.0	1 μm H_2O	60.0
	0.2 μm H_2O	0.3	0.2 μm H_2O	0.3	0.2 μm H_2O	1.0
	7 μm amorphous C	15.0	7 μm amorphous C	18.7	1 μm amorphous C	15.0
	9 μm pyroxene	27.0	9 μm pyroxene	20.1	1 μm Triton tholin	10.0
*Oberon Trailing	50 μm H_2O	25.0	50 μm H_2O	30.0	10 μm H_2O	26.0
Organic-rich model	10 μm H_2O	33.7	10 μm H_2O	29.7	1 μm H_2O	47.0
	0.2 μm H_2O	0.3	0.2 μm H_2O	0.3	0.2 μm H_2O	1.0
	7 μm amorphous C	21.0	7 μm amorphous C	20.5	1 μm amorphous C	16.0
	9 μm Triton tholin	20.0	9 μm Triton tholin	19.5	1 μm Triton tholins	10.0
*Oberon Trailing	50 μm H_2O	27.0	50 μm H_2O	22.0	10 μm H_2O	16.0
Silicate-rich model	10 μm H_2O	33.7	10 μm H_2O	38.7	1 μm H_2O	53.0
	0.2 μm H_2O	0.3	0.2 μm H_2O	0.3	0.2 μm H_2O	0.8
	7 μm amorphous C	17.0	7 μm amorphous C	20.0	1 μm amorphous C	17.0
	9 μm pyroxene	22.0	9 μm pyroxene	19.0	1 μm pyroxene	13.2

**Oberon trailing models are intimate mixtures, scaled to 97%, with 3% pure CO_2 ice added linearly to represent areally segregated deposits (see Appendix B in Cartwright et al., 2015).*

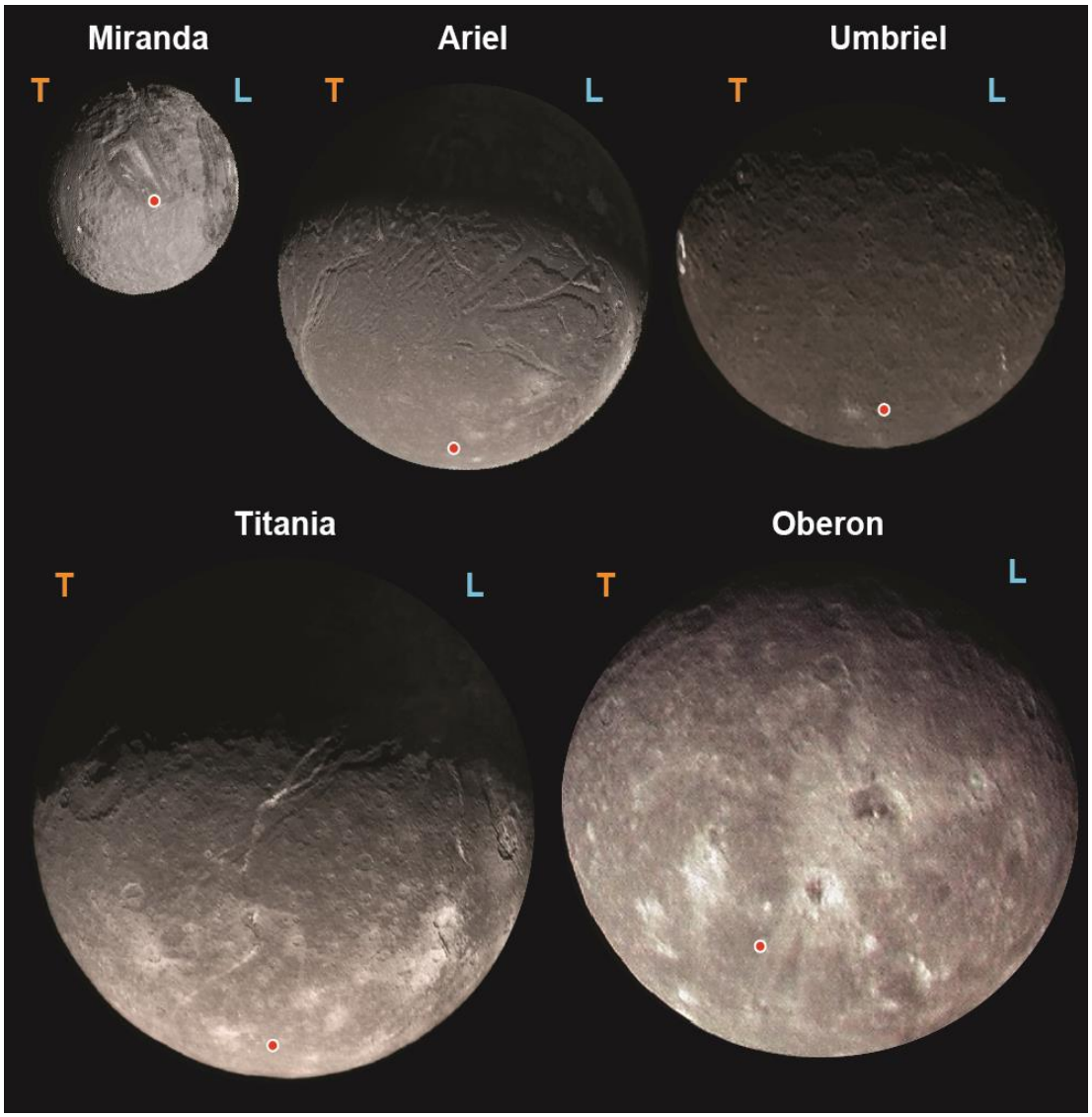

Figure 3.1. Voyager 2/ISS image mosaics of the classical Uranian satellites (courtesy NASA/JPL/-Caltech/USGS), with night-side sections of Ariel and Titania revealed using 'Uranus shine' (Stryk and Stooke, 2008), qualitatively scaled to their relative sizes (radius and mass of each moon listed in Table 3.1). Imaged sections of each moon's leading (blue L) and trailing (orange T) hemispheres, and the approximate location of their south poles (red circle) shown as well (subsolar point at the time of Voyager 2 encounter with Uranus, ~81°S). Spatial resolution ranges from a few hundred m/pixel for Miranda to ~6 km/pixel for Oberon. See Figure 3.2 for map-projected versions of these Voyager 2/ISS image mosaics, which include other lower quality images not shown here, in particular for the leading hemisphere of Ariel.

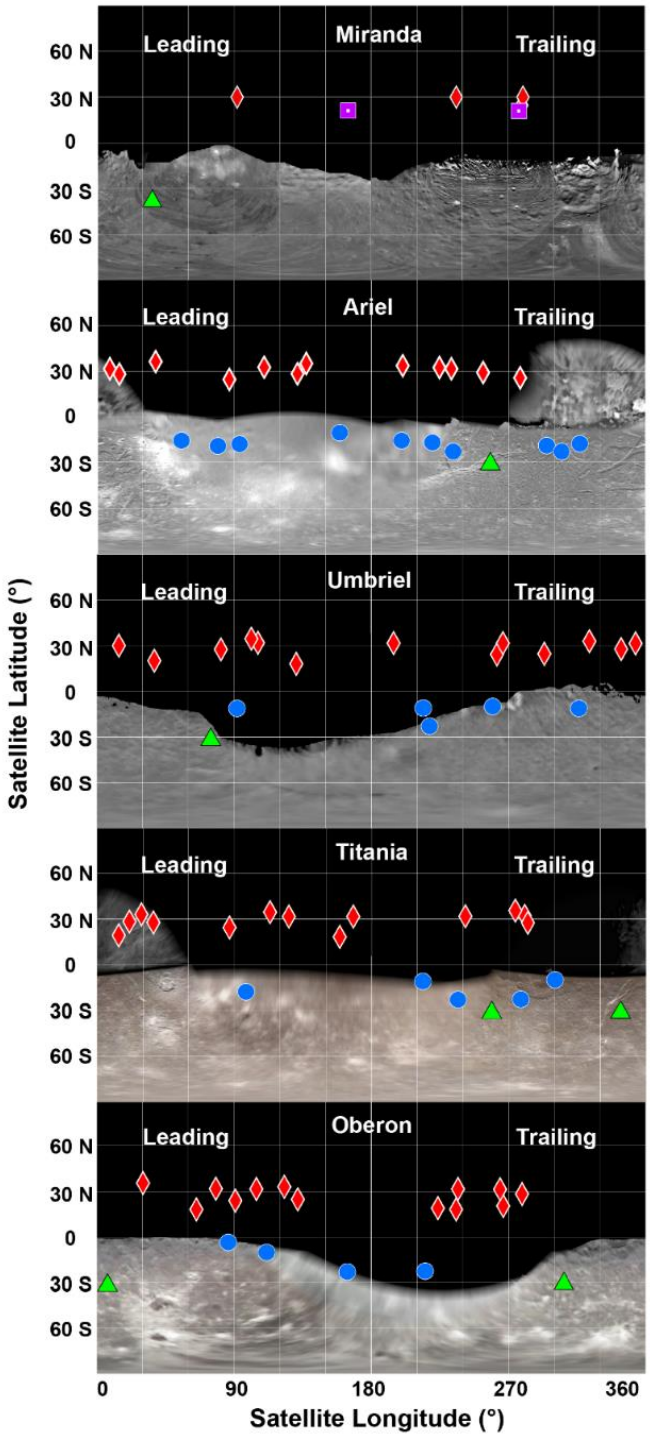

Figure 3.2. Mid-observation satellite longitudes and latitudes of the classical Uranian satellites, made by three different teams using IRTF/SpeX: Red diamonds (PI Cartwright, 2012 - 2017), blue circles (PI Grundy, 2001 - 2006), green triangles (PI Rivkin, 2000), and purple squares (PI Gourgeot, 2012). Base maps are Voyager 2/ISS image mosaics (courtesy NASA/JPL/-Caltech/USGS,http://maps.jpl.nasa.gov/uranus.html). Night-side sections of Ariel and Titania revealed using 'Uranus shine' (Stryk and Stooke, 2008).

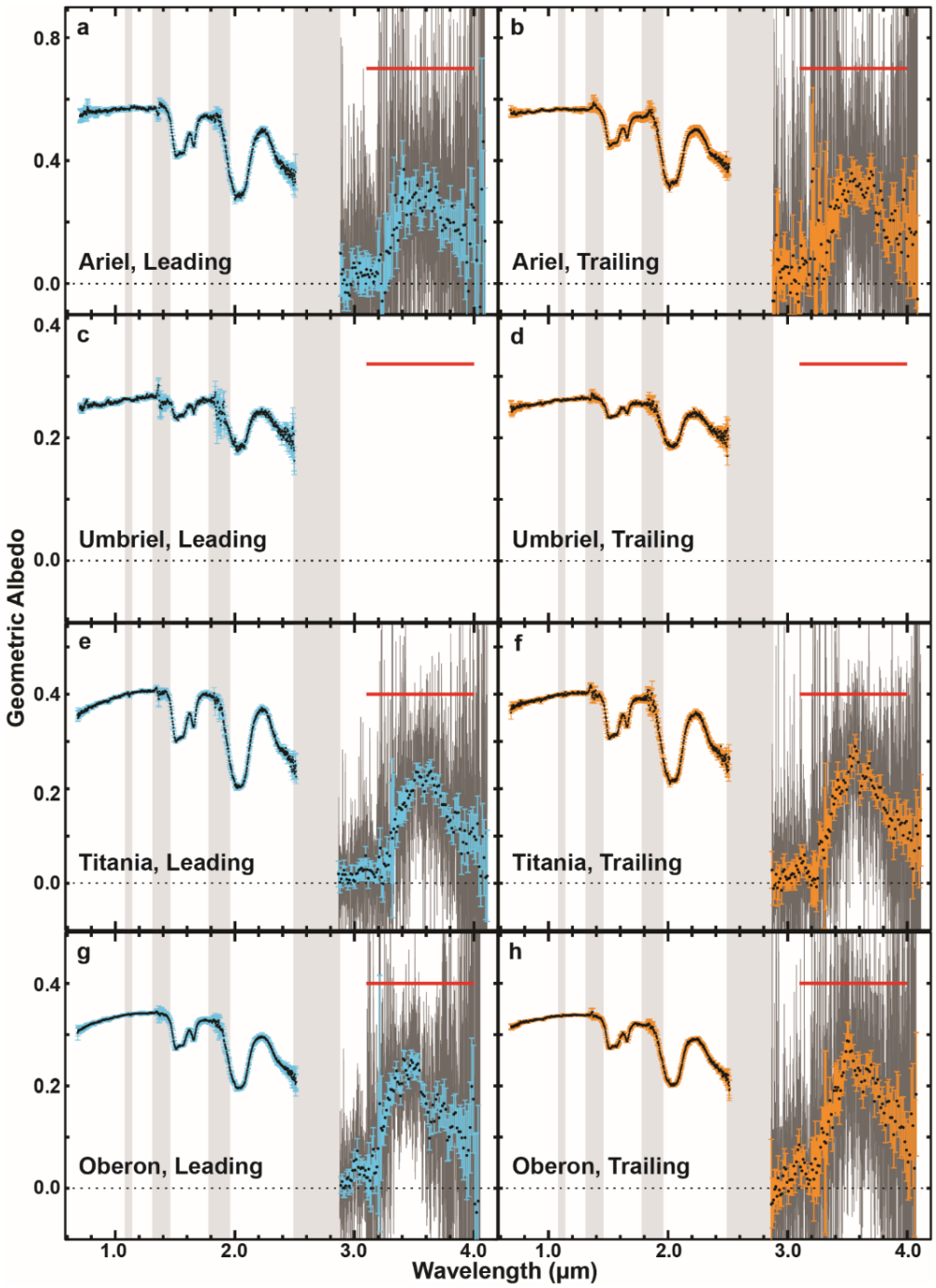

Figure 3.3. 'Grand average' PRISM mode SpeX spectra and the six 'native-resolution' LXD mode SpeX spectra we have gathered (dark gray), along with 'binned' versions of the LXD spectra (50 pixel wide binning window). All spectra shown are scaled to geometric albedo at ~0.96 mm (summarized in Table 3.1). (a, c, e, g) Leading hemisphere spectra (blue 1σ error bars) and (b, d, f, h) trailing hemisphere spectra (orange 1σ error bars) are displayed for each moon. Wavelength range of telluric bands (light gray regions) and IRAC channel 1 (~3.1 - 4.0 mm, red bars) are indicated.

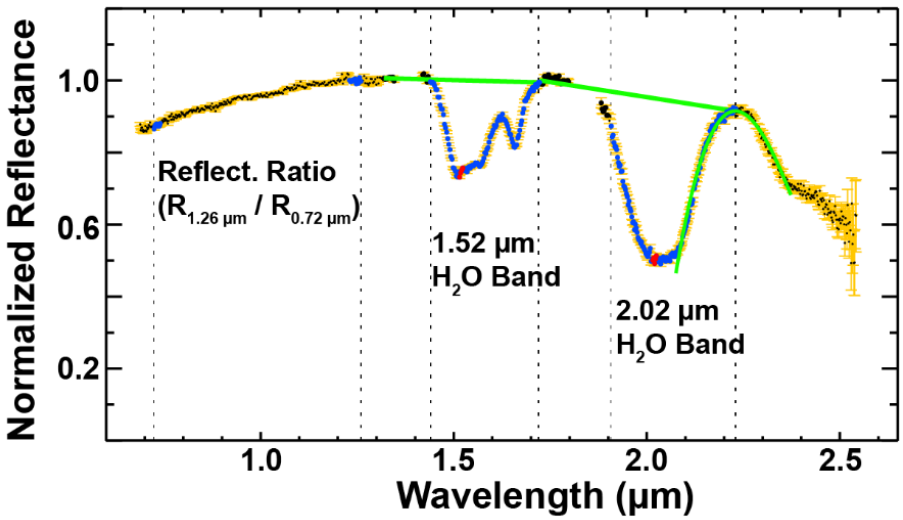

Figure 3.4. Examples of spectral measurements conducted on a SpeX spectrum (PRISM mode) gathered over Titania's leading hemisphere (mid observation satellite longitude 21°). Data points used in reflectance ratio (R1.26 µm / R0.72 µm) and H2O band area measurements (blue) and H_2O band center measurements (red) are highlighted. Continua for H_2O band area measurements also shown, including third order polynomial utilized to identify long wavelength end of 2.02-H_2O µm band (green lines).

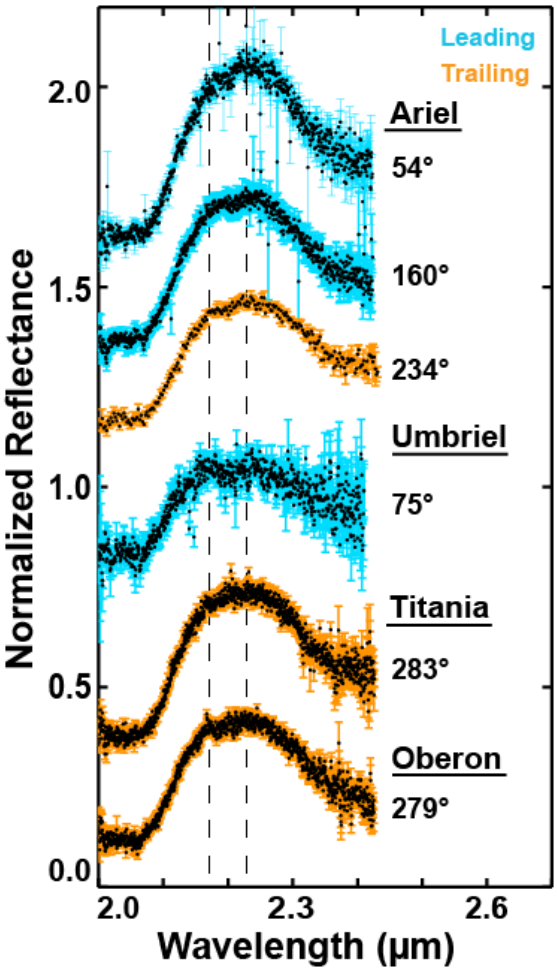

Figure 3.5. SpeX spectra of Ariel, Umbriel,Titania, and Oberon that hint at the possible presence of an NH_3-hydrate feature, centered near 2.2 μm, between the two black dashed lines (see Bauer et al. (2002) for a similar feature on Miranda). Leading (blue error bars) and trailing (orange error bars) hemisphere spectra indicated.

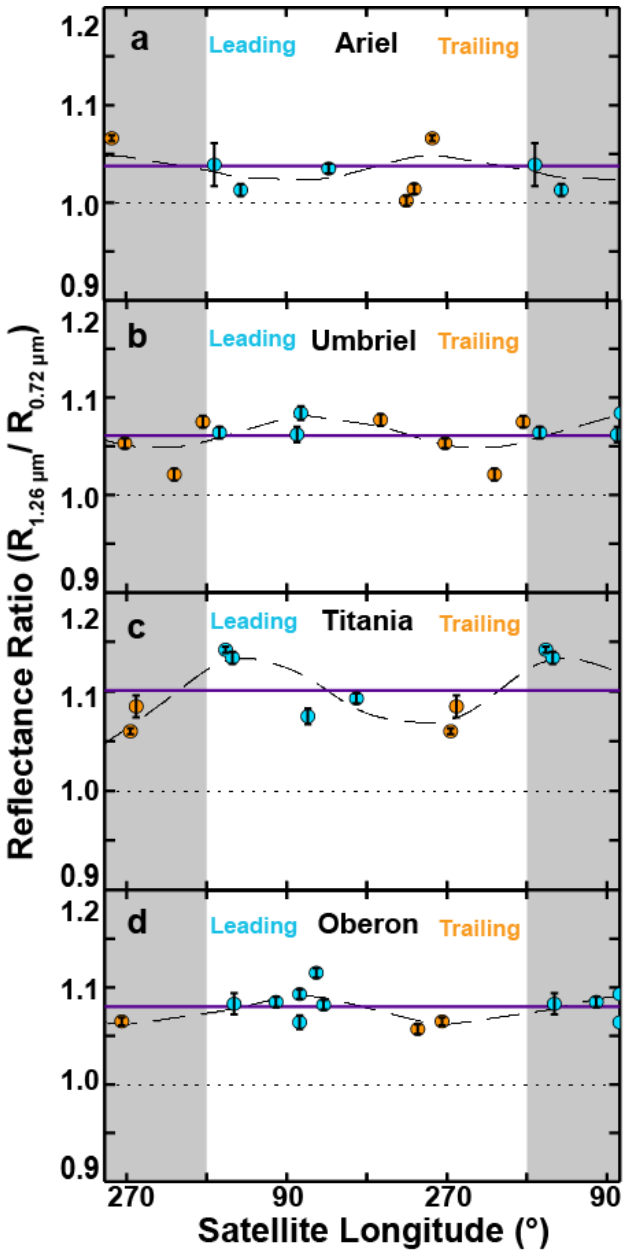

Figure 3.6. Reflectance ratios (R1.26 µm/ R0.72 µm) as a function of satellite longitude (1σ uncertainties) for Ariel, Umbriel, Titania and Oberon (a - d, respectively). Leading (blue) and trailing (orange) hemisphere measurements indicated. Dashed black lines represent sinusoidal fits to the data and solid purple lines show the mean reflectance ratio for each moon.

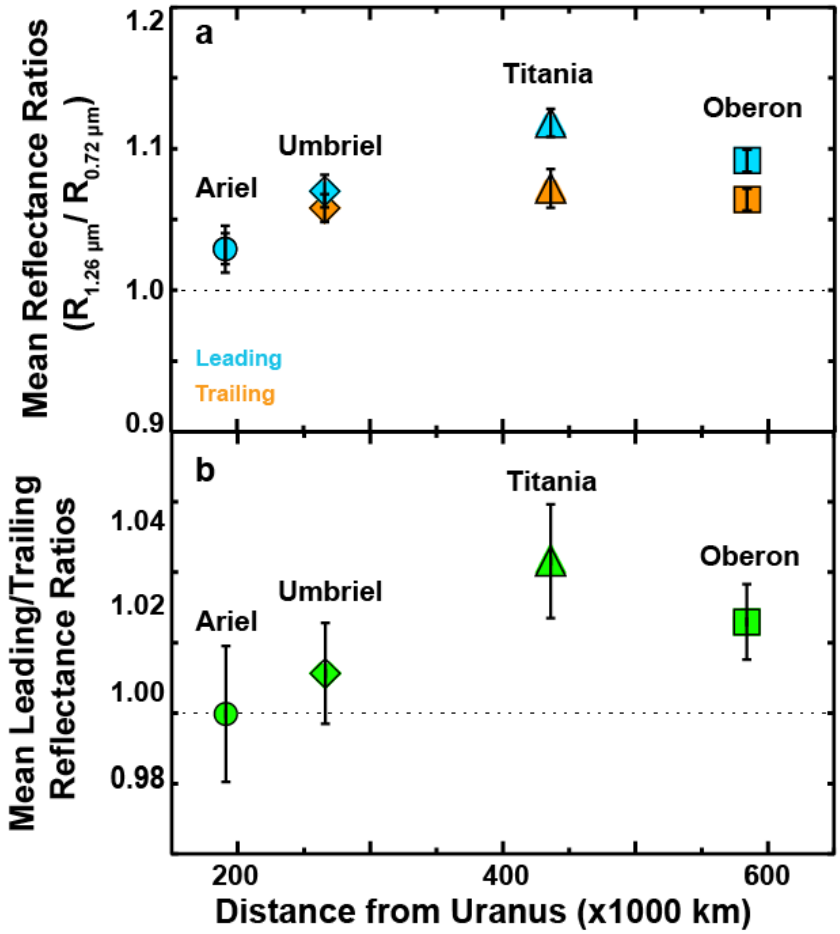

Figure 3.7. (a) Mean reflectance ratios (R1.26 µm/ R0.72 µm) and 2σ uncertainties for the leading (blue) and trailing (orange) hemispheres of Ariel (circles), Umbriel (diamonds), Titania (triangles), and Oberon (squares) as a function of planetocentric distance. (b) Mean leading/trailing reflectance ratios for these moons (2σ uncertainties), with the same symbology as shown in (a).

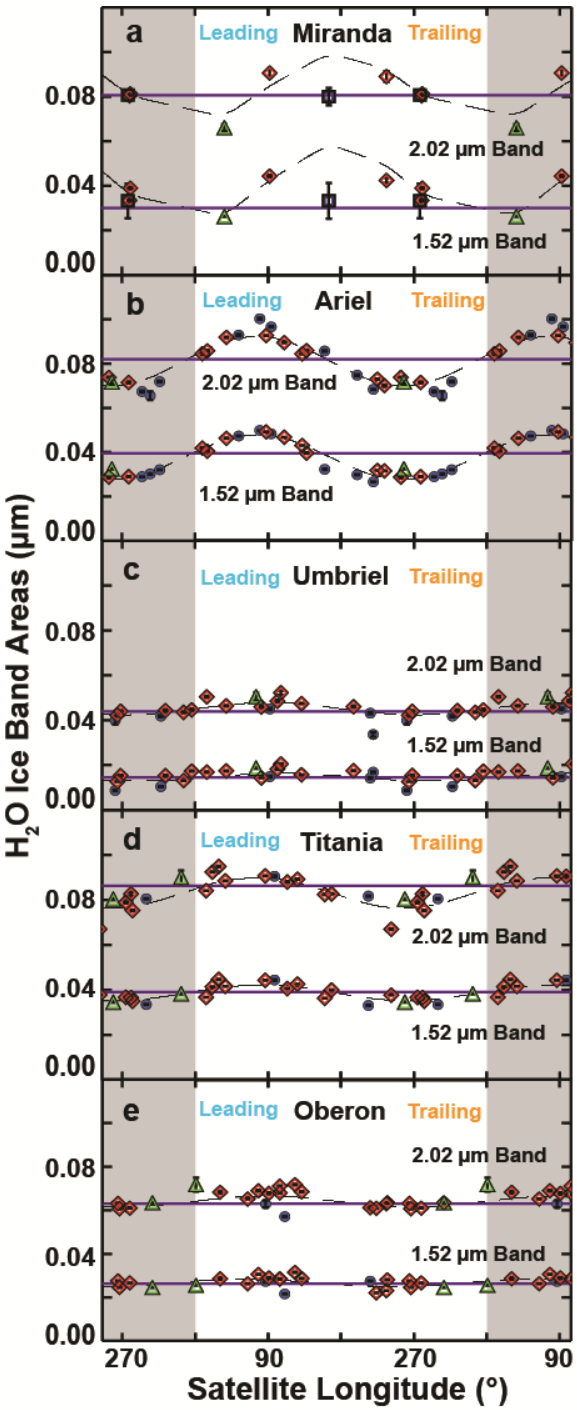

Figure 3.8. Band areas and 1σ uncertainties for the 1.52-μm and 2.02-μm H_2O ice bands (bottom and top set of data points in each plot, respectively) as a function of satellite longitude for Miranda Ariel, Umbriel, Titania, Oberon (a - e, respectively). Dashed black lines represent sinusoidal fits to the data and solid purple lines show the mean 1.52-μm and 2.02-μm H_2O band area for each moon. Symbols are the same as shown iin Figure 2: Red diamonds (Cartwright), blue circles (Grundy), green triangles (Rivkin), purple squares (Gourgeot).

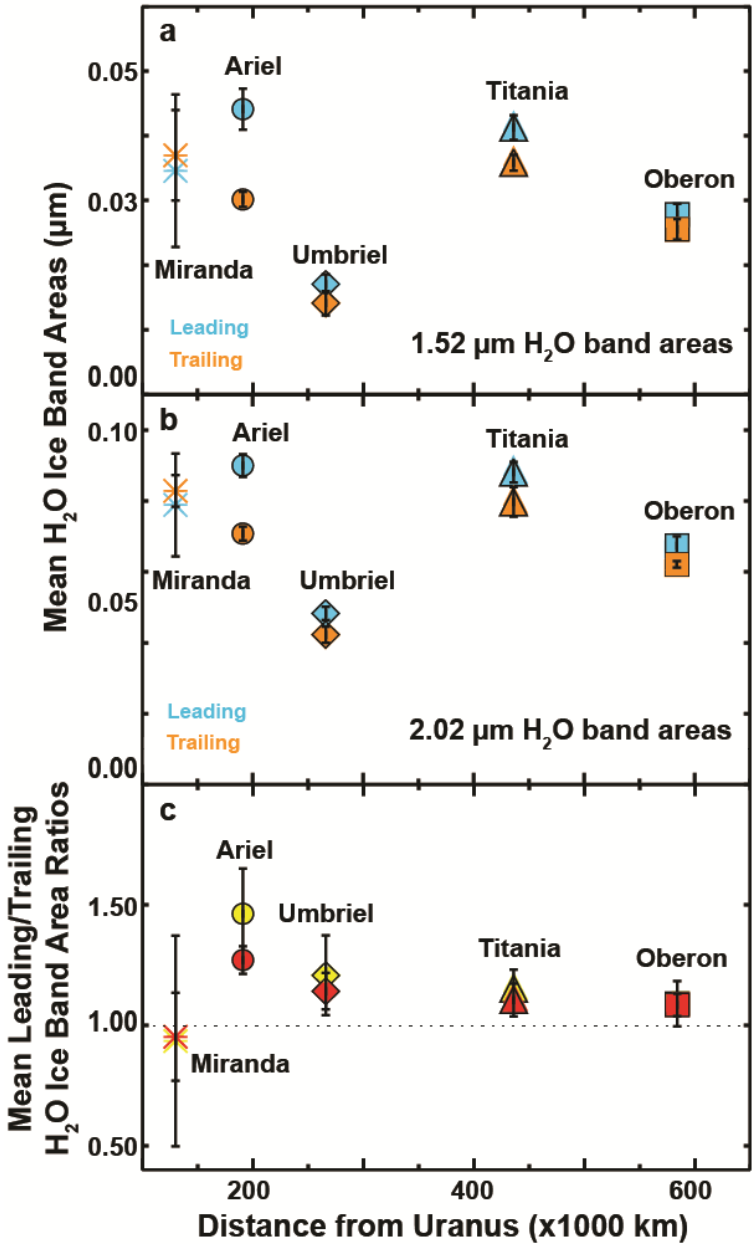

Figure 3.9. Mean band areas and 2σ uncertainties for (a) the 1.52-μm and (b) 2.02-μm H_2O ice bands for the leading (blue) and trailing (orange) hemispheres of the Uranian satellites. (c) Mean Leading/Trailing H_2O ice band area ratios for the 1.52-μm (yellow) and 2.02-μm (red) bands (2σ uncertainties). In all three plots: Miranda (asterisks), Ariel (circles), Umbriel (diamonds), Titania (triangles), and Oberon (squares).

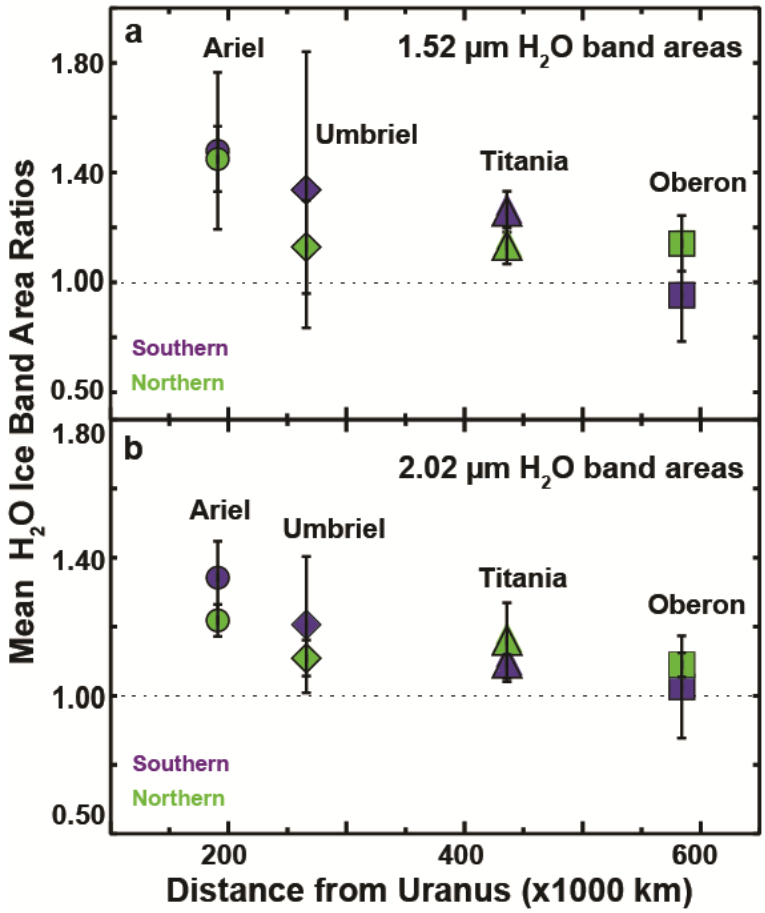

Figure 3.10. Mean leading/trailing H_2O ice band area ratios and 2σ uncertainties for spectra collected over southern latitudes (purple) and northern latitudes (green) for (a) the 1.52-μm and (b) the 2.02-μm H_2O ice bands. In both plots: Ariel (circles), Umbriel (diamonds), Titania (triangles), and Oberon (squares).

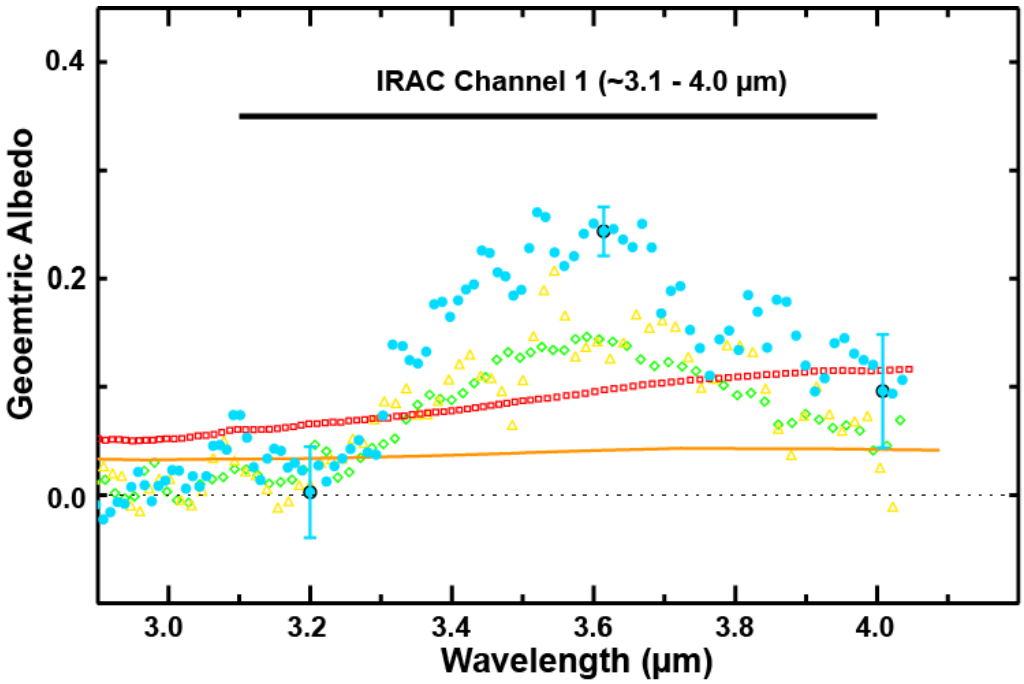

Figure 3.11. Comparison of binned versions of SpeX/LXD spectra of Oberon (light blue circles, shown in Figure 3.11), Rhea (green diamonds) and Tethys (yellow triangles) (Emery et al., 2005), Callisto (red squares), and a Visual Imaging Mapping Spectrometer spectrum of dark material on Iapetus (solid orange line, published in Pinilla-Alonso et al., 2011). Error bars have been suppressed for clarity. 1σ errors for the Oberon spectrum at ~3.2, 3.6, and 4.0 μm are shown to illustrate the range in uncertainties (1σ uncertainties for the other spectra are comparable or smaller). Wavelength range of IRAC channel 1 is also shown (solid black line).

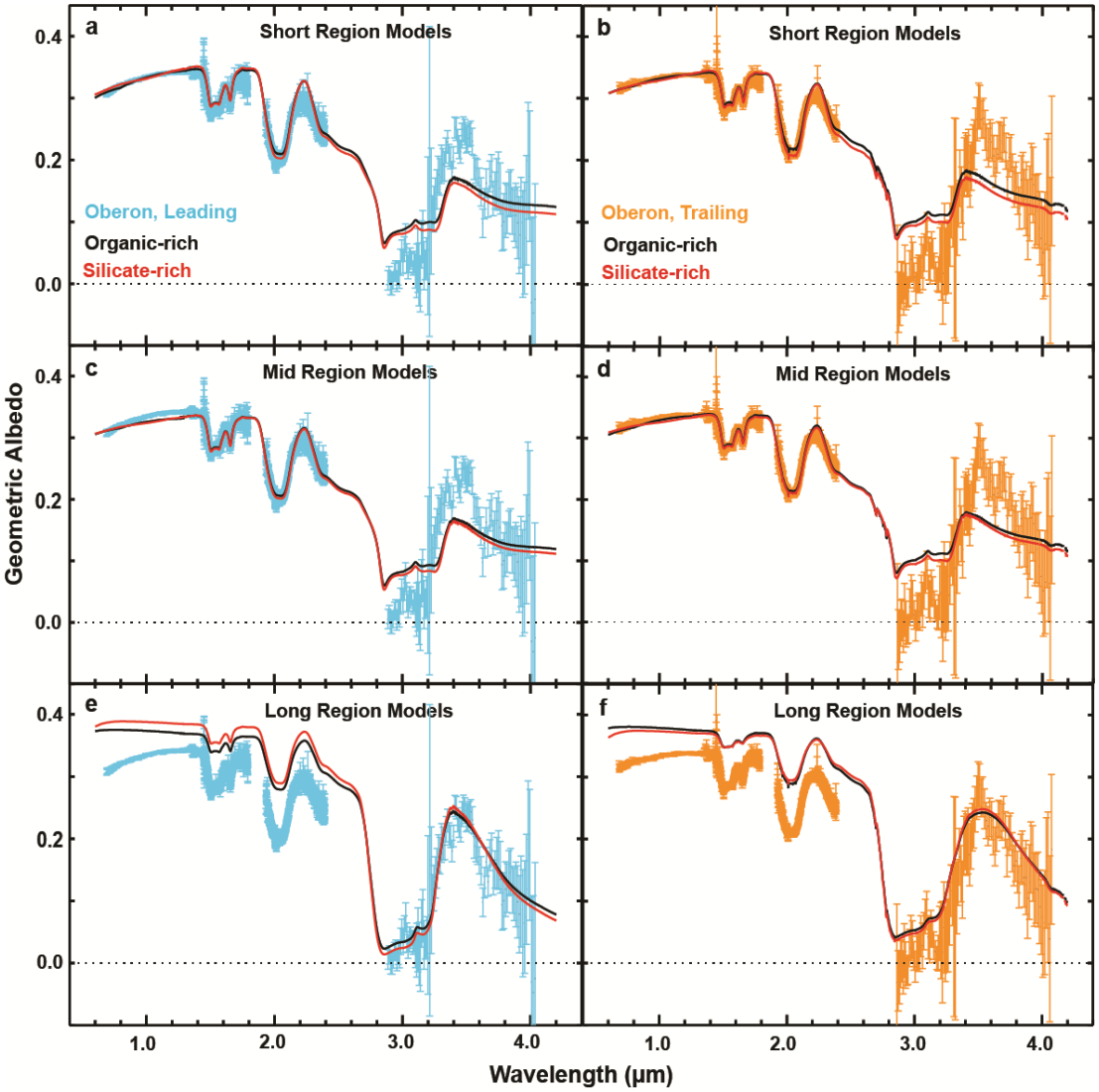

Figure 3.12. Best fit spectral models for the short, mid, and long wavelength regions of Oberon's leading (blue error bars) and trailing (orange error bars) hemisphere. Models including Triton tholins (black) and pyroxene (red) shown for each wavelength region. (see Table 3.14 for summary of model components and constituent grain sizes).

Appendix 3-A: IRTF/SpeX spectra analyzed in this study

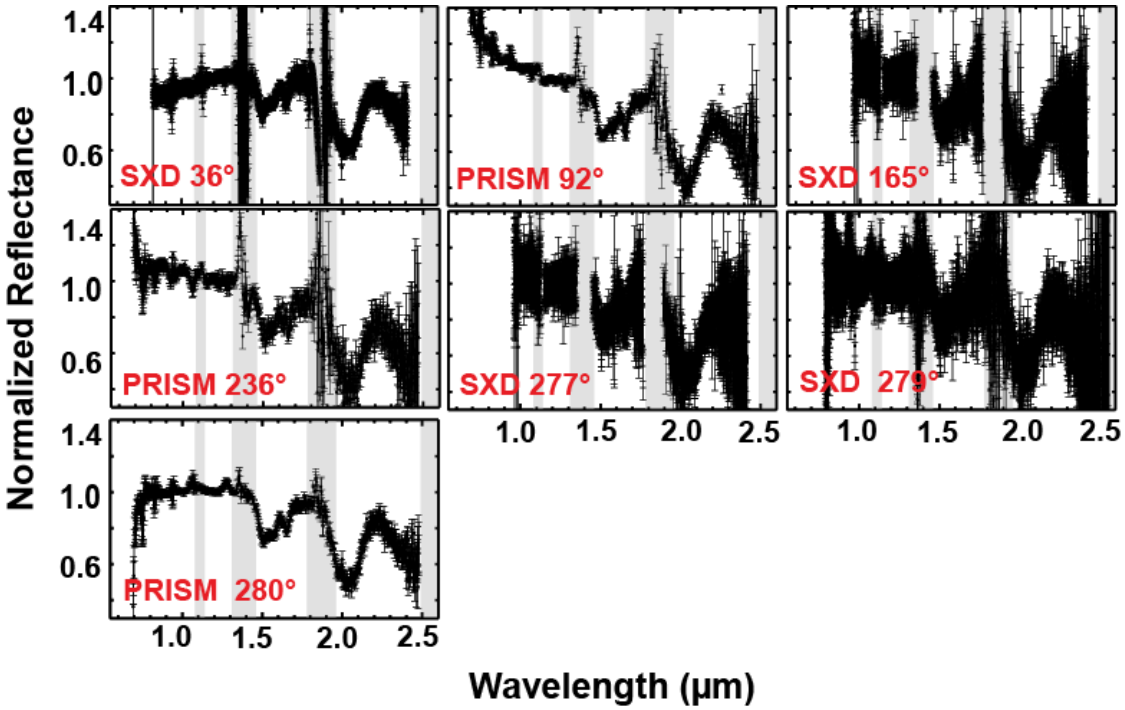

Figure 3-A.13. Seven SpeX spectra of Miranda (SXD and PRISM modes), organized by increasing mid-observation satellite longitude (listed in bottom lefthand corner of each plot). Each spectrum is normalized to its mean reflectance between 1.20 and 1.22 μm. Wavelength range of telluric bands are indicated by light gray shaded regions.

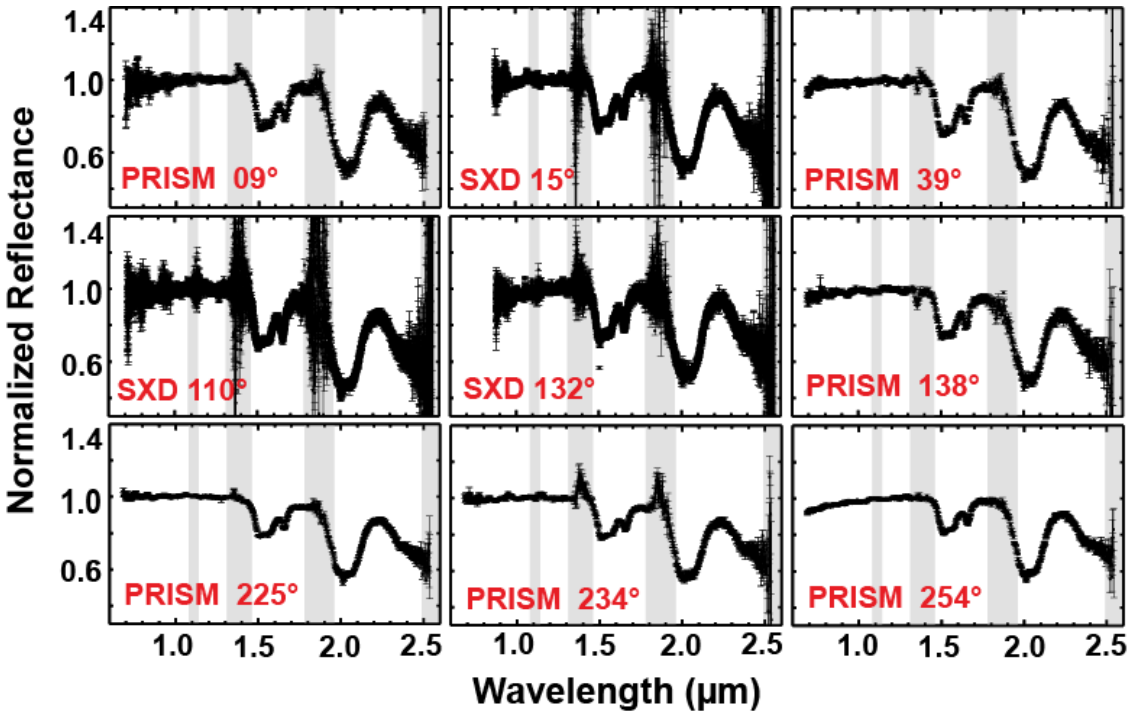

Figure 3-A.14. Nine SpeX spectra of Ariel (SXD and PRISM modes), organized by increasing mid-observation satellite longitude (listed in bottom lefthand corner of each plot). Each spectrum is normalized to its mean reflectance between 1.20 and 1.22 μm. Wavelength range of telluric bands are indicated by light gray shaded regions.

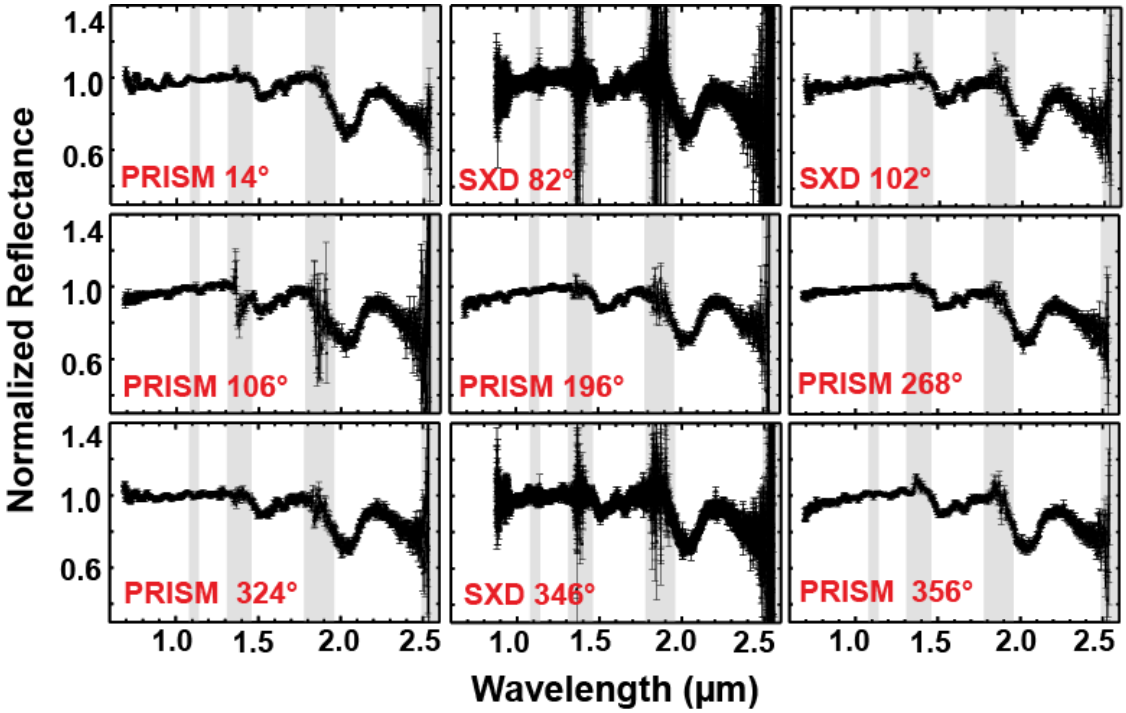

Figure 3-A.15. Nine SpeX spectra of Umbriel (SXD and PRISM modes), organized by increasing mid-observation satellite longitude (listed in bottom lefthand corner of each plot). Each spectrum is normalized to its mean reflectance between 1.20 and 1.22 μm. Wavelength range of telluric bands are indicated by light gray shaded regions.

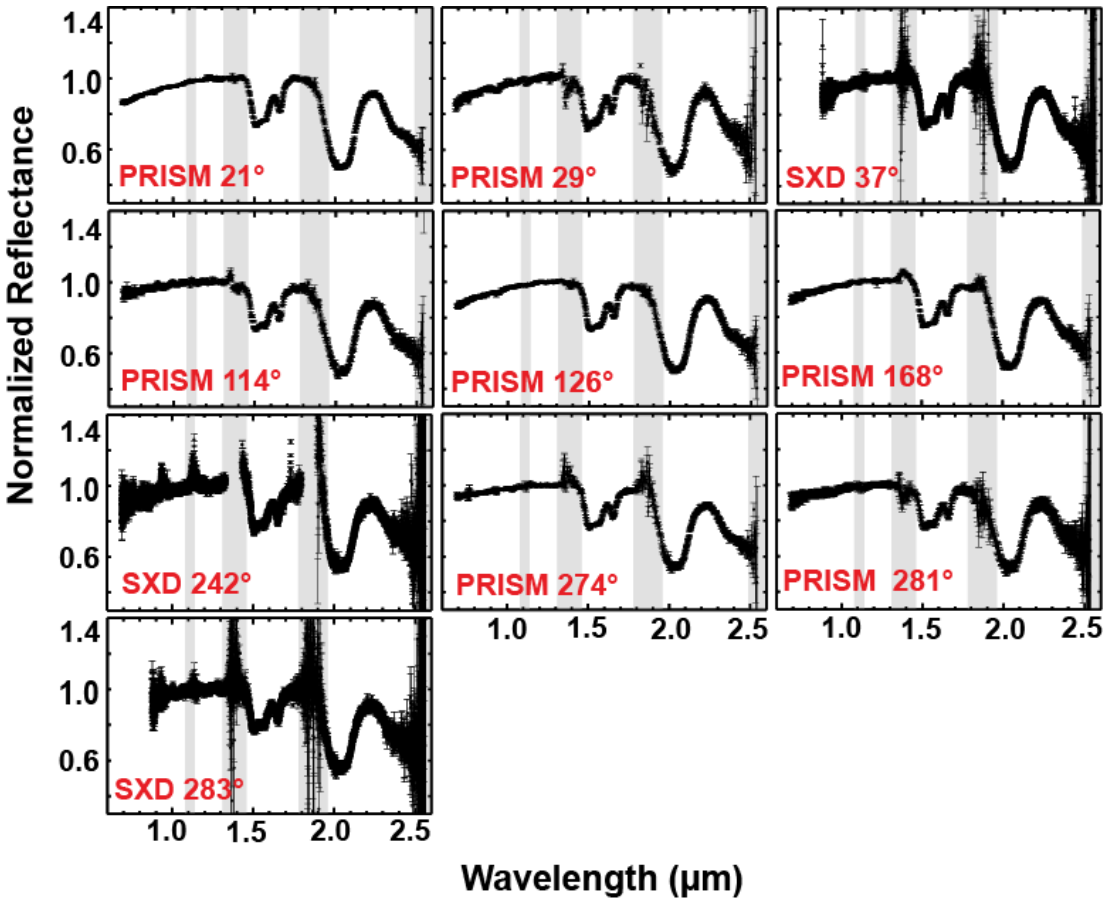

Figure 3-A.16. Ten SpeX spectra of Titania (SXD and PRISM modes), organized by increasing mid-observation satellite longitude (listed in bottom lefthand corner of each plot). Each spectrum is normalized to its mean reflectance between 1.20 and 1.22 μm. Wavelength range of telluric bands are indicated by light gray shaded regions.

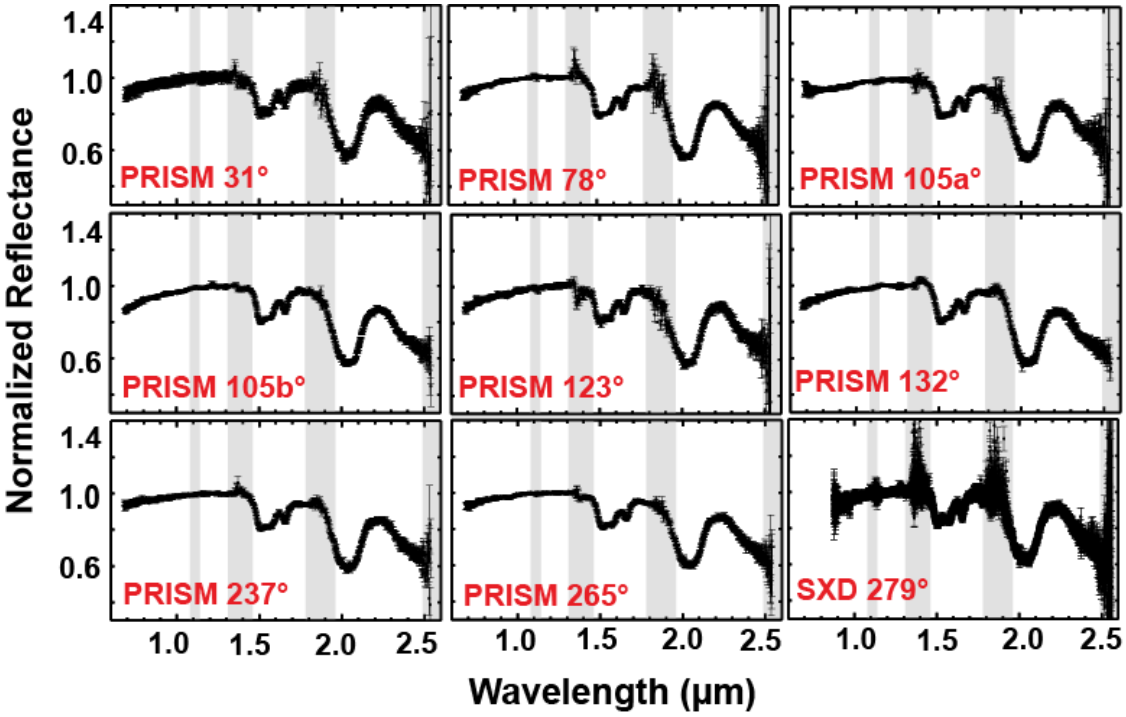

Figure 3-A.17. Nine SpeX spectra of Oberon (SXD and PRISM modes), organized by increasing mid-observation satellite longitude (listed in bottom lefthand corner of each plot). Each spectrum is normalized to its mean reflectance between 1.20 and 1.22 μm. Wavelength range of telluric bands are indicated by light gray shaded regions.

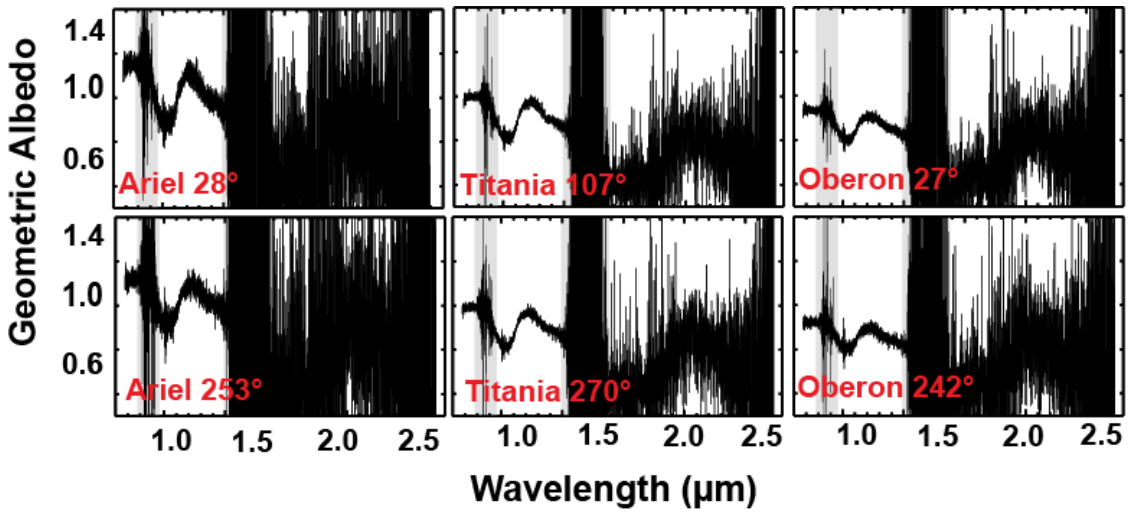

Figure 3-A.18. Six SpeX spectra (LXD mode) of Ariel, Titania, and Oberon, organized by increasing mid-observation satellite longitude (listed in bottom lefthand corner of each plot). Each spectrum is normalized to its geometric albedo. Wavelength range of telluric bands are indicated by light gray shaded regions.

CONCLUSIONS

This dissertation investigates surface modification by space weathering processes on the classical Uranian moons and fluvial modification of Saturn's moon, Titan. Exploration of these processes increases our knowledge of the evolving surfaces of both airless icy bodies and those with large atmospheres, which could provide key insight into similar icy objects orbiting stars beyond our Solar System. In Chapter 1, I find that CO_2 ice is present primarily on the trailing hemispheres of the inner moons, Ariel and Umbriel. The longitudinal and planetocentric trends in the distribution of CO_2 ice support my hypothesis that charged particle bombardment drives a radiolytic production cycle of CO_2 on these moons. Furthermore, the spectral characteristics of the detected CO_2 ice bands (relative band strengths and central positions) are consistent with pure and segregated CO_2 ice, indicating that this constituent is concentrated in deposits of mostly pure CO_2. These results, from data gathered over the northern latitudes of these moons (subsolar point ~17 – 35ºN), are consistent with previous detections of CO_2 in spectra collected over their southern hemispheres (subsolar point ~6 – 25ºS). Therefore, CO_2 ice deposits appear to be concentrated at low latitudes on these moons, with no identifiable northern or southern latitudinal preference.

In Chapter 2, I find that the radar backscatter (in terms of σ^0) from low- and mid-latitude possible fans on Titan are consistent with debris flow fans along the Panamint Range, and that σ^0 for high latitude possible fans are consistent with Panamint sheetflood fans. These results do not support my linked hypotheses that (1) sheetflood fan formation mechanisms dominate fan development at low and mid latitudes on Titan, where giant sand seas offer clear evidence of sand available for transport, and (2) debris flows dominate fan formation at high latitudes, where sand seas are absent, suggesting transportable sand grains are relatively scarce. I offer a suite of scenarios to explain my curious results, including: sheetflood deposits on Titan are relatively bright compared to those on Earth, debris flow deposits are relatively dark, alluvial fan formation mechanisms operate differently in the low gravity environment of Titan, and fan-shaped fluvial features formed by non-alluvial processes.

In Chapter 3, I find that red material is concentrated on the leading hemispheres of the outer satellites, Titania and Oberon (subsolar point ~17 – 35ºN), consistent with Voyager 2 observations of these moons (subsolar point ~81ºS), indicating that spectrally red material is present at all observed latitudes. The planetocentric, longitudinal, and latitudinal trends in the distribution of red material on these moons are consistent with the accumulation of red dust from retrograde irregular satellites, thereby supporting my hypothesis. I also uncovered other compositional mysteries while investigating the classical Uranian moons, including: the distribution of constituents appears to be different on Miranda compared to the other large moons, H_2O ice bands are slightly stronger on the northern-trailing quadrants of Ariel, Umbriel, and Titania compared to their southern-trailing quadrants, and the leading hemisphere of Titania is significantly redder than Oberon (unlike the Voyager 2 results). Furthermore, some of the spectra for each moon display a weak absorption band centered near 2.2 μm, which hint at the possible presence of NH_3-hydrates on these moons.

VITA

Richard J. Cartwright was born on September 10, 1979, in Stoke on Trent, UK. He is the son of Patricia and Terence Cartwright and has one younger brother, Jonathan Cartwright. At the age of ten, his family immigrated to the United States of America, where they all currently reside. After moving to the USA, he lived in Sarasota, FL, and then Atlanta, GA. He attended college at Oglethorpe University in Atlanta, graduating in 2002 with an B.A. in English. After a few years in the private sector, he decided to follow his passion for knowledge, in particular for planetary science, and pursued a Master's degree in Geosciences at Georgia State University. He graduated in 2009, with an M.A. in Geosciences. His Master's thesis focused on fluvial modification of Saturn's moon, Titan, written under the guidance of Dr. Jordan Clayton. He then pursued a Ph.D. in Geology at the University of Tennessee, under the guidance of Dr. Devon Burr and Dr. Joshua Emery, and committee members Dr. Jeffrey Moersch and Dr. Nicholas Nagle. After finishing his doctorate, he will continue his career as a planetary astronomer, working with Dr. Dale Cruikshank at NASA's Ames Research Center in Mountain View, CA.